UC Santa Barbara
UC Santa Barbara Electronic Theses and Dissertations

Title

Investigating the C–H Bond Activation Mechanism at Phosphorus(V) Oxides using Vanadium Phosphorus Oxide (VPO) Model Complexes

Permalink

https://escholarship.org/uc/item/1q14d1pv

Author

Carroll, Timothy Gary

Publication Date

2020

Peer reviewed|Thesis/dissertation

UNIVERSITY OF CALIFORNIA

Santa Barbara

Investigating the C–H Bond Activation Mechanism at Phosphorus(V) Oxides using

Vanadium Phosphorus Oxide (VPO) Model Complexes

A dissertation submitted in partial satisfaction of the

requirements for the degree Doctor of Philosophy

in Chemistry

by

Timothy Gary Carroll

Committee in charge:

Professor Gabriel Ménard Chair

Professor Trevor Hayton

Professor Susannah Scott

Professor Mahdi Abu-Omar

September 2020

The dissertation of Timothy Gary Carroll is approved.

_____

Trevor Hayton

_____

Susannah Scott

_____

Mahdi Abu-Omar

_____

Gabriel Ménard, Committee Chair

August 2020

Investigating the C–H Bond Activation Mechanism at Phosphorus(V) Oxides using

Vanadium Phosphorus Oxide (VPO) Model Complexes

ACKNOWLEDGEMENTS

committee, including Prof. Lior Sepunaru, for their guidance, time, and helpful discussions throughout my PhD.

Next, I would like to thank my family. Words cannot begin to describe how indebted I am to my parents. Mom, thank you for your constant support. You were always just a phone call away, but you never hesitated to fly across the country to simply lift me back up when I was down. Dad, thank you exemplifying honesty, integrity, and hard work. You are my utmost role model. Thank you to all of my sisters, Maddy, Nikki, Leann, and Olivia, as well as all the extended family (there are way too many to name), and of course the little ones - Vera, Inara, Myra, Aldan, and Lucas, who always manage to brighten my day. Finally, to my best friend and partner, Maša. Thank you for encouraging, supporting, and loving me every step of the way. Volim te.

TIMOTHY GARY CARROLL

Santa Barbara, CA · 610-858-3744 · TimCarroll53@gmail.com
https://www.linkedin.com/in/timothy-carroll-615545162/

EDUCATION

Ph.D. in Chemistry | University of California, Santa Barbara (UCSB)   2020
Certificate in College and University Teaching

B.S. in Chemistry, *Summa cum laude* | Lebanon Valley College, PA   2015

RESEARCH PUBLICATIONS

1. Keener, M.; Hunt, C.; **Carroll, T. G**.; Dobrovetsky, R.; Hayton, T. W.; Ménard, G.* "Redox-Switchable Chelation for Uranium Capture and Release" *Nature.* **2020**, *577,* 652-655.
2. **Carroll, T. G**.; Hunt, C.; Garwick, R.; Wu, G.; Dobrovetsky, R.; Ménard, G.* "An Untethered C_{3v}-Symmetric Triarylphosphine Oxide Locked by Intermolecular Hydrogen Bonding." *Chem Commun.* **2019**, *55*, 3761-3764.
3. **Carroll, T. G**.; Chu, J.[‡]; Wu, G.; Telser, J. Dobrovetsky, R.; Ménard, G.* "Probing Hydrogen Atom Transfer at a Phosphorus(V) Oxide Bond Using a "Bulky Hydrogen Atom" Surrogate: Analogies to PCET," *J. Am. Chem. Soc.*, **2018**, *140*, 15375-15383.
4. **Carroll, T. G**.; Garwick, R.; Wu, G.; Ménard, G.* "A Mono-, Di-, and Trivanadocene Phosphorus Oxide Series: Synthesis, Magnetism, and Chemical/Electrochemical Properties." *Inorg. Chem.* **2018**, *57*, 11543-11551.
5. **Carroll, T. G**.; Garwick, R.; Telser, J.; Wu, G.; Ménard, G.* "Synthesis, Characterization, and Electrochemical Analyses of Vanadocene Tetrametaphosphate and Phosphinate Derivatives." *Organometallics* **2018**, *37*, 848-854.

RESEARCH PRESENTATIONS

1. **Carroll, T. G**.; Ménard, G.* *Gordon Research Seminar: Inorganic Reaction Mechanisms.* Galveston, TX. March 2019. (Invited oral presentation and poster presentation)
2. **Carroll, T. G**.; Ménard, G.* *The Chemical Student Seminar Series.* University of California, Santa Barbara. March 2019. (Oral presentation).
3. **Carroll, T. G**.; Ménard, G.* *Southern California Organometallics Seminar.* University of Southern California. Los Angeles, CA. February 2019. (Oral and poster presentation).
4. **Carroll, T. G**.; Ménard, G.* *Southern California Organometallics Seminar.* University of California, Los Angeles, CA. December 2016. (Oral and poster presentation).
5. **Carroll, T. G**.; Ménard, G.* Wu, G.; *ACS National Meeting and Expo.* Philadelphia, Pa. Sept. 2016. (Poster presentation).
6. **Carroll, T. G**.; Ménard, G.; Wu, G.; *ACS National Meeting and Expo.* San Diego, Ca. March 2016. (Poster presentation).

INSTUCTIONAL AND TEACHING EXPERIENCE

General Chemistry III, *Lecturer* | UCSB   2019
- Taught a section of over 100 undergraduate students three times a week
- Collaborated with colleagues on curriculum development and student learning outcome evaluations
- Developed original teaching materials, applied innovative instructional technology, integrated current associated literature, and provided demonstrations

Organic Chemistry Lab I/II, *Lab Teaching Assistant* | UCSB   2017, 2018, 2019, 2020
- Taught chemical instrumentation (NMR, UV/Vis, FTIR, etc.) as well as organic laboratory techniques (chromatography, recrystallization, distillation, extractions, sublimations, etc.) twice a week to four sections of undergraduate students while enforcing laboratory safety

Advanced Inorganic Chemistry, *Graduate Teaching Assistant* | UCSB   2018, 2019
- Led discussion sections and elaborated difficult inorganic chemistry concepts to 45 advanced undergraduate and graduate students twice a week, receiving positive evaluations
- Collaborated and co-taught with the senior professor to maintain currency of curriculum

Inorganic Synthesis Lab, *Lab Teaching Assistant* | UCSB   2017, 2020
- Integrated aspects of quantitative chemical analysis, physical chemistry and inorganic synthesis to guide a class of twenty senior undergraduate chemistry students through multi-week procedures utilizing GC-MS, AAS, and Fluorescence spectroscopy

General Chemistry Lab I/II/III, *Laboratory Teaching Assistant* | UCSB   2015-2016
- Developed and delivered pre-lab lectures twice a week to seven sections of primarily freshmen undergraduate students; totaling over 200 students

HONORS AND AWARDS

Phillip Joshua Chase Mabe Memorial Fellowship	2019
Sandra Lamb Memorial Award	2019
Robert H. DeWolfe Graduate Teaching Award (x3)	2017,2018, 2019
Outstanding Service to the Department Award (x3)	2017, 2018, 2019
Mellichamp Academic Initiative in Sustainability Fellowship	2016

ABSTRACT

Investigating the C–H Bond Activation Mechanism at Phosphorus(V) Oxides using

Vanadium Phosphorus Oxide (VPO) Model Complexes

by

Timothy Gary Carroll

Alkanes, or saturated hydrocarbons, have long been zealously exploited for their

energy content through combustion processes; however, practical processes for

converting them directly to higher value commodity chemicals remain limited. This

stems from the inherent inertness of alkanes and the subsequent difficulty in activating

their strong and localized C–C and C–H bonds. The introduction of functionality into

unactivated C–H bonds incites many practical advantages – from offering new

methodologies for fine chemical synthesis, to far-reaching implications of replacing our

current alkane petrochemical feedstocks. For the past several decades, there has been

tremendous work in utilizing transition-metal complexes to activate inert C–H bonds and

install functionality under mild conditions. While profitable practical applications remain

a long-term goal, our mechanistic understanding of these transition-metal mediated

transformations has advanced tremendously, and has provided a framework to recognize

new strategies for useful C–H bond activation.

For example, recent computational studies suggest that the phosphate support in

the commercial vanadium phosphate oxide (VPO) catalyst – used for the partial oxidation

of butane to maleic anhydride – may play a critical role in initiating butane C–H bond activation through a mechanism termed reduction-coupled oxo activation (ROA), similar to proton-coupled electron transfer (PCET); however, there has been a general lack of experimental evidence to support this mechanism. Herein, we present a wide library of molecular model compounds to examine the validity of the proposed ROA mechanism, which incites C–H bond activation through a main-group/transition metal cooperative mechanism. We report the synthesis, characterization, and reactivity of a series of mono/multi-metallic vanadium phosphate complexes, including the first experimental evidence supporting the proposed ROA mechanism using 1,4-(bistrimethylsilyl)-pyrazine as a "bulky hydrogen" surrogate. Detailed analyses of possible reaction pathways, involving the isolation and full characterization of potential step-wise intermediates, as well as the determination of minimum experimentally and computationally derived thermochemical values are described. Additionally, ongoing work has shown that careful electronic tuning of these vanadium phosphate complexes can enable enhanced reactivity towards weak C–H bonds.

TABLE OF CONTENTS

LIST OF SCHEMES

LIST OF TABLES

Chapter 1

Introduction

1.1 The Chemistry and Environmental Implications of C–H bonds

Alkanes constitute the cheapest and most abundant feedstock for organic chemicals. They are often referred to as "hydrocarbons" owing to their saturated carbon and hydrogen skeletons. However, manipulating these carbon-carbon (C–C) and carbon-hydrogen (C–H) bonds represents a highly difficult task, which is in part due to the high thermodynamic stability and kinetically inert nature of hydrocarbons.[1,2] Consequently, for the last two centuries we have exploited alkanes and hydrocarbons for the chemical energy stored in their inert C–C and C–H bonds via combustion. Today, over 80% of the world's primary energy comes from burning hydrocarbons in the form of fossil fuels (oil, natural gas, coal), which has contributed to the accelerated rise in global atmospheric carbon dioxide levels (CO_2), the fully oxidized byproduct of hydrocarbon combustion.[3] As of 2018, atmospheric CO_2 concentrations have skyrocketed from pre-industrial levels (~280 ppm) to over 410 ppm, with the overwhelming consensus among the scientific community that the continued rise in anthropogenic carbon emissions will have irrevocable impacts on the global climate.[4-5]

The shift away from burning fossil fuels with require considerable technological innovation and socioeconomic changes. For the past several decades, researchers have investigated ways of installing functionality into the carbon-hydrogen skeletons of fossil

fuels rather than simply burning them for their energy content.[6-13] Although there are several challenges associated with practical alkane conversion, arguably the most difficult challenge arises from selectivity among C–H bonds as the reactivity is governed by the trends in relative bond strength (tertiary C–H < secondary C–H < primary C–H < CH_4). The terminal positions of primary alkanes will therefore be the least reactive as they have the strongest C–H bonds, leading to the overall order of reactivity: tertiary C–H > secondary C–H > primary C–H > CH_4 (Scheme 1.1).[14] Unfortunately, the terminal positions of alkanes are often the most desirable in terms of installing functionality and upscaling commodity chemicals. For example, plasticizer and detergent alcohols contain a hydroxyl group at the end of an alkyl chain,[15] while diols or diamines for polymerization reactions contain two hydroxyl or amino groups at either end of the alkyl chain. Moreover, as functionality is installed into the hydrocarbon skeleton, C–H bonds adjacent to functional groups tend to become more reactive than the original alkane, which may impede the overall selectivity of the product stream.[16,17]

Scheme 1.1: Thermodynamics of gas-phase C–H bond homolysis.[13]

Increasing Reactivity

H−CH₃   H−CH₂CH₃

104.9 kcal/mol   101.1 kcal/mol   98.6 kcal/mol   96.5 kcal/mol

Increasing Bond Strength
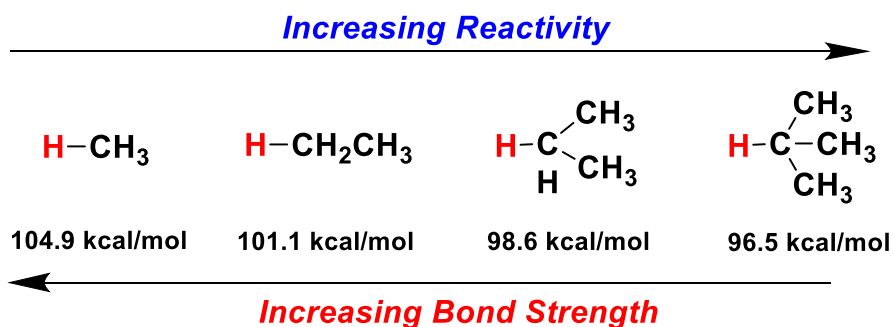
In order to overcome these challenges, transition metal complexes have been employed to activate and functionalize a variety of C–H bonds, often under remarkably mild conditions and with good selectivity. Unfortunately, the majority of these methods utilize unsustainable precious metals and remain impractical for large-scale commercial operations.[1,2,18-21] Nevertheless, our mechanistic understanding of metal mediated C–H bond activation has advanced significantly, with the two major approaches encompassing direct and indirect reactions with transition metal centers. Direct transition metal mediated C–H bond activation mechanisms include: oxidative addition, sigma-bond metathesis, electrophilic substitution, and 1,2 addition (Scheme 1.2).[1,22-25] Oxidative addition reactions typically involve coordinately unsaturated, electron-rich metal centers, and increases both the oxidation state and coordination number of the metal center. On the other hand, sigma-bond metathesis reactions typically occur at electron deficient metal centers with d^0 configurations. In all direct reaction cases there is the formation of metal-alkyl complexes, but there has also been evidence for indirect metal mediated C–H bond activation through a radical rebound mechanism (Scheme 1.2).[26,27] In this case, (most commonly invoked in mechanistic investigations of the enzyme cytochrome P450)[28] transition metal-oxo moieties initiate C-H bond activation to form a metal hydroxide and an alkyl radical.[29-31] The alkyl radical can then recombine with the metal hydroxide to generate the corresponding alcohol.

Scheme 1.2: Traditional Organometallic C–H bond activation mechanisms.

1) Direct Reaction with Transition Metal

a) Oxidation Addition

$$R\text{-}H + M^n\text{-}X \longrightarrow \left[\begin{array}{c} R\text{---}H \\ M\text{-}X \end{array} \right]^{\ddagger} \longrightarrow M^{n+2}(R)(H)(X)$$

c) Sigma-Bond Metathesis

$$R\text{-}H + M^n\text{-}R' \longrightarrow \left[\begin{array}{c} R\text{---}H \\ M\text{---}R' \end{array} \right]^{\ddagger} \longrightarrow R\text{-}M^n + R'\text{-}H$$

b) Electrophilic Substitution

$$R\text{-}H + M^n\text{-}X \longrightarrow \left[\begin{array}{c} R\text{---}H \\ M\text{---}X \end{array} \right]^{\ddagger} \longrightarrow R\text{-}M^{n+} + X\text{-}H$$

d) 1,2 Addition

$$R\text{-}H + M^n\text{-}X \longrightarrow \left[\begin{array}{c} R\text{---}H \\ M\text{=}X \end{array} \right]^{\ddagger} \longrightarrow R\text{-}M^n\text{-}XH$$
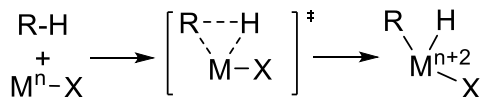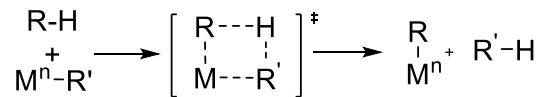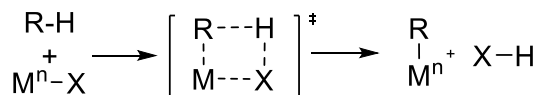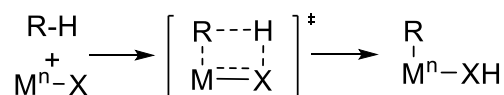
2) Indirect Reaction with Transition Metal

a) Radical Rebound

$$R\text{-}H + O\text{=}M^n \longrightarrow \left[\begin{array}{c} O\text{-}H\text{-}R \\ M^n \end{array} \right]^{\ddagger} \longrightarrow HO\text{-}M^{n-1} + R\cdot \longrightarrow H\text{-}O(R)\text{-}M^{n-2}$$
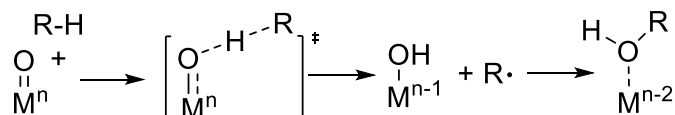
Mechanistic probes have been the key to unlocking the advantages and disadvantages for each of these classic organometallic C–H activation mechanisms, and has led to the development of many transition metal catalysts for the selective functionalization of C–H bonds. Consider for example how mechanistic probes of σ-bond metathesis pathways have resulted in a clear progression in the discovery of catalysts that better activate as well as functionalize C−H bonds.[32] Despite these advances, Scheme 1.2 is certainly not an exhaustive list of C–H activation mechanisms. For example, recent computational work by Goddard and co-workers has suggested a mechanism, similar to a multisite proton-coupled electron transfer (MS-PCET), coined "reduction coupled-oxo activation" for the intial C–H bond activation of butane over vanadium phosphorus oxide (VPO) heterogeneous catalysts.[33] In order to better understand this proposed mechanism, we will first consider the history, structure, and reactivity of VPO catalysts.

1.2 A Brief Background on Vanadium Phosphorus Oxide (VPO) Catalysts

The vanadium-phosphorus oxide catalyst is an industrial heterogeneous catalyst mediating the selective partial oxidation of butane to maleic anhydride. Starting from the initial C–H activation of butane, this catalyst undergoes a remarkable 14-electron transformation involving the abstraction of eight hydrogen atoms and the insertion of three oxygen atoms to eventually provide maleic anhydride in moderate yield (50-55%) (Scheme 1.3).[34-36] In comparison with other selective industrial hydrocarbon oxidation processes, it is considered one of the most mechanistically complex and is one of the few industrial oxidation catalysts involving direct alkane activation.[37]

Scheme 1.3: partial oxidation of butane to maleic anhydride
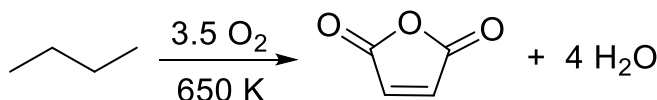
This highly selective catalyst (65-70%) is responsible for the production of over 500 kilotons of maleic anhydride annually, which is commonly used as starting material or resin for various polymerizations. Therefore, countless studies have been conducted to not only improve the overall catalyst yield, but to also gain a deeper mechanistic understanding of this complex reaction sequence.[35,38-41]

Elucidating the mechanism of butane oxidation over VPO has largely been impeded by the inherent complexity of the heterogeneous systems used, which may be regarded as a three-phase system: (i) a gas phase, (ii) a solid phase, and (iii) a two-dimensional surface

region at the gas-solid interface composed of the surface solid phases and interacting adsorbed molecules.[42] Therefore, mechanistic investigations of heterogeneous catalysts often require a multidisciplinary approach that combines concepts from various subsets of chemistry and engineering.

1.2.1 Structure of the VPO catalyst

The structure of VPO can be broadly described as a conglomerate of vanadyl polyhedra tethered together with tetrahedral phosphate linkers. The main phase of the catalyst has been identified as the reduced vanadyl pyrophosphate, $(VO)_2P_2O_7$, denoted as VOPO.[43] The idealized valence bond depiction of VOPO is depicted in Figure 1.1, and has been studied in great detail.[44-47] Note that each vanadium atom has a V=O bond oriented *trans* to one another, leading to a V^{IV} oxidation state with a singly occupied d_{xy} orbital located on the vanadium atom. Each layer within the crystalline VOPO lattice is approximately 3.91 Å apart with evidence of antiferromagnetic coupling.[48] The phosphorus atoms have three P–O single bonds that link together two vanadium atoms and one neighboring phosphorus atom, thus leaving the P=O double bond capable of datively bonding with a neighboring vanadium atom.
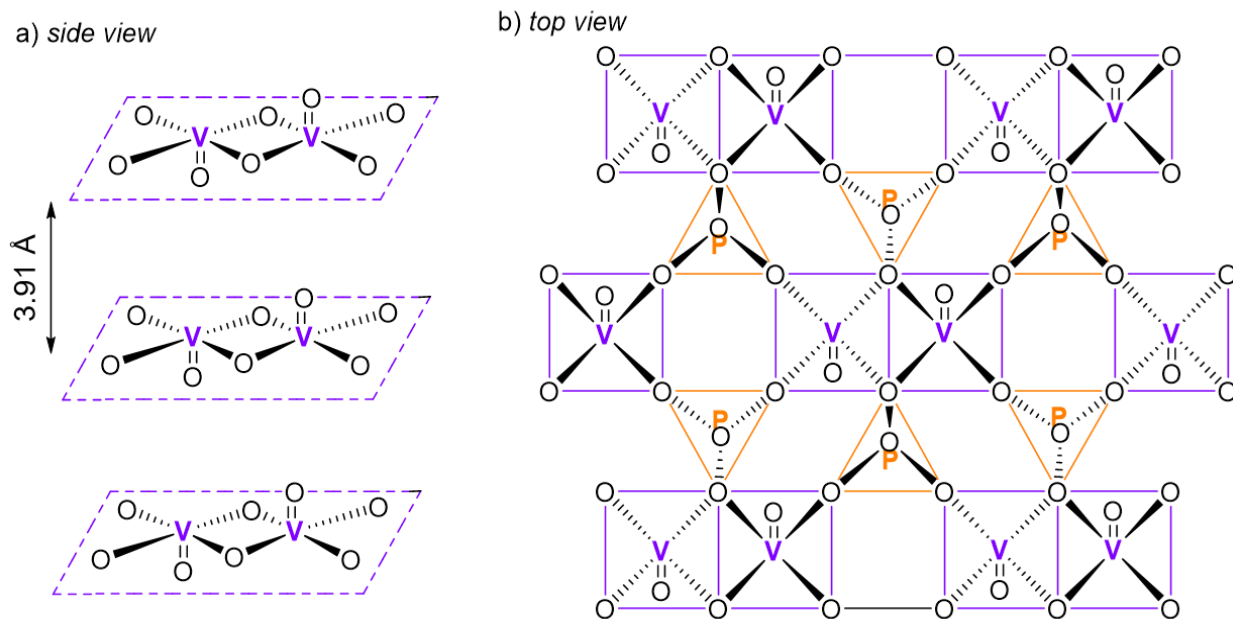
Figure 1.1: Valence bond description of crystalline $(VO)_2P_2O_7$ (VOPO). a) side view of the interstitial vanadyl layers, with an average distance of 3.91 Å between each layer. b) top view of a single layer of connectivity between vanadyls and the phosphate support linkers.

While VOPO has been identified as the main phase of the VPO catalyst, there has been evidence that participation of V^{5+} species is necessary for butane oxidation.[49,50] Certainly high-valent vanadium species has been shown to homogeneously oxidize alkanes and furans, thus participation from V^{5+} is highly likely.[51] Upon exposure to oxygen at high temperatures, the ordered VOPO lattice is capable of oxidation to $VOPO_4$, thereby changing the surface morphology of the working catalyst. There are five predominant phases of the oxidized catalyst $VOPO_4$: α_1, α_2, β, δ, and X1. The calculated phase stability in reference to VOPO are as follows: X1 (-49.6 kcal/mol), α_1 (-193.4 kcal/mol), α_2 (-211.2 kcal/mol), β (-218.6 kcal/mol), δ (-219.7 kcal/mol), with the X1 phase considered as the

highest energy phase.[52] In comparison to the extended structure of VOPO (Figure 1.1), the oxidized phases of VOPO$_4$ show very little structural change at the vanadium atoms, however, the phosphorus linkers exhibit changes in connectivity. All phases (α_1, α_2, β, δ, and X1) retain the square pyramidal vanadyl structure prevalent in VOPO, but the pyrophosphate is proposed to be converted into an orthophosphate in concurrence with oxidation of the vanadium atom (Scheme 1.4).[35] Understanding these subtle differences in connectivity and oxidation state is important for identifying the active phase of the VPO catalyst.

Scheme 1.4: Valence Bond description of the proposed oxidation of VOPO to VOPO$_4$. The vanadyl groups are omitted for clarity.
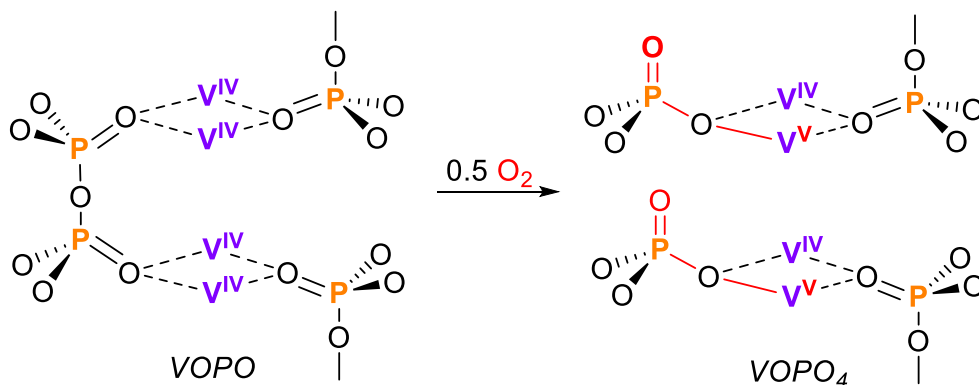
In addition to the VPO phases described above, there has been evidence of other vanadium-phosphorus phases. For example, the formation of $VO_2(H_2PO_4)_2$ has been characterized as a byproduct of incomplete activation of the $VOHPO_4 \cdot 0.5\ H_2O$ catalyst precursor.[53-54] $V(PO_3)_3$, $VO(PO_3)_2$, and other polyphosphates, including poorly crystalline/amorphous VPO phases, have also been identified in the working VPO catalyst,

however these phases are considered to contribute to catalyst degradation and are inactive to butane oxidation.[55-60]

The complexity that arises from the facile changes in VPO morphology, oxidation state, and V:P ratio, has led to contradictory findings regarding the identity of the catalyst's active phase. Volta et al. suggested that the active site consists of a mixture of well crystallized VOPO and an amorphous $VOPO_4$ surface phase of V^{5+}.[59-60] Similarly, Bordes and Courtine[61,62] suggested that the active site exists at the interface between discrete layers of oxidized $VOPO_4$ and VOPO. On the contrary, Buchanon et al.[57] noted increased catalytic performance after removing soluble V^{5+} surface species with a methanol wash, suggesting – in agreement with Wenig and Schrader – that only VOPO is the active and selective phase in n-butane oxidation to maleic anhydride.[63,64] This debate over the active phase of the catalyst has impeded mechanistic elucidation regarding the initial C–H bond cleavage.

1.3 Proposed mechanisms for oxidation of butane to maleic anhydride over VPO catalysts.

1.3.1 Vanadyl Linkages and Reactive Oxygen Species Proposed as Responsible for C–H Bond Activation of Butane.

After decades of research on VPO catalysts, there is still no consensus for the mechanism of butane oxidation to maleic anhydride. Kinetics data agree that the first step is alkane activation, the mechanism for which still remains uncertain. It has long been assumed that the vanadyl moieties in the VOPO or $VOPO_4$ phases were responsible for C–H bond cleavage through a radical rebound type mechanism similar to that shown in Scheme 1.2.[34,35] Others have challenged this assumption by proposing that adsorbed

oxygen on the VPO catalyst can generate reactive oxygen species (O^{2-}, O^-) capable of abstracting hydrogen atoms from inert alkanes.[34,65,66] However, this hypothesis would seem to contradict the observed selectivity exhibited by the VPO catalyst. In contrast, recent computational studies by Goddard and co-workers advocate that neither the vandyl moieties or reactive oxygen species are capable of butane activation; instead, they suggest that the P=O bonds in the phosphate support participate in the C–H activation step through a "reduction coupled oxo activation" mechanism.[33,52,67,68]

1.3.1 The Reduction-Coupled Oxo Activation Mechanism

Goddard and co-workers have recently reported a series of computational studies examining the active site of the VPO catalyst. The approximate calculated activation barrier for each proposed reactive site according to equation 1.5, where E_a = activation energy, δ = endothermic transition state energy ($\approx$ 5-10 kcal/mol), D_{C-H} = bond energy for the secondary C–H bonds of butane ($\approx$ 100 kcal/mol), D_{SS-H} = bond energy for the resulting "surface site" –H bond.[52] Based on previous reports, the activation barrier for the C–H activation of butane is estimated to be between 12.9-23.6 kcal/mol,[69] therefore the minimum D_{SS-H} bond energy needs to be approximately 81 kcal/mol.

Scheme 1.5: Activation energy (Ea) formula for the C-H bond activation of butane over VPO surface sites (SS).

$$E_a = \delta + (D_{C-H} - D_{SS-H})$$

First, the D_{SS-H} bond energies for the V–O bonds in the $(VO)_2P_2O_7$ (VOPO) reduced phase, in accordance with the previous dogma that the metal oxide bonds were

responsible for the initial C–H bond activation of butane. However, calculations on the bulk surface of VOPO revealed that neither the V=O bond (vanadyl) or the bridging V–O–P bond were capable of C–H activation of butane with D_{SS-H} bond energies of 58.2 kcal/mol and 17.0 kcal/mol, respectively (Figure 1.2). The minimum calculated E_a values for the vanadyl and bridging V–O–P bond would be approximately 47 kcal/mol and 88 kcal/mol respectively – far too high for the observed reactivity. Therefore, it was determined that the reduced VOPO phase could not be responsible for the C–H bond activation of butane.[52]
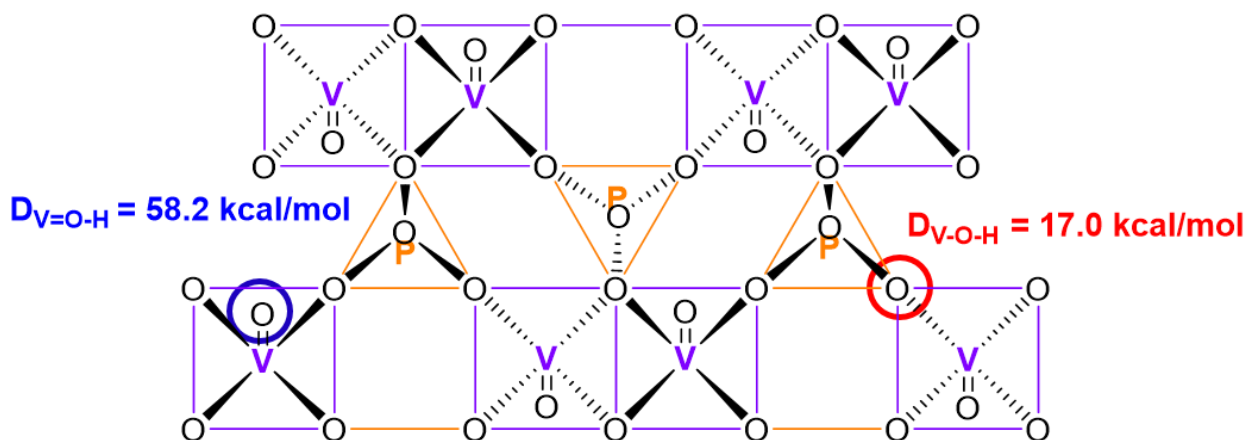
Figure 1.2: Valence bond depiction for the calculated D_{SS-H} bond energies on the well-defined crystalline VOPO surface.

The next logical step was to investigate adsorbed oxygen species as the active site for butane oxidation, as these reactive oxygen species have also been speculated to be responsible for the initial C–H activation step.[34, 65,66] However, the calculated D_{SS-H} bond energies for oxygen on the VOPO surface (D_{O-H} = 70.0 kcal/mol), as well as dissociatively adsorbed oxygen (D_{O-H} = 58.9 kcal/mol) were both too low to be considered the reactive sites.[52]

This systematic approach was also applied to each of the oxidized phases (α_1, α_2, β, δ, X1-VOPO$_4$) of the VPO catalyst, but once again none of the V–O bonds exhibited a strong enough D_{SS-H} bond energy capable of explaining the H–atom abstraction from butane. After eliminating all probable metal-oxo reactive sites, the phosphate linkers were next investigated. Generally, the phosphate moieties have always been considered as an unreactive catalyst support system that simply serve to bridge together the reactive vanadium catalyst, but there has been increasing evidence that phosphate supports may indeed be active in catalysis through various mechanisms, such as spillover effects, strong metal-support interactions, and more.[70-73]

Finally, interrogation of the P=O double bond on the surface of the X1-VOPO$_4$ phase resulted in a calculated D_{PO-H} bond energy (84.3 kcal/mol) sufficiently large enough to activate the C–H bonds of butane (Scheme 1.6).[52] Consequently, the calculated E_a for the P=O bond would be approximately 20.7 kcal/mol, which is the only site to fall within the range of the estimated E_a for the C–H activation of butane (12.9-23.6 kcal/mol). The surprising reactivity exhibited at the typically "unreactive" P=O was rationalized by a mechanism coined "reduction-coupled oxo activation." Similar to a proton coupled electron transfer (PCET),[74] the electron and proton from the H–atom transfer are decoupled onto two different elements. Reacting the H–atom with the P^V=O bond leads to a P-O-H bond, however instead of the unpaired electron residing on the P^{IV}, a new P^V=O bond is formed and the electron is transferred onto one of the high-valent V^V atoms, thereby reducing it to V^{IV} (Scheme 1.6). Therefore, the P^V=O serves as the proton acceptor and the V^V accepts the electron. The oxidizing power of the V^{+5} center likely contributes to the observed strong D_{PO-H} bond.

Scheme 1.6: Valence bond description of the reduction-coupled oxo activation mechanism and the calculated D_{PO-H} bond energy on the X1-VOPO$_4$ phase. Vanadyl moieties are excluded for clarity.
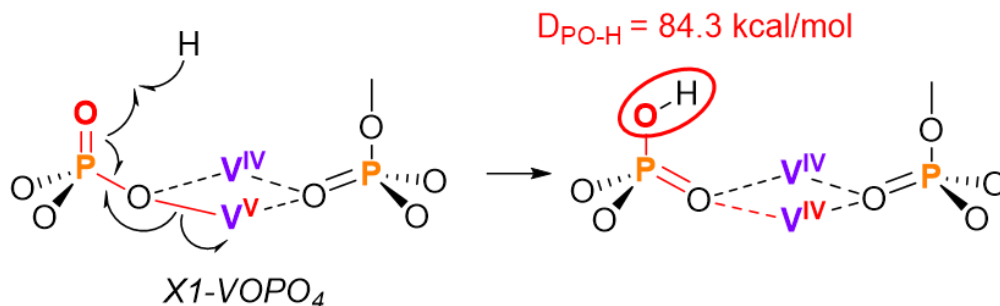
1.4 Mechanistic Implications for Heterogeneous and Homogeneous Catalysts

The proposed ROA mechanism is particularly intriguing because it proposes powerful reactivity and selectivity at a main-group oxide bond, thereby mitigating the need for expensive precious metals. Since main-group oxides are common supports for many heterogeneous catalysts, it may be possible that these "unreactive" catalyst supports may indeed play a bigger role than previously thought. For example, the main-group Te=O bonds of Mo–V–Nb–Te–O catalysts have recently been invoked as the reactive site for the ammoxidation of propane through a similar ROA type pathway.[75-76] The insights gained here could help develop the next generation of heterogeneous catalysts for alkane activation.

Similarly, these concepts may also be useful in designing new homogeneous organometallic catalysts for alkane C–H activation and functionalization. Activating C–H bonds through a ROA-type mechanism may help limit unwanted side reactions on the transition metal, since the transition metal is decoupled from the active site. Additionally, since the C–H activation power is separated by both the basicity of the protonated P=O bond, as well as the reduction potential of the transition metal, there exists some flexibility in tuning each component for selective activation. Prior to our work, however, there was little experimental evidence that homogeneous organometallic compounds were capable of undergoing any ROA-type reactivity, in part because organometallic compounds bearing a well-defined monomeric M-L-P=O motif (M = transition metal, L = organic linker N, O, etc.) are rare in the literature.[77-79]

1.5 Scope of Thesis

As will be described in this thesis, we sought to build homogeneous model compounds with phosphate oxide bonds tethered to transition metals in order to study the proposed ROA mechanism for alkane activation and functionalization. This research began with the synthesis and characterization of a series of new vanadocene-derived tetrametaphosphate or diphenylphosphinate complexes, bearing the general V–O–P=O motif (Chapter 2). While these complexes did not exhibit any observed ROA type reactivity, the unique dimerization pathways are described using electrochemical analyses. Chapter 3 expands this library of vanadocene-derived phosphinate complexes with the synthesis of $B(C_6F_5)_3$-coordinated mono-, di-, and trivanadocene phosphorus oxide complexes. Trends in the Lewis basicity of the P=O bonds, as well as the metal reduction

potentials are described in relation to the ROA mechanism. Additionally, a unique *para*-substituted triphenylphosphine oxide with terminal vanadocene centers is reported, and is, to our knowledge, the first example of an untethered C_{3v}-symmetric triarylphosphine oxide in the solid state (Chapter 4). While none of these initial model compounds exhibited ROA-type reactivity (Chapters 2-4), we aimed to redesign our compounds utilizing high-valent V^V metal centers. Chapter 5 describes molecular model compounds, which are reactive to both weak H atom donors and a Me$_3$Si$^•$ (a "bulky hydrogen atom" surrogate) donor. This research provides the first experimental evidence supporting a ROA-type mechanism and helped inform current work in tuning the reactivity of our model compounds to engage in C–H activation chemistry (Chapter 6).

For Chapters 2, 3, 4, and 6 all synthetic work and spectroscopic characterizations, excluding elemental analyses, were performed by the author. EPR analyses were performed by Prof. Joshua Telser at Roosevelt University. All DFT calculations throughout this report were performed by Prof. Roman Dobrovetsky at Tel Aviv University. Part of the syntheses and spectroscopic analyses were conducted in collaboration with Rachel Garwick, an exemplary undergraduate student. Dr. Guang Wu was invaluable in solving and refining the solid-state structures for all compounds reported. Dr. Camden Hunt was responsible for the electrochemical simulations reported in Chapter 4. For Chapter 5, compounds **5.2, 5.3,** and their corresponding derivatives were initially synthesized and characterized by Dr. Jiaxiang Chu, a former post-doctoral fellow in the group. I would like to thank Dr. Chu for his tremendous contribution, and Gab for the opportunity to collaborate and complete this work. Portions of each chapter are either published or have been drafted at the time of writing:

Chapter 2: Carroll, T. G.; Garwick, R.; Telser, J.; Wu, G.; Ménard, G. *Organometallics* **2018,** *37*, 848-854.

Chapter 3: Carroll, T. G.; Garwick, R.; Wu, G.; Ménard, G. *Inorg. Chem.* **2018**, *16*, 2447-2558

Chapter 4: Carroll, T. G.; Hunt, C.; Garwick, R.; Wu, G.; Dobrovetsky, R.; Ménard, G. *Chem. Comm.* **2019**, *55*, 3761

Chapter 5: Chu, J.*; Carroll, T. G.*; Wu, G.; Telser, J.; Dobrovetsky, R.; Ménard, G. *J. Am. Chem. Soc.*, 2018, **140**, 15375

Chapter 6: *Manuscript in Progress*

1.6 References

(1)   Balcells, D.; Clot, E.; Eisenstein, O. *Chem. Rev.* **2010**, *110*, 749-823.

(2)   Bercaw, J. E.; Labinger, J. A.; *Nature.* **2002**, *417*, 507-514.

(3)   Ritchie, H.; *Fossil Fuels,* Retrieved from: 'https://ourworldindata.org/fossil-fuels',

2017

(4)   *Global Energy and CO$_2$ Status Report*; International Energy Agency, **2018**.

(5)   Kellogg, W. W.; Schware, R. Climate Change and Society: Consequences of

Increasing Atmospheric Carbon Dioxide; Routledge Abingdon, **2019**.

(6)   Liu, W.; Yang, W.; Zhu, J.; Guo, Y.; Wang, N.; Ke, J.; Yu, P.; He, C.; *ACS*

Catal., **2020**,   7207-7215

(7)   Dong, Y.; Clarke, R. M.; Porter, G. J.; Betley, T. A. *J. Am. Chem. Soc.,* **2020**

(8)   Li, C.; Lang, K.; Lu, H.; Hu, Y.; Cui, X.; Wojtas, L.; Zhang, X. P. *Angew.*

Chem., Int. Ed. **2018**, *57*, 16837.

(9)   Lu, H.; Hu, Y.; Jiang, H.; Wojtas, L.; Zhang, X. P. *Org. Lett.* **2012**, *14,* 5158.

(10)   Lu, H.; Jiang, H.; Hu, Y.; Wojtas, L.; Zhang, X. P. *Chem. Sci.* **2011**, *2*, 2361.

(11)   Lu, H.; Lang, K.; Jiang, H.; Wojtas, L.; Zhang, X. P. *Chem. Sci.* **2016**, *7*, 6934.

(12)   Lu, H.; Li, C.; Jiang, H.; Lizardi, C. L.; Zhang, X. P. *Angew. Chem., Int. Ed.* **2014**, *53,* 7028.

(13)   Wilson, E.; *Chem. Eng. News*, **1999**, *77*, 24.

(14)   Crabtree, R. H.; *J. Chem. Soc., Dalton Trans.*, **2001**, 2437–2450.

(15)   Falbe, J.; Bahrmann, H.; Lipps, W.; Mayer, D.; Frey, G. D.; In Ullmann's Encyclopedia of Industrial Chemistry; *Wiley-VCH Verlag GmbH & Co. KGaA*: **2000**.

(16)   Hartwig, J. F.; Larson, M. A.; *ACS Cent. Sci.* **2016**, *2*, 281-292.

(17)   Newhouse, T.; Baran, P. S. *Angew. Chem., Int. Ed.* **2011**, *50*, 3362−3374.

(18)   Crabtree, R. H.; Mellea, M. F.; Mihelcic, J. M.; Quirk, J. M. *J. Am. Chem. Soc.* **1982**, *104*, 107.

(19)   Xu, W. W.; Rosini, G. P.; Gupta, M.; Jensen, C. M.; Kaska, W. C.; Krogh-Jespersen, K.; Goldman, A. S. *Chem. Commun.* **1997**, 2273.

(20)   Liu, F. C.; Pak, E. B.; Singh, B.; Jensen, C. M.; Goldman, A. S. *J. Am. Chem. Soc.* **1999**, *121*, 4086.

(21)   Goldman, A. S.; Roy, A. H.; Huang, Z.; Ahuja, R.; Schinski, W.; Brookhart, M. *Science*, **2006**, *312*, 257.

(22)   Lin, Z. *Coord. Chem. Rev.* **2007**, *251*, 2280

(23)   Bennett, J. L.; Wolczanski, P. T. *J. Am. Chem. Soc.* **1997**, *119*, 10696.

(24)   Slaughter, L. M.; Wolczanski, P. T.; Klinckman, T. R.; Cundari, T. R. *J. Am. Chem. Soc.* **2000**, *122*, 7953.

(25) Cundari, T. R.; Klinckman, T. R.; Wolczanski, P. T. *J. Am. Chem. Soc*. **2002**, *124*, 1481.

(26) Groves, J. T. *J. Chem. Educ*. **1985**, *62*, 928.

(27) Groves, J. T.; McClusky, G. A. *J. Am. Chem. Soc*. **1976**, *98*, 859.

(28) *Cytochrome P450: Structure, Mechanism, and Biochemistry*; de Montellano, P. R. O., Ed.; Springer: New York, **2005**

(29) Metal-Oxo and Metal-Peroxo Species in Catalytic Oxidations (Structure and Bonding); Meunier, B., Ed.; Springer-Verlag: Berlin, **2000**.

(30) *Catalytic Activation and Functionalisation of Light Alkanes- Advances and Challenges*; Derouane, E. G., Haber, J., Lemos, F., Ribeiro, F. R., Guisnet, M., Eds.; Springer: Dordrecht, The Netherlands, **1998**.

(31) *Biomimetic Oxidations Catalyzed by Transition Metal Complexes*; Meunier, B., Ed.; Imperial College Press: London, **2000**.

(32) Waterman, R. *Organometallics,* **2013**, *24*, 7249-7263.

(33) Cheng, M.-J.; Goddard, W. A. *J. Am. Chem. Soc*. **2013**, *135*, 4600−4603.

(34) Handbook of Advanced Methods and Processes in Oxidation Catalysis: from Laboratory to Industry; Duprez, D., Imperial College Press: London, **2014**.

(35) Centi, G.; Trifiro, F.; Ebner, J. R.; Franchetti, V. M. *Chem. Rev.* **1988**, *88*, 55−80.

(36) Contractor, R. M.; Bergna, H. E.; Horowitz, H. S.; Blackstone, C. M.; Malone, B.; Torandi, C. C.; Griffiths, B.; Chowdhry, U.; Sleight, A. W.; *Catal. Today,* **1987**, *1*, 49-58.

(37) Dadyburjor, D. B.; Jewar, S. S.; Ruckenstein, R. *Catal. Rev. Sci. Eng*. **1979**, *19*, 293

(38) Zhang-Lin, Y.; Forissier, M.; Sneeden, R. P.; Vedrine, J. C.; Volta, J. C. *J. Catal.*

1994, *145*, 256−266.

(39)   Chen, B.; Munson, E. J. *J. Am. Chem. Soc.* **1999**, *121*, 11024− 11025.

(40)   Chen, B.; Munson, E. J. *J. Am. Chem. Soc*. **2002**, *124*, 1638−1652.

(41)   Cavani, F.; De Santi, D.; Luciani, S.; Löfberg, A.; Bordes-Richard, E.; Cortelli, C.; Leanza, R. *Appl. Catal*., **2010**, *376*, 66−75.

(42)   In Proceedings, 8th International Congress on Catalysis; Haber, J., Dechema: Frankfurt am Main, **1984**; Vol. I, 85.

(43)   *Heterogeneous catalytic oxidation*. Hodnet, B. K., Wiley: New York, **2000**.

(44)   Gorbunova, Yu. E.; Linde, S. A. *Sov. Phys. Dokl*. **1979**, *24*, 138.

(45)   Nguyen, P. T.; Hoffman, R. D.; Sleight, A. W. *Mater. Res. Bull.*, **1995**, *30*, 1055.

(46)   Saito, T.; Terashima, T.; Azuma, M.; Takano, M.; Goto, T.; Ohta, H.; Utsumi, W.; Bordet, P.; Johnston, D. C. *J. Solid State Chem.,* **2000**, *153*, 124–131.

(47)   Yamauchi, T.; Narumi, Y.; Kikuchi, J.; Ueda, Y.; Tatani, K.; Kobayashi, T. C.; Kindo, K.; Motoya, K. *Phys. Rev. Lett*., **1999**, *83*, 3729–3732.

(48)   Cheng, M. J.; Nielsen, R. J.; Tahir-Kheli, J.; Goddard, W. A. *Phys. Chem. Chem. Phys.*, **2011**, *13*, 9831-1938.

(49)   Bordes, E.; *Topics Catal.*, **2000**, *11*, 61-65

(50)   Coulston, G. W.; Bare, S. R.; Kung, H.; Birkeland, K.; Bethke, G. K.; Harlow, R; Herron, N.; Lee, P. L.; Science, **1997**, *275,* 191-193.

(51)   Langeslay, R. R.; Kaphan, D. M.; Marshall, C. L.; Stair, P. C.; Sattelberger, A. P.; Delferro, M.; *Chem. Rev.*, **2019**, *119* (4), 2128-2191.

(52)   Cheng, M.; Goddard, W. A.; Fu, R.; *Top. Catal*, **2014**, *57*, 1171–1187.

(53)   Van Geem, P. C.; Nobel, A. P. *P. Catal. Today* **1987**, *1*, 5-14.

(54)   Pyatnitskaya, A. I.; Komashko, G. A.; Zazhigalov, V. A.; Gorokhovatskii, Ya. B.
         React. Kinet. Catal. Lett. **1977**, *6*, 341-351.

(55)   Ladwig, G. Z. *Chem.* **1968**, *8*, 307.

(56)   Moser, T. P.; Schrader, G. L. *J. Catal*. **1985**, *92*, 43.

(57)   Buchanan, J. S.; Apostolakis, J.; Sundaresan, S. *Appl. Catal.* **1985**, *19*, 65.

(58)   Martini, G.; Trifiro, F.; Vaccari, A. *J. Phys. Chem*. **1982**, *86*, 1573.

(59)   Bergeret, G.; David, M.; Broyer, J. P.; Volta, J. C.; Hecquet, G. *Catal. Today* **1987**,
         1, 37. (60) Bergeret, G.; Broyer, J. P.; David, M.; Gallezot, P.; Volta, J. C.; Hecquet,
         G. *J. Chem. Soc., Chem. Commun..* **1986**, 825.

(61)   Bordes, E.; Courtine, P. *J. Chem. Soc., Chem. Commun*. **1985**, 294.

(62)   Courtine, P. *In Solid State Chemistry in Catalysis*; Grasselli, R. K., Brazdil, J. F.,
         Eds.; American Chemical Society: Washington, DC, 1985; ACS Symp. Ser. 279.

(63)   Wenig, R. W.; Schrader, G. L. *Ind. Eng. Chem. Fundam*. **1986**, *25*, 612.

(64)   Wenig, R. W.; Schrader, G. L. *J. Phys. Chem*. **1986**, *90*, 6480.

(65)   Kung, H. H.; Ind. Eng. Chem. Prod. Res. Dev. **1986**, 25, 171.

(66)   Joly, J. P.; Mehier, C.; Bere, K. E.; Abon, M. *Appl. Catal. A*. **1998**, *169*, 55.

(67)   Cheng, M.-J.; Fu, R.; Goddard, I. I. I. W. A. *Chem. Commun.* **2014,** *50*, 1748-
         1750.

(68)   O'Leary, W. C.; Goddard, W. A.; Cheng, M.-J. *J. Phys. Chem. C.,* **2017**, *121*,
         24069- 24076.

(69)   Schuurman, Y.; Gleaves, J. T. Ind. Eng. Chem. Res. **1994**, *33*, 2935.

(70)   I. A. Ibarra, T. W. Hesterberg, J.-S. Chang, J. W. Yoon, B. J. Holliday and S. M.
         Humphrey, *Chem. Commun.,* 2013, 49, 7156.

(71)   X.-J. Li, F.-L. Jiang, M.-Y. Wu, L. Chen, J.-J. Qian, K. Zhou, D.-Q. Yuan and
        M.-C. Hong, Inorg. Chem., 2014, 53, 1032.

(72)   Y. Wang, Y. Li, Z. Bai, C. Xiao, Z. Liu, W. Liu, L. Chen, W. He, J. Diwu, Z.
        Chai, T. E. Albrecht-Schmitt and S. Wang, Dalton Trans., 2015, 44, 18810.

(73)   S. M. Humphrey, P. K. Allan, S. E. Oungoulian, M. S. Ironside and E. R. Wise,
        Dalton Trans., 2009, 2298.

(74)   Weinberg, D. R.; Gagliardi, C. J.; Hull, J. F.; Murphy, C. F.; Kent, C. A.;
        Westlake, B. C.; Paul, A.; Ess D. H.;, McCafferty, D. G.; Meyer, T. J. *Chemical
        Reviews*, **2012**, *112* (7), 4016-4093.

(75)   Cheng, M. J.; Goddard, W. A. *J. Am. Chem. Soc.* **2015**, *137*, 13224-13227.

(76)   Barman, S.; Niladri, M.; Bhatte, K.; Ould-Chikh, S.; Dachwald, O.; Haeßner, C.;
        Saih, Y.; Abou-Hamad, E.; Llorens, I.; Hazemann, J. L.; Köhler, K.; D' Elia, V.;
        Basset, J. M. *ACS Catal.*, **2016**, *6*, 5908-5921.

(77)   Marino, N.; Hanson, S. K.; Muller, P.; Doyle, R. P.; *Inorg. Chem*., **2012**, *51*,
        10077–10079.

(78)   Herron, N.; Thorn, D. L.; Harlow, R. L.; Coulston, G. W.; *J. Am. Chem. Soc*.,
        1997, *119*, 7149–7150.

(79)   Solis-Ibarra, D.; Silvia, J. S.; Jancik, V.; Cummins, C. C. *Inorg. Chem*., **2011**, *50*,
        9980–9984.

Chapter 2

Synthesis, Characterization, and Electrochemical Analyses of Vanadocene Tetrametaphosphate and Phosphinate Derivatives

2.1 Introduction

Considerable interest lies in the structure and bonding of vanadium phosphate complexes due to their varied applications, such as in size-selective inorganic hosts, ion exchangers, and magnetic systems.[1–4] From an industrial perspective, DuPont's "butox" process utilizes a surface vanadium phosphate oxide (VPO) catalyst for the oxidative conversion of butane to maleic anhydride (MA) on a 500-kiloton scale (Scheme 2.1a). The commodity chemical is used as a resin, a food additive, and an agricultural chemical, as well as in pharmaceuticals.[5] The conversion of butane to MA is considered one of the most complex in industry, involving the abstraction of 8 hydrogen atoms and the insertion of 3 oxygen atoms, as part of an overall 14 electron process. As such, this process has been the subject of extensive mechanistic investigations over the decades[5–9] and continues to be the subject of considerable interest today.[10–14] However, in spite of these extensive studies, no consensus mechanism yet exists as to the exact steps of this transformation.

Recent gas-phase studies by Schwarz and co-workers have described the ability of simple oxidized oxide clusters, such as $[P_4O_{10}]^{\bullet+}$ and $[V_4O_{10}]^{\bullet+}$, to abstract a hydrogen atom from methane or other simple hydrocarbons, through an H-atom transfer (HAT) process. It was further found that the in situ generated $[P_4O_{10}]^{\bullet+}$ was more reactive than the metallic

analogue $[V_4O_{10}]^{\bullet+}$.[15,16] The increased reactivity upon phosphorus incorporation into the clusters was further demonstrated by comparison of the smaller oxide cations $[VPO_4]^{\bullet+}$ and $[V_2O_4]^{\bullet+}$, wherein the former was more reactive toward HAT than the latter. These experimental conclusions were further supported by theoretical work by Goddard and co-workers, who proposed that the terminal P=O linkages in VPO are responsible for C−H functionalization at butane (Scheme 2.1 b,c). The mechanism, coined "reduction-coupled oxo activation" (ROA), occurs as a result of the strong basicity at the P=O bond coupled with the neighboring high-valent, oxidative V^V centers which undergo reduction[10,12] and is in many respects analogous to well-studied proton-coupled electron transfer (PCET) reactions common to both biological and artificial systems.[17−21]

Scheme 2.1 (a) Partial Oxidation of Butane to Maleic Anhydride Using the VPO Catalyst at High Temperature, (b) Partial Representation of the Surface VPO catalyst Comprised of Terminal V=O and P=O Bonds at the Surface, and (c) Proposed ROA Mechanism for the C−H Reaction at a P=O Bond. The dashed box represents the target motif used for the synthesis of the complexes in this chapter.
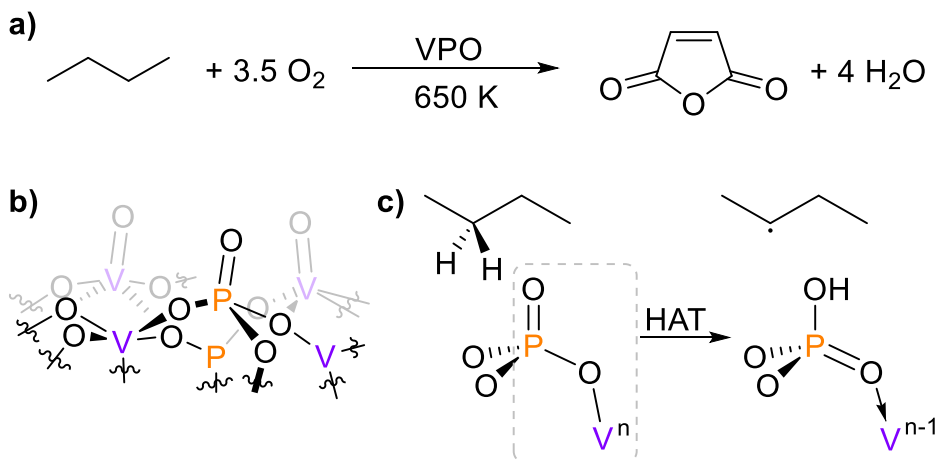
While several heterogeneous and homogeneous VPO model complexes have been synthesized in order to elucidate the reaction mechanism,[22–31] the vast majority of these contain vanadyl (V=O) linkages, hindering the ability to distinguish V=O from terminal P=O bond reactivity (Scheme 2.1c).[30,32–35] In the cases where V=O is absent, bimetallic species bridged by −OPR$_2$O− linkers dominate, with very few having terminal P=O bonds present.[36] In order to probe possible new C−H bond functionalization pathways, such as the proposed ROA mechanism, new VPO model complexes are needed containing terminal P=O linkages bound to encapsulated vanadium centers. This chapter describes the synthesis, characterization, and electrochemical analysis of a series of vanadocene-based molecular precursors encompassing the central V−O−P=O linkage (Schemes 1c (box) and 2). Preliminary reactivity studies with H-atom donors are also described.

2.2 Results and Discussion

2.2.1 Synthesis and Characterization of a Vanadocene Tetrametaphosphate Complex

In order to target molecular V−O−P=O linkages, we employed the known,[37] coordinatively saturated, and basic methylvanadocene (Cp$_2$VMe) complex in conjunction with Cummins' reported cyclic dihydrogen tetrametaphosphate acid ([PPN]$_2$[P$_4$O$_{12}$H$_2$])[38]. Addition of a dichloromethane (DCM) solution of [PPN]$_2$[P$_4$O$_{12}$H$_2$] to 1 equivalent of Cp$_2$VMe in DCM resulted in an immediate color change from black to pale blue. Monitoring this reaction in a sealed J. Young NMR tube revealed the formation of CH$_4$ and protonated CpH by ^{1}H NMR spectroscopy. Removal of the volatile byproducts and purification resulted in the isolation of the salt **2.1** as a pale blue powder in 60% yield (Scheme 2.2). The structure of **2.1** was confirmed by single-crystal X-ray diffraction

(XRD) studies (Figure 2.1). The solid-state structure of **2.1** revealed a piano-stool ligand arrangement around V with the phosphate oxo groups occupying the basal tetragonal plane and the Cp capping the apical end. Bond metrics in **2.1** are mostly unremarkable, with the exception of slightly shortened P=O double bonds (average 1.453(6) Å). To the best of our knowledge, **2.1** is only the second example of the tetrametaphosphate ligand binding in a κ^4 fashion to a metal center.[38] The diamagnetically corrected[39] magnetic moment (μ_{eff} = 2.82 μ_B) was determined using the Evans method[40] and is consistent with an expected spin-only value (μ_{eff} = 2.83 μ_B) for a high-spin, S =1 V^{III} center. The effects of this paramagnetism are seen in the ^{31}P and ^{1}H NMR spectra, displaying the expected diamagnetic resonances for the cations ([PPN]$^+$) and paramagnetically silent resonances for the anion ([CpV(P$_4$O$_{12}$)]$^{2-}$).

Scheme 2.2 Synthesis of vanadium(III) tetrametaphosphate (**2.1**) through protonolysis
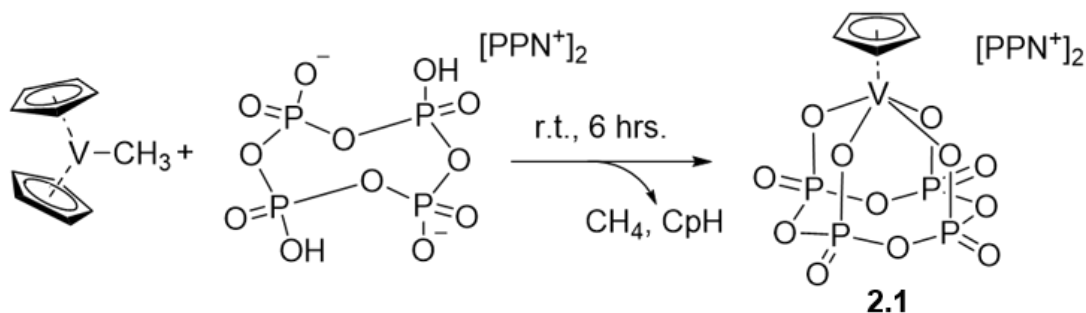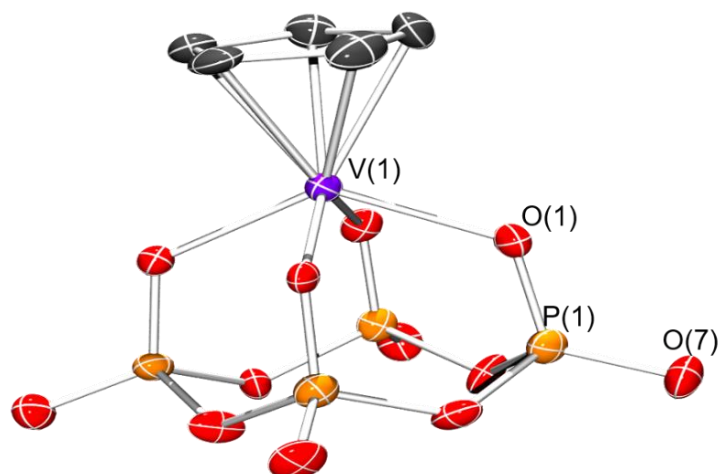
Figure 2.1 Solid-state molecular structure of the anion of **2.1**. Hydrogen atoms, [PPN]$^+$ cations, and co-crystallized solvent are omitted for clarity

In order to probe the redox properties of **2.1**, we studied its electrochemistry by cyclic voltammetry (CV). The CV of **2.1** dissolved in DCM with 0.1 M [Bu$_4$N][PF$_6$] as supporting electrolyte was analyzed at varying scan rates (Figure 2.2). While a quasi-reversible oxidation event is observed at fast scan rates, this event becomes irreversible at slow scan rates (Figure 2.2, inset). These data suggest that the electron transfer (oxidation) event results in a chemical transformation, as part of a proposed EC mechanism.[46] We attempted to chemically isolate the oxidized product using various oxidants, such as cerium ammonium nitrate, nitrosonium tetrafluoroborate, and tris(4-bromophenyl)ammoniumyl hexachloroantimonate; however, the isolation of a pure product has proven to be unsuccessful.
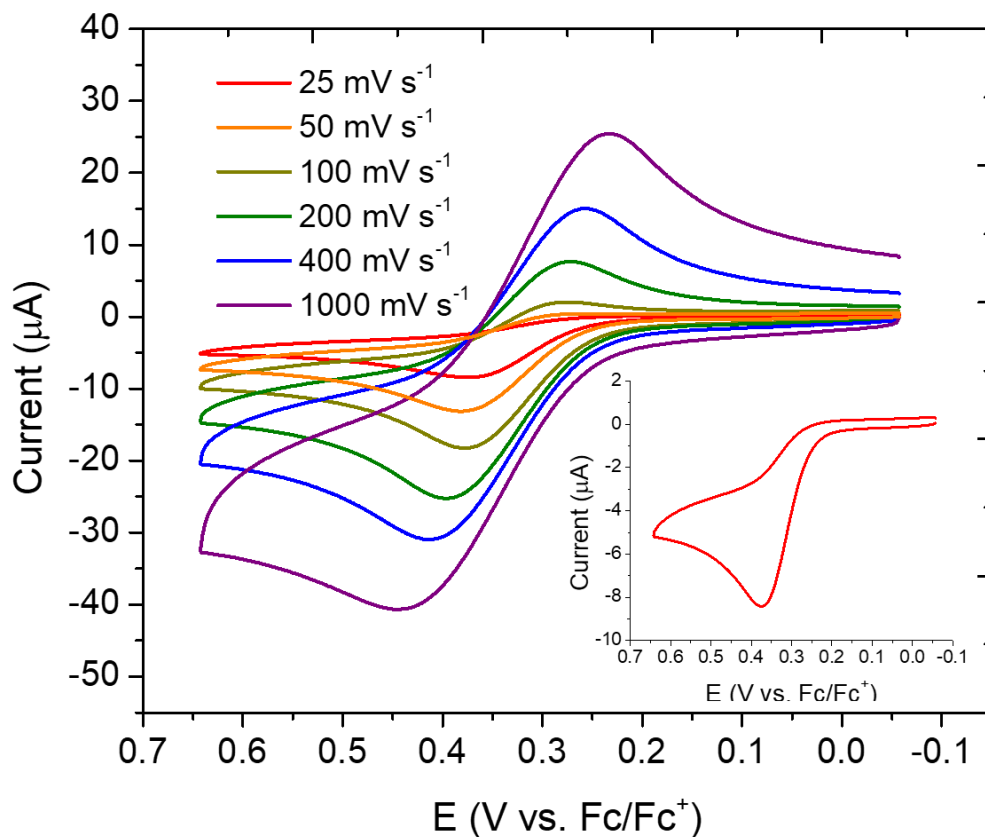
Figure 2.2. CVs of **2.1** (1.0 mM) in 0.1 M [Bu$_4$N][PF$_6$] DCM solution at varying scan rates using a glassy-carbon working electrode and platinum-wire counter electrode, referenced to the Fc/Fc$^+$ couple. Inset: CV at a 25 mV s^{-1} scan rate

2.2.2 Synthesis and Characterization of a Vanadocene Phosphinate Derivatives

Next, we targeted systems with reduced V:P ratios using the acid Ph$_2$P(O)OH as our phosphorus source. Addition of an equimolar slurry of Ph$_2$P(O)OH in dichloromethane to a cold (−40 °C) solution of Cp$_2$VMe resulted in methane generation and an immediate color change from black to blue. Following workup, the pure product (**2.2**) was isolated in good yield (63%) and its structure confirmed by single-crystal XRD studies (Scheme 2.3

and Figure 2.3). The structure of **2.2** revealed a bent Cp$_2$V conformation with a V(1)−O(1)−P(1) bond angle of 145.21(1)°. The P(1)=O(2) bond length (1.500(2) Å) is consistent with a typical phosphine oxide double bond,[41] while the P(1)−O(1) bond (1.5560(19) Å) is contracted in comparison to typical P−O single bonds (∼1.63 Å).[41] The V(1)−O(1) bond length (2.043(2) Å) is similar to reported single bonds.[28] While most vanadium phosphates contain bridging phosphates, **2.2** is a rare example of a monomeric vanadium phosphate with a V:P ratio of 1:1.[29,36,42−44] The magnetic moment of **2.2** was determined using the Evans method (μ_{eff} = 2.90 μ_B) and is consistent with a high-spin V^{III} center.[39,40] The paramagnetic nature of **2.2** resulted in absent ^{1}H NMR signals for the Cp ring protons and broadened resonances for the phenyl ring protons. Complex **2.2** was indefinitely stable on storage in the glovebox at −40 °C but is unstable in solution at room temperature, as decomposition is observed after several days. The products of decomposition remain unknown.
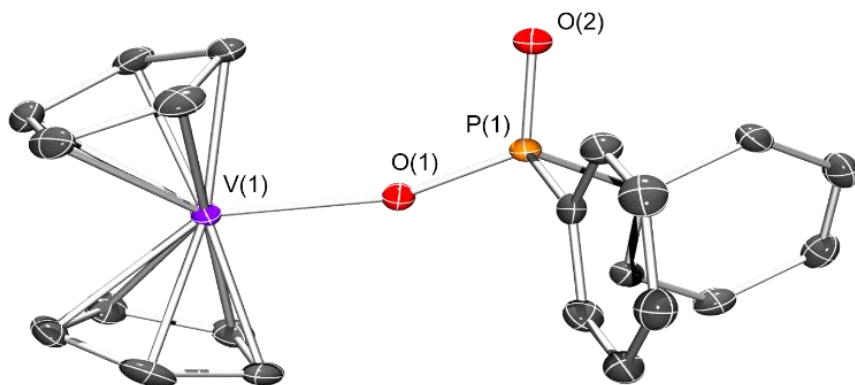
Figure 2.3. Solid-state molecular structure of **2.2**. Hydrogen atoms are omitted for clarity.

Scheme 2.3. Synthesis of complexes **2.2-2.4**.
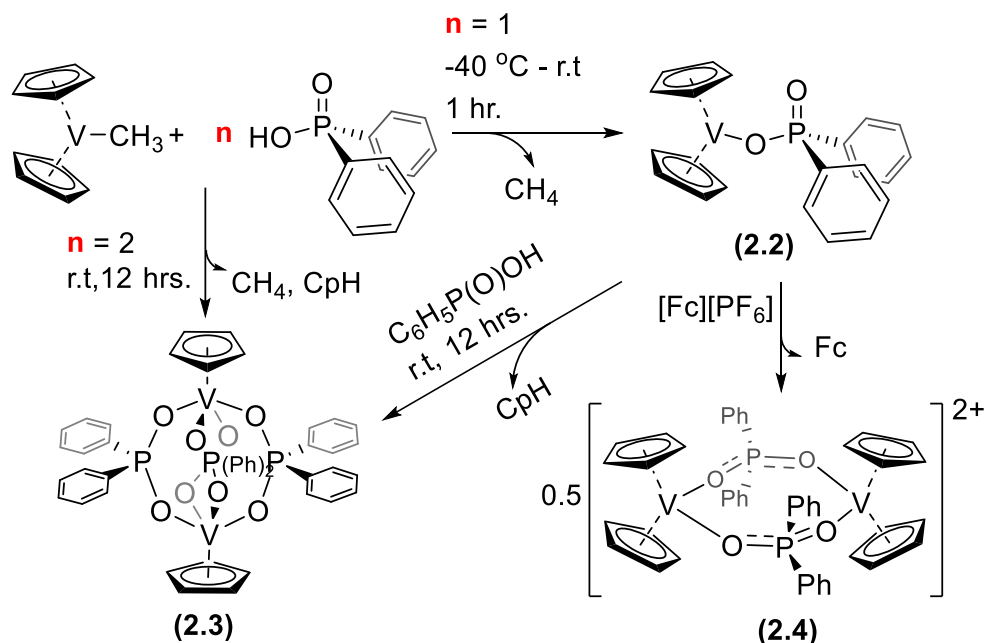
As noted above, complex **2.2** represents a rare example of a monomeric vanadium phosphorus oxide complex. However, we observed that the synthesis of **2.2** was sensitive to excess Ph$_2$P(O)OH. Treatment of Cp$_2$VMe with 2 equiv. of Ph$_2$P(O)OH resulted in an initial blue solution (consistent with **2.2**), followed by a subsequent change to green. ^{1}H NMR analysis of a sealed reaction mixture revealed the formation of both CH$_4$ and CpH over time (12 h). Green octahedral shaped single crystals suitable for XRD analysis were grown directly from the acetonitrile (MeCN) reaction mixture and confirmed the formation of the bimetallic caged structure **2.3** (Scheme 2.3 and Figure 2.4). The solid-state structure of **2.3** revealed a cagelike motif with each V bordered by a tetragonal phosphinate ligand field in the basal plane and a Cp at the apical position, similarly to **2.2** and to previous bridged V species.[22,43] In contrast to **2.2**, the P−O bonds in **2.3** are essentially equivalent (~1.50−1.51 Å), indicative of a delocalized π framework. Additionally, the O-P-O bond

angles deviate slightly from their rigid tetrahedral framework (117.6º), while the V-O-P bond angles are at a much more obtuse angle (135.6º). While we assign each vanadium atom to the +3 oxidation state and each is likely high spin as in complexes **2.1** and **2.2**, attempts to acquire solution-phase magnetic measurements using the Evans method were hampered due to the extremely poor solubility of **2.3**. Complex **2.3** could also be synthesized by addition of 1 equiv of $Ph_2P(O)OH$ to **2.2** (Scheme 2.3), and was often seen as a byproduct in the protonolysis route towards **2.2**.
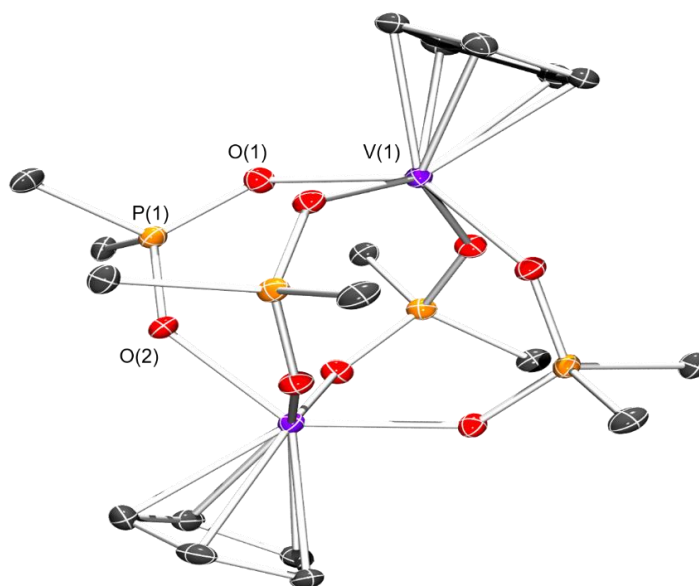
Figure 2.4. Solid-state molecular structure of **2.3**. Hydrogen atoms, phenyl groups (except *ipso*-carbon), and cocrystallized solvent are omitted for clarity.

In order to better approximate the V(IV)-V(V) oxidation catalysts employed in industry we sought to chemically oxidize complex **2.2**. Upon addition of ferrocenium hexafluorophosphate to a frozen solution of complex **2.2** in dichloromethane, the bright

blue V(III) complex was immediately oxidized to a green V(IV) complex (Scheme 2.3). After allowing the solution to warm to room temperature a green powder crashed out of the solution of dichloromethane to generate **2.4** in high yield (92.1%). Green block-shaped crystals suitable for X-ray diffraction were grown from slow vapor diffusion of an acetonitrile solution with ether at -40 °C (Figure 2.5). The structure reveals that upon oxidation of **2.2** the V-O-P=O moiety dimerizes through the terminal P=O double bond to form a cyclic vanadium(IV) complex bridged through the phosphinate ligands. Similar to **2.3**, the P-O bonds in **2.4** become equivalent throughout the ring, with each P-O bond = 1.51(0) Å. The V–O bond lengths become equivalent throughout the ring and show no deviatation from the V–O bond lengths of complex **2.2**. Dinuclear vanadium(IV) organophosphorus-bridged complexes are well documented in the literature, and a geometric classification of the V(OPO)$_2$V core has been established.[19] Based on the classification developed by Carrano and co-workers the solid state structure of complex **2.4** adopts an eight membered retracted chair conformation rather than a planar ring conformation.[20] It is currently not completely understood how the conformation of these dinuclear vanadium(IV) organophosphorus-bridged complexes correlate to observed changes in magnetic susceptibility and electronic structure.
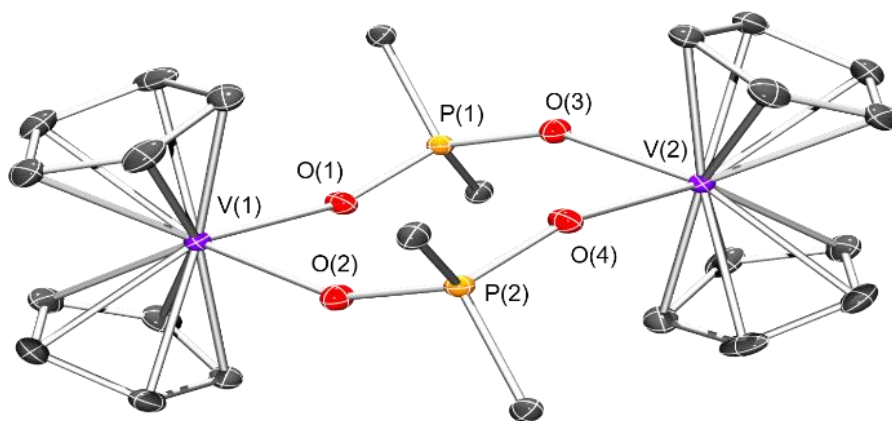
Figure 2.5: Solid-state molecular structure of **2.4**. Phenyl rings, hydrogen atoms, and PF_6^- counter ions omitted for clarity.

The electronic structure of **2.4** was probed using Evan's method. The diamagnetically corrected magnetic moment was found to be 1.95 μ_B ($\chi_m T$: 0.47 cm^3-K/mol).[16] Assuming ferromagnetic coupling between two vanadium(IV) centers would yield a spin-only magnetic moment of approximately 2.83 μ_B for an $S = 1$ system. However, if each vanadium(IV) center is considered independently ($S_1 = S_2 = \frac{1}{2}$), then the sum of the calculated spin only magnetic moments for each center should be 2.44 μ_B according to the equation ($\mu_{theor} = 2[\sqrt{\sum S(S+1)}]$). The room temperature experimental value of 1.95 μ_B for complex **2.4** is significantly less than either of these two approximations, and suggests an anti-ferromagnetic interaction between the two vanadium centers possibly through a superexchange mechanism.

The magnetic properties of **2.4** were further studied by SQUID magnetometry. The molar magnetic susceptibility as a function of temperature is given in Figure 2.6. The data revealed an initial broad maximum at 50 K attributed to internuclear antiferromagnetic coupling. A least-squares fit of the χ_M vs T data from 2 to 300 K using the dimeric exchange Hamiltonian, $\hat{H}_{ex} = -2J_{12}S_1S_2$ ($S_1 = S_2 = 1/2$) with a temperature independent paramagnetism (TIP) correction yielded good agreement with the experimental data for the parameters: $J = -21.8$ cm^{-1}, $g = 1.972$ (from EPR measurements), and TIP = 796.1 × 10^{-6} emu (Figure 2.6, blue trace). These values agree well with reported analogous antiferromagnetically coupled vanadium phosphate extended structures.[3,51−54] Below 8 K the magnetic susceptibility increases sharply rather than dropping to zero as modeled for the dimer. This is attributed to a small amount (~3% by mass) of monomeric V^{IV} (**2.2$^+$**, S

= 1/2) centers exhibiting Curie-like behavior (Figure 2.6, red trace), as is often observed with bimetallic complexes.[51,52,54] Summation of the dimer and monomer models results in a satisfactory fit to the experimental data (Figure 2.6, dotted black trace).
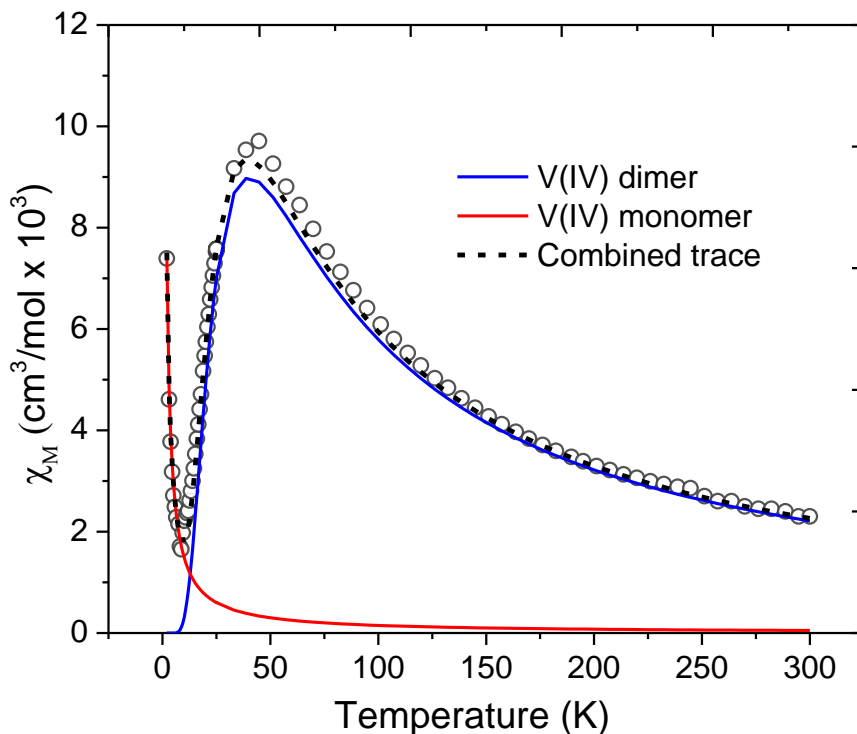
Figure 2.6: Molar magnetic susceptibility (χ_M) vs. temperature measurements for bulk crystalline **2.4** collected from 2-300 K with an applied 0.1 T field (gray circles). The final fit (black dashed) is a summation of a dimeric (**2.4**) contribution (blue trace), as well as a small (3%) monomeric (**2.2$^+$**) contribution (red trace).

Compound **2.4** was further analyzed by X-band EPR spectroscopy. While the room-temperature spectrum of **2.4** in MeCN is silent, frozen-solution spectra (100 and 4 K) are readily observed (Figure 2.7). The 100 K spectrum (Figure 2.7a) revealed a single, mostly unstructured isotropic signal (g = 1.972) similar to those of reported exchange-coupled

divanadium(IV) systems and is ascribed to the low-lying triplet excited state of the dimer,[23,54,55] wherein the zero-field splitting of the triplet is small in magnitude so that the appearance resembles that of an isotropic $S = 1/2$ species.[56,57] In addition to this major absorption, some minor fine structure is also observed and is the result of a small amount (~3%) of the monomeric **2.2**$^+$ (which is S = 1/2), resulting in a superimposed eight-line pattern due to hyperfine coupling to the ^{51}V (I = 7/2, 100% abundance) center. In contrast, the 4 K spectrum reveals a much more intense contribution from the monomeric **2.2**$^+$ resulting in a readily observable spectrum more typical of V^{IV}, including $[Cp_2V]^{2+}$ species,[58,59] exhibiting resolved hyperfine coupling[60] (simulation parameters: g = [2.02, 1.99, 1.945] (g_{avg} = 1.985), A(^{51}V) = [80, 80, 350] MHz (a_{avg} = 170 MHz), W (Gaussian, hwhm) = 50 MHz).[61] The breadth of this spectrum is ascribed to an underlying contribution from the spin triplet **2.4**, although this contribution is greatly reduced in comparison to the 100 K spectrum, consistent with the magnetic measurements above (Figure 2.6).
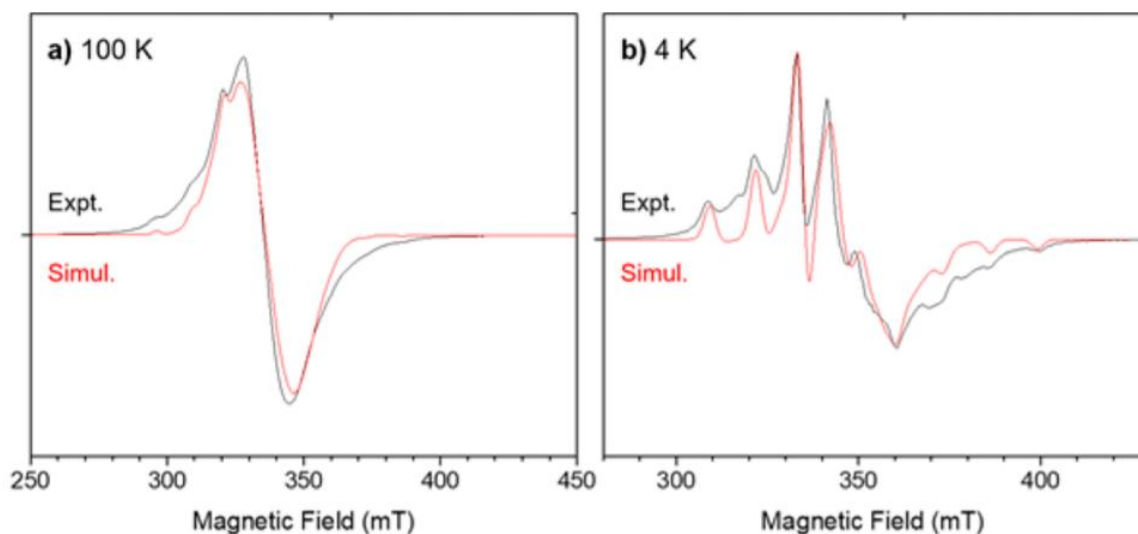
Figure 2.7: X-band EPR spectra of **2.4** in MeCN at (a) 100 K and (b) 4 K. The experimental

traces are in black and the simulations in red. The relative intensities between (a) and (b) are arbitrary.

Details regarding the simulation of the X-band EPR spectrum of the dimetallic complex **2.4** in MeCN at 100 K and 4 K are shown in Figure 2.8. The colored traces are simulated spectra of the sum of two species: a) simulation generated using an $S = 1/2$ spin Hamiltonian (phenomenologically acceptable for a spin triplet with negligible zero-field splitting), with $g_{iso} = 1.972$, W (Gaussian, hwhm) = 300 MHz, and $A(^{51}V) = 80$ MHz, so that the number of EPR transitions can be compared to that with resolved ^{51}V hyperfine coupling, b) simulation generated using an $S = 1/2$ spin Hamiltonian with g = [2.02, 1.99, 1.945], $A(^{51}V) = [80, 80, 350]$ MHz, W (Gaussian, hwhm) = 50 MHz, which describes **2.2**$^{+}$, a mono V^{IV} species. The relative amounts of species (b) are indicated on the figure. Figure 2.7 employed the ratio of (a):(b) = 40:1 (i.e., the simulation for (b) was scaled by 0.025 and then added to that for (a)). This ratio is not meant to be quantitative, only that the amount of the mono-V^{IV} (**2.2**$^{+}$) species is relatively small, but observable due to its sharp hyperfine transitions, which are pointed out by the dotted vertical guidelines. The amount of the mono-V^{IV} (**2.2**$^{+}$) species 2 + is still not dominant, even at 4 K
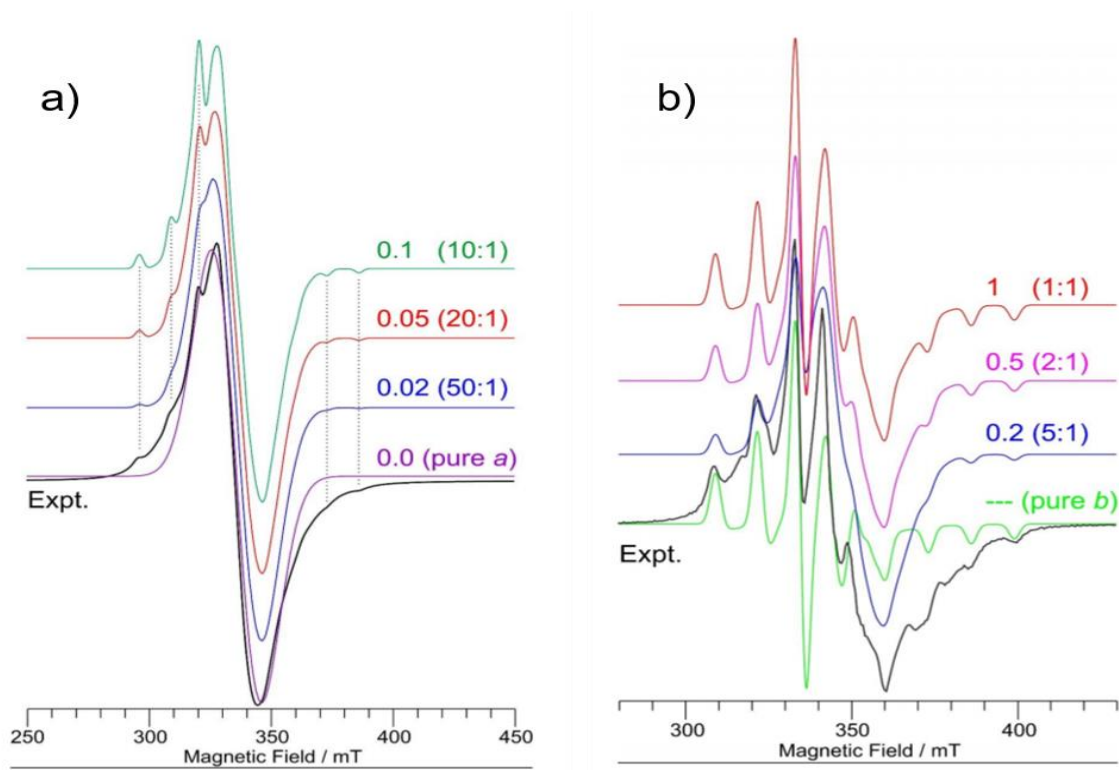
Figure 2.8: X-band EPR spectra of **2.4** and simulations in MeCN at (a) 100 K and (b) 4 K.

2.2.3 Mechanistic Insight of the Oxidation of 2.2 using Cyclic Voltammetry

Intrigued by the propensity for the vanadium center to dimerize through the phosphinate ligand upon oxidation we sought to understand the mechanism of oxidation and dimerization through electrochemical techniques. Cyclic voltammetry was used to probe the mechanism by examining the V(III)-V(IV) redox couple of a 1 mM solution of **2.2** in 0.1 M NBu$_4$PF$_6$ in CH$_2$Cl$_2$ using a glassy carbon working electrode, platinum wire counter electrode, and Ag/Ag$^+$ reference electrode at varying scan rates: 10 mVs^{-1}, 25 mVs^{-1}, 100 mVs^{-1}, 200 mVs^{-1}, 400 mVs^{-1} (Figure 2.9). All voltammograms were repeated in duplicate, and referenced to the ferrocene/ferrocenium redox couple.
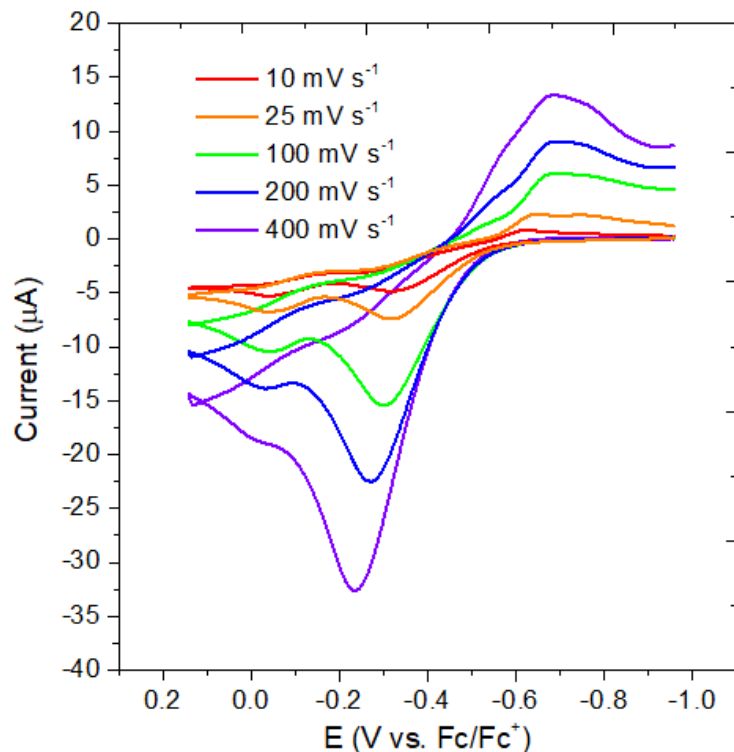
Figure 2.9: CVs of **2.2** (1.0 mM) in 0.1 M [Bu₄N][PF₆] DCM solution at varying scan rates

The voltammograms differ based on the variable scan rates. The slowest scan rate (10 mV s^{-1}) reveals the emergence of two irreversible oxidation events which coalesce to a single feature at faster scan rates (Figure 2.10, black traces). Probing the oxidation at a 400 mVs^{-1} scan rate from low (1 mM) to high (10 mM) concentrations reveals the reemergence of the second oxidation event (Figure 2.10, red trace). This data taken together was used to propose an *ECE* (electrochemical, chemical, electrochemical) reaction mechanism for the oxidation of **2.2**.
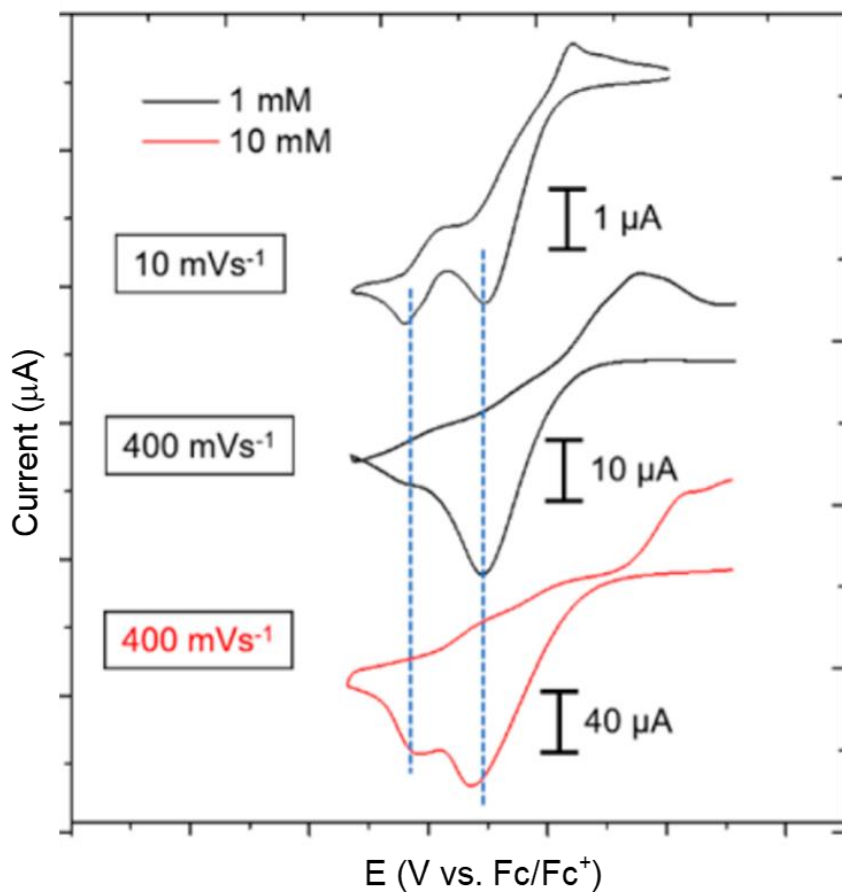
Figure 2.10: Stacked CVs of **2.2** at 1 mM (black) and 10 mM (red) concentrations with designated scan rates.

Based on the voltammograms the following *ECE* mechanism can be proposed: upon initial electrochemical oxidation of **2.2** to **2.2$^+$**, the unstable **2.2$^+$** chemically reacts with the bulk analyte **2.2** to afford a mixed valent (**2.2-2.2$^+$**) dimer. The mixed-valent dimer then undergoes a second electrochemical oxidation event to afford the chemically isolated species **2.4** (Scheme 2.4).[25-27]

Scheme 2.4: Proposed *ECE* mechanism for the oxidation and dimeriation of **2.2**

At faster sweep rates only one oxidation peak is evident near -0.25 V vs. Fc/Fc$^+$ since the kinetics of the dimerization reaction are 'outrun' by the voltage timescale. As the scan rate is decreased to 10 mVs^{-1}, however, a second peak corresponding to the proposed **2.2-2.2$^+$** mixed valent complex appears at potentials near -0.02 V. In this case the voltage timescale is slow enough to allow the dimerization reaction to occur, and the subsequent oxidation of the **2.2-2.2$^+$** dimer can be observed at -0.02 V. The emergence of the second peak correlates with the loss of the back peak in the quasi-reversible **2.2/2.2$^+$** wave. When the concentration of the bulk analyte **2.2** is increased tenfold, the second **2.2-2.2$^+$/2.4** oxidation feature starts to reappear even at higher scan rates (Figure 2.10 red trace). Mechanistically, as the concentration of the bulk analyte **2.2** is increased there is a

subsequent increase in the rate of dimerization to form the mixed valent species **2.2-2.2⁺** which renders the second **2.2-2.2⁺/2.4** oxidation feature clearly evident even at fast scan rates.

An analysis of the number of electrons transferred in the first oxidation event centered at -0.20 V vs. Fc/Fc⁺ was conducted using the Randles-Ševčik equation for an irreversible process.[28]

$$I = 2.99 \text{ x } 10^5 n(n'+\alpha)^{1/2} A D^{1/2} C v^{1/2} \tag{1}$$

where I is the peak current, n is number of electrons in the overall chemical process, n' is the number of electrons involved prior to the rate determining step (0 in this case), A is the surface area of the glassy-carbon working electrode (3 mm diameter), D is the diffusion coefficient (1.74 x 10⁻⁵ cm²s⁻¹, calculated using the Wilkes-Chang equation below), C is the concentration of analyte (1 mM), v is the scan rate (Vs⁻¹), and α is the charge transfer coefficient (0.68, obtained from a Tafel plot). The diffusion coefficient D was calculated using the Wilkes-Chang equation:

$$D_{AB} = 7.4 \times 10^{-8} \frac{(xM)^{1/2}T}{\eta V^{0.6}} \tag{2}$$

Where x is the association parameter ($x=1$ for non-associative solvents), M is the molar mass of the solvent, T is temperature, η is the solvent viscosity, and V is the molar volume of the analyte. The molar volume of the analyte V was calculated using the unit cell volume (V_{cell}) from the unit cell parameters for complex **2.2**. The theoretical model is based off a one electron transfer.

At slow scan rates the experimental data agrees nicely with the theoretical plot for a one electron transfer; however, at faster scan rates the experimental fit increasingly

deviates from the theoretical model indicating a slightly less the 1 electron transfer (Figure 2.11), which may be attributed to efficiency loss at faster scan rates.
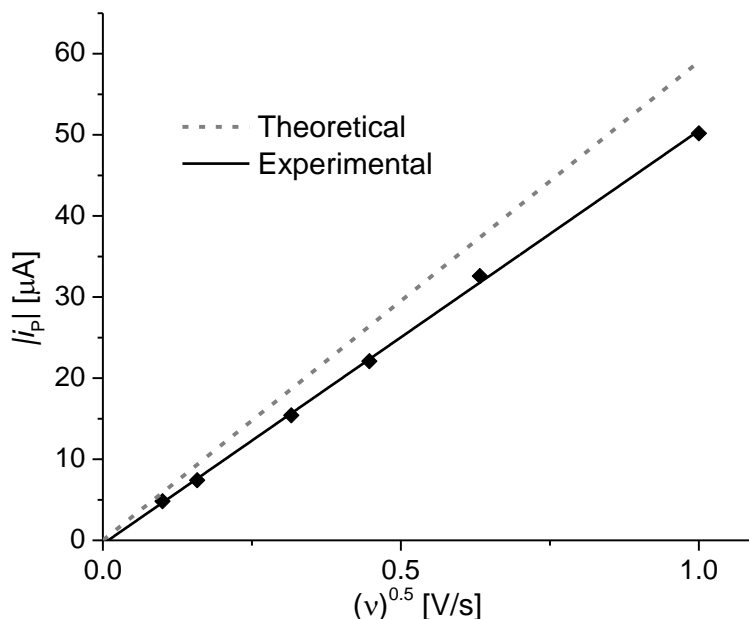
Figure 2.11: Randles-Ševčik plot for an n=1 irreversible oxidation and theoretical fit (i_p = peak current; v = scan rate).

2.2.4 Reactivity Studies with H-atom Transfer Reagents

With the new compounds in hand, we have tried to probe possible reduction couple oxo-activation reactions at the P=O multiple bonds.[10,12] Both **2.1** and **2.2**, containing unbound P=O bonds, were exposed to various H atom donors (HADs), such as 1,4-cyclohexadiene (CHD), 9,10-dihydroanthracene (DHA), and 1-hydroxy-2,2,6,6-tetramethylpiperidine (TEMPO-H). Deuterated DCM or MeCN solutions of **2.1** with varying equivalents of CHD, DHA, and TEMPO-H (0.5− 10 equiv.) at both room temperature and elevated temperatures (80 °C) revealed no reactions as observed by 1 H

NMR spectroscopy. Similarly, the reaction of **2.2** with CHD or DHA under analogous, varying conditions also revealed no reactions with the HADs. Only the production of CpH was observed; however, this is also observed upon heating **2.2** in the absence of HADs and is, thus, attributed to thermal decomposition of **2.2** (vide supra). The resulting decomposition pathway produces small amounts of **2.3**. While there was no observed with C-H bonds, **2.2** does react with TEMPO-H, but the data seems to suggest an O atom transfer mechanism generating a vanadyl (V=O) bond, rather than an ROA mechanism

2.3 Conclusion

In this chapter, we have outlined the synthesis and characterization of a series of new vanadocene-derived cyclic tetrametaphosphate or diphenylphosphinate complexes (**2.1-2.4**), as well as the electrochemical behaviors of **2.1** and **2.2**. Complex **2.1** was found to undergo an irreversible *EC* mechanism upon oxidation, the product of which remains unknown. In contrast, the electrochemical data on **2.2** are consistent with a proposed stepwise *ECE* mechanism, forming the dimeric product **2.4**. The electronic structure of **2.4** was also probed using SQUID magnetommetry and EPR spectroscopy and was found to contain antiferromagnetically coupled V^{IV} centers with a low-lying accessible triplet state, as well as a small contribution from monomeric **2.2$^+$**. The reactivity with these complexes with common HAT reagents did not demonstrate any proposed ROA type reactivity.

2.4 Experimental Section

2.4.1 General Considerations

All manipulations were performed under an atmosphere of dry, oxygen-free N_2 by

means of standard Schlenk or glovebox techniques (MBRAUN UNIlab Pro SP Eco equipped with a -40 °C freezer). Pentane, tetrahydrofuran, diethyl Ether, hexanes, and dichloromethane (Sigma Aldrich) were dried using an MBRAUN-Solvent Purification System and stored over 4Å molecular sieves for two days prior to use. Acetonitrile (Sigma) was dried over CaH_2 for 2 days then distilled over 4Å molecular sieves. Deuterated solvents were purchased from Cambridge Isotope Labs, then degassed and stored over molecular sieves for at least 2 days prior to use. Celite 435 (EM Science) was dried by heating above 250 °C under dynamic vacuum for at least 48 h prior to use. Glassware was oven dried for at least three hours at temperatures greater than 150 °C. Diphenylphosphinic acid, [Fc][PF_6], were purchased from Aldrich and used without further purification. Vanadocene[31] (purified by sublimation), Cp_2VMe[32], and [PPN]$_2$[P_4O_{12}][29] were prepared according to literature procedures.

NMR spectra were obtained on a Agilent Technologies 400 MHz spectrometer, and referenced to residual solvent or externally (^{31}P: 85% H_3PO_4, ^{19}F: $CFCl_3$). Chemical shifts (δ) are recorded in ppm and the coupling constants are in Hz. Elemental analyses (C, H) were recorded at the University of California, Berkeley using a Perkin Elmer 2400 Series II combustion analyzer. UV-Vis spectroscopy was performed using a Shimadzu UV-2401PC UV-Vis recording spectrophotometer with quartz cuvettes equipped with a J-young air-tight adaptor. Magnetic susceptibility measurements were conducted through analysis of solvent shifts using a 400 MHz Agilent Technologies spectrometer and were repeated in triplicate. Perpendicular-mode X-band EPR spectra were collected on a Bruker EMX EPR Spectrometer equipped with an Oxford ESR 900 liquid helium cryostat. Cyclic Voltammetry was performed on a CH Instruments Electrochemical Analysis potentiometer,

equipped with a 3 mm diameter glassy carbon working electrode, a Ag wire pseudo-reference electrode, and a Pt wire counter electrode with $[Bu_4N][PF_6]$ (0.1 M) supporting electrolyte solution in dichloromethane. The glassy carbon working electrode was cleaned prior to each experiment by polishing with 1, 0.3, 0.05 mm alumina (CH Instruments Inc.) in descending order followed by sonication in distilled water. Background scans were conducted for each reported scan rate in a solution of just supporting electrolyte, and was then subtracted from each experiment. Ferrocene was used as an internal reference. X-ray intensity data was collected on a Bruker KAPPA APEX II diffractometer equipped with an APEX II CCD detector using a TRIUMPH monochromator with a Mo Kα X-ray source (α = 0.71073 Å). The crystals were mounted on a cryoloop with Paratone-N oil, and all data were collected at 100(2) K using an Oxford nitrogen gas cryostream system. A hemisphere of data was collected using ω scans with 0.5° frame widths. Data collection and cell parameter determination were conducted using the APEX2 program. Integration of the data frames and final cell parameter refinement were performed using SAINT software. Absorption correction of the data was carried out using SADABS. Structure determination was done using direct or Patterson methods and difference Fourier techniques. All hydrogen atom positions were idealized and rode on the atom of attachment. Structure solution, refinement, and creation of publication materials was performed using Olex2.

2.4.2 Synthesis of Compounds

Synthesis of [PPN]₂[CpV(P₄O₁₂)] (2.1): In the glovebox a 20 mL scintillation vial with a stirbar was charged with $(C_5H_5)_2VCH_3$ (0.020 g, 0.102 mmol) and dissolved in dichloromethane (5 mL). A separate solution of $[PPN]_2[P_4O_{12}H_2]$ (0.142 g, 0.102 mmol) was dissolved in dichloromethane (5 mL) and added dropwise at r.t. Immediately after

addition the solution turned a pale blue color. The solution was allowed to stir for 6 hours then filtered over a pad of Celite through a fine porosity Buchner funnel. The filtrate was dried *in vacuo* to yield a blue residue. The residue was triturated with hexanes and dried *in vacuo* to yield a fluffy light blue powder (0.091 g, 0.060 mmol, 59.7%). Blue plate-shaped single crystals suitable for X-ray diffraction were grown by slow vapor diffusion of pentane into a concentrated solution of **2.1** in DCM.

^{1}H NMR (400 MHz, CD$_2$Cl$_2$): δ 7.48 (bs, 12H, *p*-C$_6$H$_5$), 7.66 (bs, 48H, *o,m*- C$_6$H$_5$). **^{31}P{^{1}H} NMR** (161.9 MHz, CD$_2$Cl$_2$): δ 21.11 (s, 4P, 2[PPN]$^{+}$). **Anal Calc.** for C$_{77}$H$_{65}$N$_2$O$_{12}$P$_8$V: C, 61.28; H, 4.34; N, 1.96. **Found:** C, 61.15; H, 4.26; N, 1.98. **UV-Vis.** λ$_{max}$ (nm): 245 (max), 262, 407, 578. **Mag. Suscept**. μ$_{eff}$: 2.82 μ$_B$, χ$_m$T: 0.99 cm^3-K/mol.

Synthesis of [Cp$_2$VOP(O)Ph$_2$] (2.2): Inside the glovebox a 100 mL roundbottom with a magnetic stir bar was charged with Cp$_2$VMe (0.550 g, 2.81 mmol) and dissolved in dichloromethane (20 mL). The black solution was cooled to -40 ºC by placing it in the freezer. A separate slurry of diphenylphosphinic acid, Ph$_2$P(O)OH (0.510 g, 2.30 mmol) was prepared in dichloromethane (10 mL) and added cold dropwise. The mixture was allowed to warm to r.t. over 1 h, then filtered over a pad of celite through a fine porosity Buchner funnel. The bright blue filtrate was dried *in vacuo*. The resulting blue residue was triturated with hexanes (25 mL) to yield a bright blue powder and recrystallized out of dichloromethane (5 mL) layered with pentane (5 mL) at -40 ºC (0.576 g, 1.45 mmol, 62.9%). Blue plate-shaped single crystals suitable for X-ray diffraction were grown by slow vapor diffusion of pentane into a concentrated solution of **2.2** in DCM.

^{1}H NMR (400 MHz, CD$_2$Cl$_2$): δ 7.46 (bs, C$_6$H$_5$), 7.68 (bs, C$_6$H$_5$), 9.63 (bs, C$_6$H$_5$). **Anal.**

Calc. for $C_{22}H_{20}O_2PV$: C, 66.30; H, 5.06. Found: C, 66.12; H, 4.87. **UV-Vis** λ_{max} (nm): 338 (max), 604, 752. **Mag. Suscept**. μ_{eff}: 2.90 μ_B, $\chi_m T$: 1.05 cm³-K/mol.

Synthesis of [CpV(OP(O)Ph₂)₂]₂ (2.3): Inside the glovebox a 20 mL scintillation vial with a stirbar was charged with $(C_5H_5)_2VCH_3$ (0.040 g, 0.20 mmol) and dissolved in acetonitrile (5 mL). A separate slurry of diphenylphosphinic acid, $Ph_2P(O)OH$ (0.089 g, 0.41 mmol) was prepared in acetonitrile (5 mL) and added dropwise. Immediately the solution turned a bright blue color, but after stirring for 12 hours a bright green precipitate crashed out of solution. The precipitate was filtered using a fine porosity Buchner funnel, washed with acetonitrile (10 mL) and dried *in vacuo*. (0.069 g, 0.063 mmol, 30.7%). Green octahedral-shaped single crystals were grown directly from the reaction mixture in MeCN.

¹H NMR (400 MHz, CD_2Cl_2): δ 6.57 (bs, C_6H_5), 7.34 (bs, C_6H_5). **Anal. Calc.** for $C_{58}H_{50}O_8P_4V_2$: C, 62.29; H, 4.58. Found: C, 60.05; H, 4.39. The reduced carbon percentage can be attributed to the facile formation of Vanadium carbide upon combustion.[33] Samples were run in duplicate. **UV-Vis** λ_{max} (nm): 328 (max), 458, 645.

Synthesis of [Cp₂V(μ₂-O₂PPh₂)₂VCp₂][PF₆]₂ (2.4): In the glovebox a 50 mL roundbottom flask with a stirbar was charged with $(C_5H_5)_2VOP(O)(C_6H_5)_2$ **(1)** (0.040 g, 0.10 mmol) and dichloromethane (10 mL). The solution was cooled to -78 °C using a cold well inside the glovebox. A separate solution of $[Fc][PF_6]$ (0.036 g, 0.11 mmol) in dichloromethane (5 mL) was added dropwise. The solution was allowed to warm to r.t. for 1 hour while stirring and a green solid precipitated from solution. The mixture was filtered over a pad of celite and the green solid was washed with ether (10 mL) followed by benzene (10 mL). The green solid was eluted with acetonitrile (5 mL) and dried *in vacuo* (0.050 g,

0.092 mmol, 92.1%). Green plate-shaped single crystals were grown by slow diffusion of ether into a saturated MeCN solution of 4.

^{31}P{^{1}H} NMR (161.9 MHz, CD$_2$Cl$_2$): δ -144.62 (sep, 2P, 2[PF$_6$]$^-$). ^{19}F{^{1}H} NMR (376 MHz, CD$_2$Cl$_2$): δ -72.46 (d, 12F, 2[PF$_6$]$^-$). **Anal Calc.** for C$_{44}$H$_{40}$F$_{12}$O$_4$P$_4$V$_2$: C, 48.64; H, 3.71. **Found:** C, 48.39; H, 3.58. **UV-Vis.** λ_{max} (nm): 280 (max), 355. **Mag. Suscept.** μ_{eff} (μ_B): 1.95 μ_B, $\chi_m T$: 0.47 cm^3-K/mol.

2.5 References

(1)   Collison, D.; Eardley, D. R.; Mabbs, F. E.; Powell, A. K.; Turner, S. S. *Inorg. Chem.* **1993**, *32*, 664−671.

(2)   Johnson, J. W.; Jacobson, A. J.; Butler, W. M.; Rosenthal, S. E.; Brody, J. F.; Lewandowski, J. T. *J. Am. Chem. Soc.* **1989**, *111*, 381−383.

(3)   Roca, M.; Amoros, P.; Cano, J.; Marcos, M. D.; Alamo, J.; ́Beltran-Porter, A.; Beltra ́n-Porter, D. ́*Inorg. Chem.* **1998**, *37*, 3167− 3174.

(4)   Reuter, H. *Angew. Chem., Int. Ed. Engl.* **1992**, *31*, 1185−1188.

(5)   Centi, G.; Trifiro, F.; Ebner, J. R.; Franchetti, V. M. *Chem. Rev.* **1988**, *88*, 55−80.

(6)   Zhanglin, Y.; Forissier, M.; Sneeden, R. P.; Vedrine, J. C.; Volta, J. C. *J. Catal.* **1994**, *145*, 256−266.

(7)   Chen, B.; Munson, E. J. *J. Am. Chem. Soc.* **1999**, *121*, 11024− 11025.

(8)   Chen, B.; Munson, E. J. *J. Am. Chem. Soc.* **2002**, *124*, 1638−1652.

(9)   Cavani, F.; De Santi, D.; Luciani, S.; Löfberg, A.; Bordes-Richard, E.; Cortelli, C.; Leanza, R. *Appl. Catal.*, **2010**, *376*, 66−75.

(10)   Cheng, M.-J.; Goddard, W. A. *J. Am. Chem. Soc.* **2013**, *135*, 4600−4603.

(11)   Dietl, N.; Wende, T.; Chen, K.; Jiang, L.; Schlangen, M.; Zhang, X.; Asmis, K. R.;

Schwarz, H. *J. Am. Chem. Soc.* **2013**, *135*, 3711−3721.

(12) Cheng, M.-J.; Goddard, W. A.; Fu, R. *Top. Catal*. **2014**, *57*, 1171−1187.

(13) Zhang, M.-Q.; Zhao, Y.-X.; Liu, Q.-Y.; Li, X.-N.; He, S.-G. *J. Am. Chem. Soc*. **2017**, *139*, 342−347.

(14) Wang, P.; Fu, G.; Wan, H. *ACS Catal*. **2017**, *7*, 5544−5548.

(15) Feyel, S.; Dö bler, J.; Schrö der, D.; Sauer, J.; Schwarz, H. *Angew. Chem., Int. Ed*. **2006**, *45*, 4681−4685.

(16) Dietl, N.; Engeser, M.; Schwarz, H. *Angew. Chem., Int. Ed*. **2009**, *48*, 4861−4863.

(17) Binstead, R. A.; Moyer, B. A.; Samuels, G. J.; Meyer, T. J. *J. Am. Chem. Soc*. **1981**, *103*, 2897−2899.

(18) Tommos, C.; Babcock, G. T. *Acc. Chem. Res*. **1998**, *31*, 18−25.

(19) Chang, C. J.; Chang, M. C. Y.; Damrauer, N. H.; Nocera, D. G. *Biochim. Biophys. Acta, Bioenerg*. **2004**, *1655*, 13−28.

(20) Mayer, J. M.; Rhile, I. J. *Biochim. Biophys. Acta, Bioenerg*. **2004**, *1655*, 51−58.

(21) Warren, J. J.; Tronic, T. A.; Mayer, J. M. *Chem. Rev*. **2010**, *110*, 6961−7001.

(22) Bond, M. R.; Czernuszewicz, R. S.; Dave, B. C.; Yan, Q.; Mohan, M.; Verastegue, R.; Carrano, C. *J. Inorg. Chem*. **1995**, *34*, 5857−5869.

(23) Bond, M. R.; Mokry, L. M.; Otieno, T.; Thompson, J.; Carrano, C. *J. Inorg. Chem*. **1995**, 34, 1894−1905.

(24) Thorn, D. L.; Harlow, R. L.; Herron, N. *Inorg. Chem*. **1995**, *34*, 2629−2638.

(25) Herron, N.; Thorn, D. L.; Harlow, R. L.; Coulston, G. W. *J. Am. Chem. Soc*. **1997**, *119*, 7149−7150.

(26) Ikotun, O. F.; Marino, N.; Kruger, P. E.; Julve, M.; Doyle, R. P. *Coord. Chem. Rev*.

2010, *254*, 890−915.

(27)   Solis-Ibarra, D.; Silvia, J. S.; Jancik, V.; Cummins, C. C. *Inorg. Chem.* **2011**, *50*, 9980−9984.

(28)   Anderson, A. E.; Weberski, M. P.; McLauchlan, C. C. *Inorg. Chem.* **2012**, *51*, 8719−8728.

(29)   Manna, C. M.; Nassar, M. Y.; Tofan, D.; Chakarawet, K.; Cummins, C. C. *Dalton Trans.* **2014**, *43*, 1509−1518.

(30)   Marino, N.; Hanson, S. K.; Müller, P.; Doyle, R. P. *Inorg. Chem.* **2012**, *51*, 10077−10079.

(31)   Yucesan, G.; Armatas, N. G.; Zubieta, J. *Inorg. Chim. Acta* **2006**, *359*, 4557−4564.

(32)   Hirao, T. *Chem. Rev.* **1997**, *97*, 2707−2724.

(33)   Ganduglia-Pirovano, M. V.; Popa, C.; Sauer, J.; Abbott, H.; Uhl, A.; Baron, M.; Stacchiola, D.; Bondarchuk, O.; Shaikhutdinov, S.; Freund, H.-J. *J. Am. Chem. Soc.* **2010**, *132*, 2345−2349.

(34)   Sedai, B.; Diaz-Urrutia, C.; Baker, R. T.; Wu, R.; Silks, L. A. P.; Hanson, S. K. *ACS Catal.* **2011**, *1*, 794−804.

(35)   Riart-Ferrer, X.; Anderson, A. E.; Nelson, B. M.; Hao, F.; McLauchlan, C. C. *Eur. J. Inorg. Chem.* **2012**, *201*, 4585−4592.

(36)   Bonavia, G.; Haushalter, R. C.; O'Connor, C. J.; Zubieta, *J. Inorg. Chem.* **1996**, *35*, 5603−5612.

(37)   Bouman, H.; Teuben, J. H. *J. Organomet. Chem.* **1976**, *110*, 327−330.

(38)   Jiang, Y.; Chakarawet, K.; Kohout, A. L.; Nava, M.; Marino, N.; Cummins, C. C. *J. Am. Chem. Soc.* **2014**, *136*, 11894−11897.

(39) Bain, G. A.; Berry, J. F. *J. Chem. Educ.* **2008**, *85*, 532−536.

(40) Evans, D. F. *J. Chem. Soc.* **1959**, 2003−2005.

(41) Bartell, L. S.; Su, L.-S.; Yow, H. *Inorg. Chem.* **1970**, *9*, 1903− 1912.

(42) Agarwal, P.; Piro, N. A.; Meyer, K.; Müller, P.; Cummins, C. C. *Angew. Chem., Int. Ed*. **2007**, *46*, 3111−3114.

(43) Dean, N. S.; Mokry, L. M.; Bond, M. R.; Mohan, M.; Otieno, T.; O'Connor, C. J.; Spartalian, K.; Carrano, C. *J. Inorg. Chem.* **1997**, *36*, 1424−1430.

(44) Salta, J.; Zubieta, J. *J. Cluster Sci.* **1996**, *7*, 531−551.

(45) Galloni, P.; Conte, V.; Floris, B. *Coord. Chem. Rev*. **2015**, 301− 302, 240−299.

(46) Compton, R. G.; Banks, C. E. *Understanding Voltammetry, 2nd ed*.; Imperial College Press: London, **2011**.

(47) Shimizu, K.; Sepunaru, L.; Compton, R. G. *Chem. Sci.* **2016**, *7*, 3364−3369.

(48) Nicholson, R. S.; Shain, I. *Anal. Chem.* **1965**, *37*, 178−190.

(49) Nadjo, L.; Saveant, J. M. *J. Electroanal. Chem. Interfacial Electrochem*. **1971**, *33*, 419−451.

(50) Nadjo, L.; Saveant, J. M.́ *J. Electroanal. Chem. Interfacial Electrochem.* **1971**, *30*, 41−57.

(51) Guliants, V. V.; Benziger, J. B.; Sundaresan, S. *Chem. Mater*. **1995**, *7*, 1485−1492.

(52) Guliants, V. V.; Benziger, J. B.; Sundaresan, S.; Wachs, I. E.; Jehng, J. M. *Chem. Mater*. **1995**, *7*, 1493−1498.

(53) Huan, G.; Johnson, J. W.; Brody, J. F.; Goshorn, D. P.; Jacobson, A. J. *Mater. Chem. Phys*. **1993**, *35*, 199−204.

(54) Villeneuve, G.; Suh, K. S.; Amoros, P.; Casan-Pastor, N.; Beltran-Porter, D. *Chem.*

Mater. **1992**, *4*, 108−111.

(55)   Hahn, C. W.; Rasmussen, P. G.; Bayon, J. C. *Inorg. Chem.* **1992**, *31*, 1963−1965.

(56)   Telser, J. EPR Interactions − Zero-Field Splittings. In eMagRes.; Wiley: Chichester, U.K., **2007**.

(57)   As such, this triplet signal was simulated phenomenologically as a spin doublet with giso = 1.975 and W (Gaussian, hwhm) = 300 MHz.

(58)   Gö rlitz, F. H.; Gowik, P. K.; Klapötke, T. M.; Wang, D.; Meier, R.; Welzen, J. v. J. *Organomet. Chem*. **1991**, *408*, 343−355.

(59)   For comparison, complexes of formula [Cp$_2$V(THF)0,1X2,1] +,0 (X = AsF$_6^-$, SbF$_6^-$) gave as polycrystalline solids g⊥ = 2.000(2) and g‖ = 1.925(5) and in fluid (THF) solution giso = 1.990(5), aiso(51V) = 220(5) MHz (see ref 57).

(60)   Krzystek, J.; Ozarowski, A.; Telser, J.; Crans, D. C. *Coord. Chem. Rev*. **2015**, 301−302, 123−133.

(61)   Chasteen, N. D. Vanadyl(IV) EPR Spin Probes Inorganic and Biochemical Aspects. In *Biological Magnetic Resonance*; Berliner, L. J., Reuben, J., Eds.; Plenum: New York, **1981**; Vol. 3, pp 53−119.

(62)   Kowaleski, R. M.; Basolo, F.; Trogler, W. C.; Gedridge, R. W.; Newbound, T. D.; Ernst, R. D. *J. Am. Chem. Soc.* **1987**, *109*, 4860− 4869.

(63)   Belford, R. L.; Belford, G. G. J. Chem. Phys. 1973, 59, 853−854. (64) Worrell, W. L.; Chipman, J. *J. Phys. Chem*. **1964**, *68*, 860−866

Chapter 3

A Mono-, Di-, and Tri-Vanadocene Phosphorus Oxide Series: Synthesis, Magnetism, and Chemical/Electrochemical Properties

3.1 Introduction

Considerable interest in the structure, bonding, and reactivity of vanadium phosphates exists, in part due to the industrially relevant vanadium phosphorus oxide (VPO) heterogeneous catalyst for the conversion of butane to maleic anhydride. This net 14 e$^-$ process involves the abstraction of eight hydrogen atoms and insertion of three O atoms and has been the topic of numerous mechanistic studies.[1-6] Despite these extensive studies, no consensus mechanism yet exists. While these studies suggest a key role for terminal high-valent vanadyls (V=O) in the initial rate-determining C–H activation at butane, both gas-phase experimental studies by Schwarz *et al.*,[7-10] as well as computational studies by Goddard *et al.*[11-13] offer an alternative pathway involving the assumed "innocent" terminal P^V=O linkages of the support. Gas phase studies of the heteronuclear cluster ions, $[V_xP_{4-x}O_{10}]^{\bullet+}$ (x = 0, 2-4), have been reported to undergo homolytic C–H bond activation (Scheme 1a).[8-9] The missing $[VP_3O_{10}]^{\bullet+}$ cation could not be prepared, but the structure and reactivity were computationally elucidated. While the metal free $[P_4O_{10}]^{\bullet+}$ cluster was found to be more reactive than the all metal analog, $[V_4O_{10}]^{\bullet+}$ – with C–H activation occurring at a terminal oxyl radical in both species – the resulting PO–H bond

strengths were found to increase with increasing V incorporation into the clusters. For instance, a single V substitution from $[P_4O_{10}]^{\cdot+}$ to $[VP_3O_{10}]^{\cdot+}$ increased the resulting PO–H bond strength from 28.2 to 60.5 kcal/mol, and increased further to 84.3 and 89.2 kcal/mol for di- and tri-substituted clusters, respectively (Scheme 3.1a). Computational studies using DFT on the VPO catalyst by Goddard complement in part Schwarz's gas-phase results. The unusual proposed butane C–H reactivity at terminal $P^V=O$ bonds in VPO was proposed to be the result of the strong basicity at P=O coupled with highly oxidizing neighboring V^V centers.

Scheme 3.1: a) Valence bond description of the hydrogen abstraction process by P=O using finite cluster models. b) Complex 1 as a model compound for VPO reactivity.

a) *Previous DFT and gas-phase studies*

(DFT)   (gas)   (gas)
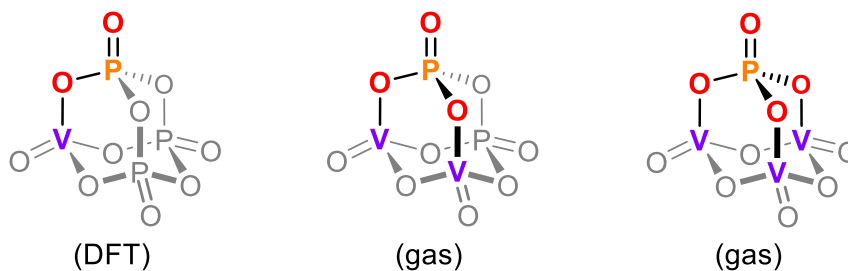
b) *This work: Synthetic analogs*

3.1 (LA = blank)
3.2 (LA = B(C$_6$F$_5$)$_3$)
3.8 (LA = BPh$_3$)   **3.3** (LA = B(C$_6$F$_5$)$_3$)   **3.4** (LA = B(C$_6$F$_5$)$_3$)
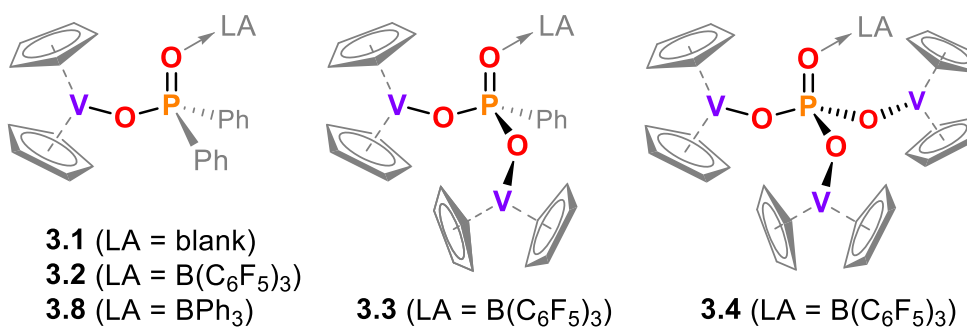
Our lab was interested in investigating this proposed main-group/metal cooperative reactivity. In Chapter 2 we reported the synthesis and preliminary reactivity of a vanadium phosphinate model complex bearing an isolated V^{III}-O-P^V=O linkage (**3.1**, Scheme 3.1b). In this study, we expand the set of complexes to include di- and tri-substituted central P^V=O fragments tethered to vanadocene fragments, and further probe their magnetic, chemical, and electrochemical properties. We further probed the reactivity of these new complexes upon oxidation and isolated a series of complexes which underwent rearrangement reactions altering the total metal nuclearity of the starting complexes.

3.2 Results and Discussion

3.2.1 Synthesis and Characterization of Multimetallic Vanadocene Complexes

In Chapter 2 we reported the synthesis of **3.1** involved the protonolysis of Cp$_2$VMe[14] with diphenylphosphinic acid, Ph$_2$P(O)OH.[15] After our initial report, we discovered a cleaner, higher yielding route (74% vs. 63%) involving trimethylsilyl fluoride (Me$_3$Si-F, TMS-F) elimination from the known compounds Cp$_2$VF and Ph$_2$P(O)OTMS.[16-17] This improved synthesis is reported in the experimental section. We utilized this same strategy to target the series of mono-(**3.2**, **3.8**), di-(**3.3**, **3.5**), and tri-metallic (**3.4**) complexes reported here (Scheme 3.2).

Scheme 3.2. Synthesis of select reported compounds.
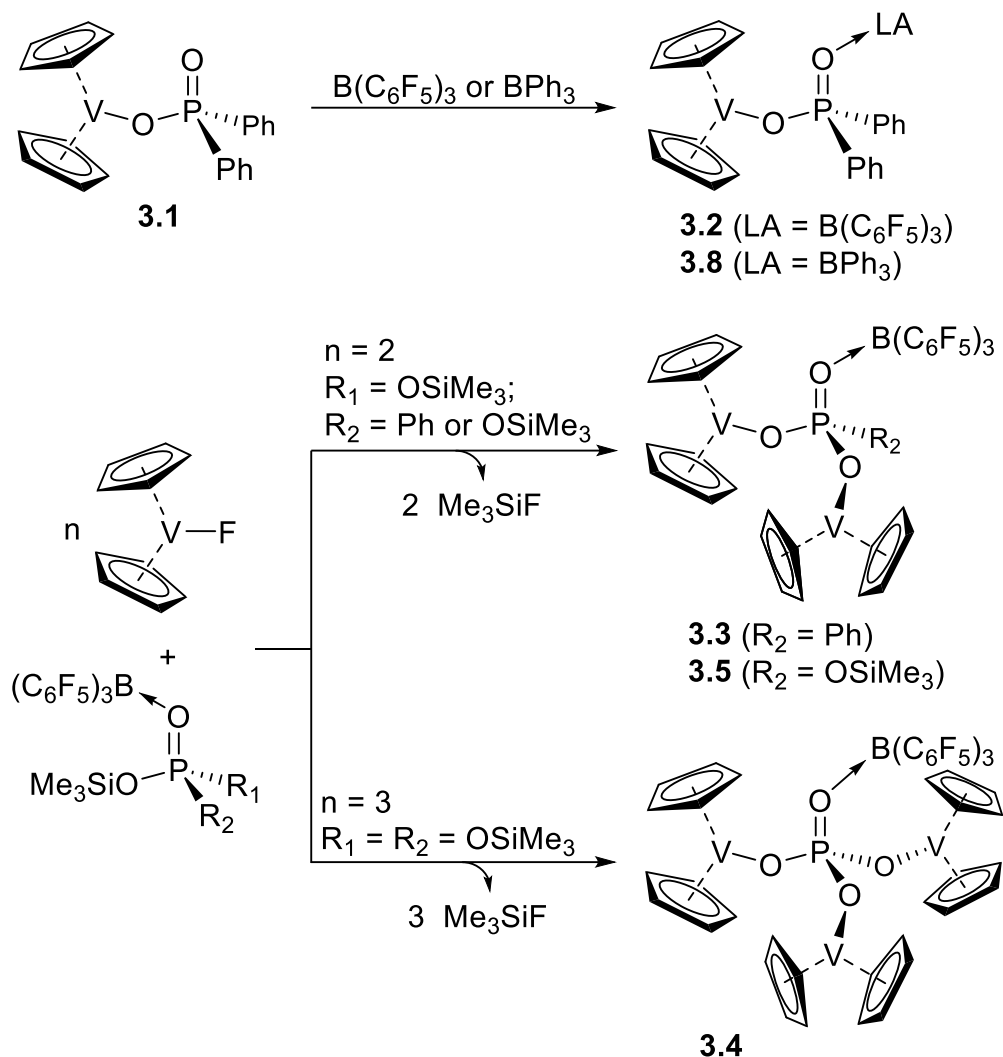
As will be described, a Lewis acidic "cap" coordinated to the P=O bond was required to generate stable multi-metallic complexes (**3.3-3.5**; Scheme 2). In order to compare the entire series, a "capped" variant of **3.1** was also synthesized. We chose tris(pentafluorophenyl)borane, $B(C_6F_5)_3$, as the Lewis acid (LA) and treatment of a slight excess of this to **3.1** in toluene afforded the clean production of the capped product **3.2** in

84% yield (Scheme 3.2). Blue plate shaped single crystals suitable for X-ray diffraction (XRD) studies were grown by vapor diffusion of pentane into a concentrated dichloromethane (DCM) solution of **3.2**. The solid-state structure of **3.2** (Figure 3.1) revealed that incorporation of the electron withdrawing $B(C_6F_5)_3$ leads to elongation of the P(1)-O(2) double bond (1.5369(15) Å) and contraction of the P(1)-O(1) bond (1.5015(15) Å) relative to **3.1** (1.500(2) Å and (1.5560(19) Å, respectively). A full comparison of selected bond distances and angles is shown in Table 3.1. Consistent with an expected paramagnetic species (*vide infra*), the Ph and Cp proton resonances are broadened and silent, respectively, in the ^1H NMR spectrum. Both ^{51}V and ^{31}P NMR resonances are also silent, whereas the ^{19}F NMR spectrum revealed shifted and broadened diagnostic *para* and *meta* and absent *ortho* resonances. Lastly, the ^{11}B NMR resonance is in the expected region for a four-coordinate B center.[18]
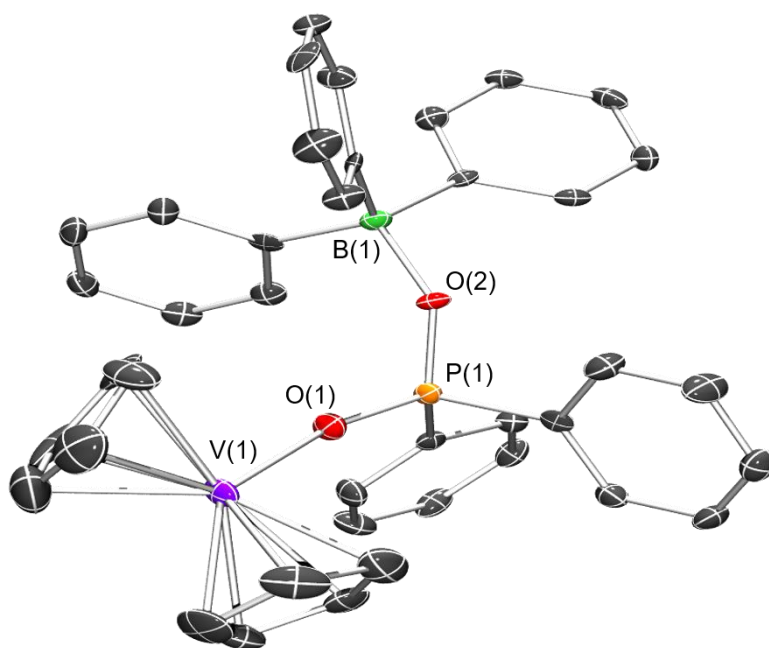
Figure 3.1: Solid-state molecular structure of **3.2**. H and F atoms and solvent molecules omitted for clarity.

Our initial attempts at synthesizing a dimetallic complex involved mixing a 1:2 ratio of the known compound PhP(O)(OTMS)$_2$[19] with Cp$_2$VF, analogous to the synthesis of **3.1**. While quantitative production of TMS-F was observed by ^{1}H and ^{19}F NMR spectroscopy, the solution quickly turned black and no pure product could be obtained. Free CpH is also observed in the ^{1}H NMR spectrum, which may suggest intramolecular ligation of the free P=O bond to the V center as a single-electron decomposition pathway. To test this premise, we capped the basic P=O linkage with B(C$_6$F$_5$)$_3$. The putative Lewis acid-base adduct, Ph(TMSO)$_2$P=O→B(C$_6$F$_5$)$_3$, was generated *in situ* in DCM and subsequently exposed to 2 equivalents of Cp$_2$VF. In contrast to the uncapped reaction, the solution retained its bright blue color and displayed no signs of decomposition. The product was isolated in 47% yield. Single crystals suitable for XRD studies were grown by vapor diffusion of hexanes into a concentrated toluene solution. In contrast to **3.2**, the solid-state structure of **3.3** (Figure 3.2) revealed an elongation of the P(1)-O(2) double bond (1.554(7) Å) which is longer than a typical P=O bond (~1.50 Å).[20] Additionally the B(1)-O(2) bond length is slightly contracted (1.505(14) Å) compared to **2** (1.527(3) Å) which may indicate a stronger Lewis acid-base adduct. Similar to **3.2**, the paramagnetic nature of **3.3** results in silent ^{51}V and ^{31}P NMR resonances and broadened Ph resonances in the ^{1}H NMR spectrum. The ^{19}F NMR spectrum displays paramagnetically shifted signals tentatively assigned to *ortho* F (-30.9 ppm) and overlapping *meta* and *para* F (-160.5 ppm). A ^{11}B resonance for **3** is again observed, yet it is downfield shifted relative to **2** (9.65 vs 0.08 ppm).
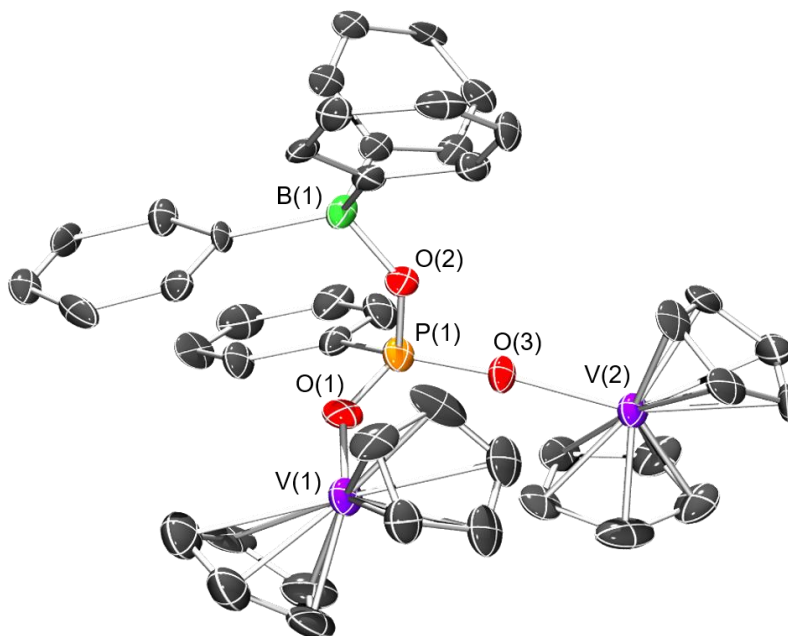
Figure 3.2: Solid-state molecular structure of **3.3**. H and F atoms and solvent molecules omitted for clarity.

Similar to the dimetallic (**3.3**), a trimetallic species could not be isolated without a capping LA. Thus, the *in situ* generated adduct, $(TMSO)_3P=O\rightarrow B(C_6F_5)_3$, was treated to 3 equivalents of Cp_2VF in tetrahydrofuran (THF) (Scheme 3.2). The solution was stirred for 48 h and the pure product isolated in 43% yield following purification. Blue plate shaped single crystals suitable for XRD studies were grown by slow diffusion of pentane into a concentrated THF solution of **3.4** (Figure 3.3). The bond metrics in **3.4** remain fairly unchanged compared to **3.3** (Table 1). Consistent with a paramagnetic species, the ^1H, ^{31}P, and ^{51}V NMR resonances were absent, whereas again a set of close *meta* and *para* ^{19}F resonances were present. The ^{11}B NMR spectrum of **3.4** again displayed a downfield shifted resonance at 14.07 ppm.
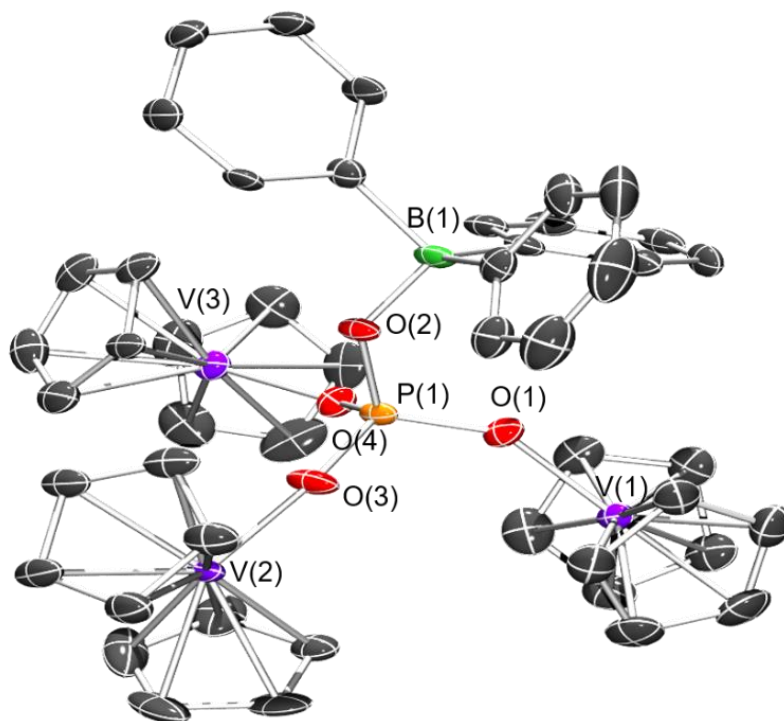
Figure 3.3: Solid-state molecular structure of **3.4**. H and F atoms and solvent molecules omitted for clarity.

We noticed that in the attempted synthesis of **3.4** in DCM rather than THF, only 2 equivalents of TMS-F were produced after four days at room temperature as observed by ^{1}H NMR spectroscopy. Upon work-up of the reaction mixture, single crystals suitable for XRD studies were grown by vapor diffusion of pentane into a saturated DCM solution of the product. The solid-state molecular structure confirmed the composition as the dimetallic species, $(Cp_2VO)_2(TMSO)POB(C_6F_5)_3$ (**5**) (Figure 3.4). Bond metrics and spectroscopic properties are similar to **3.3** and **3.4** (see experimental section and Table 3.2). Based on these results, it appears that the substitution of TMS for VCp$_2$ is solvent dependent with the reaction stopping after di-substitution in DCM, whereas full

substitution occurs in THF. All reported multimetallic complexes exhibited thermal sensitivity and were stored at -40 ºC in the glovebox to prevent decomposition. The likely thermal decomposition pathway occurs after the LA adduct is removed and internal attack of the P=O bond can occur.
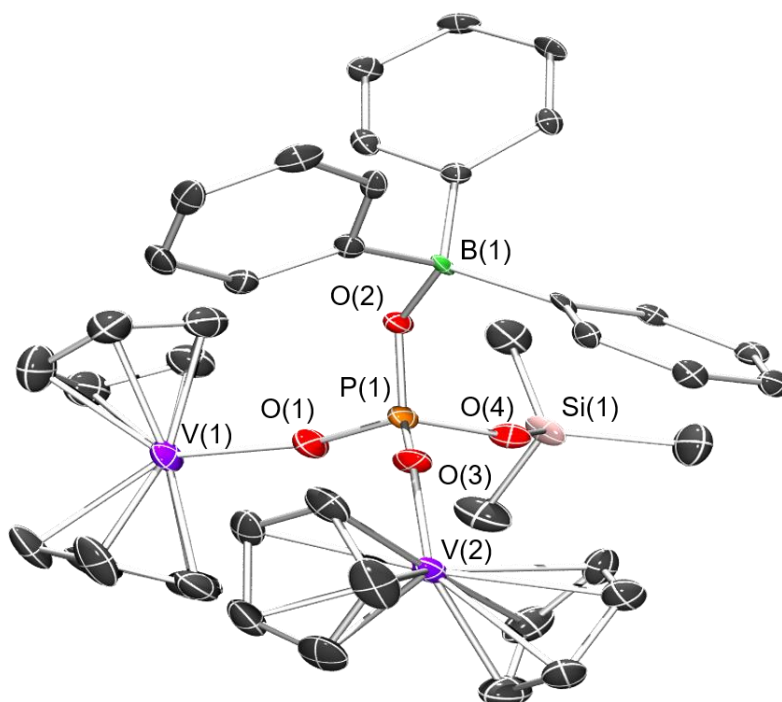
Figure 3.4: Solid-state molecular structure of **3.5**. H and F atoms and DCM solvent molecules omitted for clarity.

Table 3.1: Selected Bond Distances (Å) and Bond Angles (º) for Complexes **3.2-3.4**.

	(3.2)	(3.3)	(3.4)
V(1)-O(1)	2.0284(14)	2.019(8)	1.975(4)
V(2)-O(3)	-	1.989(7)	1.958(4)
V(3)-O(4)	-	-	2.003(5)
P(1)-O(1)	1.5015(15)	1.508(8)	1.522(5)
P(1)-O(2)	1.5369(15)	1.554(7)	1.559(4)
P(1)-O(3)	-	1.509(7)	1.514(4)
P(1)-O(4)	-	-	1.531(5)
O(2)-B(1)	1.527(3)	1.505(14)	1.491(8)
V(1)-O(1)-P(1)	148.34(10)	146.9(5)	144.4(3)
V(2)-O(3)-P(1)	-	174.4(5)	168.8(4)
V(3)-O(4)-P(1)	-	-	144.6(3)
O(1)-P(1)-O(2)	-	111.0(4)	108.0(2)
O(3)-P(1)-O(2)	-	107.4(4)	106.8(2)
O(4)-P(1)-O(2)	-	-	108.5(2)
P(1)-O(2)-B(1)	136.10(14)	139.9(7)	133.2(4)

3.2.2 Electronic Characterization of Multimetallic Vanadocene Complexes

We were next interested in studying in more detail the electronic properties of **3.2-3.4** in order to determine the impact of increasing the metal count around the central P=O linkage, as well as the extent of metal-metal electronic communication, if any. To examine these properties, we utilized a combination of spectroscopic, electrochemical, and magnetometric techniques.

As described above, the ^{11}B NMR chemical shifts for complexes **3.2**, **3.3**, and **3.4**

become increasingly downfield shifted (Figure 3.5). This trend suggests increasingly electron rich systems resulting in more Lewis basic P=O moieties, and thus stronger donation to B. This is also observed by the decreasing B–O bond lengths from **3.2**→**3.4** (Table 3.1). More electron rich four coordinate boron centers appear more downfield than similar electron poor congeners, although anomalies to this general trend are not uncommon.[18, 21] Additionally, the decreasing B-O bonds across the series decreases as would be expected for the steric bulk of the mono, di, and tri-substituted species respectively. Once again indicating a stronger donation to the LA.
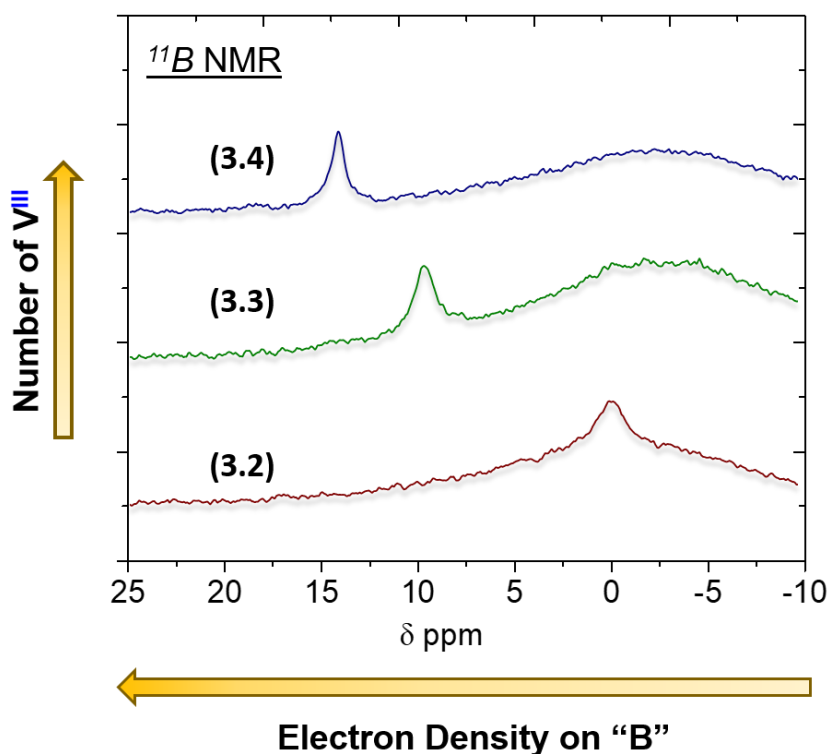
Figure 3.5: ^{11}B NMR signals of **3.2**, **3.3** and **3.4**.

In order to investigate the perceived increase in basicity, we probed the redox properties of **3.2**, **3.3**, and **3.4** by cyclic voltammetry (CV).[22] The CVs of **3.2**, **3.3**, and **3.4**

were taken at a 25 mV/s scan rate in DCM with [Bu$_4$N][PF$_6$] supporting electrolyte and referenced to the ferrocene/ferrocenium (Fc/Fc$^+$) redox couple (Figure 3.6a). The voltammogram for **3.2** displays a single irreversible oxidation event at E_{ox} = 0.05 V vs. Fc/Fc$^+$. In contrast, the voltammograms for **3.3** and **3.4** show two (E_{ox} = 0.09, -0.08 V) and three (E_{ox} = 0.09, -0.08, -0.28 V) irreversible oxidation events, respectively, with each being sequentially more cathodically shifted than the previous (Figure 3.6b). With the number of oxidation events corresponding to the number of V^{III} centers per complex, it is likely that each event corresponds to sequential oxidations of the individual V^{III} centers to V^{IV}. In addition, the CVs clearly demonstrate that increasing the number of –OVCp$_2$ fragments systematically decreases the first V^{III}/V^{IV} oxidation event – with a full 0.37 V difference between the first oxidations in **3.2** and **3.4** – thus indicating more electron rich complexes, further supporting the NMR data (Figure 3.5).
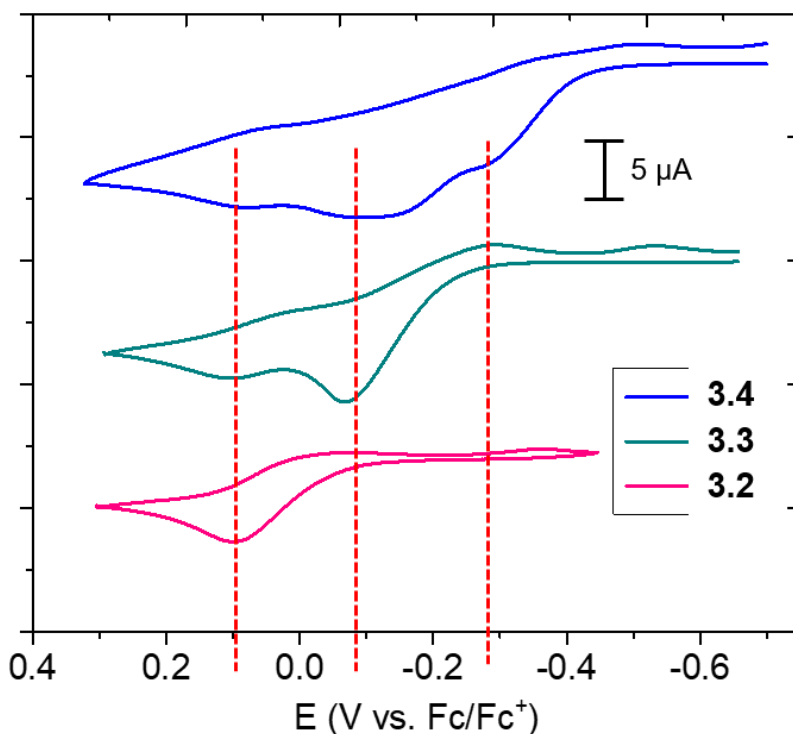
Figure 3.6: CVs of **3.2**, **3.3**, and **3.4** (1.0 mM) in 0.1 M [Bu$_4$N][PF$_6$] DCM solution at a 25 mV s^{-1} scan rate using a glassy carbon working electrode, platinum wire counter electrode, and referenced to the Fc/Fc$^+$ couple.

The electronic structures of **3.2**, **3.3**, and **3.4** were further investigated using SQUID magnetometry. Magnetic susceptibility (χ_MT) measurements for **3.2**, **3.3**, and **3.4** were collected at variable temperatures (2-300 K) under a static 0.1 T field (Figure 3.7). All samples exhibit Curie-like paramagnetic behavior over most of the temperature range surveyed, indicated by a plateauing χ_MT versus T line. The χ_MT for **3.2**, **3.3**, and **3.4** plateau at 1.02 (T > 10 K), 1.99 (T > 50 K), and 3.08 cm^3 K/mol (T > 100 K), respectively (Figure 3.7). These values are consistent with non-interacting spin manifolds – with each V center adopting a high-spin S = 1 state – approximated by the general formula, χ_MT = [$\sum S_i(S_i + 1)$]/2) (assuming g = 2.0), yielding χ_MT values of 1.00, 2.00, and 3.00 cm^3 K/mol for mono-, di-, and tri-metallic systems, respectively. The data were fit for each system using the following parameters (where D and E/D are the axial and rhombic zero-field splitting (ZFS) parameters and J is the magnetic exchange coupling constant): for **3.2**, g = 2.02, D = 6.1 cm^{-1}, and E/D = 0.07; for **3.3**, $g_1 = g_2$ = 2.02; J_{12} = -0.67 cm^{-1}, $D_1 = D_2$ = 5.1 cm^{-1}, $E/D_1 = E/D_2$ = 0.09; and for **3.4**, $g_1 = g_2 = g_3$ = 2.02; $J_{12} = J_{13} = J_{23}$ = -0.79 cm^{-1}; $D_1 = D_2 = D_3$ = 4.8 cm^{-1}; $E/D_1 = E/D_2 = E/D_3$ = 0.07. Considering the analogous geometries and spin states at each V center, and to avoid overparameterization, we set all g factors equivalent at 2.02. All other values are similar from complex to complex and are within expected ranges.[23] The J values are fairly small for **3.3** and **3.4**, which is expected considering the long distances between V centers (>5 Å), excluding the possibility of a

64

superexchange mechanism.[24] Together, the fit parameters may help explain some of the observed trends. For **3.2** and **3.3**, a sharp decrease in $\chi_M T$ is observed below 8 K and 50 K, respectively, likely the result of ZFS. For **3.4**, this downward trend begins around 100 K and is more gradual, perhaps indicating a mixture of ZFS and weak antiferromagnetic coupling effects.
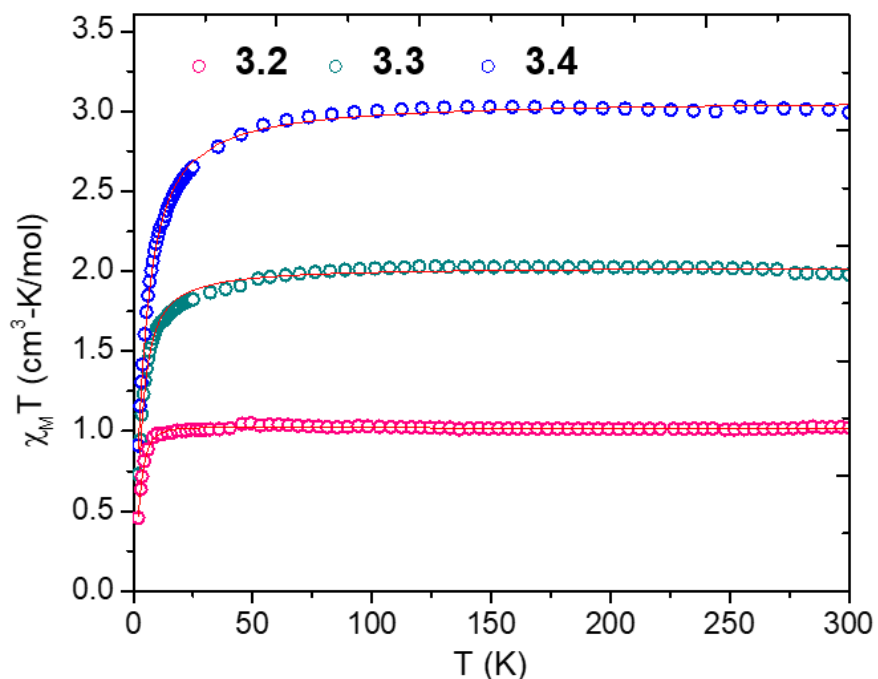
Figure 3.7: Molar magnetic susceptibility (χ_M) vs. temperature measurements for bulk crystalline **3.2**, **3.3**, and **3.4** collected from 2-300 K (colored circles) at 0.1 Tesla. Red trace represents theoretical fit.

The combined spectroscopic, electrochemical, and magnetometric data on complexes **3.2**, **3.3**, and **3.4** clearly show that increasing the number of metals makes the complexes progressively more electron rich, yet the metals themselves are both

electrochemically and magnetically distinct, operating mostly independently of each other.

3.2.3 Chemical Oxidation and Characterization

The irreversible CVs of complexes **3.2**-**3.4** (Figure 3.6) suggested that electron transfer was followed by a chemical transformation (*EC* mechanism). In order to better understand the chemistry of these potential VPO models, we were next interested in isolating the products of these oxidations. We previously reported in Chapter 2 that the voltammogram of the uncapped species **3.1** featured two redox events (Figure 3.8, black trace) which we demonstrated were indicative of an electron transfer–chemical reaction–electron transfer (*ECE*) mechanism resulting in its oxidative dimerization to $[Cp_2V(\mu_2$-$O_2PPh_2)_2VCp_2]^{2+}$ (**3.6**) (Scheme 3.3).[15] In contrast to **3.1**, the CV of the LA capped **3.2** revealed a single anodically shifted irreversible oxidation event at $E_{ox} = 0.05$ V vs. Fc/Fc$^+$, a 0.37 V shift in potential relative to **3.1** (Figure 3.8, blue trace) and consistent with reported LA-induced anodic shifts in various complexes.[23-25]
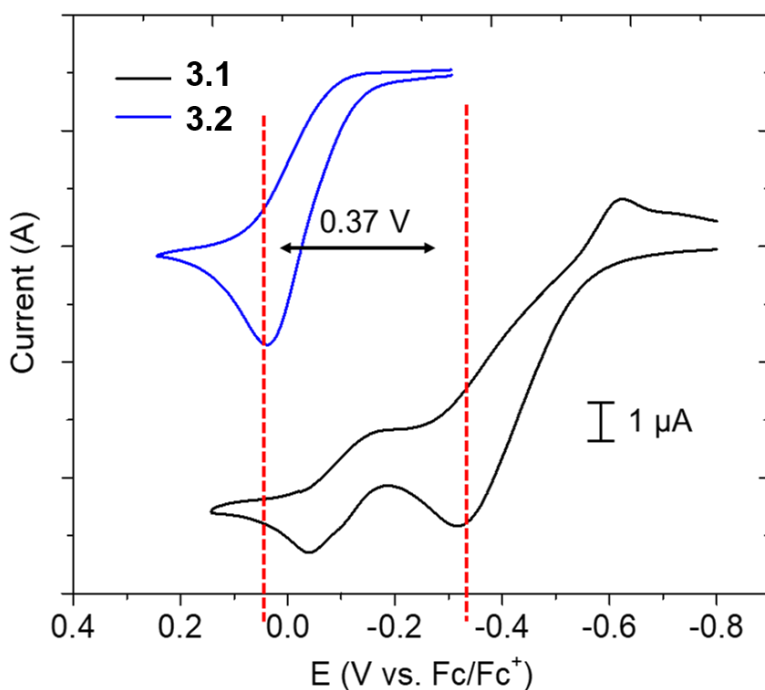
Figure 3.8: CVs of **3.1** and **3.2** (1.0 mM) in 0.1 M [Bu$_4$N][PF$_6$] DCM solution at a 10 mV s^{-1} scan rate using a glassy carbon working electrode, platinum wire counter electrode, and referenced to the Fc/Fc$^+$ couple.

Compound **3.2** was further analyzed at varying scan rates and displays an irreversible oxidation event at slow sweep rates which becomes increasingly reversible at faster sweep rates (Figure 3.9).
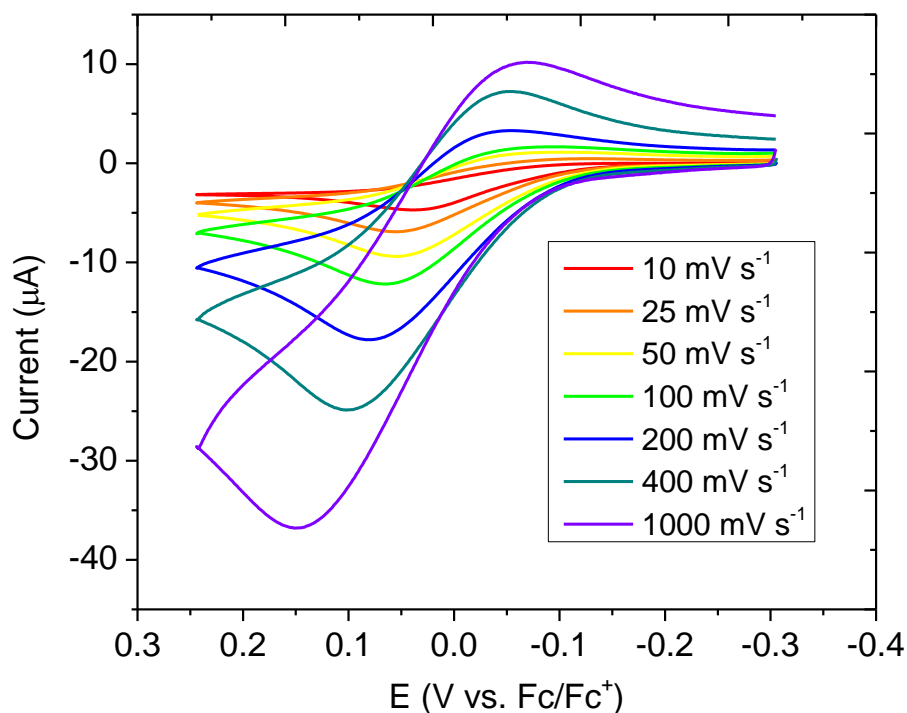
Figure 3.9: CVs of **2.1** (1.0 mM) in 0.1 M [Bu$_4$N][PF$_6$] DCM solution at varying scan rates using a glassy carbon working electrode, platinum wire counter electrode, and referenced to the Fc/Fc$^+$ couple.

The first oxidation event of **3.2** was analyzed using the Randles-Ševčik equation for an irreversible system:[1-2]

$I = 2.99 \times 10^5 n(n'+\alpha)^{1/2} A D^{1/2} C v^{1/2}$ (1)

where I is the peak current, n is number of electrons in the overall chemical process, n' is the number of electrons involved prior to the rate determining step (0 in this case), A is the surface area of the glassy-carbon working electrode (3 mm diameter), D is the diffusion coefficient, C is the concentration of analyte (1 mM), v is the scan rate (V s^{-1}),and α is the charge transfer coefficient. The diffusion coefficient D was estimated using the Wilkes-Chang equation:[3]

$$D_{AB} = 7.4 \times 10^{-8} \frac{(xM)^{1/2}T}{\eta V^{0.6}}$$ (2)

Where x is the association parameter ($x = 1$ for non-associative solvents), M is the molar mass of the solvent (84.93 g mol^{-1}), T is temperature (298 K), η is the solvent viscosity (0.041 g cm^{-1}s^{-1}), and V is the molar volume of the analyte. The molar volume of the analyte V was calculated using the unit cell volume (V_{cell}) from the unit cell parameters for complex **3.2**. The theoretical model is based off a one electron transfer. An analysis of this oxidation event using the Randles-Ševčik equation for an irreversible process was inconsistent with a simple single electron transfer process (Figure 3.10).[26-27] These data suggest an *EC* mechanism may be at play, rather than the proposed *ECE* mechanism for **3.1**.[26]
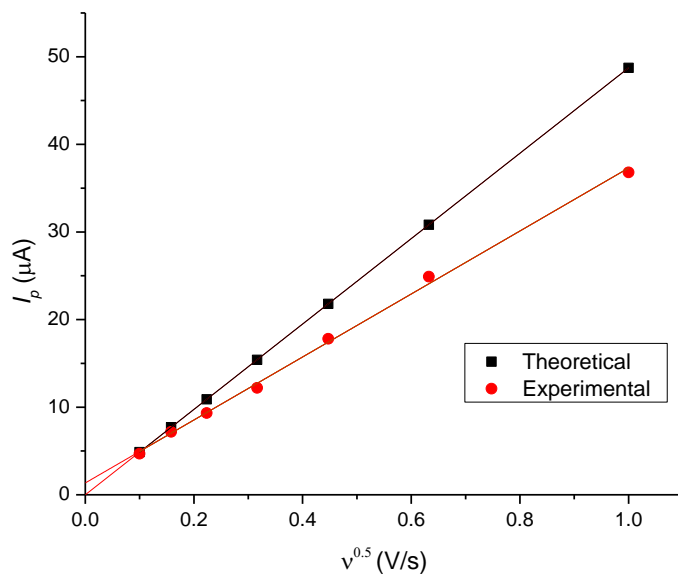
Figure 3.10: Randles-Ševčik plot for an n = 1 irreversible oxidation and theoretical fit for complex **3.2** (I_p = peak current; ν = scan rate).

Scheme 3.3: Chemical oxidation of complexes **3.1**, **3.2**, and **3.8**.
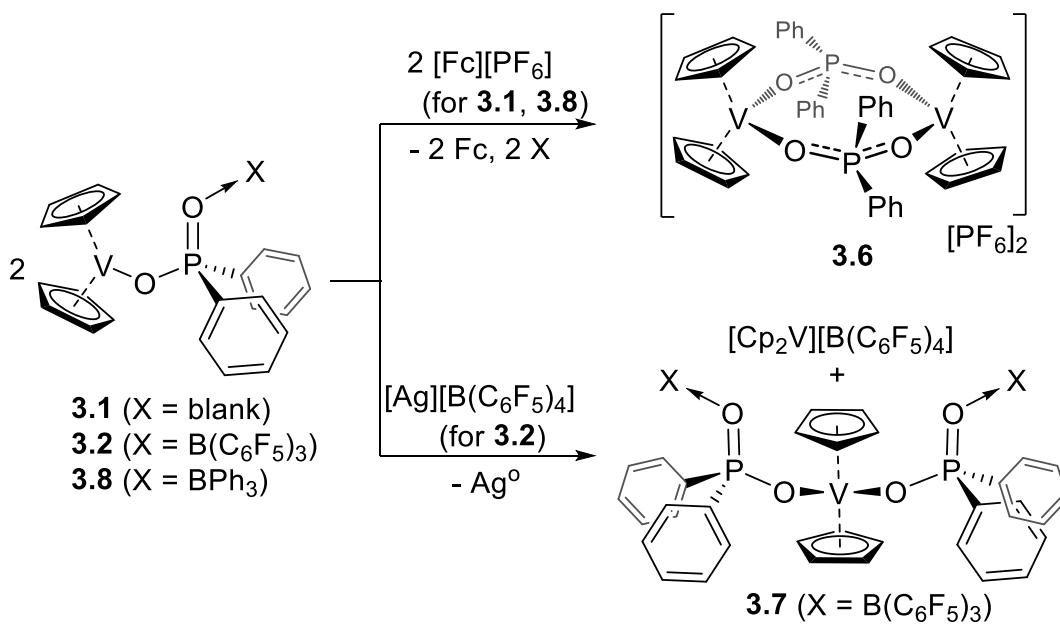
Attempts to oxidize **3.2** with traditional ferrocenium hexafluorophosphate showed no reactivity owing to the increase in oxidation potential from the BCF adduct. Nevertheless, Chemical oxidation of **3.2** in DCM with half an equivalent of $[Ag][B(C_6F_5)_4]$ resulted in an immediate color change from bright blue to green and gradual precipitation of Ag metal. Upon workup, single green crystals suitable for XRD studies were grown from vapor diffusion of pentane into a concentrated toluene solution of **3.7** at -40 °C, and the solid-state structure confirmed the composition as the new diphosphonate V^{IV} product, **3.7** (Scheme 3.3, Figure 3.11). Bond metrics are fairly unremarkable for this structure (Table 3.2 *vide infra*). These results are consistent with the electrochemical measurements indicating an *EC* mechanism. Through mass balance, we assume that the by-product of this reaction is the vanadocenium salt, $[VCp_2][B(C_6F_5)_4]$ (Scheme 3.3),[28] although it was never isolated.
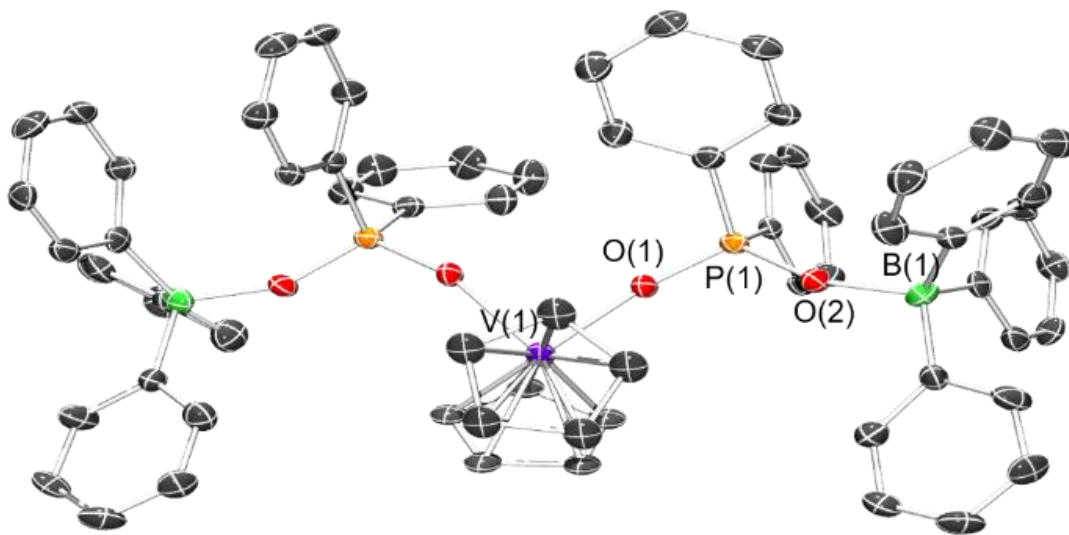
Figure 3.11: Solid-state molecular structure of **3.7**. Hydrogen atoms, fluorine atoms, and co-crystalized DCM are ommitted for clarity

The rearrangement from **3.2**→**3.7** is similar to the transformation of **3.1**→**3.6**, wherein oxidation results in additional coordination at the V center, going from three coordinate to four coordinate; however, LA coordination in the reagent has a clear impact on product formation. We were curious to see to what extent the LA would alter the course of the reaction. We decided to synthesize an analog of **3.2** with a poorer LA, namely BPh₃. The BPh₃-coordinated precursor, **3.8** (Scheme 3.2), was synthesized in an analogous fashion to **3.2** and was fully characterized, including by XRD studies (Figure 3.12). In contrast to **3.2**, compound **3.8** displayed an analogous CV to **3.1** likely indicating a similar *ECE* reaction pathway (Figure 3.13). Indeed, chemical oxidation of **3.8** with [Fc][PF₆] resulted in the quantitative isolation of **3.5** with expulsion of the weaker capping LA, BPh₃. These results indicate that the course of reaction can be controlled by judicious choice of LA (Scheme 3.3).
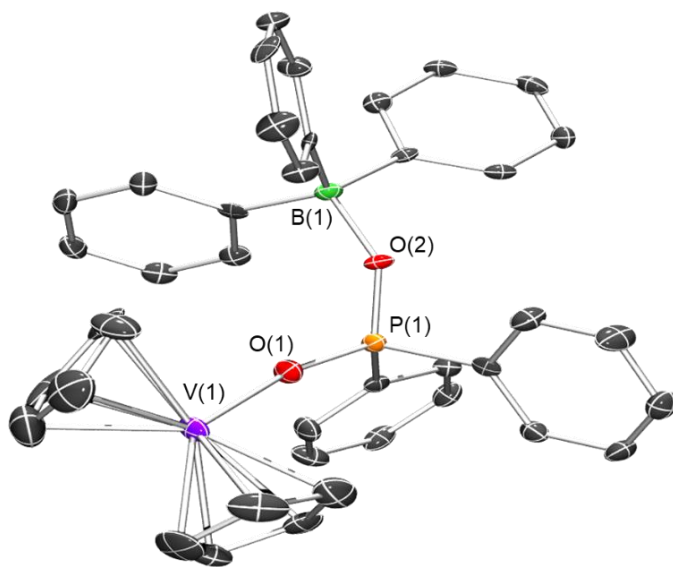
Figure 3.12: Solid-State structure of **3.8**. Hydrogen Atoms omitted for clarity
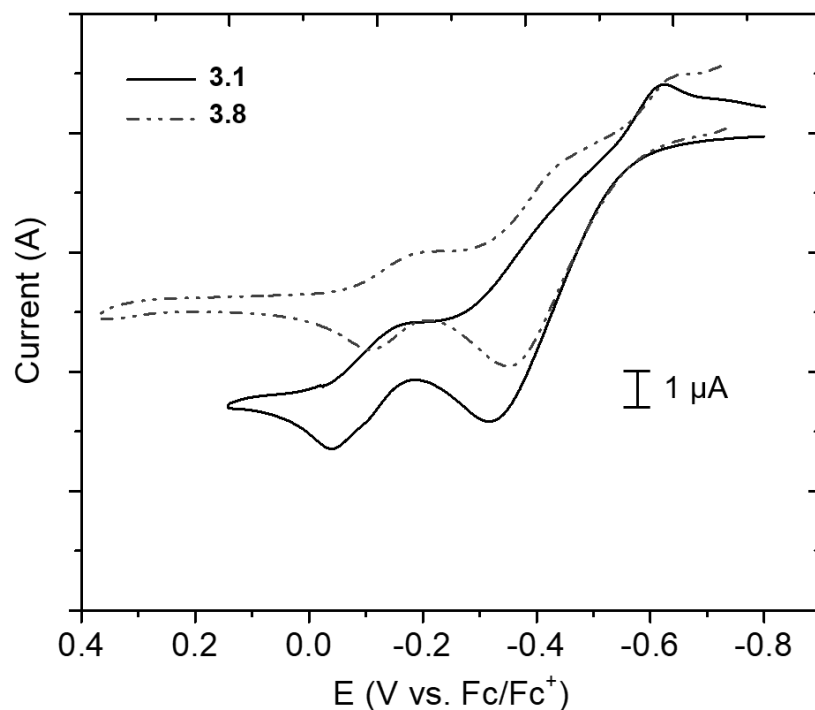
Figure 3.13: Cyclic voltammogram of **3.1** (solid trace) and **3.8** (dotted trace) (1.0 mM) in 0.1 M [Bu$_4$N][PF$_6$] supporting electrolyte in CH$_2$Cl$_2$ using a glassy carbon working electrode, platinum wire counter electrode, and Ag/Ag$^+$ reference electrode. Scan rate: 10 mV s^{-1}. Referenced to Fc/Fc$^+$.

We next attempted to chemically oxidize the multi-metallic complexes, **3.3** and **3.4**. Unfortunately, no clean product could be isolated upon oxidation of **3.3,** and reaction monitoring seemed to indicate decomposition and loss of Cp$^-$. However, **3.4** could be oxidized using the trityl salt, [Ph$_3$C][B(C$_6$F$_5$)$_4$]. Treatment of **3.4** to one equivalent of [Ph$_3$C][B(C$_6$F$_5$)$_4$] resulted in an immediate color change from blue to dark green, as well as the formation of one equivalent of Ph$_3$C-C$_6$H$_5$-CPh$_2$ (Gomberg's dimer)[29-30] as observed by ^{1}H NMR spectroscopy. After work-up and repeated recrystallizations, green block-shaped single crystals suitable for X-ray diffraction were grown by slow diffusion of

pentane into a concentrated solution of toluene to yield the dimetallic complex, **3.9** (Figure 3.14, Scheme 3.4). The solid-state structure of **3.9** revealed that one VCp$_2$ moiety is expelled upon oxidation of **3.4** – similar to the oxidation of **3.2**→**3.7** (Scheme 3.3) – yielding a mixed-valent V^{III}/V^{IV} product, and presumably [Cp$_2$V][B(C$_6$F$_5$)$_4$] (Scheme 3.4). While the latter by-product was again not isolated, the oxidation could be similarly performed using trityl chloride (Ph$_3$CCl). In this case, **3.9** was again produced with the presence of the by-product, Cp$_2$VCl,[31] being confirmed by XRD studies.
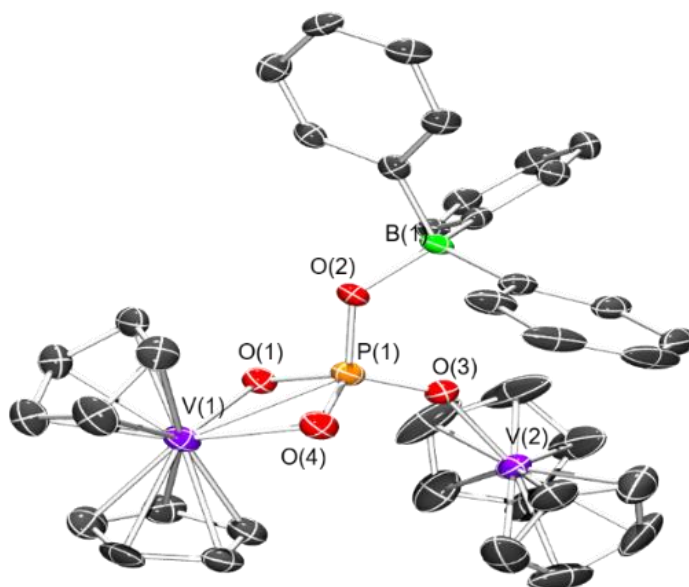
Figure 3.14: Solid-state molecular structure of **3.9**. Hydrogen atoms, fluorine atoms, and co-crystalized toluene and pentane ommitted for clarity

Scheme 3.4: Oxidation of **3.4** to **3.9**
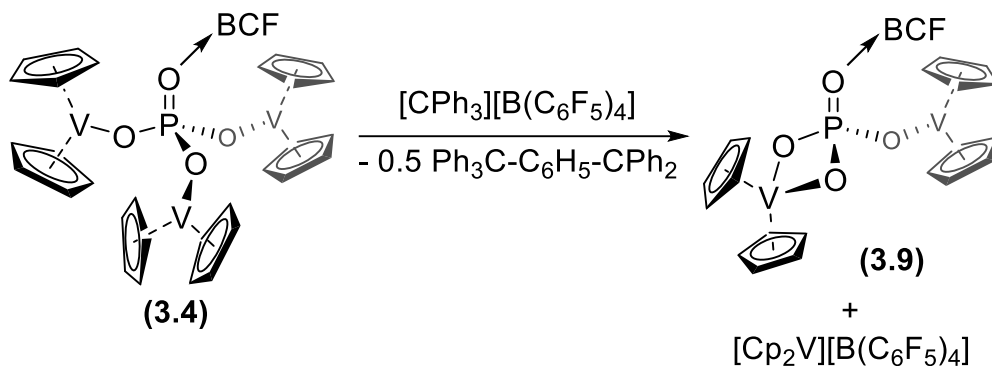
Bond metrics for **3.9** are similar to the other multimetallic complexes reported above (Table 3.2), with the exception of a closer V(1)-P(1) distance (2.6479(16) Å), owing to the newly adopted κ^2 coordination of the phosphate around the V^{IV} center. The paramagnetic nature of **3.9** results in silent ^{31}P and ^{1}H NMR resonances and broadened ^{11}B and ^{19}F resonances. Complex **3.9** was analyzed by X-band EPR spectroscopy, yet surprisingly the r.t. and 100 K spectra of **3.9** in toluene and DCM were EPR silent, perhaps due to fast relaxation caused by the neighboring V^{III} center.[32] Lastly, variable temperature magnetic susceptibility measurements data was collected on **3.9** from 2-300 K. A plot of $\chi_M T$ versus temperature (Figure 3.15) plateaus above 100 K with a $\chi_M T$ value of 1.32 cm^3 K/mol. The data was modeled using a two-spin manifold where $S_1 = 1$ and $S_2 = \frac{1}{2}$, and fit to the parameters $g_1 = 2.017$, $g_2 = 1.978$; $J_{12} = -5.553$ (Figure 3.15 red trace). The small negative J_{12} value indicates weak antiferromagnetic interaction between the two metal centers which may explain the drop in $\chi_M T$ from 50 to 2 K. Interestingly the magnetization data suggests independent spin manifolds with little interaction between the vanadocene moieties through the phosphate linker.
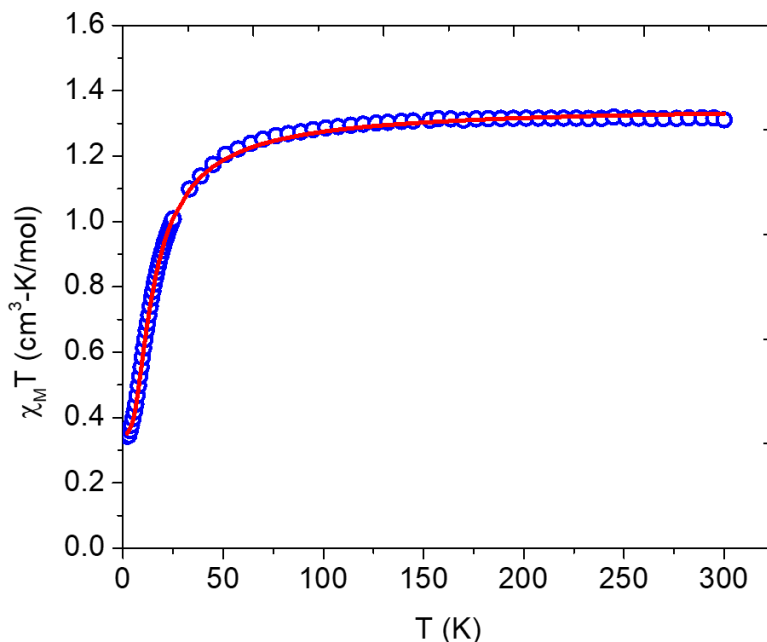
Figure 3.15: Molar magnetic susceptibility (χ_M) vs. temperature measurement for bulk crystalline **3.9** collected from 2-300 K (blue circles) at 1.0 Tesla. Red trace represents theoretical fit.

Table 3.2: Selected Bond lengths (Å) and Bond Angles (º) for Complexes **3.5**, **3.7-3.9**

	(3.5)	**(3.7)**	**(3.8)**	**(3.9)**
V(1)-O(1)	2.005(4)	2.025(4)	2.013(3)	2.039(4)
V(2)-O(3)	1.996(4)	-	-	2.005(4)
P(1)-O(1)	1.507(4)	1.508(4)	1.499(3)	1.521(5)
P(1)-O(2)	1.546(4)	1.523(4)	1.510(3)	1.552(4)
P(1)-O(3)	1.497(4)	-	-	1.515(4)
P(1)-O(4)	1.568(4)	-	-	1.553(4)
O(2)-B(1)	1.491(7)	1.538(9)	1.572(5)	1.492(7)
V(1)-O(1)-P(1)	150.1(3)	158.6(3)	165.93(19)	50.16(16)
V(2)-O(3)-P(1)	163.3(3)	-	-	144.9(3)
O(1)-P(1)-O(2)	110.2(2)	112.8(2)	111.0(4)	110.8(3)
O(3)-P(1)-O(2)	109.5(2)	-	-	108.3(2)
O(4)-P(1)-O(2)	106.9(2)	-	-	108.2(2)
P(1)-O(2)-B(1)	132.7(3)	154.0(4)	115.58(16)	131.6(4)

2.2.4 Reactivity Studies with H-atom Transfer Reagents

With this new library of mono-, di-, and tri-vanadocene phosphorus oxide complexes, we attempted to undergo reactivity studies using common H-atom transfer reagents. Compounds **3.2-3.4** were exposed to various H atom donors (HADs), such as 1,4-cyclohexadiene (CHD), 9,10-dihydroanthracene (DHA), however there was no apparent reactivity at room temperature and at elevated temperatures (80 $^\circ$C) there appeared to be decomposition in the multimetallic complexes. Similarly, reactions with **3.5-3.9** with CHD or DHA under varying conditions also revealed no reactions with the HADs. Only the production of CpH was observed; however, this is also observed upon heating these complexes in the absence of HADs and is, thus, attributed to thermal decomposition. While the LA seems to stabilize the formation of these multimetallic compounds, it also seems to prevent any reactivity through the proposed reactive P=O bond. Reactivity with small molecules such as CO_2, H_2, CO, and NO_2 was also tested but led to inconclusive reactivity.

3.3 Conclusion

In this chapter, we have outlined the synthesis and characterization of a series of new vanadocene-derived phosph(onate/ate) complexes (**3.2-3.9**). Using BCF to "cap" the P=O bond, we systematically tethered multiple vanadocene fragments onto a central phosphate moiety to isolate a series of unique multimetallic complexes. Characterization of **3.2**, **3.3**, and **3.4** by ^{11}B NMR and XRD suggested that each additional vanadocene moiety increases the overall basicity of the complexes from **3.2 < 3.3 < 3.4**, while

electrochemical characterization indicated a decrease in initial oxidation potential from **3.4** < **3.3** < **3.2**. In contrast to **3.1**, which was studied in detail in Chapter 1, the electrochemical data for **3.2** displayed a 0.37 V cathodically shifted irreversible oxidation potential found to undergo an irreversible *EC* mechanism upon chemical oxidation to yield complex **3.7.** Alternatively, chemical oxidation of the weaker Lewis acid B(Ph$_3$) adduct **3.8** yielded the bridging complex **3.6** analogous to **3.1.** Chemical oxidation of **3.4** using the trityl cation resulted in the mixed valent V(IV)/V(III) complex **3.9** and expulsion of one vanadocene fragment. The electronic structures of **3.2**, **3.3**, **3.4**, and **3.9** were probed using SQUID magnetometry and the data fit excellently with little to no antiferromagnetic interactions between the vanadium centers. Reactivity studies seemed to show no indication of the proposed reduction coupled oxo-activation mechanism.

3.4 Experimental Section

3.4.1 General Considerations

All manipulations were performed under an atmosphere of dry, oxygen-free N$_2$ by means of standard Schlenk or glovebox techniques (MBRAUN UNIlab Pro SP Eco equipped with a -40 °C freezer). Pentane, tetrahydrofuran, diethyl ether, hexanes, and dichloromethane (Aldrich) were dried using an MBRAUN-Solvent Purification System and stored over activated 4Å molecular sieves for two days prior to use. Acetonitrile (Aldrich) was dried over CaH$_2$ for 2 days then distilled over 4Å molecular sieves. Deuterated solvents were purchased from Cambridge Isotope Labs, then degassed and stored over 4Å molecular sieves for at least 2 days prior to use. Celite was dried by heating

above 250 °C under dynamic vacuum for at least 48 h prior to use. Silver(I) fluoride, trimethylsilyl phosphate and chlorodimethylsilane were purchased from Aldrich and used without further purification. Tris(pentaflurophenyl)borane was purchased from Boulder Scientific, sublimed under vacuum, treated with excess chlorodimethylsilane for 2 hours and resublimed after removal of volatiles. Vanadocene was prepared according to a literature procedure and purified through sublimation.[33] Trityl tetra(pentafluorophenyl)borate were purchased from Strem Chemicals and silver(I)tetrakis(pentafluorophenyl)borate was prepared according to a literature procedure.[34] Trimethylsilyldiphenylphosphonate and bis(trimethylsilyl)phenylphosphonate were prepared according to literature procedures.[17-19]

NMR spectra were obtained on a Agilent Technologies 400 MHz spectrometer, and referenced to residual solvent or externally ([31]P: 85% H_3PO_4, [19]F: $CFCl_3$, [11]B: $(Et_2O)BF_3$). Chemical shifts (δ) are recorded in ppm and the coupling constants are in Hz. Elemental analyses (C, H, N) were recorded at the University of California, Berkeley using a Perkin Elmer 2400 Series II combustion analyzer. UV-Vis spectroscopy was performed using a Shimadzu UV-2401PC spectrophotometer with quartz cuvettes equipped with a J-young air-tight adaptor. Solution magnetic moment determinations were performed by the Evans method using fluorobenzene as residual solvent and were repeated in triplicate. Magnetic data for **3.2**, **3.3**, **3.4**, and **3.9** was collected using a Quantum Design MPMS SQUID Magnetometer in the RSO mode. The sample was prepared in the glovebox using eicosene to suspend the sample in an air-free environment. Magnetic susceptibility data was corrected for diamagnetism of the sample, estimated using Pascal's constants.[35] $\chi_M T$ data

was fit using the exchange Hamiltonian, $\widehat{H_{ex}} = -2\sum_{i=1}^{ns-1}\sum_{j=i+1}^{ns}J_{ij}\,S_iS_j$ where J_{ij} are the exchange coupling constants of spins i and j, and ns is the number of spins, as well as the zero-field splitting Hamiltonian, $\widehat{H_{ZFS}} = \sum_{i=1}^{ns}D_i[S_{z,i}^2 - \frac{1}{3}S_i(S_i+1) + {E_i}/{D_i}\left(S_{x,i}^2 - S_{y,i}^2\right)]$ where D_i, and E_i/D_i are the local axial and rhombic zero field splitting parameters respectively. The experimental data was fit by a least squares fitting using the JulX modeling software.

Cyclic voltammetry was performed on a CH Instruments 630E electrochemical analysis potentiostat, equipped with a 3 mm diameter glassy carbon working electrode, a Ag wire pseudo-reference electrode, and a Pt wire counter electrode with $[Bu_4N][PF_6]$ (0.1 M) supporting electrolyte solution in DCM. The glassy carbon working electrode was cleaned prior to each experiment by polishing with 1, 0.3, 0.05 mm alumina (CH Instruments) in descending order, followed by sonication in distilled water for 2 minutes. Background scans were conducted for each reported sweep rate in a solution containing only electrolyte, and was then subtracted from each experiment. All voltammograms were repeated in duplicate and referenced to the Fc/Fc^+ redox couple. All individual voltammograms can be found in the supporting information.

Intensity data was collected on a Bruker KAPPA APEX II diffractometer equipped with an APEX II CCD detector using a TRIUMPH monochromator with a Mo Kα X-ray source ($\alpha = 0.71073$ Å). The single crystals were mounted on a cryoloop with Paratone-N oil, and all data were collected at 100(2) K using an Oxford nitrogen gas cryostream system. A hemisphere of data was collected using ω scans with 0.5° frame widths. Data collection and cell parameter determination were conducted using the APEX2 program. Integration of the data frames and final cell parameter refinement were performed using

SAINT software. Absorption correction of the data was carried out using SADABS. Structure determination was done using direct or Patterson methods and difference Fourier techniques. All hydrogen atom positions were idealized and rode on the atom of attachment. Structure solution, refinement, and creation of publication materials was performed using Olex2.

3.4.2 Synthesis of Compounds

Synthesis of Cp$_2$VF: The synthesis described is derived from a literature procedure.[16] Inside the glovebox a 100 mL roundbottom equipped with a magnetic stir bar was charged with Cp$_2$V (0.520 g, 2.87 mmol) and THF (25 mL). The roundbottom was covered in aluminum foil. A slurry of AgF (0.364 g, 2.87 mmol) in THF (15 mL) was added drop-wise at r.t. and the dark purple slurry was allowed to stir for 12 hours. The solution slowly turned a dark blue followed by gradual precipitation of silver metal after stirring for 12 hours. The precipitate was filtered through a fine porosity Buchner funnel over a pad of Celite and the filtrate was dried *in vacuo* to yield a dark blue solid. The dark blue solid was washed with hexanes (25 mL) and dried *in vacuo* (0.421 g, 2.10 mmol, 73.3%). The resulting Cp$_2$VF was recrystallized from toluene (5 mL) layered with pentane (5 mL) at -40 °C to yield a blue solid (0.386 g, 1.93 mmol, 67.2%).

UV-Vis λ$_{max}$ (nm): 317 (max), 621, 774. **Anal Calc**. for C$_{10}$H$_{10}$FV: C, 60.02; H, 5.04. Found: C, 59.10; H, 5.01. The reduced carbon percentage can be attributed to the facile formation of Vanadium carbide upon combustion. Single crystals suitable for X-ray crystallography agree with literature data.

Synthesis [Cp$_2$VOP(O)Ph$_2$] (3.1): The following is an alternative method to the procedure

described previously.[15] Inside the glovebox a 100 mL roundbottom equipped with a magnetic stir bar was charged with $(C_5H_5)_2VF$ (0.200 g, 1.00 mmol) and dissolved in DCM (15 mL). The blue solution was cooled to -40 °C. A separate solution of $(Ph)_2P(O)OSiMe_3$ (0.285 g, 0.98 mmol) was prepared in DCM (5 mL) and added cold dropwise. The solution was allowed to warm to r.t. over 1 h after which time the solvent and fluorotrimethylsilane were removed *in vacuo*. The blue solid was washed with hexanes (15 mL) and recrystallized out of DCM (5 mL) layered with pentane (2 mL) at -40 °C (0.290 g, 0.723 mmol, 74.4%). Blue plate-shaped single crystals suitable for XRD studies were grown by slow diffusion of pentane into a concentrated solution of **3.1** in DCM.

^{1}H NMR (400 MHz, CD_2Cl_2): δ 7.45 (bs, C_6H_5), 7.68 (bs, C_6H_5), 9.63 (bs, C_6H_5). **Anal. Calc**. for $C_{22}H_{20}O_2PV$: C, 66.30; H, 5.06. Found: C, 66.12; H, 4.87. **UV-Vis** λ (nm): 338 (max), 604, 752. **μ_{eff} (Evans):** 2.90 μ_B

Synthesis of [Cp$_2$VOP(O-B(C$_6$F$_5$)$_3$)Ph$_2$] (3.2): In the glovebox a 50 mL roundbottom equipped with a stirbar was charged with Cp$_2$VOP(O)Ph$_2$ **(3.1)** (0.200 g, 0.502 mmol) and toluene (10 mL). A separate solution of $B(C_6F_5)_3$ (0.282 g, 0.553 mmol) in toluene (5 mL) was added dropwise to the bright blue solution of **3.1** while stirring. The resulting solution was allowed to stir at r.t. for 5-6 h. The solution was concentrated to half the volume (~7 mL) and carefully layered with pentane (~5 mL). The solution was cooled to -40 °C and left to recrystallize for 24 hours. The resulting blue precipitate was filtered on a glass frit, washed with hexanes and dried *in vacuo* (0.383 g, 0.420 mmol, 83.7%). Blue plate-shaped single crystals suitable for XRD studies were grown by slow diffusion of pentane into a concentrated solution of **3.2** in DCM.

¹H NMR (400 MHz, CD$_2$Cl$_2$): δ 7.37 (bs, C$_6$$H_5$), 7.73 (bs, C$_6$$H_5$), 9.68 (bs, C$_6$$H_5$). **¹⁹F{¹H} NMR** (376 MHz, CD$_2$Cl$_2$): δ -158.7 (bs, 3F, p-C$_6$F$_5$), -162.1 (bs, 6F, m-C$_6$F$_5$), -55.91 (bs, 6F, o-C$_6$F$_5$). **¹¹B NMR** (128 MHz, CD$_2$Cl$_2$): δ 0.08 (bs). **Anal. Calc.** C$_{40}$H$_{20}$BF$_{15}$O$_2$PV • pentane: C, 54.84; H, 3.27. Found: C, 55.12; H, 2.94. **UV-Vis** λ$_{max}$ (nm): 325 (max), 619, 736.

Synthesis of [(Cp₂VO)₂P(O-B(C₆F₅)₃)Ph] (3.3): In the glovebox a 20 mL vial equipped with a stirbar was charged with bis(trimethylsilyl)phenylphosphonate (15.2 µL, 0.050 mmol), B(C$_6$F$_5$)$_3$ (0.026 g, 0.050 mmol) and DCM (5 mL). The solution was allowed to stir at r.t. for 1 hour. In a separate 20 mL vial a solution of Cp$_2$VF (0.020 g, 0.100 mmol) was prepared in DCM (5 mL). The bright blue solution of Cp$_2$VF was added dropwise to the stirring solution and the resulting blue solution was allowed to stir at r.t. for 18 hours. The solvent was removed *in vacuo* and the blue residue was triturated with pentane. The resulting blue solid was washed with hexanes and dried *in vacuo* (0.024 g, 0.023 mmol, 46.6%). Blue plate-shaped single crystals suitable for XRD studies were grown by slow diffusion of hexanes into a concentrated solution of **3.3** in toluene. **¹H NMR** (400 MHz, CD$_2$Cl$_2$): δ 7.92 (bs, C$_6$$H_5$), 8.81 (bs, C$_6$$H_5$). **¹⁹F{¹H} NMR** (376 MHz, CD$_2$Cl$_2$): δ -30.9 (br, 6F, o-C$_6$F$_5$), -160.4 (br, 3F, p-C$_6$F$_5$), -160.6 (br, 6F, m-C$_6$F$_5$). **¹¹B NMR** (128 MHz, CD$_2$Cl$_2$): δ 9.65 (bs). **Anal Calc.** for C$_{44}$H$_{25}$BF$_{15}$O$_3$PV$_2$ • tol: C, 54.56; H, 2.96. Found: C, 54.64; H, 3.32. **UV-Vis** λ$_{max}$ (nm): 322 (max), 629, 741.

Synthesis of [(C₅H₅VO)₃P((O)-B(C₆F₅)₃)] (3.4): In the glovebox a 50 mL schlenk flask equipped with a stir bar was charged with tris(trimethylsilyl)phosphate (40.22 µL, 0.121 mmol), B(C$_6$F$_5$)$_3$ (0.062 g, 0.121 mmol), and THF (5 mL). The solution was allowed to stir

in the glovebox at r.t. for 1 hour. In a separate 20 mL vial a solution of Cp_2VF (0.075 g, 0.375 mmol) was prepared in THF (5 mL). The bright blue solution of Cp_2VF was added dropwise to the stirring solution at r.t. The resulting blue solution was allowed to stir at room temperature for 48 hours. The solvent was removed *in vacuo* and the blue solid was washed with hexanes (20 mL) followed by toluene (20 mL). The remaining blue solid was then recrystallized from a concentrated solution of DCM (1 mL) layered with pentane (1 mL) (0.060 g, 0.052 mmol, 43.2%). Blue plate-shaped single crystals suitable for XRD studies were grown by slow diffusion of pentane into a concentrated solution of **3.4** in THF.

$^{19}F\{^{1}H\}$ NMR (376 MHz, CD_2Cl_2): δ -160.5 (br, 3F, *p*-C_6F_5), -161.4 (br, 6F, *m*-C_6F_5). **^{11}B NMR** (128 MHz, CD_2Cl_2): δ 14.07 (bs). **Anal. Calc.** for $C_{48}H_{30}BF_{15}O_4PV_3$: C, 50.12; H, 2.63. Found: C, 50.13; H, 2.65. **UV-Vis λ_{max}** (nm): 313 (max), 630, 747.

Synthesis of [(Cp₂VO)₂P(O-B(C₆F₅)₃)OSiMe₃] (3.5): In the glovebox a 25 mL roundbottom equipped with a stirbar was charged with tris(trimethylsilyl)phosphate (62.3 µL, 0.187 mmol), $B(C_6F_5)_3$ (0.096 g, 0.187 mmol) and DCM (10 mL). The solution was allowed to stir at r.t. for 1 hour. In a separate 20 mL vial a solution of Cp_2VF (0.075 g, 0.375 mmol) was prepared in DCM (5 mL). The bright blue solution of Cp_2VF was added dropwise to the stirring solution and the resulting blue solution was allowed to stir at r.t. for 24 hours. The solvent was removed *in vacuo* and the blue residue was triturated with pentane. The resulting blue solid was washed with hexanes and dried *in vacuo* (0.170 g, 0.168 mmol, 90.0%). Blue plate-shaped single crystals suitable for XRD studies were grown by slow diffusion of pentane into a concentrated solution of **3.5** in DCM.

^{1}H NMR (400 MHz, CD_2Cl_2): δ 0.23 (bs, Si(C*H₃*)₃). **$^{19}F\{^{1}H\}$ NMR** (376 MHz, CD_2Cl_2):

δ -32.9 (br, 6F, o-C$_6$F$_5$), -160.3 (br, 3F, p-C$_6$F$_5$), -162.4 (br, 3F, m-C$_6$F$_5$). **^{11}B NMR** (128 MHz, CD$_2$Cl$_2$): δ 12.89 (bs). **Anal. Calc.** for C$_{41}$H$_{29}$BF$_{15}$O$_4$PSiV$_2$ • (CH$_2$Cl$_2$)$_2$: C, 44.58; H, 2.74. Found: C, 44.90; H, 3.03. **UV-Vis λ$_{max}$** (nm): 331 (max), 611, 721.

Synthesis of Cp$_2$V(OP(OB(C$_6$F$_5$)$_3$)Ph$_2$)$_2$ (3.7). Note that this complex was only isolated as single crystals in low yield. In the glovebox, a 20 mL vial equipped with a magnetic stir bar was charged with **3.2** (0.025 g, 0.027 mmol) and DCM (5 mL). The solution was chilled to −40 °C and a separate solution of [Ag][B(C$_6$F$_5$)$_4$]·(C$_6$H$_6$)$_3$ (0.014 g, 0.013 mmol) in DCM (2 mL) was added dropwise to the bright blue solution of **3.2** while stirring. Immediately the solution turned green and stirred for 1 h at room temperature. The solution was allowed to stand at −40 °C for 3 h and a fine precipitate settled on the bottom of the vial. The solution was filtered through a fine porosity Buchner funnel and the green filtrate was dried *in vacuo*. The resulting green solid was washed with hexanes and dried in vacuo. Green needleshaped single crystals suitable for XRD studies were grown by slow vapor diffusion of pentane into a concentrated solution of **3.7** in toluene over several days.

Synthesis of [Cp$_2$VOP(O-B(Ph)$_3$)Ph$_2$] (3.8): In the glovebox a 20 mL vial equipped with a stirbar was charged with Cp$_2$VOP(O)Ph$_2$ **(3.1)** (0.100 g, 0.251 mmol) and toluene (5 mL). A separate solution of B(C$_6$H$_5$)$_3$ (0.067 g, 0.277 mmol) in toluene (5 mL) was added dropwise to the bright blue solution of **(3.1)** while stirring. The resulting solution was allowed to stir at r.t. for 5-6 h. The solution was concentrated to half the volume (~5 mL) and carefully layered with pentane (~5 mL). The solution was cooled to -40 °C and left to recrystallize for 24 hours. The resulting blue precipitate was filtered on a fine porosity

Buchner funnel, washed with hexanes and dried *in vacuo* (0.086 g, 0.134 mmol, 53.5%).

Blue plate-shaped single crystals suitable for XRD studies were grown by slow diffusion

of pentane into a concentrated solution of **3.8** in DCM.

^{1}H NMR (400 MHz, CD_2Cl_2): δ 7.02-8.12 (bm, C_6H_5), 9.00 (bs, C_6H_5). **Anal. Calc.** for

$C_{40}H_{35}BO_2PV$: C, 75.02; H, 5.69. Found: C, 74.74; H, 5.69. **UV-Vis λ_{max}** (nm): 326 (max),

633, 742. **μ_{eff} (Evans):** 2.96 μ_B.

Synthesis of [(Cp$_2$VO$_2$)P(O-B(C$_6$F$_5$)$_3$)OVCp$_2$] (3.9): In the glovebox a 20 mL

scintillation vial equipped with a stirbar was charged with freshly synthesized **3.4** (0.090

g, 0.078 mmol), and DCM (10 mL). The solution was cooled to -78 °C using a dry

ice/acetone cooled cold well inside the glovebox. A separate solution of trityl chloride

(0.022 g, 0.078 mmol) in DCM (3 mL) was added dropwise. The resulting dark green

solution was allowed to warm to r.t. while stirring for 1 hour. The solvent was removed *in*

vacuo and the green/blue residue was washed with hexanes (3 x 10 mL). The residue was

dissolved in a minimum amount of toluene (3 mL), layered with pentane (3 mL), and stored

at -40 °C for 24 hours to yield a dark green solid and a blue solution. The solution was

decanted and the dark green solid was recrystallized two more times (0.048 g, 0.049 mmol,

63.0%). Green block-shaped crystals suitable for XRD studies were grown by slow vapor

diffusion of pentane into a concentrated solution of **3.9** in toluene.

^{19}F{^{1}H} NMR (376 MHz, CD_2Cl_2): δ -117.41 (br, 6F, *o*-C_6F_5), -161.3 (br, 3F, *p*-C_6F_5), -

162.5 (br, 6F, *m*-C_6F_5). **^{11}B NMR** (128 MHz, CD_2Cl_2): δ 6.64 (bs). **Anal. Calc.** for

$C_{38}H_{20}BF_{15}O_4PV_2$: C, 47.09; H, 2.08. Found: C, 46.91; H, 2.27. **UV-Vis λ_{max}** (nm): 331

(max), 611, 721.

Table 3.3: Crystallographic Parameters for reported complexes

	3.2 • (C$_5$H$_{12}$)$_2$	3.3 • (C$_6$H$_{14}$)$_{0.5}$ (tol)	3.4 • (THF)$_{1.67}$ (C$_5$H$_{12}$)$_{0.33}$	3.5 • (CH$_2$Cl$_2$)$_2$
Empirical formula	C$_{45}$H$_{32}$BF$_{15}$O$_2$PV	C$_{54}$H$_{40}$BF$_{15}$O$_3$PV$_2$	C$_{56.33}$H$_{46}$BF$_{15}$O$_{5.67}$PV$_3$	C$_{86}$H$_{66}$B$_2$Cl$_8$F$_{30}$O$_8$P$_2$Si$_2$V$_4$
Moiety formula	C$_{40}$H$_{20}$BF$_{15}$O$_2$PV, (C$_5$H$_{12}$)$_2$	C$_{44}$H$_{25}$BF$_{15}$O$_3$PV$_2$ (C$_7$H$_8$) (C$_6$H$_{14}$)$_{0.5}$	C$_{48}$H$_{30}$B$_1$F$_{15}$O$_4$PV$_3$ (C$_4$H$_8$O)$_{1.67}$ (C$_5$H$_{12}$)$_{0.33}$	(C$_{41}$H$_{29}$BF$_{15}$O$_4$PSiV$_2$)$_2$ (CH$_2$Cl$_2$)$_4$
Formula weight	982.47	1165.57	1246.89	2424.58
Crystal system	Orthorhombic	Triclinic	Triclinic	Triclinic
Space group	P2$_1$2$_1$2$_1$	P-1	P-1	P-1
a (Å)	11.1191(3)	12.860(3)	12.716(4)	12.087(3)
b (Å)	16.1938(5)	12.884(3)	15.839(5)	12.490(4)
c (Å)	22.6586(6)	15.264(3)	16.443(5)	16.921(6)
α (º)	90	86.091(6)	65.238(5)	83.461(9)
B (º)	90	78.427(5)	69.340(5)	73.171(8)
γ (º)	90	80.021(6)	77.236(5)	79.889(9)
V (Å^3)	4079.9(2)	2438.9(10)	2803.4(15)	2401.6(13)
Z	4	2	2	1
T, (K)	100	100	100	100
λ, (Å)	0.71073	0.71073	0.71073	0.71073
μ, (mm^{-1})	0.391	0.519	0.615	0.771
F (000)	1987.3	1180.3	1217.7	1215.7
R_1	0.0324	0.0870	0.0793	0.0747
wR_2	0.0835	0.2672	0.2674	0.2093

Table 3.4: Crystallographic Parameters for reported complexes

	3.7	3.8	3.9 • (tol)$_{2.5}$
Empirical formula	$C_{84}H_{44}B_2F_{30}O_4P_2V$	$C_{40}H_{35}BO_2PV$	$C_{56}H_{40}BF_{15}O_4PV_2$
Moiety formula	$C_{84}H_{44}B_2F_{30}O_4P_2V$	$C_{40}H_{35}BO_2PV$	$C_{38}H_{20}BF_{15}O_4PV_2$ $(C_7H_8)_{2.5}$
Formula weight	1821.69	640.46	1165.28
Crystal system	Orthorhombic	Monoclinic	Monoclinic
Space group	Pbcn	P12$_1$/n1	C12/c1
a (Å)	12.0930(18)	10.041(3)	30.0513(16)
b (Å)	31.069(4)	17.541(5)	17.0393(8)
c (Å)	19.800(3)	17.975(5)	21.7277(10)
α (º)	90	90	90
B (º)	90	91.089(9)	115.691(3)
γ (º)	90	90	90
V (Å^3)	7439.2(18)	3165.5(16)	10025.9(9)
Z	4	4	8
T, (K)	100	100	100
λ, (Å)	0.71073	0.71073	0.71073
μ, (mm^{-1})	0.307	0.400	0.508
F (000)	3652.0	1338.2	4561.5
R_1	0.0754	0.0586	0.0877
wR_2	0.2334	0.1396	0.2643

3.5 References

(1)   Centi, G.; Trifiro, F.; Ebner, J. R.; Franchetti, V. M. Chem. Rev. 1988, 88, 55−80.

(2)   Zhanglin, Y.; Forissier, M.; Sneeden, R. P.; Vedrine, J. C.; Volta, J. C. J. Catal. 1994, 145, 256−266.

(3)   Coulston, G. W.; Bare, S. R.; Kung, H.; Birkeland, K.; Bethke, G. K.; Harlow, R.; Herron, N.; Lee, P. L. Science 1997, 275, 191−193.

(4)   Herron, N.; Thorn, D. L.; Harlow, R. L.; Coulston, G. W. J. Am. Chem. Soc. 1997, 119, 7149−7150.

(5)   Chen, B.; Munson, E. J. J. Am. Chem. Soc. 2002, 124, 1638−1652.

(6)   Chen, B.; Munson, E. J. J. Am. Chem. Soc. 1999, 121, 11024−11025.

(7)   Feyel, S.; Döbler, J.; Schröder, D.; Sauer, J.; Schwarz, H. Angew. Chem., Int. Ed. 2006, 45, 4681−4685.

(8)   Dietl, N.; Engeser, M.; Schwarz, H. Angew. Chem., Int. Ed. 2009, 48, 4861−4863.

(9)   Dietl, N.; Höckendorf, R. F.; Schlangen, M.; Lerch, M.; Beyer, M. K.; Schwarz, H. Angew. Chem., Int. Ed. 2011, 50, 1430−1434.

(10)   Dietl, N.; Wende, T.; Chen, K.; Jiang, L.; Schlangen, M.; Zhang, X.; Asmis, K. R.; Schwarz, H. J. Am. Chem. Soc. 2013, 135, 3711−3721.

(11)   Cheng, M.-J.; Goddard, W. A. J. Am. Chem. Soc. 2013, 135, 4600−4603.

(12)   Cheng, M.-J.; Fu, R.; Goddard, W. A., III. Chem. Commun. 2014, 50, 1748−1750.

(13)   Cheng, M.-J.; Goddard, W. A.; Fu, R. Top. Catal. 2014, 57, 1171−1187.

(14)   Carroll, T. G.; Garwick, R.; Telser, J.; Wu, G.; Menard, G.́ Organometallics 2018, 37, 848−854.

(15)   Bouman, H.; Teuben, J. H. J. Organomet. Chem. 1976, 110, 327−330.

(16)   Harvey, B. G.; Arif, A. M.; Glöckner, A.; Ernst, R. D. Organometallics 2007, 26, 2872−2879.

(17)   Wozniak, L.; Cypryk, M.; Chojnowski, J.; Lanneau, G. Tetrahedron 1989, 45, 4403−4414.

(18)   Eaton, G. R. J. Chem. Educ. 1969, 46, 547.

(19)   Błazewska, K. M. J. Org. Chem. 2014, 79, 408−412.

(20)   Bartell, L. S.; Su, L.-S.; Yow, H. Inorg. Chem. 1970, 9, 1903−1912.

(21)   Hermanek, S. Chem. Rev. 1992, 92, 325−362.

(22)   Galloni, P.; Conte, V.; Floris, B. Coord. Chem. Rev. 2015, 301−302, 240−299.

(23)   Boca, R. Coord. Chem. Rev. 2004, 248, 757−815.

(24)   Choukroun, R.; Lorber, C.; Donnadieu, B.; Henner, B.; Frantz, R.; Guerin, C. Chem. Commun. 1999, 1099−1100.

(25)   Compton, R. G.; Banks, C. E. Understanding Voltammetry, 2nd ed.; Imperial College Press: London, 2011.

(26)   Agarwal, P.; Piro, N. A.; Meyer, K.; Müller, P.; Cummins, C. C. Angew. Chem., Int. Ed. 2007, 46, 3111−3114.

(27)   Chantarojsiri, T.; Ziller, J. W.; Yang, J. Y. Chem. Sci. 2018, 9, 2567−2574.

(28)   Henthorn, J. T.; Lin, S.; Agapie, T. J. Am. Chem. Soc. 2015, 137, 1458−1464.

(29)   Shimizu, K.; Sepunaru, L.; Compton, R. G. Chem. Sci. 2016, 7, 3364−3369.

(30)   Ogawa, K.; Kitagawa, T.; Ishida, S.; Komatsu, K. Organometallics 2005, 24, 4842−4844.

(31)   Calderazzo, F.; Ferri, I.; Pampaloni, G.; Englert, U. Organometallics 1999, 18, 2452−2458.

(32)   Gomberg, M. J. Am. Chem. Soc. 1900, 22, 757−771.

(33)   Lankamp, H.; Nauta, W. T.; MacLean, C. Tetrahedron Lett. 1968, 9, 249−254.

(34)   Gambarotta, S.; Floriani, C.; Chiesi-Villa, A.; Guastini, C. Inorg. Chem. 1984, 23, 1739−1747.

(35)   Graham, M. J.; Krzyaniak, M. D.; Wasielewski, M. R.; Freedman, D. E. Inorg. Chem. 2017, 56, 8106−8113.

(36)   Kowaleski, R. M.; Basolo, F.; Trogler, W. C.; Gedridge, R. W.; Newbound, T. D.; Ernst, R. D. J. Am. Chem. Soc. 1987, 109, 4860−4869.

(37)   Evans, D. F. 400. J. Chem. Soc. 1959, 2003−2005.

(38)   Bain, G. A.; Berry, J. F. J. Chem. Educ. 2008, 85, 532−536.

Chapter 4

An Untethered C_{3v} Symmetric Triarylphosphine Oxide Locked by Intermolecular Hydrogen Bonding

4.1 Introduction

Triphenylphosphine (TPP), and triphenylphosphine oxide (TPPO) have long been ubiquitous reagents in the field of coordination chemistry. In recent years, *para*-substituted TPP/TPPO derivatives have been employed as organic linkers to produce metal-organic frameworks (MOFs) with unique topologies and pore sizes for applications in catalysis, drug delivery, gas storage, and chemical sensing.[1-7] The symmetry, coordination mode, and hydrogen bonding characteristics of these substituted TPP/TPPO linkers have been shown to significantly impact the overall structure and function of the MOFs.[8-12] In all cases that we are aware of, the *para*-substituted TPP/TPPO linkers adopt the standard C_3-symmetric propeller-type configuration analogous to unsubstituted TPP and TPPO.[13] An exception to the propeller-type triarylphosphine/oxide conformation can be found in constrained C_{3v} symmetric 9-phosphatriptycene derivatives (Figure 4.1).[14-17] Their unique symmetry is the result of intramolecular tethering of the aryl rings forcing them to sit along the threefold symmetry planes.
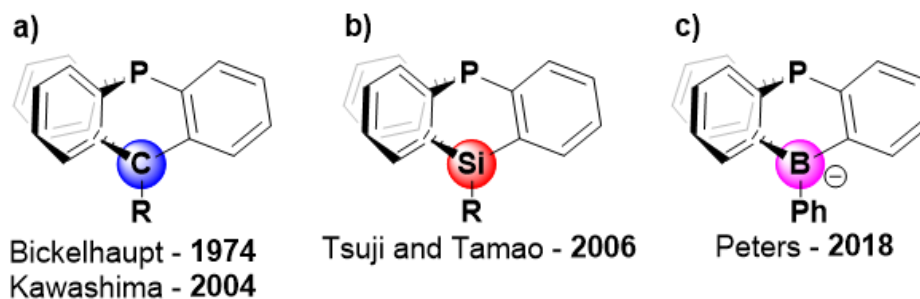
Figure 4.1: Reported C_{3v} symmetric 9-phosphatriptycene derivatives

As part of our work[18-20] investigating the vanadium phosphate oxide (VPO) surface catalyst and the related mechanistic landscape,[21-25] we synthesized a series of molecular mono- or multi-metallic VPO model complexes of the general formula, $(R_xV^n\text{-}L)_yP(O)Ar_{(3-y)}$ $(R_x = (\eta^5\text{-}C_5H_5)_2, n = +3, L = O, y = 1, 2, 3, Ar = Ph; R_x = (Ph_2N)_3, n = +5, L = N, y = 1, Ar = Ph, C_6F_5)$, and have reported them in Chapters 2 and 3. In this chapter we aimed to study the impact of a longer linker (L), such as a phenyl linker, on the redox chemistry and reactivity observed in these complexes. As mentioned in Chapter 2, decomposition pathways of previously reported multimetallic complexes seemed to involve the intramolecular attached of the P=O bond to the vanadocene appendage. A longer phenyl linker was employed to help prevent intramolecular attack. We describe here the synthesis of mono- and tri-metallic variants containing terminal vanadocene motifs $(Cp_2V; Cp = \eta^5\text{-}C_5H_5)$. Interestingly, and to the best of our knowledge, the latter complex was found to be the first untethered C_{3v} symmetric triarylphosphine oxide in the solid state and adopts a MOF-like extended structure. As will be described, crystallographic and computational studies suggest this locked geometry is maintained by intermolecular H-bonding.

4.2 Results and Discussion

4.2.1 Synthesis and Characterization of a C₃ᵥ Symmetric Triarylphosphine

Clean access to our previously reported multi-metallic Cp$_2$V-based complexes (Chapter 2) was afforded using a trimethylsilyl fluoride (Me$_3$SiF = TMSF) elimination synthetic pathway.[19] Using the well-known triacid, tris-(4-carboxylphenyl)phosphineoxide (H$_3$TPPO),[4-6,10] we employed a similar approach here by first converting H$_3$TPPO to the silylated variant (**4.1**) using TMSCl in the presence of NEt$_3$ (Scheme 1). The new compound (**4.1**) was isolated in good yield (71%) following work-up. Subsequent exposure of **4.1** to 3 equivalents of the known complex, Cp$_2$VF, in dichloromethane (DCM) resulted in the generation of free TMSF as observed by ¹H and ¹⁹F NMR spectroscopy, as well as the production of a bright blue product isolated in high yield (97%). Analysis of this blue product by multi-nuclear (⁵¹V, ³¹P, ¹H) NMR spectroscopy revealed a singlet at 26.2 ppm in the ³¹P NMR spectrum, whereas all other spectra were silent, consistent with a paramagnetic species with unpaired spin density localized on the V centres (*vide infra*). Blue plate-shaped single crystals suitable for X-ray diffraction (XRD) studies were grown by vapour diffusion of pentane into a concentrated DCM solution of the product at -40 ºC. The solid-state structure confirmed the composition as the trimetallic species, **4.2** (Scheme 4.1 (box)).

Scheme 4.1: Synthesis of **4.1** and **4.2**. Box: Solid-state structure of **4.2** with hydrogen atoms omitted for clarity
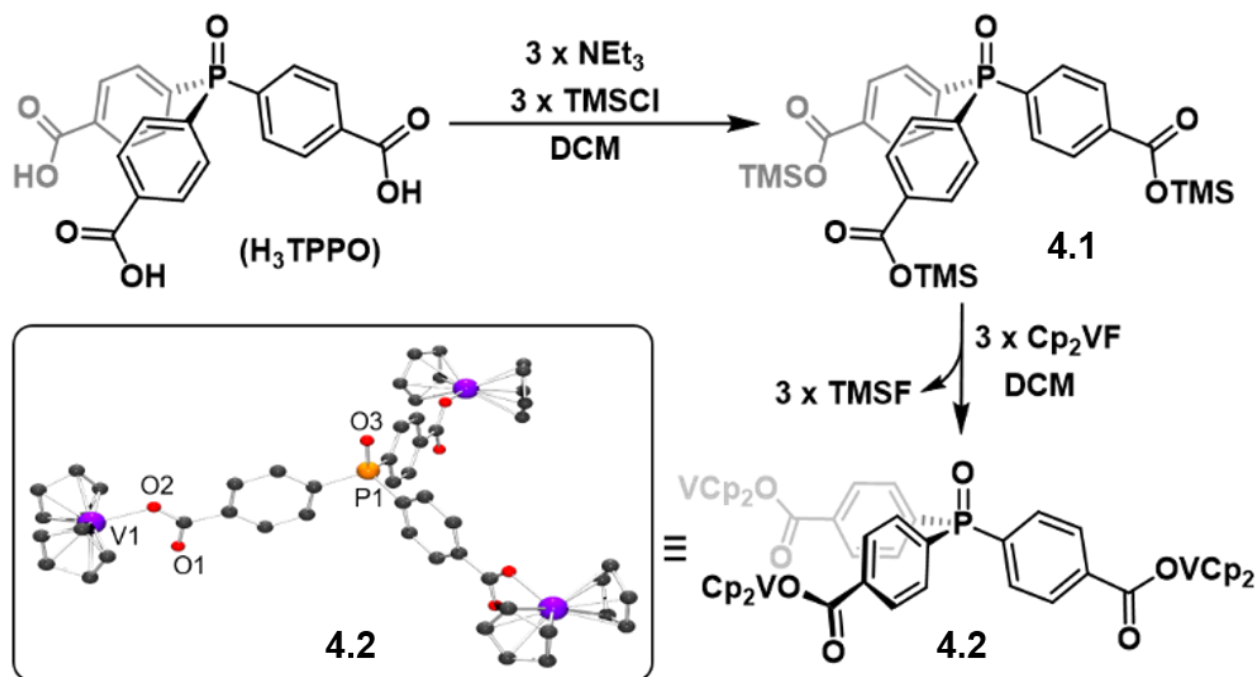
A closer look at the solid-state structure of **4.2** reveals unique and very interesting features. First, the structure crystallizes in the hexagonal space group, *P6₃/mcm*, where each molecule of **4.2** is perfectly C_{3v} symmetric (Figure 4.2a). To the best of our knowledge, this is the first such example of an untethered triarylphosphine/oxide which does not adopt the standard propeller-type geometry. The structure appears locked in this C_{3v} configuration by intermolecular H-bonding interactions (ca. 1.987 Å) between a set of phenyl C–H bonds (*ortho* to P) and a neighboring O=P bond from a second molecule of **3.2** arranged in a staggered conformation (Figure 4.2b).
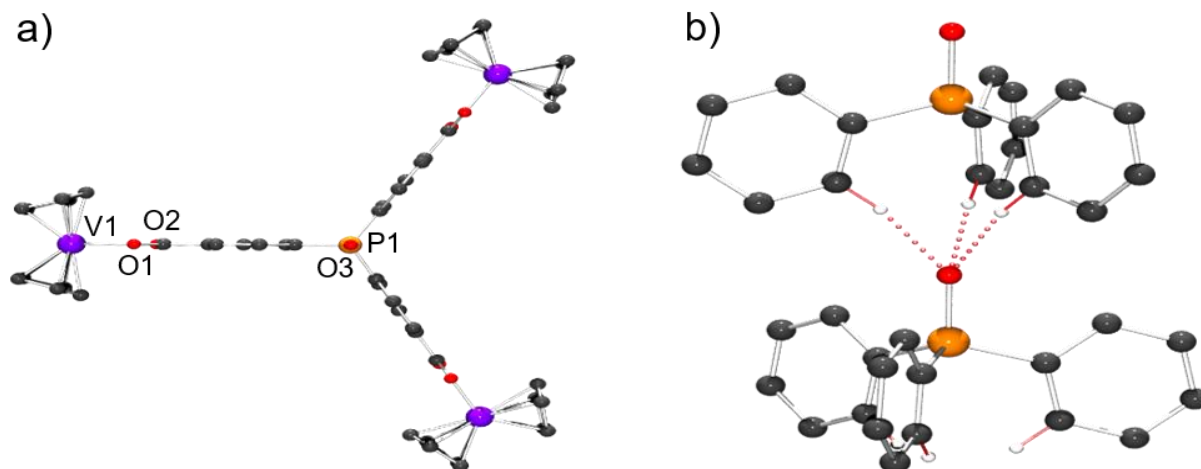
Figure 4.2: a) Depictions of the solid-state structure of **4.2** derived from single crystal

XRD. a) Top-down view along the P=O C_3 axis. b) Side view of two partial structures of

4.2 with *para* carboxy-vanadocene fragments omitted for clarity. Intermolecular H-

bonding interactions between *ortho* C-H bonds and a neighbouring oxo from P=O are

shown in dashed red bonds. H-atoms with the exception of *ortho* C-H in b), are omitted

for clarity.

(It should be noted here that the bond lengths are approximate due to the significant

disorder in the structure arising from the perfect superposition of two molecules of **4.2**

axially trans-disposed along the P=O bond vector (Table 4.1)). Together the staggered

arrangement combined with the H-bonding interactions leads to an infinite 1-dimensional

chain featuring an apparent sixfold rotational axis as observed from the normal to the

[oo1] direction of the hexagonal crystal structure (Figure 4.3). Omitting Cp rings in

Figure 4.3 reveals triangular pores with a resulting superstructure mimicking previously

reported MOFs.[26-29]
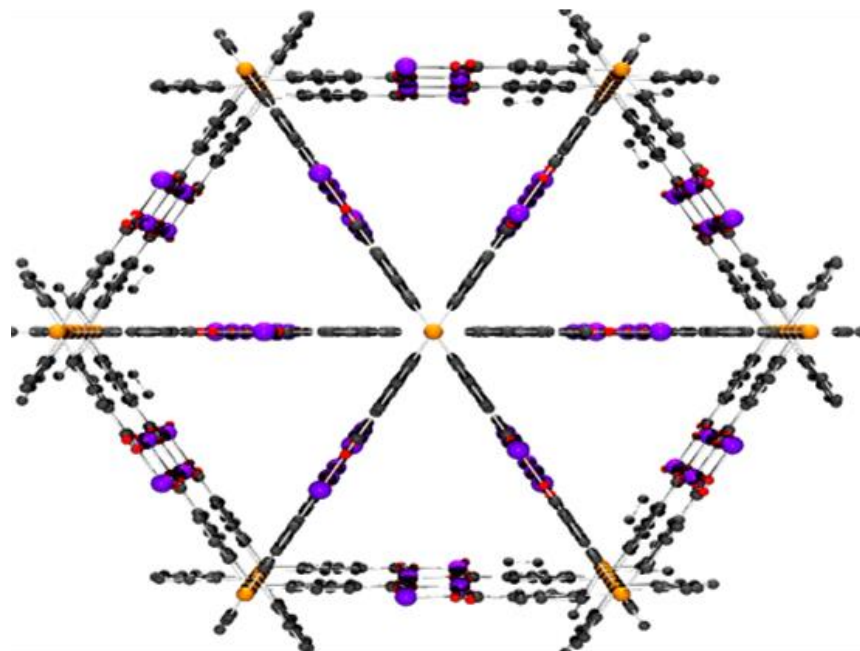
Figure 4.3: Partial 3D framework view normal to the [001] direction in the hexagonal crystal structure of **4.2**. An overall C_6 symmetry is present due to the staggered arrangement of sequential units of **4.2**. Cp fragments are removed to reveal the triangular pores. H-atoms, are omitted for clarity.

Table 4.1: Selected Bond Distances (Å) and Angles (º) for **4.2**, **4.4**, and **4.5**.

	4.2*	**4.4**	**4.5**
V1-O2	2.043	2.010(3)	2.075(2)
P1-O1	1.46(5)	1.482(3)	1.485(2)
O2-C1	1.26(2)	1.285(5)	1.275(4)
O3-C1	1.24(2)	1.220(6)	1.267(4)
V1-O2-C1	117.0(12)	119.0(3)	58.34(15)
O3-C1-O2	124.5(18)	125.7(4)	116.9(3)

* the bond lengths and angles are approximate due to the significant disorder in the structure arising from the perfect superposition of two molecules of **4.2** axially trans-

disposed along the P=O bond vector.

The electronic structure of **4.2** was probed by magnetic and voltammetric techniques. First, magnetic susceptibility ($\chi_M T$) measurements for bulk crystalline **4.2** were collected at variable temperatures (2-300 K) under a static 0.1 T field using SQUID magnetometry (Figure 4.4). The $\chi_M T$ vs. T data plateaus at 2.92 for temperatures above 25 K, consistent with three non-interacting spin manifolds, as approximated by the general formula $\chi_M T = [\sum S_i (S_i + 1)]/2$ (assuming $g = 2.0$) with each V^{III} centre adopting a high-spin $S = 1$ state. The experimental magnetization data was well fit ($R^2 = 0.995$) using the following parameters (where D is the axial zero-field splitting (ZFS) parameter, and J is the magnetic exchange coupling constant): $g_1 = g_2 = g_3 = 1.99$; $J_{12} = J_{13} = J_{23} = -0.20$ cm^{-1}; $D_1 = D_2 = D_3 = 5.5$ cm^{-1}. Owing to the high symmetry of the complex, and to avoid over-parameterization, we constrained the variables to allow $g_1 = g_2 = g_3$; $J_{12} = J_{13} = J_{23}$, and; $D_1 = D_2 = D_3$. The extracted J values are very small, indicating no significant magnetic exchange interactions between individual V centres. Consequently, the sharp decrease in $\chi_M T$ at low temperature is attributed primarily to ZFS effects. All variables are well within the range of other reported multi-metallic vanadocene complexes.[19,30,31]
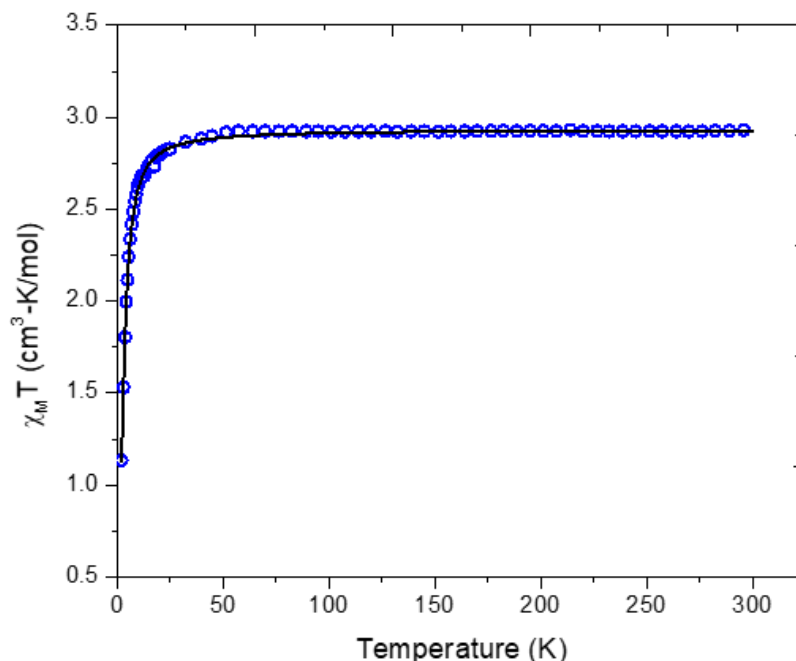
Figure 4.4: Molar magnetic susceptibility ($\chi_M T$) versus T measurements for bulk crystalline **4.2** collected from 2-300 K (blue circles) under a static 0.1 T field. The black trace represents the theoretical fit.

Second, the redox properties of **4.2** were investigated by cyclic voltammetry (CV). The CV of **4.2** was taken at varying scan rates in DCM with $[Bu_4N][PF_6]$ supporting electrolyte and referenced to the ferrocene/ferrocenium (Fc/Fc^+) redox couple. A single quasi-reversible oxidation event was observed at $E_{1/2} = -0.63$ V vs. Fc/Fc^+ (Figure 4.5). To estimate the number of e^- transferred in this event, the data was simulated using DigiSim software. The best fit was obtained assuming a 3 e^- oxidation event, where a corresponding optimized diffusion coefficient (Df) of 4.5 x 10^{-6} cm^2/s and a heterogeneous charge transfer rate constant (k_s) of 0.007 cm/s were obtained by fitting all scan rates (Figure 4.5). Together, and following the Robin-Day classification for electronic delocalization, these data are consistent with a Class I charge localized system with essentially no electronic

communication between metal centres.[32-34] We attempted to chemically isolate the oxidized product of **4.2** using various oxidants, such as [Fc][PF$_6$], [Fc][B(C$_6$F$_5$)$_4$], or [CPh$_3$][B(C$_6$F$_5$)$_4$]; however, the isolation of a pure product has thus far been unsuccessful.
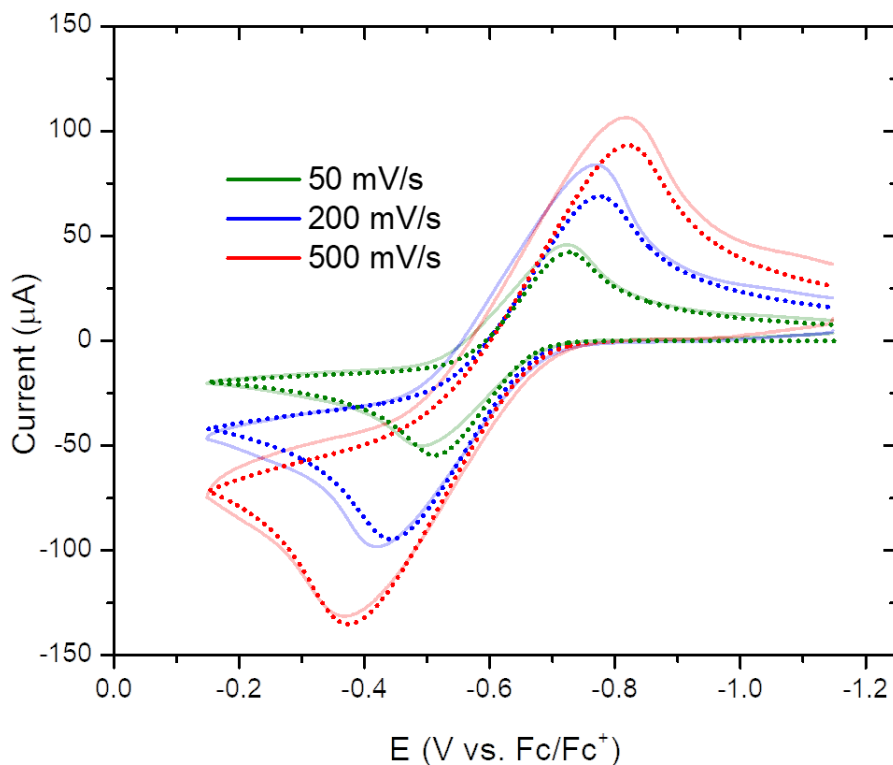
Figure 4.5: CVs of **4.2** (2.3 mM) in a 0.1 M [Bu$_4$N][PF$_6$] DCM solution at varying scan rates using a glassy carbon working electrode, platinum wire counter electrode, silver wire pseuodreference electrode, and referenced to the Fc/Fc$^+$ couple. The dotted traces represent the theoretical fits.

4.2.2 Density Functional Theory Calculations on C3v Symmetric Triarylphosphine.

We next wanted to understand the strength of the observed H-bonding likely leading to the observed ordered 1-D chain structure (Figure 4.2). Tertiary phosphine oxides are known H-bond acceptors[35] and aryl C-H bonds can act as donors.[36] To interrogate the strength of

the H-bonding interactions observed in **4.2** (Figure 4.2b), we probed this using DFT studies. Calculations were performed using the uwB97XD method[37,38] and Ahlrichs' def2-SVP basis set[39] with relativistic effects at V accounted for by the Stuttgart–Dresden ECP.[40] The H-bonding interactions were modelled using the surrogate Lewis base, Me$_3$PO, for computational ease. As expected, the optimized structure of a single molecule of **4.2** adopts the standard propeller-type geometry common to triarylphosphine oxides (Figure 4.6).
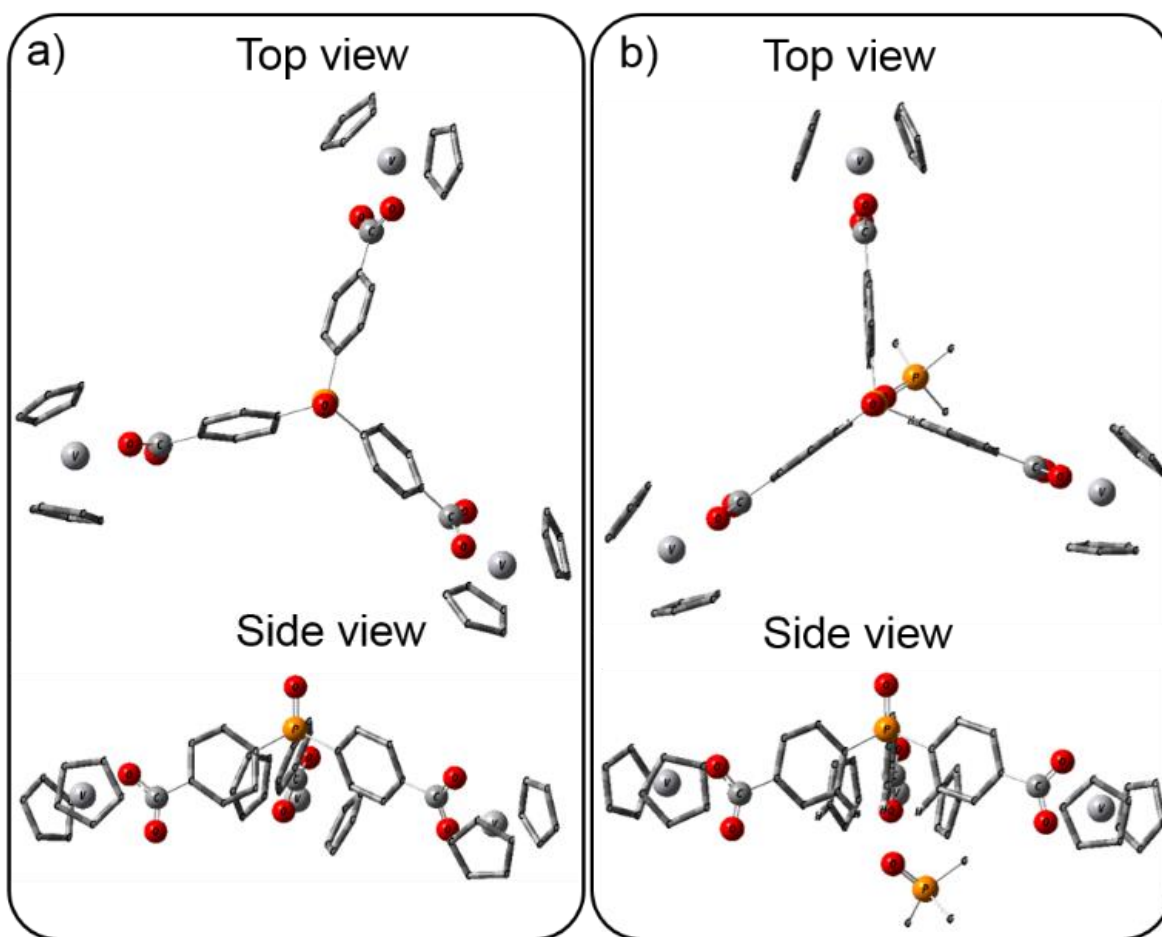
Figure 4.6: DFT optimized structure of **4.2** displaying propeller-type geometry b) Optimized structure of **4.2**·OPMe$_3$. Non-relevant hydrogen atoms were omitted for clarity.

In contrast, addition of one equivalent of Me₃PO forces **4.2** into a C_{3v} configuration as a result of the H-bonding interactions between the *ortho* C–H bonds of **4.2** and the oxide at Me₃PO, analogous to the solid-state structure observed for **4.2** and supporting the role of H-bonding interactions (Figures 4.2b, 4.3, and 4.6b). The interaction of **4.2** with Me₃PO to form the H-bonded pair was calculated to be exothermic ($\Delta H = -13.0$ kcal·mol^{-1}) and slightly exergonic ($\Delta G = -1.6$ kcal·mol^{-1}) comparable to average H-bond strengths (Scheme 4.2).[36]

Scheme 4.2: DFT results from the reaction of free **4.2** (C_3 symmetric) and **4.2** in C_{3v} symmetry enforced by the H-bond acceptor Me₃PO. H-bonds in dashed red.

$\Delta H = -13.0$ kcal·mol^{-1}
$\Delta G = -1.6$ kcal·mol^{-1}

(*C₃* propeller geometry)   (*C₃ᵥ* geometry)
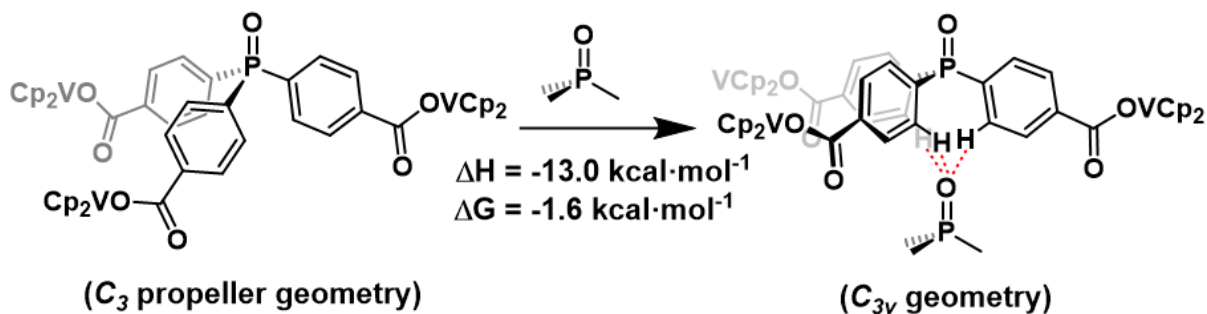
4.2.3 Synthesis and Characterization of a Mono-metallic Derivative for comparison of geometries and Hydrogen Bonding effects.

To gauge solution H-bonding interactions, the diffusion coefficient (*Df*) obtained from the CV simulations of **4.2** (Figure 4.5) may provide a clue. In order to utilize *Df* as a metric for comparison, we synthesized a mono-metallic variant and compared its *Df*. The new compound, **4.4** (Figure 3a), was prepared in two steps by initial silylation of the

known acid, (4-COOH-Ph)P(O)Ph$_2$,[41] with TMSCl in the presence of Et$_3$N to generate

the new, silylated variant, (4-TMS-Ph)P(O)Ph$_2$ (**4.3**), in an analogous fashion to the

synthesis of **4.1** (Scheme 4.3).

Scheme 4.3: Synthesis of **4.3**, metalation to **4.4**, and oxidation to **4.5**.
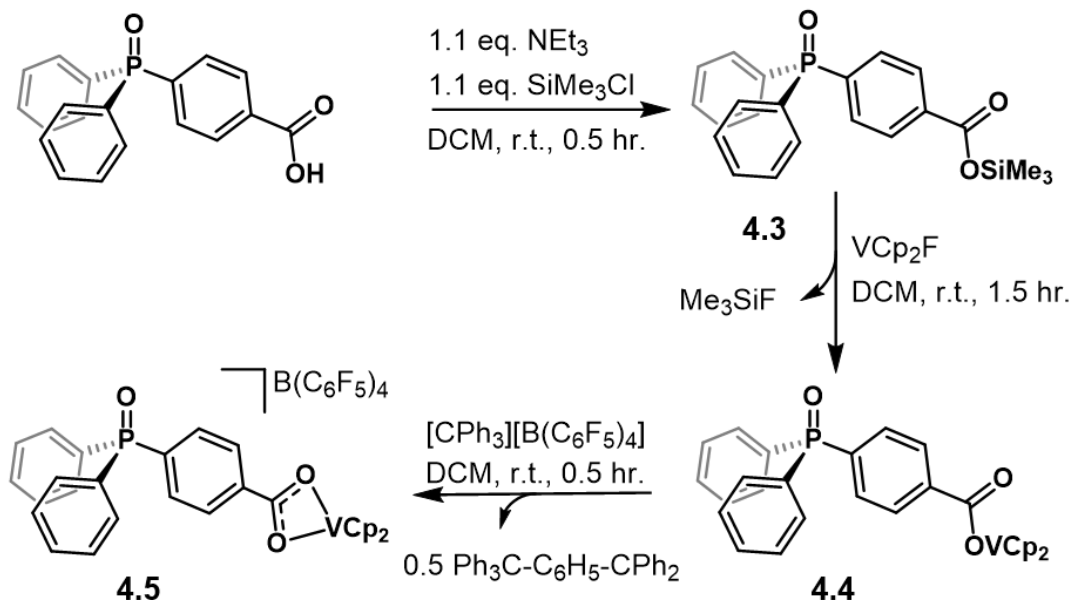
Subsequent addition of an equivalent of Cp$_2$VF to **4.3** in DCM afforded the target

complex, **4.4**, as a bright blue solid (Scheme 4.3). Blue plate-shaped single crystals were

grown by vapor diffusion of pentane into a concentrated DCM solution of **4.4**. The solid-

state structure of **4.4** (Figure 4.7) reveals a standard propeller arrangement of phenyl rings,

with the presence of possible weak intermolecular H-bonding interactions between Cp C–

H bonds and P=O (shortest: ~2.35 Å), although these are longer than in **4.2**. Moreover, the

P=O bond length of 1.482(3) Å is consistent with a double bond[42] and similar to what is

observed in Ph$_3$PO (1.46(1) Å).[43] As expected, compound **4.4** is paramagnetic resulting in

a silent ^{51}V NMR spectrum, as well as broadened ^{1}H NMR resonances. Similar to **4.2**, the

^{31}P NMR spectrum reveals a diagnostic singlet at δ = 26.9 ppm, despite the observed paramagnetic vanadium and proton signals. The magnetic moment (μ_{eff} = 2.74 μ_B) was determined using the Evans method[44] and is consistent with an expected S = 1 spin-only value (μ_{eff} = 2.83 μ_B).
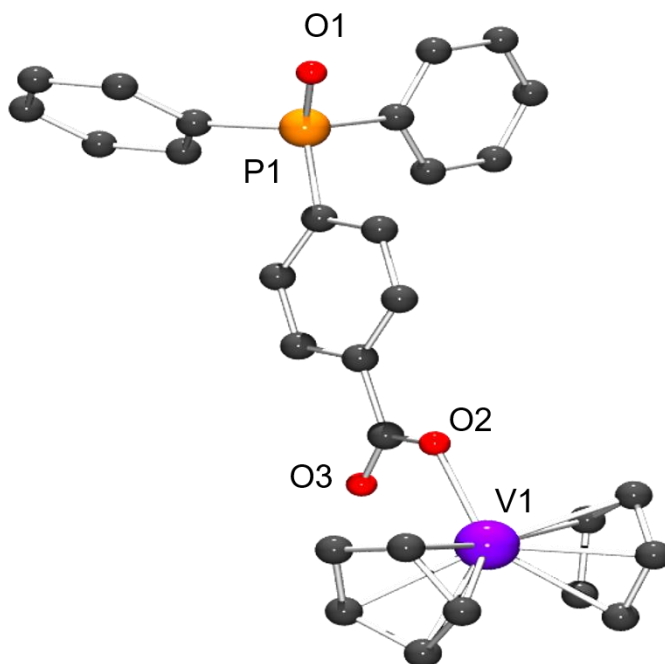
Figure 4.7: Solid-state molecular structure of **4.4** with H-atoms omitted for clarity

The redox properties of **4.4** were investigated using CV. Consistent with the assignment of **4.2** as a Class I charge localized system (*vide supra*), a single quasi-reversible oxidation event is observed for **4.4** at $E_{1/2}$ = -0.62 V vs. Fc/Fc$^+$ (Figures 4.8), nearly identical to the one seen in **4.2** ($E_{1/2}$ = -0.63 V). The CV data for **4.4** was simulated assuming a 1 e$^-$ redox event and optimized to all scan rates. Values for k_s and *Df* of 0.005 cm/s and 1.5 x 10^{-5} cm^2/s, respectively, were obtained. Notable here, while the k_s values for **4.2** and **4.4** are fairly similar (0.007 cm/s (**4.2**) vs. 0.005 cm/s (**4.4**)), the values for *Df*

(4.5 x 10^{-6} cm^2/s (**4.2**) vs. 1.5 x 10^{-5} cm^2/s (**4.4**)) reveal that **4.2** diffuses over three times

slower than **4.4** in solution, which may be indicative of significant H-bonding interactions

being maintained in solution.
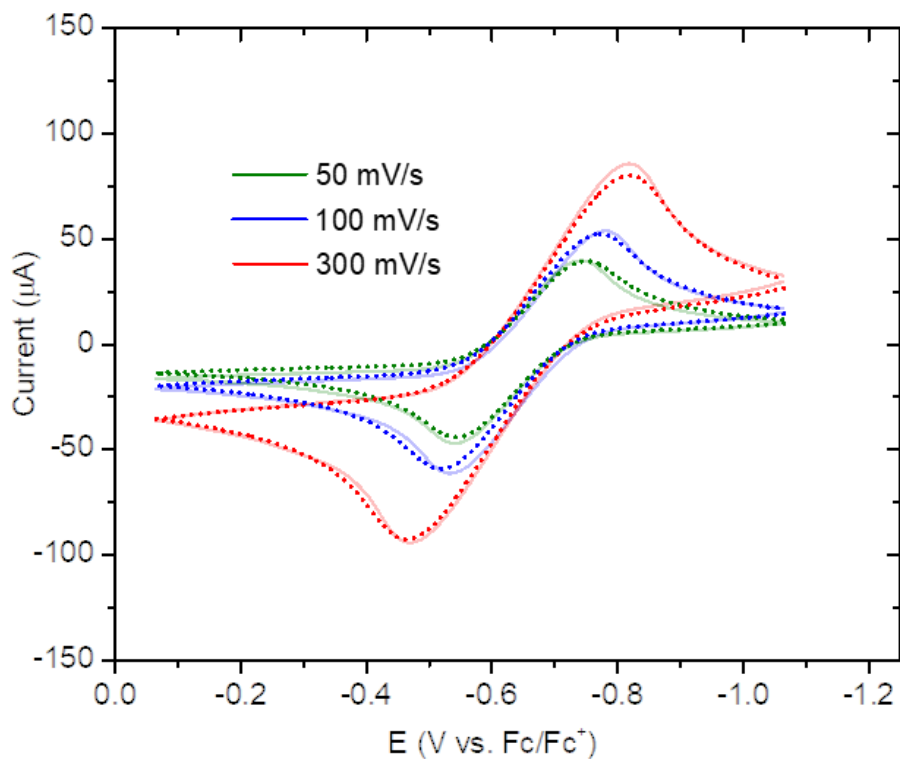
Figure 4.8: CVs of **4.4** (3.6 mM) in a 0.1 M [Bu$_4$N][PF$_6$] DCM solution at varying scan rates

using a glassy carbon working electrode, platinum wire counter electrode, and referenced to the

Fc/Fc$^+$ couple. The dotted traces represent the theoretical fit generated by DigiSim.

4.2.4 Oxidation of a Mono-metallic derivative

Finally, in contrast to **4.2**, complex **4.4** could be chemically oxidized to a stable product.

Addition of an equivalent of the trityl cation salt, [CPh$_3$][B(C$_6$F$_5$)$_4$], to **4.4** resulted in an

immediate colour change from blue to orange (Scheme 4.3). The product was isolated as a red-orange solid in 51% yield. Red plate-shaped single crystals suitable for XRD studies were grown by slow diffusion of pentane into a concentrated solution of the product in DCM, and confirmed the structure as **4.5** (Figure 4.9). Similar to **4.4**, the solid-state structure of **4.5** revealed a standard propeller type configuration with minimal intermolecular H-bonding interactions. As expected,[19] oxidation of the V center led to an increase in its coordination number which was satisfied by the carboxylate ligand adopting a κ^2 configuration with an acute O2-V1-O3 bond angle of 62.83(17)°. The propensity of the vanadocene fragments to change from three coordinate, to four coordinate upon oxidation from V^{III} to V^{IV} has been observed repeatedly in all cases reported in this thesis. Oxidation to V^{IV} was also corroborated by X-band EPR spectroscopy which revealed an expected eight-line hyperfine splitting pattern between the d^1 electron and the ^{51}V nucleus ($I = 7/2$, 100% abundance (Figure 4.10).
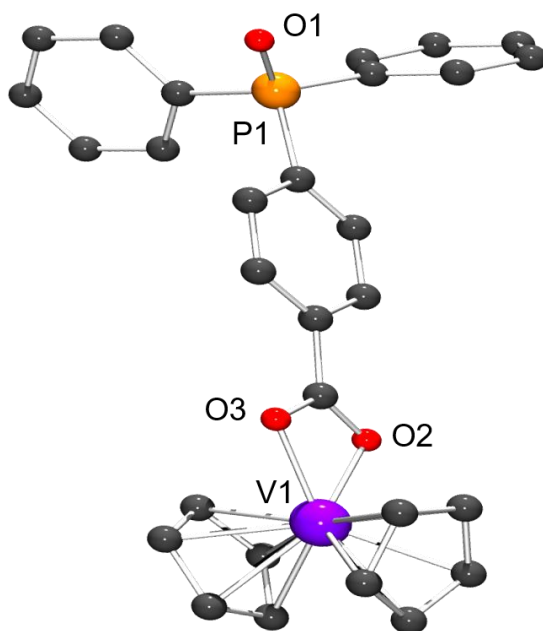
Figure 4.9: Solid-state molecular structure of **4.5** with H-atoms, co-crystallized solvent, and $[B(C_6F_5)_4]^-$ counter ion omitted for clarity.
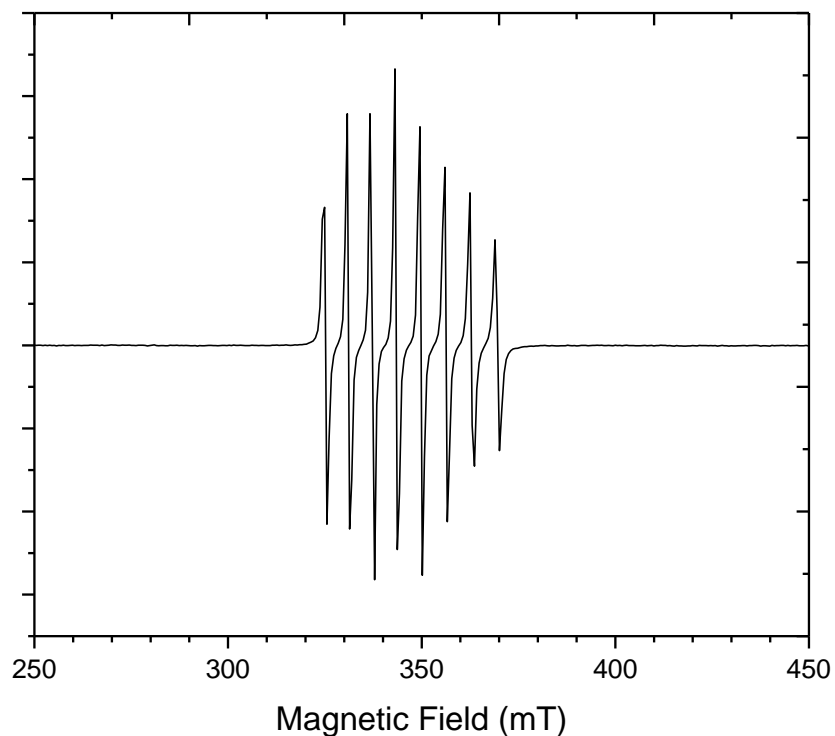
Figure 4.10: X-band EPR spectrum of **5** (DCM, 300 K).

4.3 Conclusions

While TPPO has had broad utility in almost all fields of chemistry, we present in this chapter the first structurally isolated example of a C_{3v} symmetric untethered TPPO derivative, in which the high symmetry can be attributed to intermolecular hydrogen bonding. This complex has been fully characterized by a series of spectroscopic techniques and computational analysis, and mono-metallic derivatives have been prepared as well for comparison. The monometallic do not display the C_{3v} symmetric geometry which supports the claims in chapter 2 that addition of Vanadocene appendages increases the overall basicity of the central phosphine oxide bond.

4.4 Experimental Section

4.4.1 General Considerations.

All manipulations were performed under an atmosphere of dry, oxygen-free N_2 by means of standard Schlenk or glovebox techniques (MBraun UNIlab Pro SP Eco equipped with a -38 °C freezer). Pentane, toluene, benzene, ether, tetrahydrofuran (THF), and dichloromethane (DCM) were dried using an MBraun solvent purification system. All solvents were degassed by freeze-pump-thaw and stored on activated 4 Å molecular sieves prior to use. Trimethylsilyl chloride and triethylamine were purchased from Aldrich and freshly distilled before use. AgF was purchased from Aldrich and [Ph$_3$C][B(C$_6$F$_5$)$_4$] was purchased from Strem Chemicals and both were used without further purification. Cp$_2$VF,[1] P(O)(C$_6$H$_4$-*p*-COOH)$_3$,[2] and Ph$_2$P(O)(C$_6$H$_4$-p-COOH)[3] were prepared according to literature procedures. Elemental analyses (C, N, H) were recorded at the University of California, Berkeley using a Perkin Elmer 2400 Series II combustion analyzer.

NMR spectra were obtained on an Agilent Technologies 400 MHz spectrometer, and referenced to residual solvent or externally ([11]B: BF3•Et2O; [19]F: CFCl3; [31]P: 85% H$_3$PO$_4$). Chemical shifts (δ) are recorded in ppm and the coupling constants are in Hz. X-band EPR spectra were collected on a Bruker EMX EPR Spectrometer equipped with an Oxford ESR 900 liquid helium cryostat. A modulation frequency of 100 kHz was used for all EPR spectra. UV-Vis spectroscopy was performed using a Shimadzu UV-2401PC spectrophotometer with quartz cuvettes equipped with air tight J-young adaptors. IR

spectra were recorded on a Nicolet 6700 FT-IR spectrometer with a NXR FT Raman Module.

X-ray crystallography data was collected on a Bruker KAPPA APEX II diffractometer equipped with an APEX II CCD detector using a TRIUMPH monochromator with a Mo Kα X-ray source (α = 0.71073 Å). The crystals were mounted on a cryoloop with Paratone-N oil, and all data were collected at 100(2) K using an Oxford nitrogen gas cryostream system. A hemisphere of data was collected using ω scans with 0.5° frame widths. Data collection and cell parameter determination were conducted using the SMART program. Integration of the data frames and final cell parameter refinement were performed using SAINT software. Absorption correction of the data was carried out using SADABS. Structure determination was done using direct or Patterson methods and difference Fourier techniques. All hydrogen atom positions were idealized and rode on the atom of attachment. Structure solution, refinement, graphics, and creation of publication materials were performed using SHELXTL.

Cyclic voltammetry was performed on a CH Instruments 630E electrochemical analysis potentiostat, equipped with a 3 mm diameter glassy carbon working electrode, a Ag wire pseudo-reference electrode, and a Pt counter electrode with [Bu4N][PF6] (0.1 M) supporting electrolyte solution in DCM. The glassy carbon working electrode was cleaned prior to each experiment by polishing with 1, 0.3, 0.05 mm alumina (CH Instruments) in descending order, followed by sonication in distilled water for two minutes. Background scans were conducted for each experiment in a solution containing only electrolyte, and was then subtracted from each experiment. All voltammograms were referenced to the Fc/Fc$^+$ redox couple.

All electrochemical simulations were performed using DigiSim with the same concentration, starting potential, ending potential, voltage window, and scan rate as experimental data, and the assumption that T = 298.2 K, and $r_{electrode}$ = 1.5 mm. All events were assumed to have an α/ λ ratio of 0.5, and the diffusion coefficient (Df) and the heterogeneous charge transfer constant (k_s) were fitted to all scan rates to produce the closest fits. A 1-1.2 kΩ correction factor was found to be necessary to account for the high cell impedance. k_s(**2**) and Df(**2**) were found to be 0.007 cm/s and 0.0000045 cm^2/s, respectively. k_s(**4**) and Df(**4**) were found to be 0.005 cm/s and 0.000015 cm^2/s respectively.

DFT calculations were performed using Gaussian 09.2 Geometry optimization of all the molecules were carried out using the uwB97XD method with Ahlrichs' def2-SVP basis set, and with the relativistic effect of vanadium, which was accounted for by the Stuttgart-Dresden ECP, implemented in the Gaussian 09 software.[5-8] Compound **4.2** was calculated in the triplet state. Thermal energy corrections were extracted from the results of frequency analysis performed at the same level of theory. Frequency analysis of all the molecules and intermediates contained no imaginary frequency showing that these are energy minima.

4.4.2 Synthesis of Compounds

Synthesis of P(O)(C₆H₄-p-COOSiMe₃)₃ (4.1): A 100 mL Schlenk flask equipped with a stirbar was charged with dry P(O)(C₆H₄-p-COOH)₃ (0.80 g, 1.95 mmol) and 25 mL of DCM. Using a gas-tight syringe, NEt₃ (0.95 mL, 6.82 mmol) was added dropwise under

nitrogen while stirring. The solid dissolved and the solution went clear. After stirring for ten minutes SiMe$_3$Cl (0.86 mL, 6.82 mmol) was added slowly dropwise using a gas-tight syringe. The resulting solution was allowed to stir for 30 min. and then the volatiles were removed in vacuo to afford a white solid. The solid was brought into the glovebox and brought up in benzene (10 mL). The solution was filtered through a fine porosity glass frit over a pad of celite, and then dried in vacuo to yield a flaky white solid (0.860 g, 1.37 mmol, 70.5%).

^{1}H NMR (400 MHz, C$_6$D$_6$, 25 ^{o}C): δ = 8.06-7.97 (m, 6H; o-ArH), 7.66-7.56(m, 6H; m-ArH), 0.29 (s, 27H; OSiMe$_3$). **^{13}C{^{1}H} NMR** (100 MHz, CD$_2$Cl$_2$, 25 ^{o}C): δ = -0.67 (s, Si(CH$_3$)$_3$), 129.88 (Ar), 131.82 (Ar), 134.97 (Ar), 136.97 (Ar), 165.42 (COOSi). **^{31}P{^{1}H}NMR** (162 MHz, C$_6$D$_6$, 25 ^{o}C): δ = 23.56 (s). **MS (APCI) calculated** C$_{30}$H$_{40}$O$_7$PSi$_3^+$: 627.178 (M+H$^+$), found: 627.2.

Synthesis of P(O)(C$_6$H$_4$-p-COOVCp$_2$)$_3$ (4.2): In the glovebox, a solution of P(O)(C$_6$H$_4$-p-COOSiMe$_3$)$_3$ (0.21 g, 0.33 mmol) in DCM (3 mL) was added slowly dropwise to a solution of VCp$_2$F (0.20 g, 1 mmol) in DCM (10 mL). The resulting bright blue solution was allowed to stir at room temperature for 90 min, and then the volatiles were removed *in vacuo* to afford a dark blue residue. The residue was washed with benzene (10 mL) and pentane (2 x 5 mL) and dried *in vacuo* to yield a bright blue solid (0.30 g, 0.32 mmol, 96.9%). Blue plate shaped single crystals suitable for XRD were grown by slow diffusion of pentane into a concentrated solution of **4.2** in DCM at -40 ^{o}C over several days. The product was stored at -40 ^{o}C to prevent thermal decomposition.

31P{1H} NMR (162 MHz, CD$_2$Cl$_2$, 25 °C): δ = 26.18 (s). **UV-vis: λ (nm)**: 315.5, 734.5; ε (L mol^{-1} cm^{-1}): 9640, 230. **Anal. Calc**. for C$_{51}$H$_{42}$O$_7$PV$_3$: C, 64.43; H, 4.45. Found: C, 64.12; H, 4.46.

Synthesis of Ph$_2$P(O)(C$_6$H$_4$-*p*-COOSiMe$_3$) (4.3)

A 100 mL Schlenk flask equipped with a stirbar was charged with dry Ph$_2$P(O)(C$_6$H$_4$-*p*-COOH) (0.40 g, 1.28 mmol) and 25 mL of DCM. Using a gas-tight syringe, NEt$_3$ (0.20 mL, 1.42 mmol) was added dropwise under nitrogen while stirring. The solid dissolved and the solution went clear. After stirring for 10 minutes SiMe$_3$Cl (0.18 mL, 1.42 mmol) was added slowly dropwise at room temperature using a gas-tight syringe. The resulting solution was allowed to stir for 30 mins. and then the volatiles were removed *in vacuo* to afford a white solid. The solid was brought into the glovebox and brought up in benzene (10 mL). The solution was filtered through a fine porosity glass frit over a pad of celite, and then dried *in vacuo* to yield a flaky white solid (0.22 g, 0.55 mmol, 43%).

1H NMR (400 MHz, C$_6$D$_6$, 25 °C): δ = 7.99-8.02 (m, 2H), 7.69-78 (m, 6H), 6.98-7.06 (m, 6H), 0.28 (s, 9H, OSi*Me$_3$*). **13C{1H} NMR** (100 MHz, CD$_2$Cl$_2$, 25 °C): δ = -0.64 (Si(*C*H$_3$)$_3$), 128.50 (*Ar*), 129.67 (*Ar*), 131.82 (*Ar*), 132.07 (*Ar*), 132.75 (*Ar*), 134.54 (*Ar*), 137.24 (*Ar*), 138.25 (*Ar*), 165.59 (*C*OOSi). **31P{1H}** (162 MHz, C$_6$D$_6$, 25 °C): δ = 23.56 (s). **MS (APCI) calculated** C$_{22}$H$_{23}$O$_3$PSi$^+$: 395.128 (M+H$^+$), found: 395.1

Synthesis of Ph$_2$P(O)(C$_6$H$_4$-*p*-COOVCp$_2$) (4.4): In the glovebox, a solution of Ph$_2$P(O)(C$_6$H$_4$-*p*-COOSiMe$_3$) (**4.3**) (0.137 g, 0.346 mmol) in DCM (3 mL) was added

slowly dropwise to a solution Cp$_2$VF (0.069 g, 0.346 mmol) in DCM (10 mL). The

resulting bright blue solution was allowed to stir at room temperature for 90 mins, and

then the volatiles were removed *in vacuo* to afford a dark blue residue. The residue was

washed with diethyl ether (2 x 5 mL) and dried *in vacuo* to yield a bright blue solid

(0.141 g, 0.290 mmol, 83.8%). Blue plate-shaped single crystals suitable for XRD studies

were grown by slow diffusion of pentane into a concentrated solution of **4.4** in DCM at -

40 °C over three days. The product was stored at -40 °C to prevent thermal

decomposition.

^{1}H NMR (400 MHz, CD$_2$Cl$_2$, 25 °C): δ = 8.81 (bs, 2H), 7.67 (bm, 4H), 7.57 (bm, 2H),

7.50 (bm, 4H), 6.92 (bs, 2H). **^{31}P NMR** (162 MHz, CD$_2$Cl$_2$, 25 °C): δ = 26.85 (s). **UV-vis**

λ (nm): 314, 560, 733; ε (L mol^{-1} cm^{-1}): 3750, 210, 230. **μ_{eff} (Evans):** 2.74 μ_B. **Anal.**

Calc. for C$_{29}$H$_{24}$O$_3$PV: C, 69.33%; H, 4.82%. Found: C, 68.28%; H, 4.67%. Attempts to

obtain satisfactory elemental analysis consistently resulted in reduced carbon percentages

which we attribute to incomplete combustion as a result of vanadium carbide formation.[4]

Synthesis of [Ph$_2$P(O)(C$_6$H$_4$-*p*-COOVCp$_2$)][B(C$_6$F$_5$)$_4$] (4.5): In the glovebox, a solution

[CPh$_3$][B(C$_6$F$_5$)$_4$] (0.054 g, 0.059 mmol) in DCM (3 mL) was added dropwise to a

solution of Ph$_2$P(O)(C$_6$H$_4$-*p*-COOVCp$_2$) (**4.4**) (0.030 g, 0.059 mmol) in DCM (3 mL).

The solution instantly turned a dark orange and was allowed to stir at room temperature

for 30 mins. The volatiles were removed *in vacuo* and the orange/brown residue was

washed with benzene (3 x 5 mL). The residue was dissolved in a minimal amount of

DCM (1 mL) and carefully layered with hexanes (1 mL). The solution was cooled to -40

°C and left to recrystallize for 24 h. The resulting orange precipitate was filtered and

dried *in vacuo*. (0.035 g, 0.030 mmol, 50.8%). Highly air sensitive red plate-shaped single crystals suitable for XRD were grown by slow diffusion of pentane into a concentrated solution of **4.5** in DCM at -40 °C over several days. The product was stored at -40 °C to prevent thermal decomposition.

¹H NMR (400 MHz, CD₂Cl₂, 25 °C): δ = 8.30 (bs, Ar*H*), 7.66 (bs, Ar*H*), 7.52 (bs, Ar*H*).

³¹P{¹H} NMR (162 MHz, CD₂Cl₂, 25 °C): δ = 26.37 (s). **¹⁹F{¹H} NMR** (376 MHz, CD₂Cl₂): δ = -133.20 (s, 8F, *o*-C₆*F*₅), -163.59 (s, 4F, *p*-C₆*F*₅), -167.41 (s, 8F, *m*-C₆*F*₅).

¹¹B NMR (128 MHz, CD₂Cl₂): δ = -16.65 (bs). **UV-vis: λ (nm)**: 384.0, 576.0, 722.0; ε (L mol⁻¹ cm⁻¹): 650, 470, 80. **Anal. Calc**. for C₅₃H₂₄BF₂₀O₃PV: C, 53.88%; H, 2.05. Found: C, 54.48%, H, 2.45%

4.4.3 IR Data for Reported Compounds

IR spectra of P(O)(C₆H₄-*p*-COOSiMe₃)₃ (4.1) (KBr pellet)
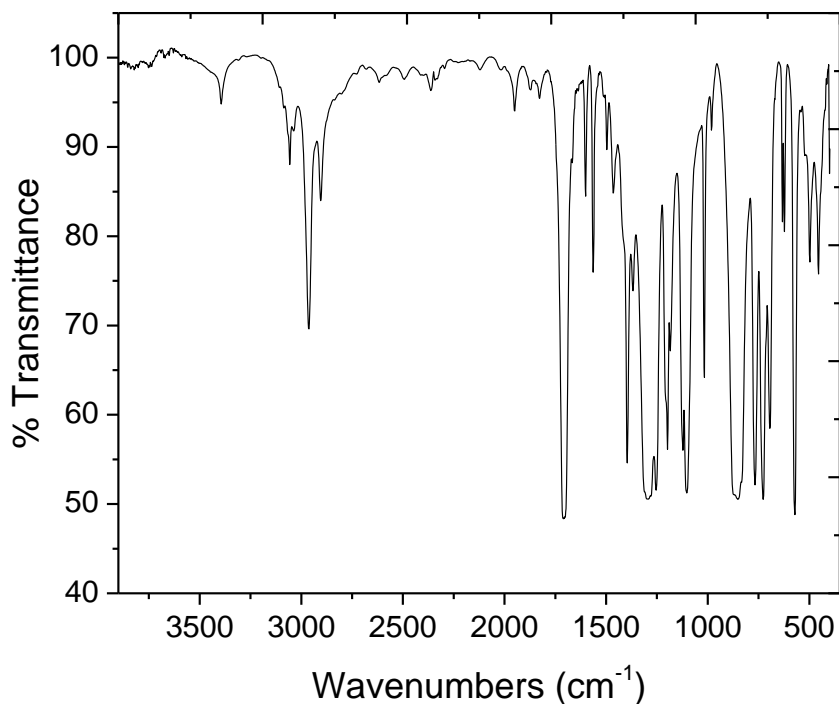
IR spectra of P(O)(C$_6$H$_4$-*p*-COOVCp$_2$)$_3$ (4.2) (KBr pellet)
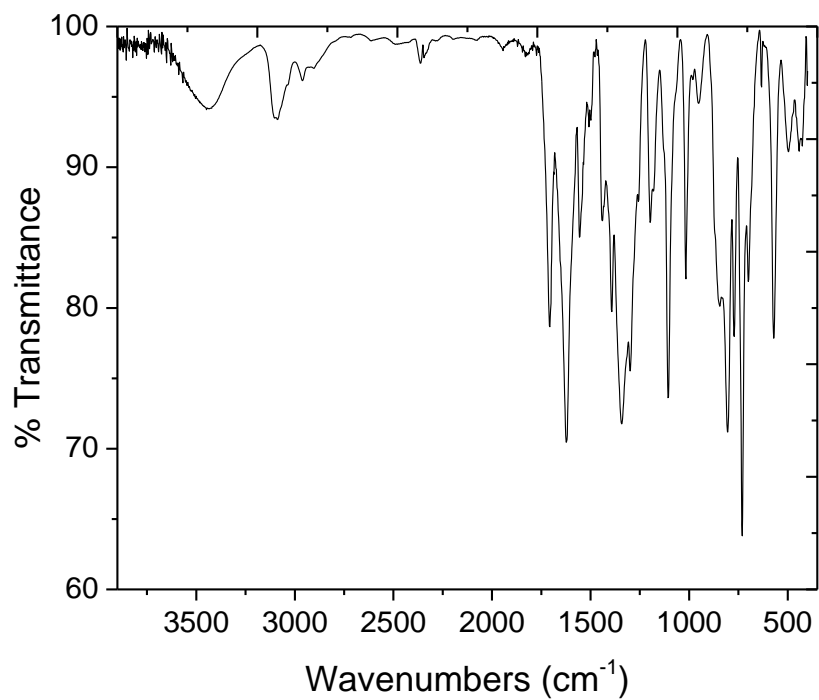
IR spectra of Ph$_2$P(O)(C$_6$H$_4$-*p*-COOVCp$_2$) (4.4) (KBr pellet)
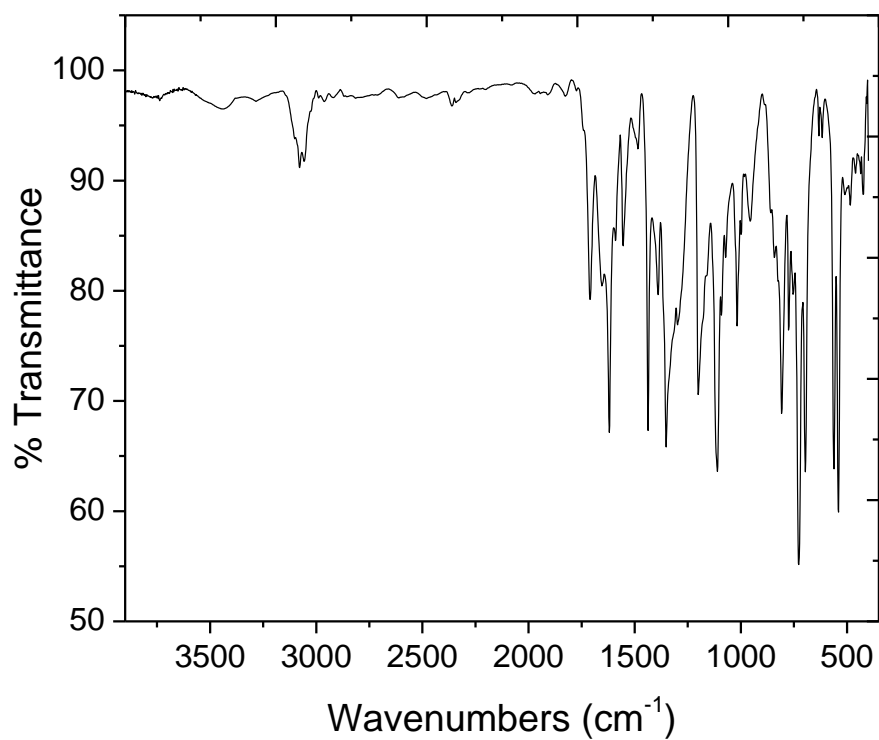
IR spectra of [Ph₂P(O)(C₆H₄-*p*-COOVCp₂)][B(C₆F₅)₄] (5.5) (KBr pellet)
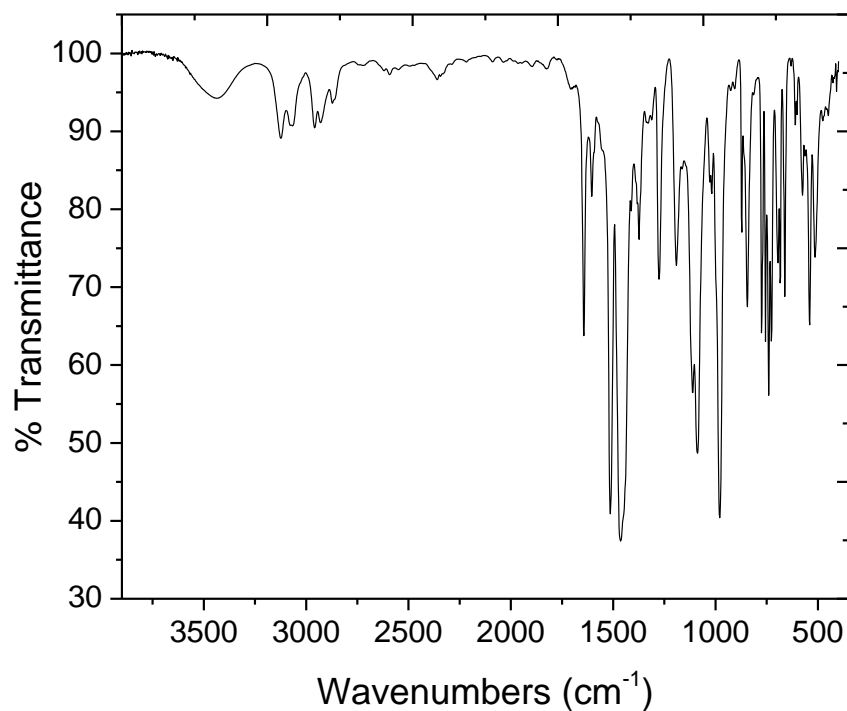
4.4.4 Crystallographic Data for reported complexes

	4.2	**4.4**	**4.5**
Empirical formula	$C_{51}H_{33}O_7PV_3$	$C_{29}H_{24}O_3PV$	$C_{54}H_{24}BCl_2F_{20}O_3PV$
Formula weight	941.61	502.43	*1264.40*
Temperature (K)	100(2)	100(2)	*100(2)*
Crystal system	Hexagonal	Monoclinic	*Monoclinic*
Space group	P 63/mcm	P 21/c	*C 2/c*
a (Å)	15.033(2)	10.190(8)	*25.0426(19)*
b (Å)	15.033(2)	11.081(9)	*33.159(2)*
c (Å)	11.491(3)	21.340(19)	*16.5246(11)*
α (deg)	90.00	90.00	*90.00*
β (deg)	90.00	97.09(6)	*115.089(4)*
γ (deg)	120.00	90.00	*90.00*

Volume ($\mathring{A}^3$)	2248.8(7)	2391(4)	12427.1(16)
Z	2	4	8
Dcalc (g/cm³)	1.390	1.396	1.352
F(000)	960.5	1042.1	5041.9
θ Range (deg)	1.56-24.84	1.92-27.15	1.414-26.520
no. of rflns collected	11757	15809	36579
no. of unique rflns	733	5178	12740
no. of obsd rflns	582	2614	7822
no. of par.	61	307	739
Final R, R_w (I > 2σ(I))	0.1347, 0.2494	0.0639, 0.2280	0.0467, 0.1358
Goodness-of-fit on F^2	**1.051**	**0.897**	**0.986**

4.5 References

(1)   F. Cao, E. Ju, C. Liu, W. Li, Y. Zhang, K. Dong, Z. Liu, J. Ren and X. Qu, Nanoscale, 2017, 9, 4128.

(2)   T. Sawano, Z. Lin, D. Boures, B. An, C. Wang and W. Lin, J. Am. Chem. Soc., 2016, 138, 9783.

(3)   X. Du, R. Fan, L. Qiang, K. Xing, H. Ye, X. Ran, Y. Song, P. Wang and Y. Yang, ACS Appl. Mater. Interfaces, 2017, 9, 28939.

(4)   L.-Q. Huo, L.-L. Gao, J.-F. Gao, F.-Q. An, X.-Y. Niu and T.-P. Hu, Inorg. Chem. Commun., 2018, 89, 83.

(5)   I. A. Ibarra, T. W. Hesterberg, J.-S. Chang, J. W. Yoon, B. J. Holliday and S. M. Humphrey, Chem. Commun., 2013, 49, 7156.

(6)   X.-J. Li, F.-L. Jiang, M.-Y. Wu, L. Chen, J.-J. Qian, K. Zhou, D.-Q. Yuan and M.-C. Hong, Inorg. Chem., 2014, 53, 1032.

(7)   Y. Wang, Y. Li, Z. Bai, C. Xiao, Z. Liu, W. Liu, L. Chen, W. He, J. Diwu, Z. Chai, T. E. Albrecht-Schmitt and S. Wang, Dalton Trans., 2015, 44, 18810.

(8)   S. M. Humphrey, P. K. Allan, S. E. Oungoulian, M. S. Ironside and E. R. Wise, Dalton Trans., 2009, 2298.

(9)   W.-J. Li, J.-F. Feng, Z.-J. Lin, Y.-L. Yang, Y. Yang, X.-S. Wang, S.-Y. Gao and R. Cao, Chem. Commun., 2016, 52, 3951.

(10)   Y. Li, Z. Weng, Y. Wang, L. Chen, D. Sheng, Y. Liu, J. Diwu, Z. Chai, T. E. Albrecht-Schmitt and S. Wang, Dalton Trans., 2015, 44, 20867.

(11)   K. Xing, R. Fan, J. Wang, S. Zhang, K. Feng, X. Du, Y. Song, P. Wang and Y. Yang, ACS Appl. Mater. Interfaces, 2017, 9, 19881.

(12)   M. Eddaoudi, J. Kim, N. Rosi, D. Vodak, J. Wachter, M. O'Keeffe and O. M. Yaghi, Science, 2002, 295, 469.

(13)   K. A. Al-Farhan, J. Crystallogr. Spectrosc. Res., 1992, 22, 687.

(14)   M. W. Drover, K. Nagata and J. C. Peters, Chem. Commun., 2018, 54, 7916.

(15)   C. Jongsma, J. P. de Kleijn and F. Bickelhaupt, Tetrahedron, 1974, 30, 3465.

(16)   H. Tsuji, T. Inoue, Y. Kaneta, S. Sase, A. Kawachi and K. Tamao, Organometallics, 2006, 25, 6142.

(17)   T. Agou, J. Kobayashi and T. Kawashim, Heteroat. Chem., 2004, 15, 437.

(18)   T. G. Carroll, R. Garwick, J. Telser, G. Wu and G. Menard, Organometallics, 2018, 37, 848.

(19)   T. G. Carroll, R. Garwick, G. Wu and G. Menard, Inorg. Chem., 2018, 57, 11543.

(20)   J. Chu, T. G. Carroll, G. Wu, J. Telser, R. Dobrovetsky and G. Menard, J. Am. Chem. Soc., 2018, 140, 15375.

(21)   G. W. Coulston, S. R. Bare, H. Kung, K. Birkeland, G. K. Bethke, R. Harlow, N. Herron and P. L. Lee, Science, 1997, 275, 191.

(22)   B. Chen and E. J. Munson, J. Am. Chem. Soc., 2002, 124, 1638.

(23)   M.-J. Cheng and W. A. Goddard, J. Am. Chem. Soc., 2013, 135, 4600.

(24)   M.-J. Cheng, R. Fu and W. A. Goddard, Chem. Commun., 2014, 50, 1748.

(25)   M.-J. Cheng, W. A. Goddard and R. Fu, Top. Catal., 2014, 57, 1171.

(26)   B. G. Harvey, A. M. Arif, A. Glöckner and R. D. Ernst, Organometallics, 2007, 26, 2872.

(27)   Z. R. Herm, B. M. Wiers, J. A. Mason, J. M. van Baten, M. R. Hudson, P. Zajdel, C. M. Brown, N. Masciocchi, R. Krishna and J. R. Long, Science, 2013, 340, 960.

(28)   S. R. Miller, P. A. Wright, C. Serre, T. Loiseau, J. Marrot and G. Fe´rey, Chem. Commun., 2005, 3850.

(29)   C. Giacobbe, E. Lavigna, A. Maspero and S. Galli, J. Mater. Chem. A, 2017, 5, 16964.

(30)   S. Friebe, B. Geppert, F. Steinbach and J. Caro, ACS Appl. Mater. Interfaces, 2017, 9, 12878.

(31)   R. Bocˇa, Coord. Chem. Rev., 2004, 248, 757.

(32)   R. Choukroun, C. Lorber, B. Donnadieu, B. Henner, R. Frantz and C. Guerin, Chem. Commun., 1999, 1099.

(33)   M. B. Robin and P. Day, in Advances in Inorganic Chemistry and Radiochemistry, ed. H. J. Emele´us and A. G. Sharpe, Academic Press, 1968, p. 247.

(34)   H. Fink, N. J. Long, A. J. Martin, G. Opromolla, A. J. P. White, D. J. Williams and P. Zanello, Organometallics, 1997, 16, 2646.

(35)   P. Zanello, in Inorganic Electrochemistry: Theory, Practice and Application, The Royal Society of Chemistry, 2003, p. 159.

(36)   I. Alkorta and J. Elguero, J. Phys. Chem. A, 1999, 103, 272.

(37)   V. S. Bryantsev and B. P. Hay, Org. Lett., 2005, 7, 5031.

(38)   J.-D. Chai and M. Head-Gordon, Phys. Chem. Chem. Phys., 2008, 10, 6615.

(39)   J.-D. Chai and M. Head-Gordon, J. Chem. Phys., 2008, 128, 084106.

(40)   F. Weigend and R. Ahlrichs, Phys. Chem. Chem. Phys., 2005, 7, 3297.

(41)   P. Schwerdtfeger, M. Dolg, W. H. E. Schwarz, G. A. Bowmaker and P. D. W. Boyd, J. Chem. Phys., 1989, 91, 1762.

(42)   C. W. Seifert, A. Paniagua, G. A. White, L. Cai and G. Li, Eur. J. Org. Chem., 2016, 1714.

(43)   F. H. Allen, O. Kennard, D. G. Watson, L. Brammer, A. G. Orpen and R. Taylor, J. Chem. Soc., Perkin Trans. 2, 1987, S1.

(44)   G. Bandoli, G. Bortolozzo, D. A. Clemente, U. Croatto and C. Panattoni, J. Chem. Soc. A, 1970, 2778.

Chapter 5

Probing the C-H Reactivity of a Phosphorus(V) Oxide Bond Using a "Bulky Hydrogen Atom" Surrogate: Analogies to PCET

5.1 Introduction

Catalyst support systems typically involve unreactive main group oxides, such as silica (SiO_2), alumina (Al_2O_3), and phosphate (PO_4^{3-}), supporting the catalytically active metal centers. Common supported commercial catalysts include (support in parentheses): the Phillips Cr catalyst for ethylene polymerization (SiO_2); the Haber-Bosch Fe catalysts for N_2 reduction to NH_3 (Al_2O_3 and others); the hydrodesulfurization catalysts for petroleum processing (Al_2O_3), and; the vanadium phosphate oxide (VPO) catalyst for the partial oxidation of butane to maleic anhydride (PO_4^{3-}).[1-4] Supports are typically assumed to act as high-surface platforms capable of binding catalytically active centers, while playing little role in the catalytic processes themselves. However, studies have shown that supports may indeed be active in catalysis through various mechanisms, such as spillover effects, strong metal-support interactions, and more,[5-8] thus requiring a rethink of the once accepted dogma.

For decades, the mechanism for the conversion of butane to maleic anhydride using the VPO catalyst has been the subject of extensive experimental studies. Key mechanistic steps, including activation of the relatively inert butane C–H bonds, were thought to occur solely at high-valent V-oxo centers. No study invoked the PO_4^{3-} support in any reactive

119

step.[4, 9-13] However, recent computational studies by Goddard and co-workers have found that PO_4^{3-} may be involved in the key C–H activation chemistry. They proposed that inert C–H cleavage at butane occurs at a terminal P^V=O bond resulting in its protonation with concurrent reduction at a neighboring V^V (Scheme 5.1a).[14-16] This proposed mechanism, coined reduction-coupled oxo activation (ROA), bears significant resemblance to well-studied proton-coupled electron transfer (PCET) reactions,[17-19] but has yet to be supported by any experimental evidence.

Scheme 5.1: a) Proposed ROA (PCET) mechanism for the C–H activation of butane at a P^V=O bond in VPO. b) Chapter 5 work highlighting the reaction of molecular VPO analogs (5.2a-5.2b) with H• and TMS• donors.

a) *COMPUTATIONAL STUDIES*

VPO

b) *THIS WORK*

5.2a (Ar = C_6F_5)
5.2b (Ar = Ph)

5.2a, **5.2b** (X = TMS)
STABLE PRODUCTS

(X = H)
DECOMP.
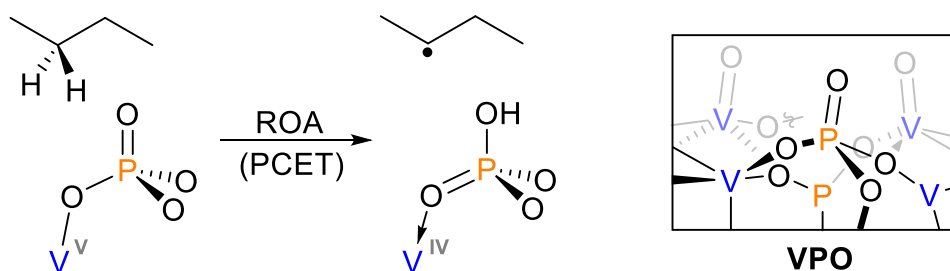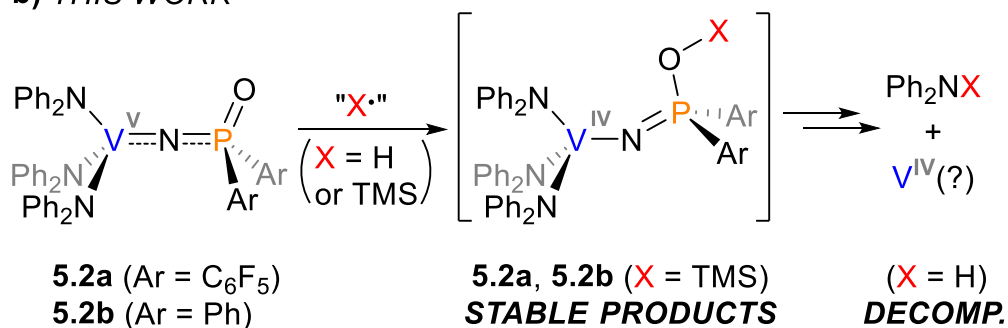
To investigate the proposed non-innocent role of terminal P^V=O bonds in VPO, we have reported in Chapters 2-4, the synthesis and preliminary reactivity of homogeneous mono- and multi-metallic vanadium phosphinate complexes bearing V^{III}–O–P^V=O linkages.[20-21] These complexes were unreactive to common H-atom donors (HADs), perhaps as a result of their relatively low V^{III} oxidation states.[10] Herein, we describe the synthesis of high-valent V^V complexes (**5.2a**, **5.2b**) bearing V^V=N–P^V=O linkages as molecular VPO models, and further probe their reactivity with both HADs and a trimethylsilyl radical (Me$_3$Si• = TMS•) donor (Scheme 5.1b). The latter involved the formation of a reduced product with a silylated P=O bond, following a pathway analogous to ROA (Scheme 5.1a). As will be outlined, we describe TMS• as a "bulky hydrogen atom" – similar to the use of TMS$^+$ as a "bulky proton"[22-24] – and together, these results describe the first direct experimental evidence supporting the proposed ROA mechanism.

5.2 Results and Discussion

5.2.1 Synthesis and characterization of Vanadium(V) phosphinate complexes

The target complexes (**5.2a**, **5.2b**) were synthesized by salt metathesis of the reported[25] vanadium nitride, $(Ph_2N)_3V(\mu\text{-N})Li(THF)_3$ (**5.1**), with di-aryl phosphinic chlorides, $(C_6F_5)_2P(O)Cl$[26] or $Ph_2P(O)Cl$, resulting in the isolation of **5.2a** or **5.2b**, respectively, following purification (Scheme 5.2).

Scheme 5.2: Synthesis of Complexes **5.2a** and **5.2b**
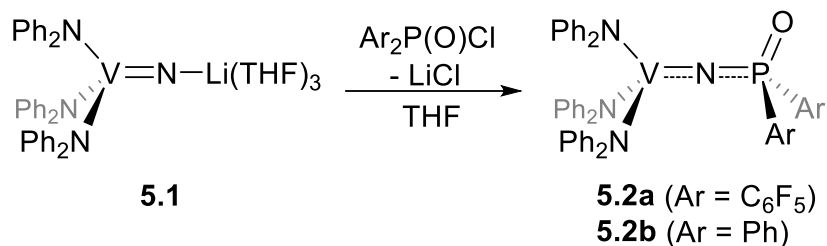
Both V^V complexes displayed significantly shifted, broad ^{51}V NMR resonances at 117 ppm (**5.2a**) and -6 ppm (**5.2b**) relative to **5.1** (-217 ppm), consistent with an increasingly deshielded V center. In contrast, the ^{31}P NMR resonances followed the opposite trend with broad signals (due to coupling to the quadrupolar (I = 7/2) ^{51}V) at -20 and 19 ppm, respectively, both shifted ~20 ppm upfield relative to the starting materials. The ^1H NMR spectrum displayed diagnostic aryl signals for the diphenyl amine ligands, and **5.2a** could also be characterized by ^{19}F NMR spectroscopy by three distinct *ortho*, *para*, and *meta* signals. Single crystals suitable for X-ray diffraction (XRD)[27] studies were grown from pentane/ether (**5.2a**, Figure 5.1a) or ether (**5.2b**, Figure 5.1b). Pertinent bond lengths and angles are compiled in Tables 5.1 and 5.2. Notable are the elongated V1–N1 bonds in **5.2a** (1.662(11) Å) and **5.2b** (1.661(7) Å) relative to **1** (1.582(3) Å)[25] both of which are also nearly identical to the N1–P1 bonds in **5.2a** (1.661(11) Å) and **5.2b** (1.674(7) Å). Combined with the near linear V1–N1–P1 angles (**5.2a**: 175.9(7)°; **5.2b**: 173.1(5)°), this suggests a delocalized π manifold, in which there is electronic communication between the vanadium and phosphorus through the nitrogen linker. This is also supported by the broad vanadium coupling seen in the ^{31}P NMR. The distances between the designed redox active centers and basic sites (V1 to O1) are about 4.1 Å in both **5.2a** and **5.2b**.
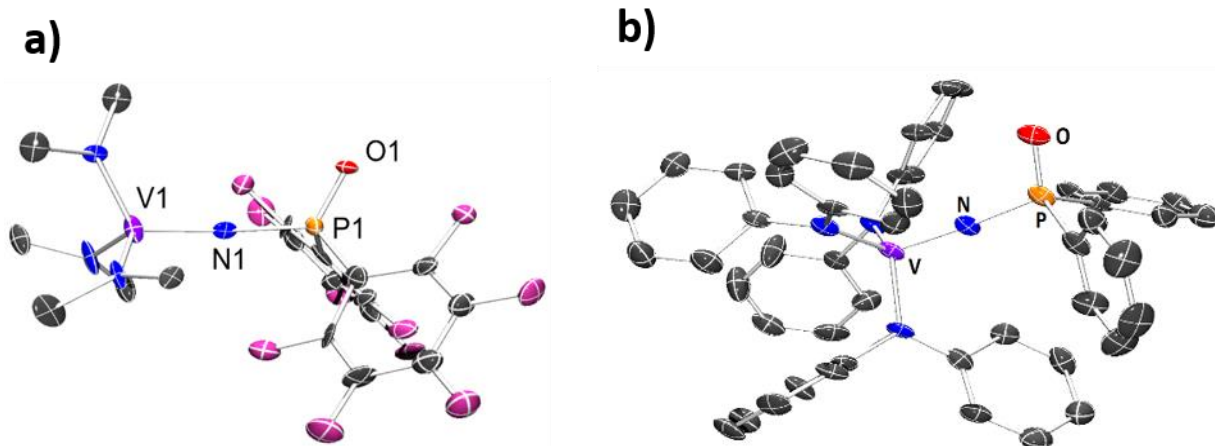
Figure 5.1: a) Solid state XRD structure of **5.2a** (C, black; N, blue; V, purple; P, orange; O, red; F, violet). Phenyl groups (excluding *ipso* carbons), and hydrogen atoms are omitted for clarity. b) Solid state XRD structure of **5.2b**; hydrogen atoms omitted for clarity.

Table 5.1: Selected Bond Distances (Å) and Angles (º) for 2a, 2a-Si$^+$, 2a$^-$, 3a

	5.2a	**5.2a-Si$^+$**	**5.2a$^-$**	**5.3a**
V1-N1	1.662(11)	1.710(11)	1.764(14)	1.837(2)
N1-P1	1.661(11)	1.592(11)	1.551(14)	1.535(2)
P1-O1	1.484(8)	1.528(9)	1.455(12)	1.5637(16)
O1-Si1	-	1.708(9)	-	1.6935(17)
V1-N1-P1	175.9(7)	169.3(6)	145.3(10)	145.90(13)
N1-P1-O1	115.8(5)	115.6(6)	122.9(7)	120.85(10)
P1-O1-Si1	-	154.1(6)	-	140.37(12)

Table 5.2: Selected Bond Distances (Å) and Angles (º) for 2b, 2b-Si$^+$, 2b$^-$, 3b

	5.2b	**5.2b-Si$^+$**	**5.2b$^-$**	**5.3b**
V1-N1	1.661(7)	1.686(16)	1.708(8)	1.782(5)
N1-P1	1.674(7)	1.595(16)	1.637(9)	1.572(5)
P1-O1	1.482(6)	1.560(13)	1.486(6)	1.579(5)
O1-Si1	-	1.690(13)	-	1.687(5)
V1-N1-P1	173.1(5)	174.3(10)	156.8(5)	146.9(3)
N1-P1-O1	113.3(3)	111.2(8)	120.1(4)	- (disordered)
P1-O1-Si1	-	161.3(8)	-	- (disordered)

5.2.2 *Reactivity of Vanadium(V) phosphinate complexes with various Hydrogen Atom Donors*

Exposure of **5.2a** and **5.2b** to common hydrogen atom donors (HADs) with various element–H bond dissociation free energies (BDFE$_{solvent}$), such as 2,4,6-tri-*tert*-butylphenol (O–H BDFE$_{MeCN}$ = 77.1 kcal/mol) and 1,4-cyclohexadiene (C–H BDFE$_{tol}$ = 72.6 kcal/mol), or TEMPO-H (O–H BDFE$_{C6H6}$ = 65.2 kcal/mol) in benzene resulted in no appreciable reaction as determined by both ^{1}H NMR and X-Band EPR spectroscopies of the reaction solutions.[17, 28] In contrast, exposure of **5.2a** to Cp(CO)$_3$Cr–H (BDFE$_{MeCN}$ = 57.3 kcal/mol) (Cp = μ^5-C$_5$H$_5$)[29-31], a common weak HAD, in C$_6$D$_6$ at room temperature resulted in the quantitative appearance of the protonated amide, Ph$_2$NH, as well as a half equivalent of the Cr dimer product, [Cp(CO)$_3$Cr]$_2$ as observed by ^{1}H NMR spectroscopy (Scheme 5.3, Figure 5.2).[32] It was proposed that the reaction may first involve protonation of the P^V=O bond, followed by reduction of the vanadium atom, as evidenced by the diagnostic eight-line EPR spectra of the reaction mixture, (Figure 5.3) to yield a transient intermediate that likely decomposes to produce diphenylamine and an unknown vanadium compound.

Scheme 5.3: ^{1}H NMR monitoring of the reaction between (Ph$_2$N)$_3$VNPO(C$_6$F$_5$)$_2$ **5.2a** and CpCrH(CO)$_3$
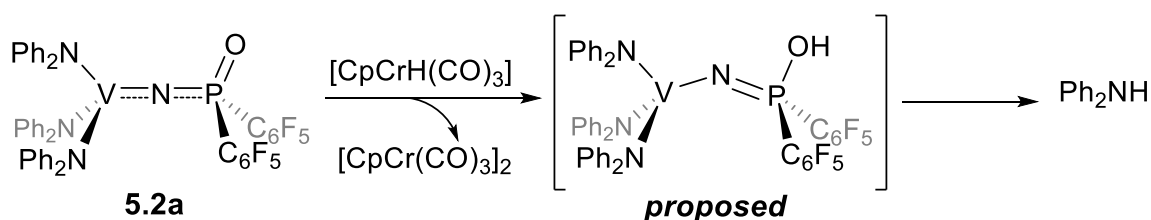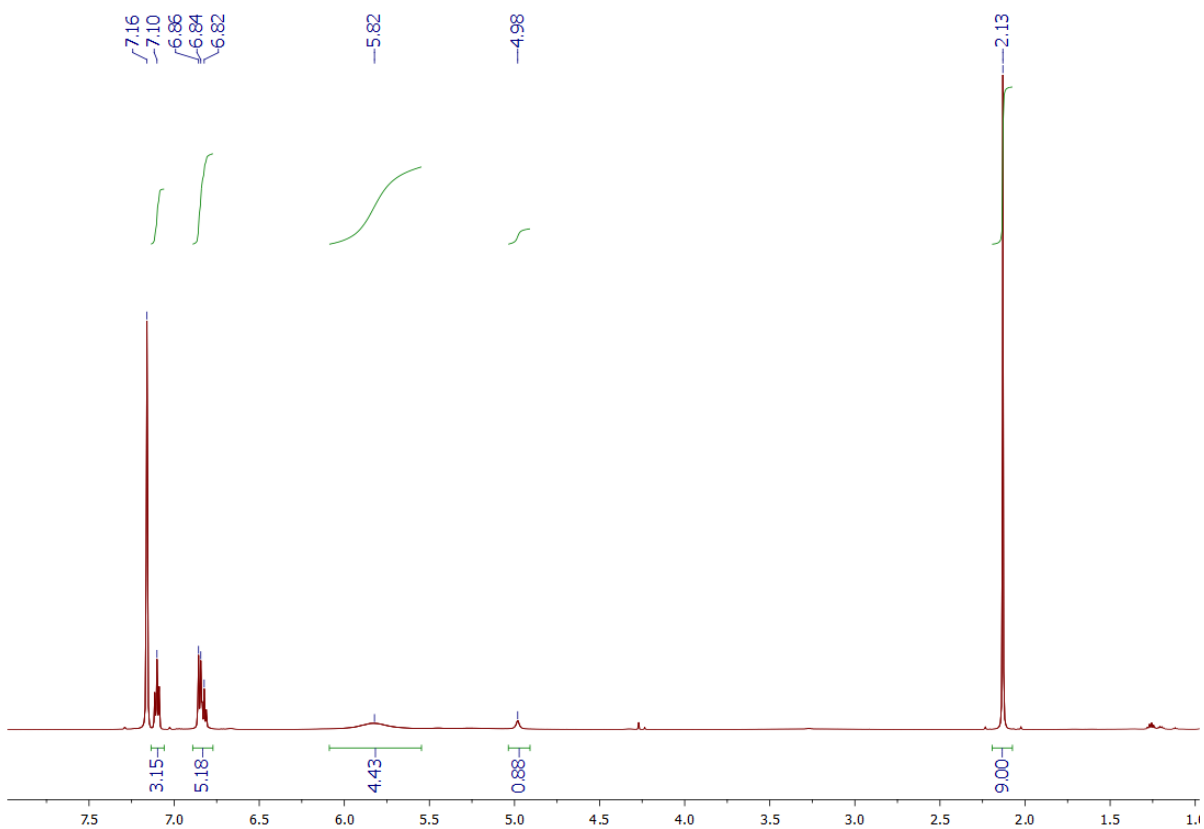
Figure 5.2: ^{1}H NMR motoring of reaction between **5.2a** and CpCrH(CO)$_3$ in d-Benzene.
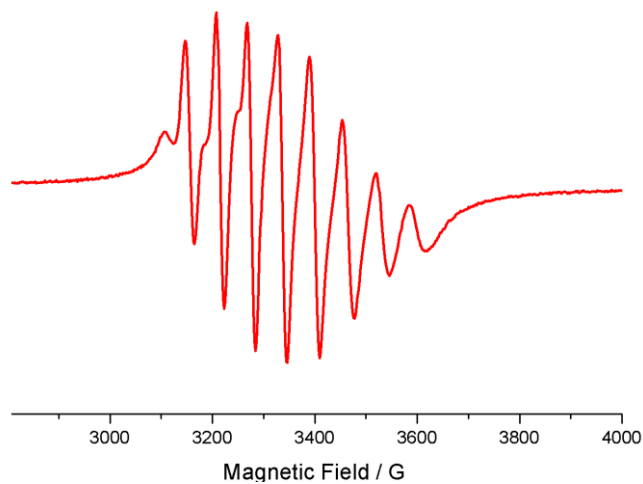
Figure 5.3: X-band EPR spectrum of reaction product between **5.2a** and CpCrH(CO)$_3$ (benzene, 298 K, g = 1.968).

The analogous reaction with the deuterium isotopomer, $Cp(CO)_3Cr–D$,[31, 33] resulted in the formation of Ph_2ND as observed by ^2H NMR spectroscopy, yet we were unable to quantify the exact amount (Figure 5.4). No reaction was observed between any of these HADs and the silane substituted complex, $(Ph_2N)_3V=NSiMe_3$ – the precursor to **5.1**[25] (Scheme 5.2) – after several days at room temperature. Together, these data may support a possible reaction pathway involving the formal transfer of H• to the terminal $P^V=O$ bond with concurrent reduction of V^V to V^{IV}, following a ROA/PCET pathway (Scheme 5.1).[14-16] However, the putative PO–H bond would be incompatible. with the basic Ph_2N^- ligands, resulting in an intramolecular acid-base reaction. DFT calculations (*vide supra*) indicates the BDFE of **2a**-H and **2b**-H in benzene as 52.5 and 57.6 kcal/mol, respectively, which consists with our experimental observations that they only react with very weak HADs, such as $Cp(CO)_3Cr–H$.

126
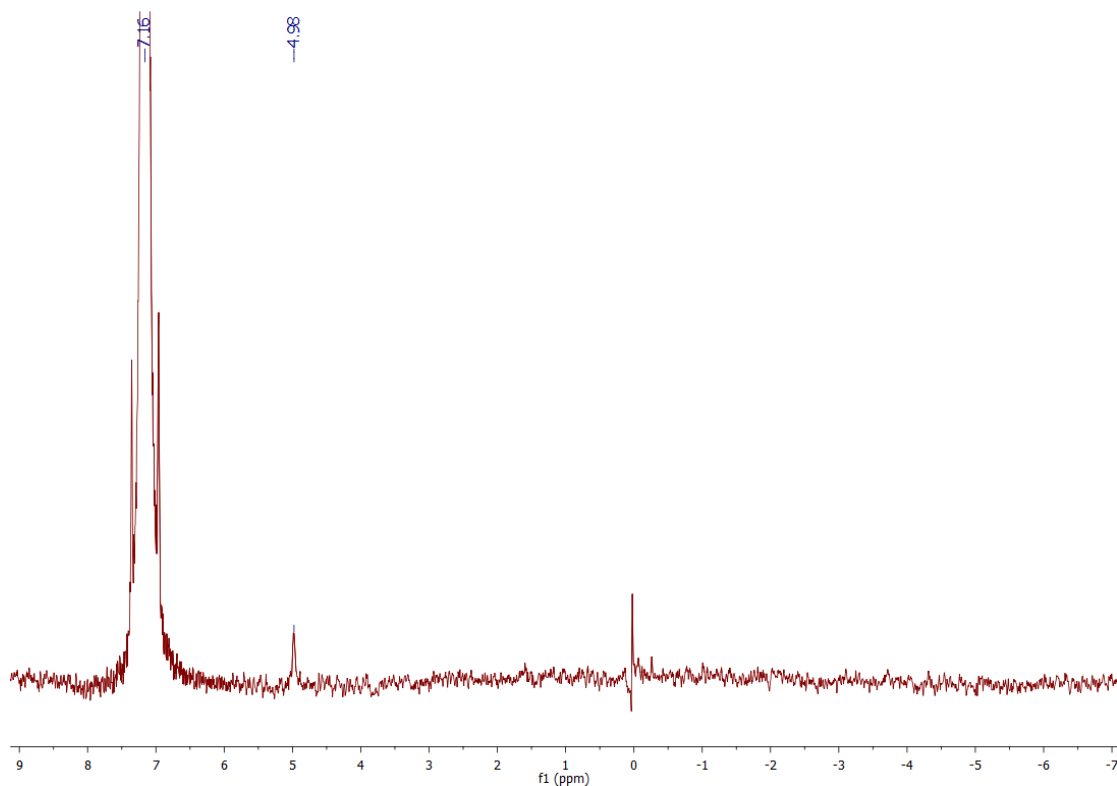
Figure 5.4. ^{2}H NMR motoring of reaction between **5.2a** and CpCrD(CO)$_3$ (400 MHz, C$_6$H$_6$, 25 °C, with two drops of C$_6$D$_6$ as internal standard). The sharp signal at 0 ppm is background signal.

5.2.3 Reactivity of Vanadium(V) phosphinate complexes with a trimethylsilyl-pyrazine reagent

Due to the difficulty in determining the reactive site in **5.2a** with the Cp(CO)$_3$Cr–H HAD, we explored whether TMS• could be used as a "bulky hydrogen atom" surrogate, generating more stable, isolable products. We used the anti-aromatic 1,4-bis(trimethylsilyl)-pyrazine (TMS$_2$-pyz) compound as our TMS• source.[34-35] Mashima and co-workers have recently demonstrated the salt-free reduction of transition metal chloride complexes with TMS$_2$-pyz involving the formal transfer of 2 equivalents of TMS•, reduction of the metal centers, as well as production of pyrazine and 2 equivalents of TMSCl.[36-38] Exposure of 2 equivalents of **5.2a** or **5.2b** to an equivalent of TMS$_2$-pyz resulted in the formation of pyrazine and the disappearance of the diamagnetic resonances for **5.2a** and **5.2b** as observed by multi-nuclear (^{51}V, ^{31}P, ^{19}F, ^{1}H) NMR spectroscopy. Single crystals suitable for XRD studies were grown for both reactions and the solid-state structures confirmed the formation of the reduced, silylated products, (Ph$_2$N)$_3$V^{IV}-N=P(OTMS)Ar$_2$ (Scheme 5.4) (**5.3a**, Ar = C$_6$F$_5$, Figure 5.5a; **5.3b**, Ar = Ph, Figure 5.5b).

Scheme 5.4: Reaction of **5.2a** or **5.2b** with TMS$_2$-pyz to generate **5.3a** or **5.3b**.
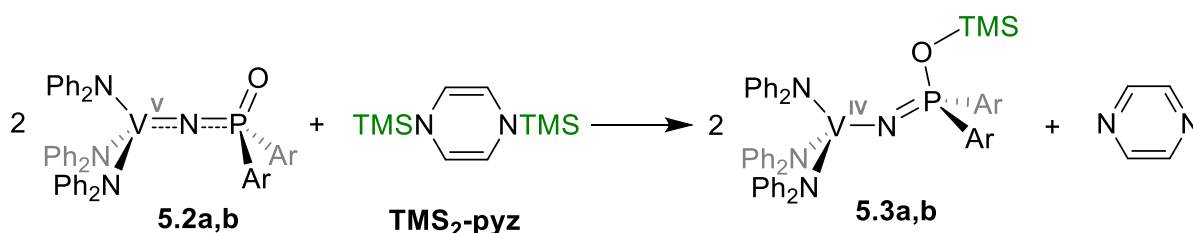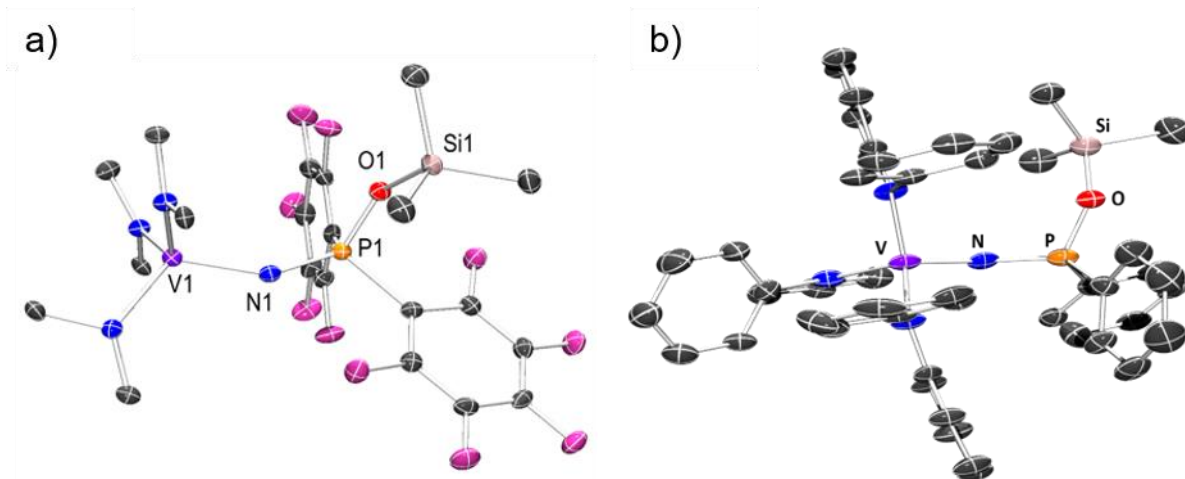
Figure 5.5: a) Solid state XRD structure of **5.3a** (C, black; N, blue; V, purple; P, orange; O, red; F, violet; Si, pink). Phenyl groups (excluding *ipso* carbons), and hydrogen atoms are omitted for clarity. b) Solid state XRD structure of **5.3b** with hydrogen atoms are omitted for clarity

In contrast to **5.2a**, **5.3a** contains a single V1–N1 (1.837(2) Å) bond and a P1–N1 double bond (1.535(2) Å), with a resulting bent V1–N1–P1 angle (145.90(13)°). The P1–O1 bond is also elongated (1.5637(16) Å) relative to **5.2a** (1.484(8) Å) consistent with more single bond character.[39] Similar bond metric differences are observed between **5.2b** and **5.3b** (Tables 5.1 and 5.2). Based on these new bond metrics, the π-delocalization of the V-N-P bond has clearly been shifted to follow more single and double bond characteristics. X-band EPR spectra in THF were collected for **5.3a** and **5.3b** and both contain similar spectral features, including expected 8-line splitting patterns at room temperature due to hyperfine coupling of the d^1 electron to the ^{51}V center ($I = 7/2$, ~100% abundance). Modelling these, as well as the anisotropic 100 K spectra, suggest that the

single unpaired electron is minimally delocalized and rests primarily at the V center (Figures 5.6-5.7).
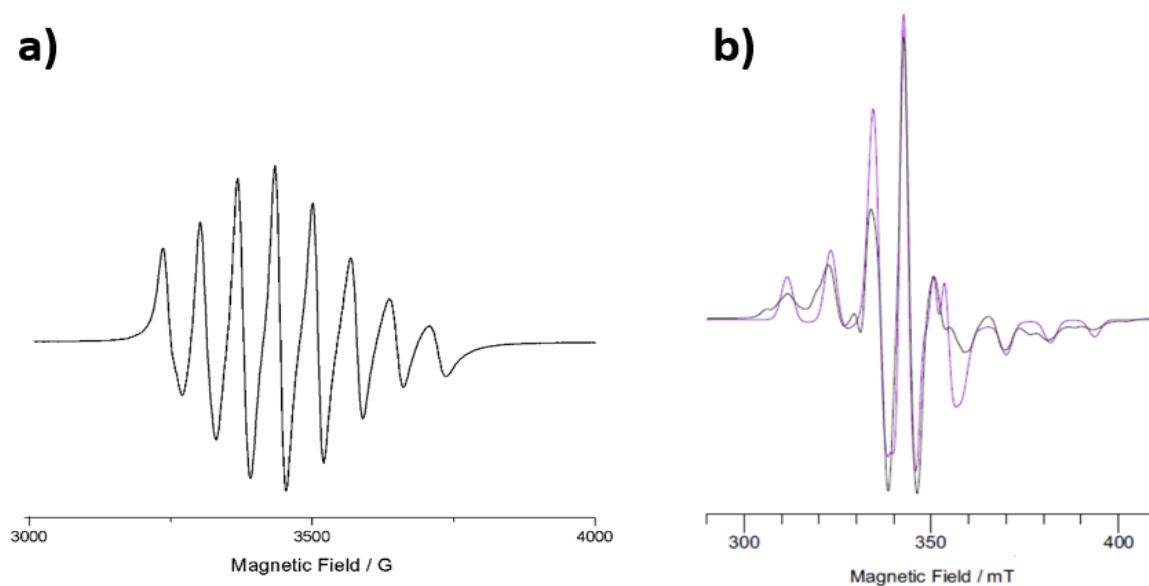
Figure 5.6: X-band EPR spectrum of **5.3a** (THF, 100 K). The experimental trace is in black and the simulation is in purple. Simulation parameters: g = [1.987, 1.987, 1.947], $A(^{51}V)$ = [70, 70, 320] MHz, W (Gaussian, hwhm) = 40, 40, 50 MHz.
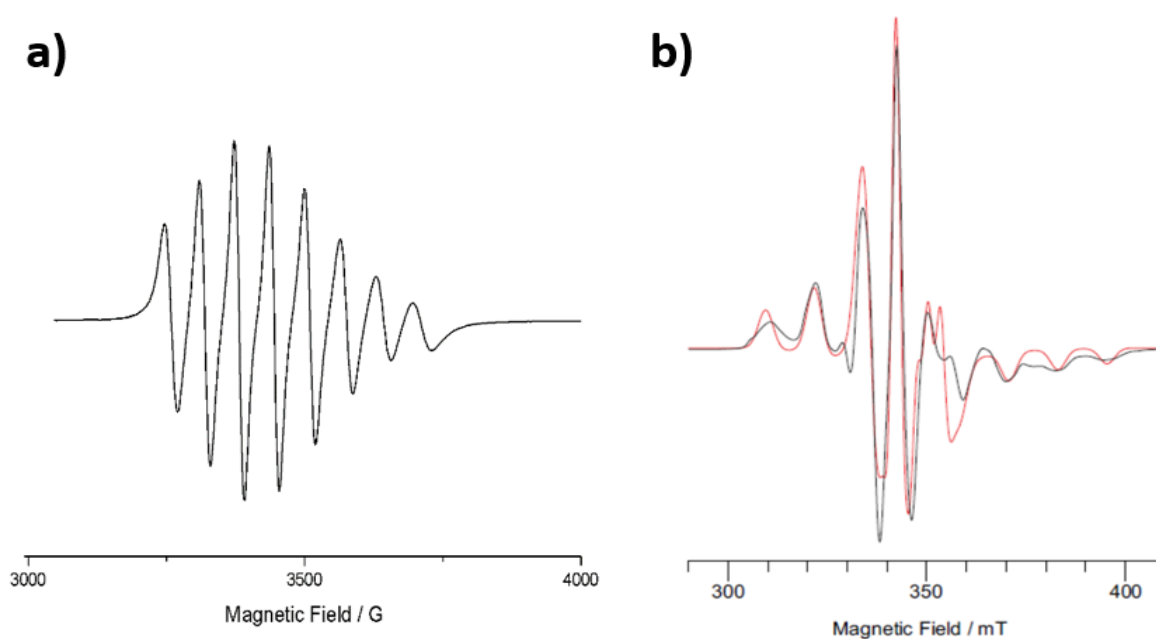
Figure 5.7: X-band EPR spectrum of **5.3b** (THF, 100 K). The experimental trace is in black and the simulation is in purple. Simulation parameters: g = [1.987, 1.987, 1.947], $A(^{51}V)$ = [70, 70, 335] MHz, W (Gaussian, hwhm) = 40, 40, 60 MHz..

5.2.4 Probing the mechanism of TMS• transfer and isolation of stepwise intermediates

The formal transfer of TMS• from TMS_2-pyz to **5.2** generating **5.3** represents what we believe is the clearest example yet of reactivity at a terminal P^V=O bond mimicking the proposed ROA/PCET mechanism (Scheme 5.1). We next wanted to probe the mechanism of this transformation. For PCET processes, distinguishing concerted (ex. H• or H^+/e^- transfer) from stepwise (ex. PT + ET) processes is performed by comparing the thermochemical values of the stepwise ground state free energy changes, $\Delta G°_{ET}$ and $\Delta G°_{PT}$, to the reaction free energy barrier, $\Delta G^{\ddagger}$. A concerted process is assumed when $\Delta G^{\ddagger}$ is lower than both stepwise free energy change values.[17, 42] In order to elucidate the mechanism of the transformation from **5.2** to **5.3**, we employed a similar strategy of dissecting and studying the individual steps of ET and silylium transfer (ST) as part of a square scheme (Scheme 5.5).[17] To distinguish a concerted from a stepwise process, the thermodynamic parameters $\Delta G°_{ST}$ (**5.2**→**5.2-Si$^+$**), $\Delta G°_{ET}$ (**5.2**→**5.2$^-$**), and $\Delta G^{\ddagger}$ are required (Scheme 5.5, Eqs. 1-2).[17] We sought to determine approximate values for these parameters by combining experimental and computational results.

$\Delta G°_{ST} = -RT \ln(K_{rel})$

(1)

$\Delta G°_{ST} = -1.37(kcal•mol^{-1})$ x [pK(**5.2-Si$^+$**) - pK(TMS_2-pyz)]

$\Delta G^\circ_{ET} = -FE^\circ$

(2)

$\Delta G^\circ_{ET} = -23.06(\text{kcal}\bullet\text{mol}^{-1}\bullet\text{V}^{-1}) \times [E^\circ(\mathbf{5.2}^{0/-}) - E^\circ(\text{TMS}_2\text{-pyz}^{+/0})]$

Scheme 5.5: Square scheme for the stepwise conversion of **5.2** to **5.3** via ST + ET or ET + ST pathways
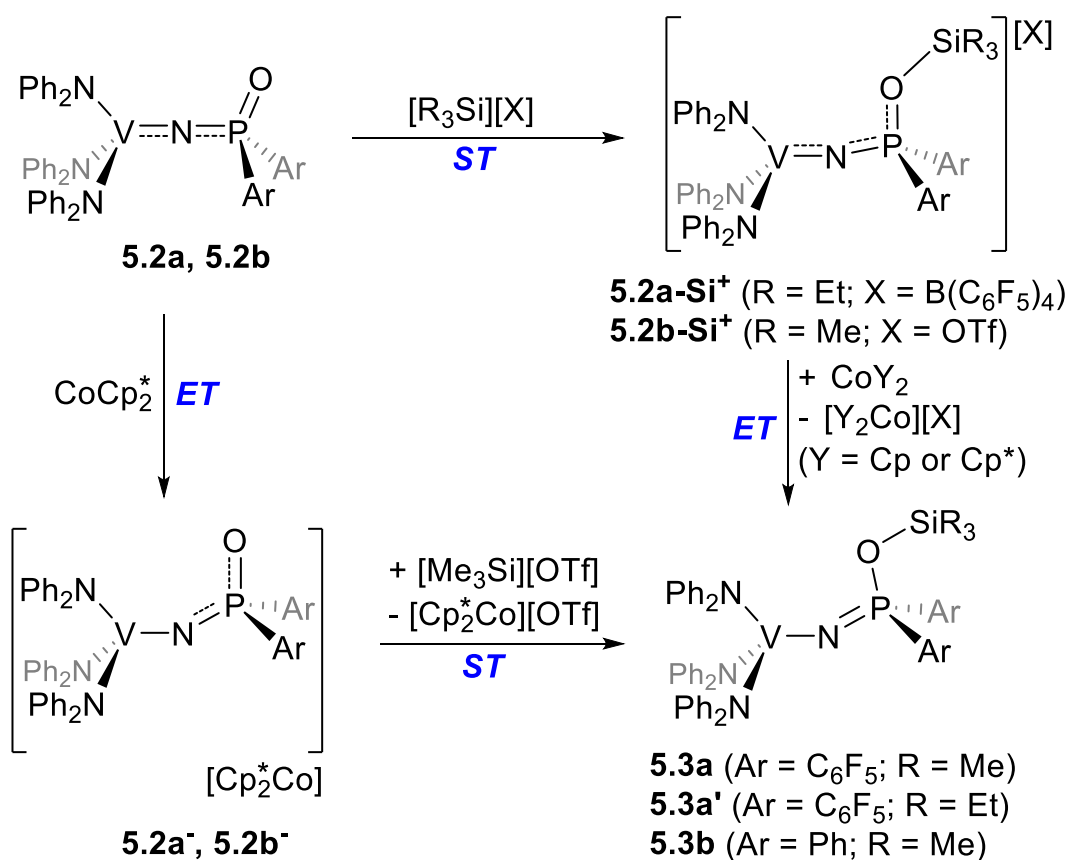
Initial ST was first investigated (Scheme 5.5). Exposure of **5.2a** and **5.2b** to one equivalent of [TMS][OTf] resulted in a reaction only with **5.2b** (OTf = -OSO$_2$CF$_3$ = triflate).[43] The new complex (**5.2b-Si⁺**) was isolated and fully characterized. The ^{51}V NMR

spectra revealed a significantly downfield shifted resonance at 229 ppm vs. -6 ppm for **5.2b**. However, the ^{31}P NMR signal did not seem to shift much in reference to **5.2b**. The solid state XRD structure (Figure 5.8) revealed a near-linear V1–N1–P1 linkage in **5.2b-Si⁺** (174.3(10)°) similar to **5.2b** (173.1(5)°, Table 5.2), but the P=O bond was clearly elongated (1.560(13) Å) compared to **5.2b** (1.482(6) Å) indicating more single bond character. Likewise, the vanadium-nitrogen bond was slightly elongated and the nitrogen-phosphorus bond was slightly contracted (Table 5.2).
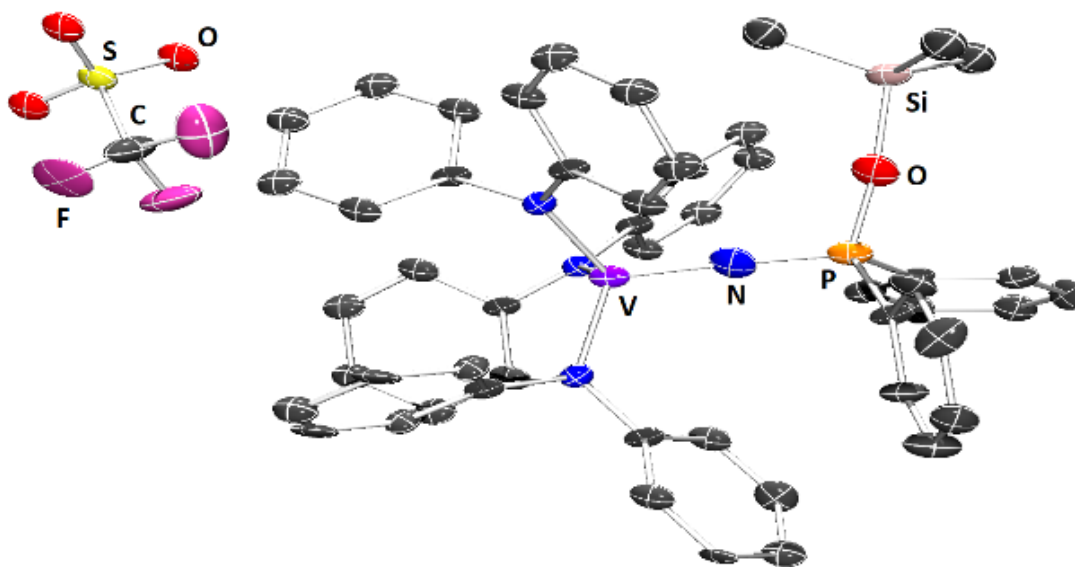
Figure 5.8: Solid-state molecular structure of **5.2b-Si⁺** with ellipsoids set at 30% probability level. Hydrogen atoms and co-crystallized solvent are omitted for clarity.

The unreactivity of **5.2a** with an equivalent of [TMS][OTf] is likely the result of its poor Lewis basicity (*vide infra*) compared to **5.2b** owing to the electron withdrawing aryl groups. However, silylation was possible using the silylium cation, $[Et_3Si][B(C_6F_5)_4]$.[44] Upon addition of one equivalent of $[Et_3Si][B(C_6F_5)_4]$ to **5.2a**, a new complex (**5.2a-Si⁺**)

was isolated as a dark green solid and fully characterized, including by XRD studies. The solid state molecular structure revealed the expected P-O–SiEt$_3$ linkage and corresponding [B(C$_6$F$_5$)$_4$]$^-$ counter-anion (Figure 5.9). Bond metrics are also similar to those found in **5.2a** (Table 5.1), and follow the same trends as described for the silylation of **5.2b**. The ^{51}V NMR signal was significantly shifted downfield to 520 ppm compared to **5.2a**, and displayed a 1:1 doublet, most likely the result of long-range coupling to the S = ½ phosphorus. The ^{31}P NMR consisted of a very broad singlet (owing to the S = 7/2 nuclear sping of V^V).
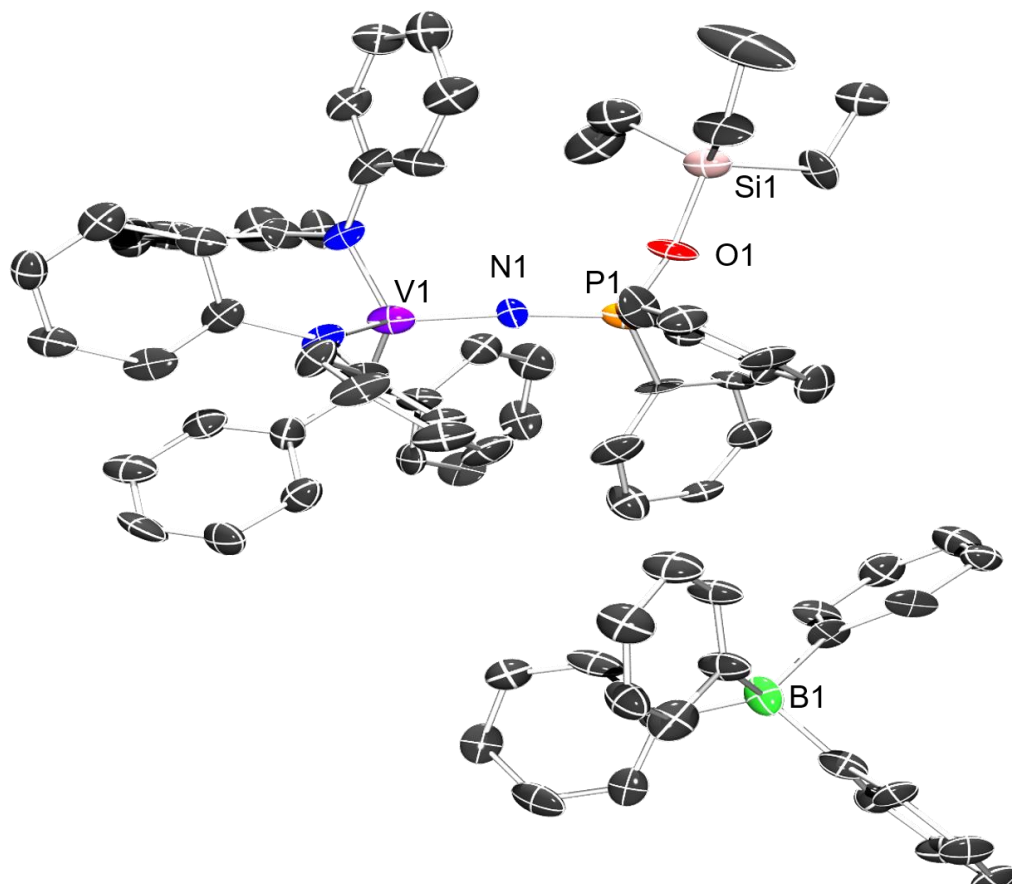
Figure 5.9: Solid state molecular structure of **5.2a-Si$^+$** with ellipsoids set at 30%

133

probability level. Hydrogen atoms and co-crystallized solvent are omitted for clarity.

Both complexes (**5.2a/b-Si$^+$**) could be readily reduced with CoCp$_2$ or CoCp*$_2$ (Cp* = μ^5-C$_5$Me$_5$) generating **5.3a'** (where R = Et) or **5.3b** (Scheme 5.5), respectively, and closing the ST + ET pathways. The formation of both products was confirmed by EPR spectroscopy (Figures S27-S28). We found that the relative weaker reductant Cp$_2$Co (compared with Cp*$_2$Co) can sufficiently reduce **5.2a-Si$^+$**, resulting in a dark brown product. Upon work-up, the ^{1}H, ^{31}P, ^{19}F and ^{51}V NMR spectra displayed completely silent resonances indicating complete conversion of **5.2a**. Additionally, the EPR spectra displayed a nearly identical spectrum to that of isolated **5.3a** confirming the completion of the square scheme (Figure 5.10a). In a similar manner, the relatively stronger reductant Cp*$_2$Co could reduce **5.2b-Si$^+$**, resulting in a dark brown product. The NMR spectra were also silent and the EPR spectra displayed a nearly identical spectrum to that of **5.3** (Figure 5.10b).

Figure 5.10: X-band EPR spectrum of **5.3b** (isolated from the reaction between **5.2b** and 1,4-bis(trimethylsilyl)-1,4-diaza-2,5-cyclohexadiene, red trace) and **5.3b** (isolated from the reaction between **5.2b-Si$^+$** and Cp$_2^*$Co, blue trace) in THF at 100 K. The EPR spectra for both reactions pathways display the same product.

To obtain estimated $\Delta G°_{ST}$ values (Eq. 1), relative pK values for **5.2a-Si$^+$** and **5.2b-Si$^+$** were needed. We define pK as the extent of TMS$^+$ dissociation from the Lewis basic (LB) P=O bonds (Scheme 5.6), in analogy to Brønsted acids (K_{rel} is the equilibrium constant relative to an arbitrary LB'). Previously reported K_{rel} values – determined by NMR spectroscopy and set against N-methylpyridone (NMP) as LB' (Eq. 3) – for pyridine (pyr), triphenylphosphine oxide (TPPO), and hexamethylphosphoramide (HMPA) were 10, $9.1 \cdot 10^{-2}$, and $1.0 \cdot 10^{-4}$, respectively, in dichloromethane (DCM).[45] The corresponding pK^{DCM} values for the LB-TMS$^+$ cations are: -1.0 (pyr), 1.04 (TPPO), and 4.00 (HMPA), consistent with an expected, more highly Lewis basic HMPA vs. TPPO and pyr.

Scheme 5.6: Extent of TMS$^+$ dissociation from the Lewis basic P^V=O bonds

$$\text{LB-TMS}^+ + \text{LB'} \underset{}{\overset{K_{rel}}{\rightleftharpoons}} \text{LB} + \text{LB'-TMS}^+$$
$$\textbf{(5.2a/b-Si}^+\textbf{)} \qquad\qquad \textbf{(5.2a/b)}$$

We performed similar competition reactions[45] and monitored each by NMR spectroscopy (^{31}P, ^{51}V). Exposing **5.2a** to a 1:1 ratio of [TPPO-TMS][OTf][46] (Scheme 5.7) in DCM revealed a broadened ^{51}V NMR resonance centered around **5.2a** (125 ppm, Figure 5.11), with a corresponding ^{31}P NMR spectrum that also displayed a broadened resonance

135

centered around [TPPO-TMS][OTf] (52 ppm, Figure 5.12). Taken together, the competition reaction data indicates that only a negligible amount of **5.2a** has been transformed to **[5.2a-Si⁺][OTf]** in the presence of [TPPO-TMS][OTf]. Thus, the phosphoryl group in TPPO is more basic than that in **5.2a**, and the equilibrium lies to the left.

Scheme 5.7: Competition reactions between **5.2a/5.2b** and [TPPO(OSiMe₃)][OTf] (1:1).

5.2a/b

[5.2a-Si⁺][OTf]/[5.2b-Si⁺][OTf]
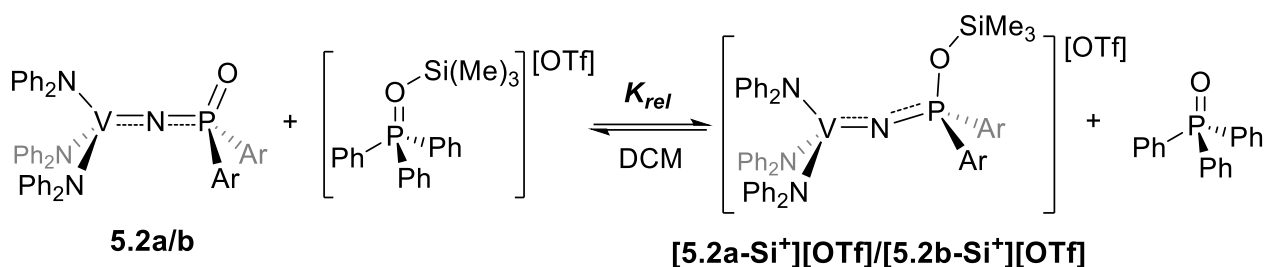
On the other hand, exposing **5.2b** to a 1:1 ratio of [TPPO-TMS][OTf][46] (Scheme 5.7) in DCM revealed a significantly shifted ^{51}V broad signal at 250 ppm (Figure 5.13) consistent with the formation of **5.2b-Si⁺**, and no appreciable signal for **5.2b** (-6 ppm). The ^{31}P NMR showed a broad signal (32.6 ppm) that lies between the ^{31}P NMR (Figure 5.14) of free TPPO (25 ppm) and [Me₃Si(Ph₃PO)][OTf] (52 ppm). Taken together, the data suggests that the phosphoryl group in TPPO is less basic that that in complex **5.2b** and the equilibrium favors the rights side of the reaction (Scheme 5.7). A relative Lewis basicity of **2a** < TPPO < **2b** can be established.
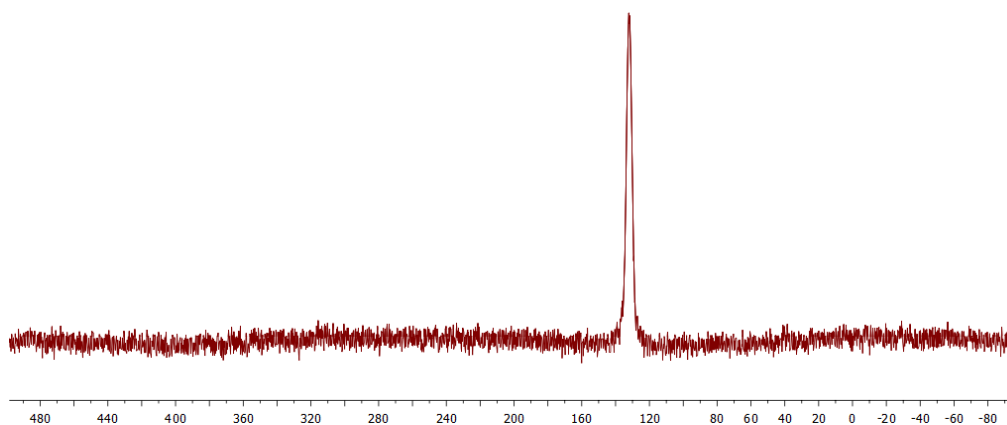
Figure 5.11: ^{51}V NMR spectrum of the mixture of **5.2a:**[Ph$_3$P(OSiMe$_3$)][OTf] (1:1)
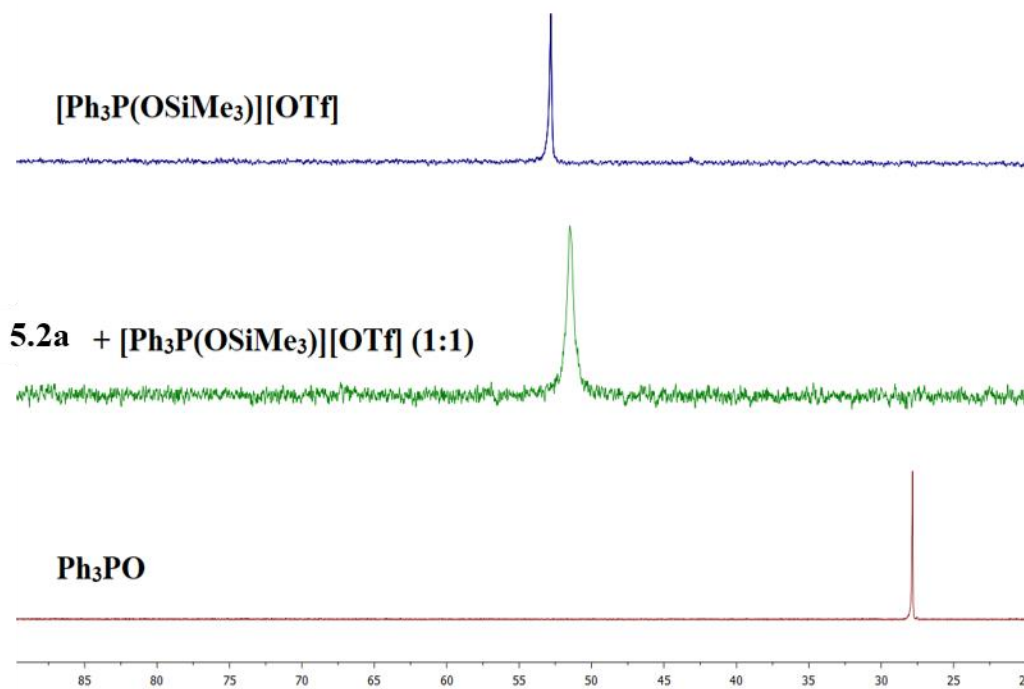
Figure 5.12: ^{31}P NMR spectrum of the mixture of **5.2a**:[TPPO(OSiMe$_3$)][OTf] (1:1) in comparison with that of [TPPO(OSiMe$_3$)][OTf] (top) and TPPO (bottom).
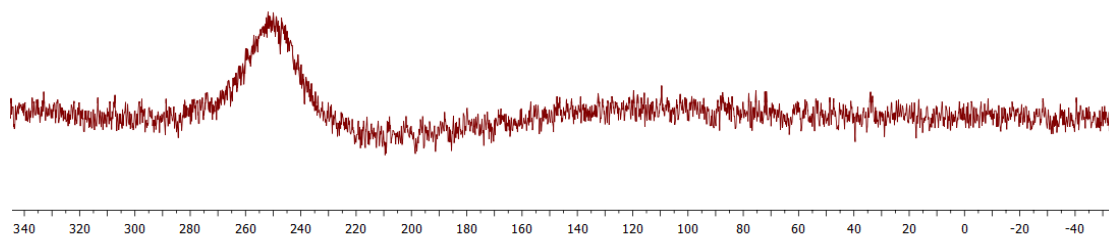
Figure 5.13: ^{51}V NMR spectrum of the mixture of **5.2b:**[Ph$_3$P(OSiMe$_3$)][OTf] (1:1)
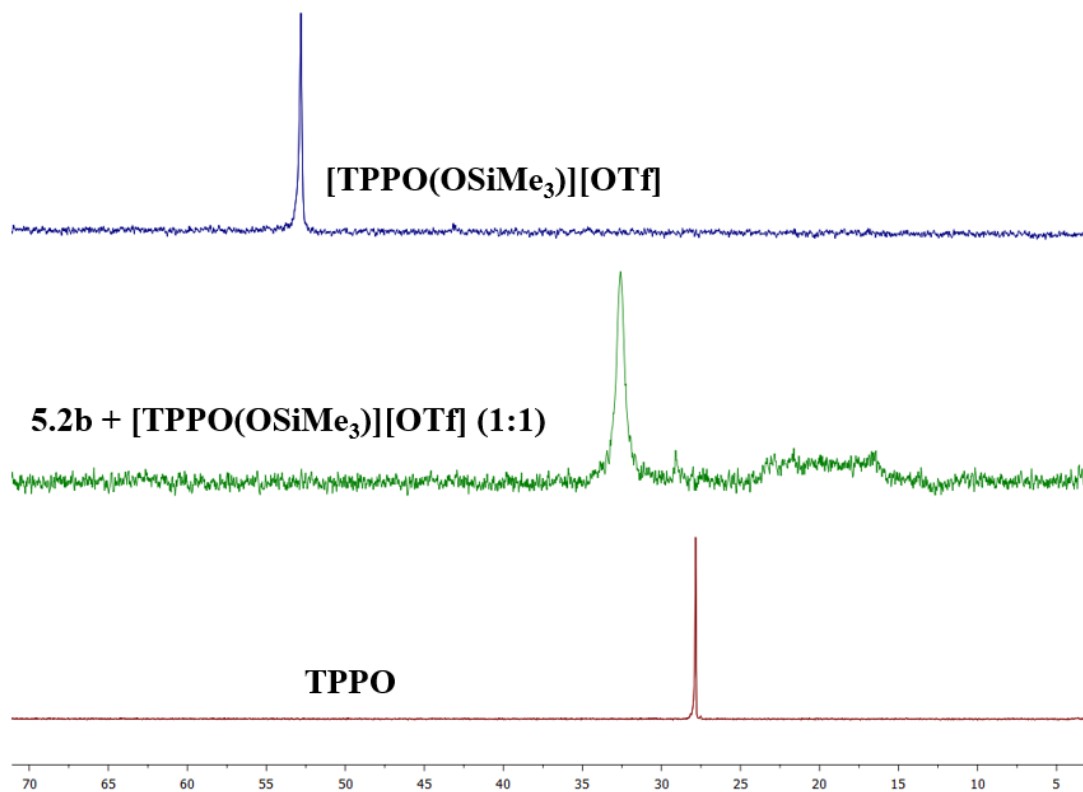
Figure 5.14: ^{31}P NMR spectrum of the mixture of **5.2b**:[TPPO(OSiMe$_3$)][OTf] (1:1) in comparison with that of [TPPO(OSiMe$_3$)][OTf] (top) and TPPO (bottom).

To bracket an upper basicity limit for **5.2b**, we exposed **5.2b-Si$^+$** to a stronger Lewis base, HMPA. Mixing **5.2b-Si$^+$** with a 1:1 ratio of HMPA in DCM and monitoring by ^{51}V

and ^{31}P NMR revealed a broad [51]V signal centered around **5.2b** and [HMPA-TMS]$^+$ with the latter confirmed by *in situ* generation of [HMPA-TMS][OTf] (Figure 5.15). This showed that the silyl cation migrates from **5.2b** to the stronger Lewis base HMPA. We also note that no reaction occurred between HMPA and TMS$_2$-pyz as observed by ^{1}H and ^{31}P NMR spectroscopy.
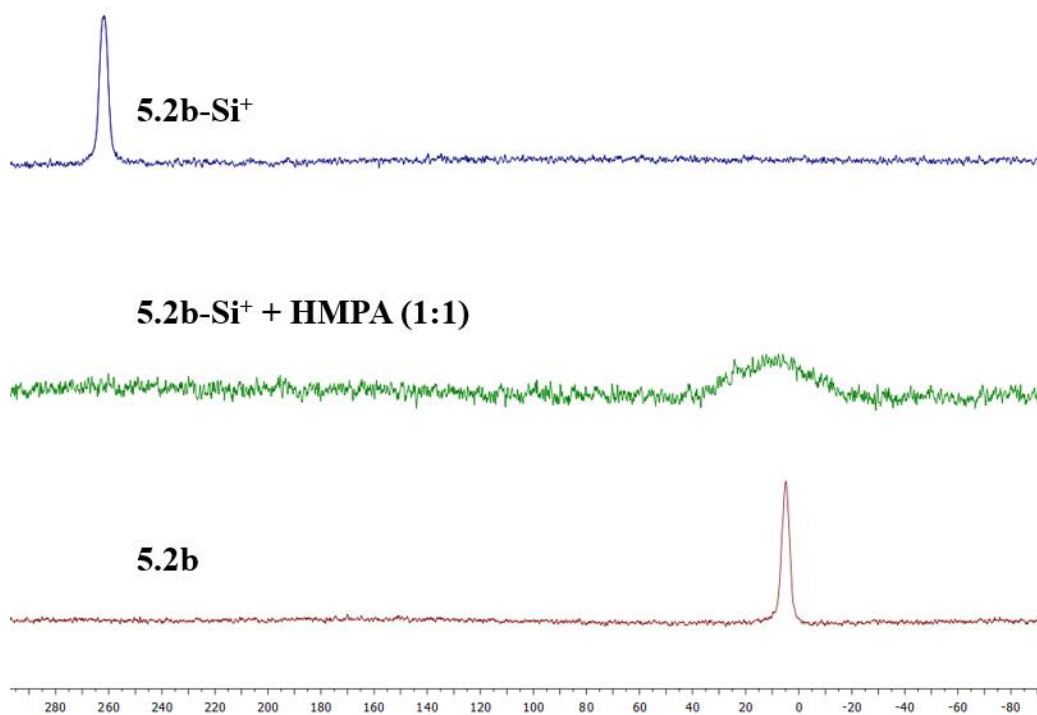
Figure 5.15: ^{31}P NMR spectrum of the mixture of **5.2b-Si**$^+$: HMPA (1:1) in comparison with that of **5.2b-Si**$^+$(top) and **5.2** (bottom).

Lastly, to bracket an upper basicity limit for **5.2a**, we exposed **5.2a-Si**$^+$ to an equivalent of pyridine, which is a weaker Lewis base than TPPO. The reaction was once again monitored by NMR, and in this case, **5.2a** was regenerated, showing migration of the silyl cation to the pyridine base. Together, an overall basicity trend of **5.2a** < pyr < TPPO

< **5.2b** < HMPA < [TMS-pyz]⁻ is assigned with corresponding experimentally bracketed pK^{DCM} values of **5.2a-Si⁺** < -1.0 and 1.04 < **5.2b-Si⁺** < 4.00.[45] A conservative *minimum* experimental $\Delta G°_{ST}$ value of ~7 kcal/mol was extracted based on the bracketed relative pK values of < -1 for **2a-Si⁺** and > 4 for TMS₂-pyz (Eq. 1). A similar approach could not be used for **2b-Si⁺** due to the possible (yet unlikely) overlapping experimental pK values for **2b-Si⁺** (1.04-4.00) and TMS₂-pyz (> 4).

We note that the above $\Delta G°_{ST}$ for **5.2a** (7 kcal/mol) is an *extremely* conservative estimate due to very few published K_{rel} values for TMS⁺ equilibria, and our analysis would benefit from studying K_{rel} values of more Lewis bases.[45] In an attempt to extract more precise values, we turned to density functional theory (DFT). Calculations were performed using the uwB97XD method,[47-48] with Ahlrichs' def2-SVPP basis set,[49] and with the relativistic effect of V, which was accounted for by the Stuttgart-Dresden effective core potential.[50] We also used the polarizable continuum model (PCM) to calculate the systems in DCM.[51-52] Initial ST involving **5.2a/b** + TMS₂-pyz → **5.2a/b-Si⁺** + TMS-pyz⁻ was calculated and extracted $\Delta G°_{ST}$ values were 64.81 kcal/mol (**5.2a**, Figure 5.16, blue) and 52.90 kcal/mol (**5.2b**, Figure 5.16, orange), much higher than the experimental minimum (7 kcal/mol). These results are consistent with the observed increased basicity from **5.2a** to **5.2b**, reflected by a calculated pK difference of ~8.7 units (Eq. 1), and resulting in a lower $\Delta G°_{ST}$. The following ET steps (**5.2a/b-Si⁺** + TMS-pyz⁻ → **5.3a/b** + TMS-pyz•) were calculated to be very downhill at -83.47 kcal/mol (**5.2a**) and -74.81 kcal/mol (**5.2b**), resulting in overall $\Delta G°_{rxn}$ values of -18.66 and -21.91 kcal/mol, respectively (Figure 5.16). Together, these data suggest that a stepwise mechanism involving initial ST is unlikely (Scheme 5.5).
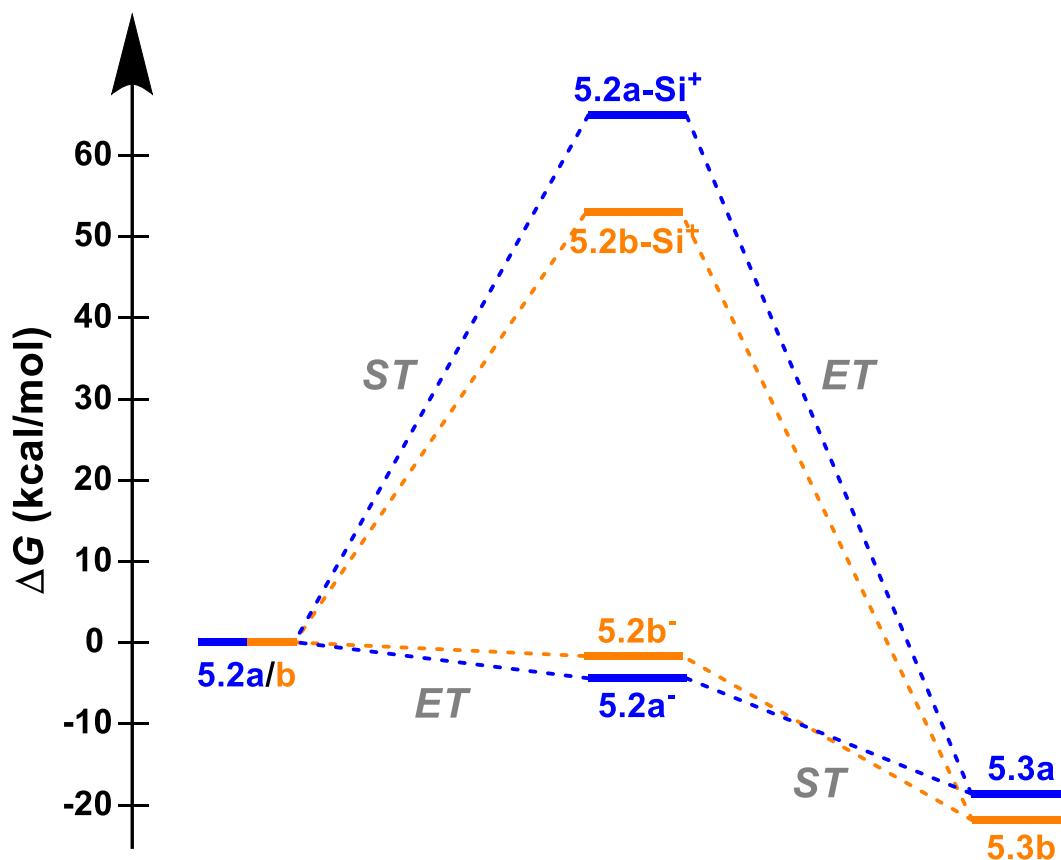
Figure 5.16: DFT calculated reaction coordinates for the stepwise conversion of **5.2a/b** to **5.3a/b** via ST + ET or ET + ST pathways. Gibbs free energies are given in kcal/mol relative to the starting materials.

The alternative stepwise process involving initial ET was also probed experimentally and computationally (Scheme 5.5, Figure 5.16). Both **5.2a** and **5.2b** were analyzed by cyclic voltammetry (CV) in DCM and each revealed quasi-reversible V^{IV}/V^{V} couples at $E_{1/2}$ = -0.99 V and -1.26 V, respectively, versus the ferrocene/ferrocenium (Fc/Fc$^+$) couple (Figure 5.17). The more oxidizing **5.2a** is consistent with the enhanced

electron withdrawing ability of the C_6F_5 substituents, which renders the vanadium metal center comparatively more difficult to reduce.
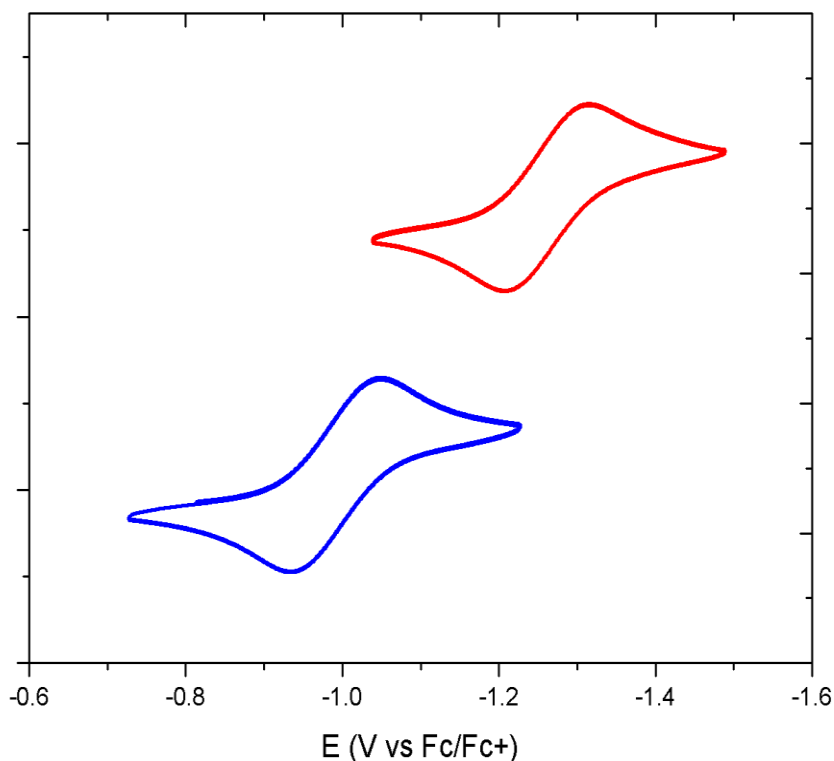
Figure 5.17: CV of **5.2a** (blue trace) and **5.2b** (red trace) in DCM (1.0 mM) with 0.1 M [Bu₄N][PF₆] electrolyte in DCM using a glassy carbon working electrode, platinum wire counter electrode, and Ag/Ag^+ pseudo reference electrode. Scan rate 100 mV/s, referenced to Fc/Fc^+.

Chemical isolation of the reduced forms, **5.2a⁻** and **5.2b⁻**, was possible using $CoCp^*_2$ ($E_{1/2}$ = -1.94 V vs. Fc/Fc^+)[53] (Scheme 5.5). Addition of one equivalent of $CoCp^*_2$ to **5.2a** in fluorobenzene resulted in the precipitation of **5.2a⁻** as a brick red solid which was isolated in 94% yield. Similarly, **5.2b⁻** could be isolated as an orange-red solid in high yield as well (94%). Single crystals were grown by slow vapor diffusion for both compound and

142

they were structurally characterized using XRD (Figures 5.18 a/b). Bond metrics for **5.2a⁻**

revealed a bent V1–N1–P1 (145.3(10)°) fragment similar to **5.3a** (145.90(13)°; Figure 5.5)

and shortened P1–N1 (1.551(14) Å) and P1–O1 (1.455(12) Å) bonds relative to **5.2a** with

similar trends observed in **5.2b⁻** (Table 5.2). Clearly, the reduction of the vanadium center

has an impact of the electron delocalization across the V1-N1-P1 bond as evidenced from

the increase in pyramidalization. While the NMR signals were silent, both complexes were

analyzed by EPR spectroscopy at room temperature and 100 K. The spectra displayed

similar simulation parameters to **5.3a** and **5.3b** (Figures 5.19). The stepwise ET + ST

sequence was closed using [TMS][OTf] (Scheme 5.5). Treatment of **5.2a⁻** or **5.2b⁻** with

[TMS][OTf] cleanly generated the products **5.3a** or **5.3b**, respectively, as confirmed by

EPR spectroscopy following removal of the [Cp*$_2$Co][OTf] by-product. We note that, in

contrast to **5.2a**, **5.2a⁻** reacts with [TMS][OTf] (*vide supra*) consistent with an expected

increase in basicity from **5.2a → 5.2a⁻** upon ET, similar to what is commonly observed in

stepwise ET + PT studies.[42] Therefore, after reduction, the complex becomes more Lewis

basic and capable of undergoing silyl transfer.
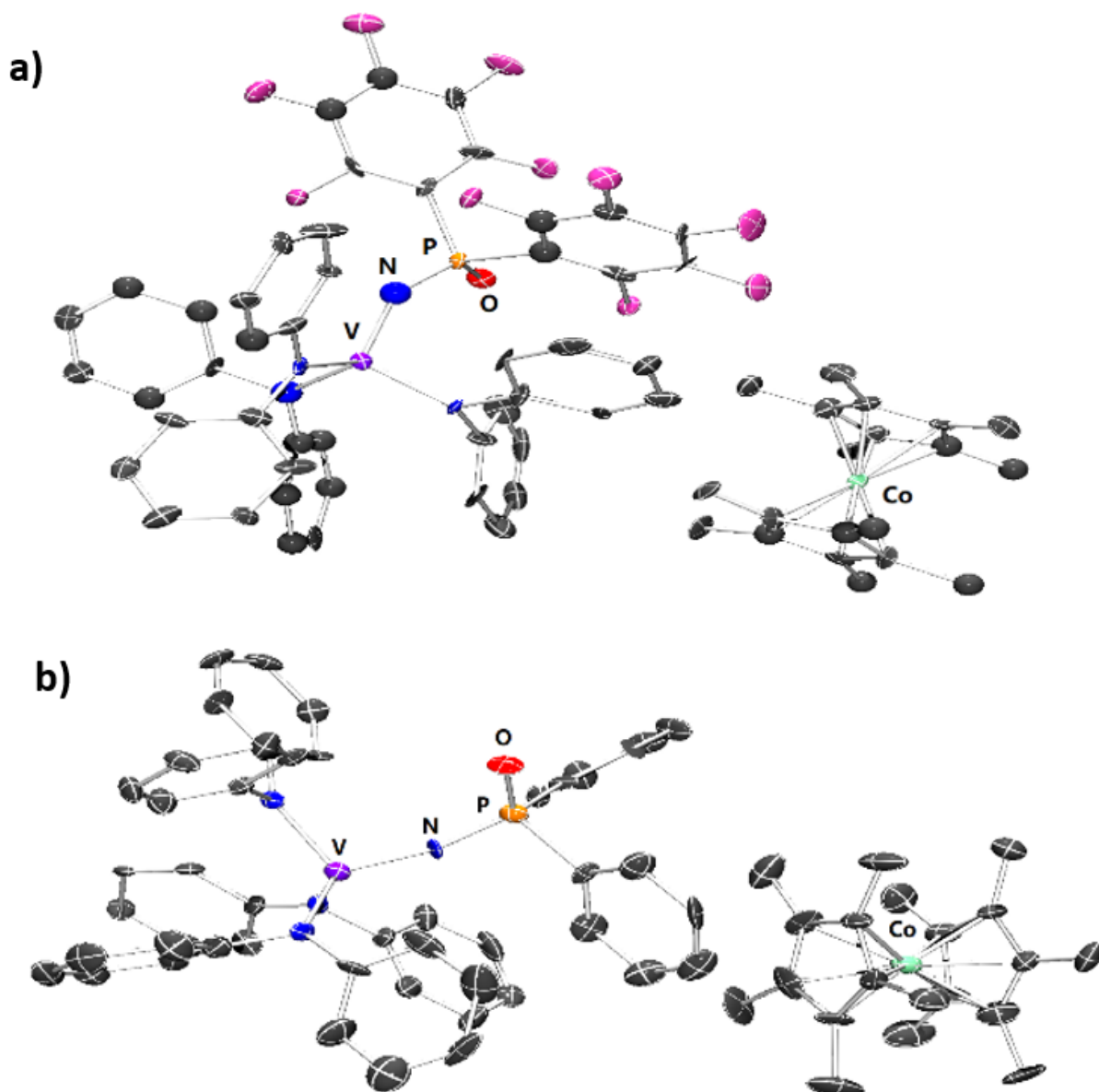
Figure 5.18: a) Solid-state molecular structure of **5.2a⁻**. Hydrogen atoms and co-crystallized solvent are omitted for clarity. b) Solid-state molecular structure of **5.2b⁻** with ellipsoids set at 30% probability level. Hydrogen atoms and co-crystallized solvent are omitted for clarity.
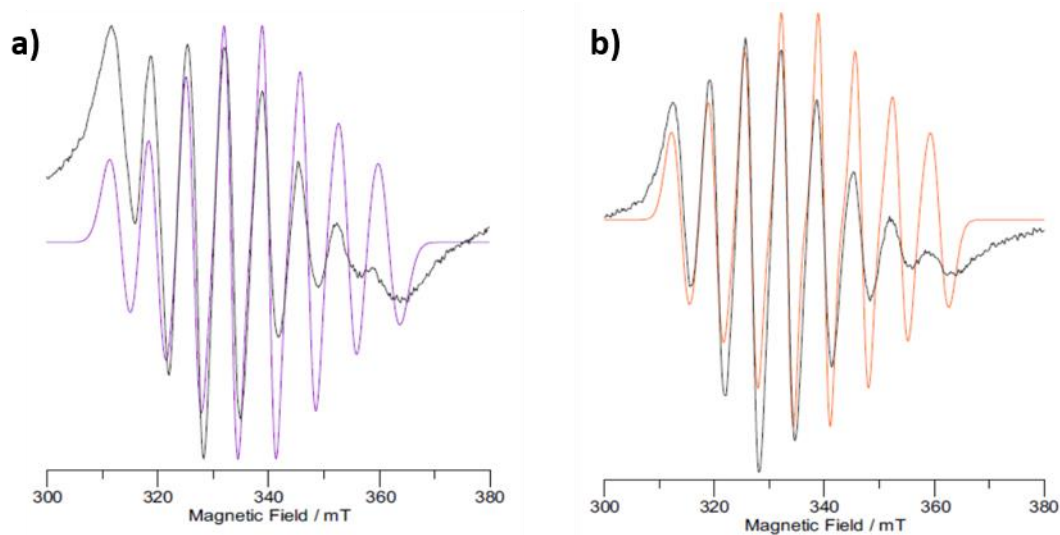
Figure 5.19: a) X-band EPR spectrum of **5.2a⁻** (benzene, 298 K). The experimental trace is in black and the simulation is in purple. Simulation parameters: $g = 1.965$, $A(^{51}V) = 190$ MHz, W (Gaussian, hwhm) = 40 MHz. b) X-band EPR spectrum of **5.2b⁻** (benzene, 298 K). The experimental trace is in black and the simulation is in orange. Simulation parameters: $g = 1.9665$, $A(^{51}V) = 185$ MHz, W (Gaussian, hwhm) = 35 MHz.

Next, experimentally derived $\Delta G°_{ET}$ values could be determined based on the obtained $E_{1/2}$ values for the **5.2⁰ᐟ⁻** couples (Eq. 2). However, we noticed a discrepancy in the reported $E_{1/2}$ of the TMS$_2$-pyz$^{+/0}$ couple ($E_{1/2}$ = -0.24 V vs. Fc/Fc⁺ in DCM).[36] Using analogous conditions, an $E_{1/2}$ = -0.97 V vs. Fc/Fc⁺ was obtained in our hands (Figure 5.20). We further corroborated our value using a different reference, Fe(μ^5-C$_5$Me$_5$)$_2$ (Fc*), and obtained an $E_{1/2}$ = -0.39 V vs. Fc*/Fc*⁺, corresponding to approximately -0.95 V vs. Fc/Fc⁺ (using an $E_{1/2}$ = -0.56 V for Fc*/Fc*⁺ vs. Fc/Fc⁺ in DCM in our hands.[54] Thus, using our $E_{1/2}$ values, rather than those reported by Mashima and co-workers, for **5.2a** (-0.99 V), **5.2b** (-1.26 V), and TMS$_2$-pyz (average of -0.96 V), we calculated experimental $\Delta G°_{ET}$ values

of 0.7 kcal/mol and 6.9 kcal/mol, respectively, for the stepwise ET steps with **5.2a** and **5.2b** (Eq. 2).
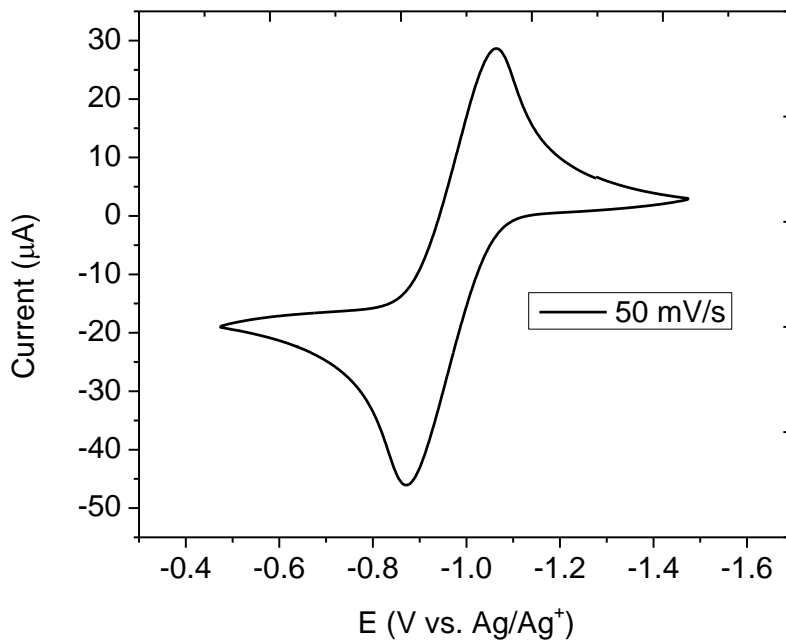
Figure 5.20: CV of 1,4-bis(trimethylsilyl)-1,4-diaza-2,5-cyclohexadiene in DCM (1.0 mM) with 0.1 M [Bu$_4$N][PF$_6$] electrolyte in DCM using a glassy carbon working electrode, platinum wire counter electrode, and Ag/Ag$^+$ wire pseudo reference electrode. Scan rate 50 mV/s, referenced to Fc/Fc$^+$).

The corresponding DFT-calculated values are both slightly exergonic at -4.49 and -1.76 kcal/mol for **5.2a** and **5.2b**, respectively (Figure 5.16). The deviation from experimental values is likely a result of the PCM solvation model which provides only a dielectric continuum and does not consider the solvent's molecular interactions with the calculated molecules. Despite this, the results follow the same trends as the experimental values.

As noted earlier, in the PCET literature, concerted PET processes are assumed when the reaction barrier ($\Delta G^{\ddagger}$) is lower than the stepwise ground state free energy changes, ΔG°_{ET} and ΔG°_{PT} (or ΔG°_{ST} in our case).[17, 42] In an analogous fashion, we attempted to obtain kinetic information by UV-Vis spectroscopy for the **5.2→5.3** transformations; however, our efforts were hampered by several factors. First, the reactions appeared to be very fast, even at the concentrations used (10^{-5} M). Second, while stopped-flow methods were attempted, the absorption spectra of **5.2a/5.3a** and **5.2b/5.3b** revealed no distinct isosbestic points amenable to clean kinetic analyses (Figure 5.21).
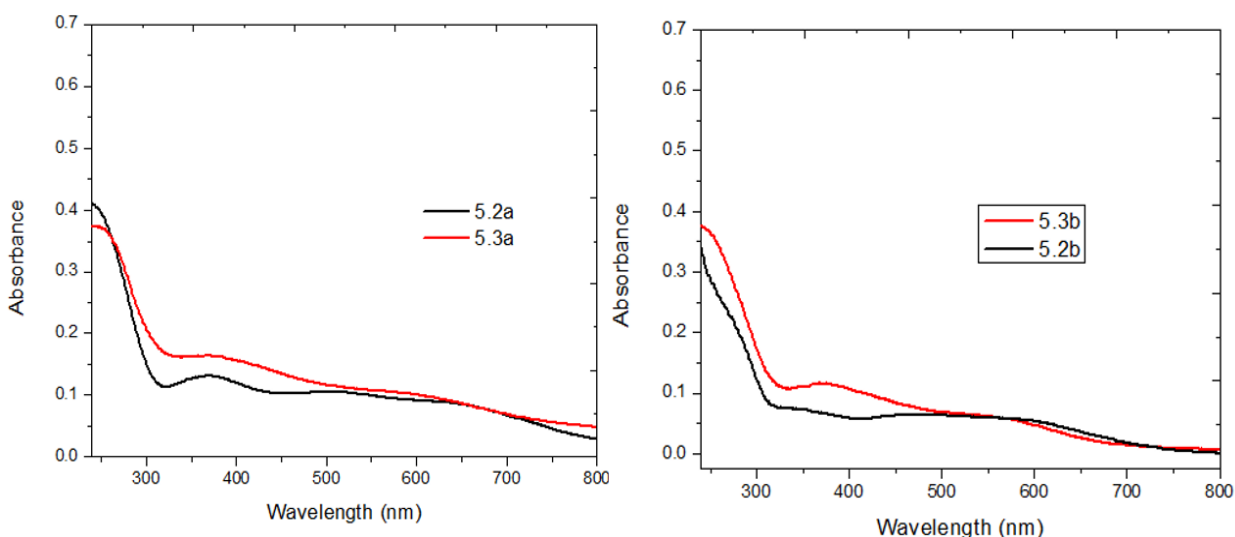
Figure 5.21: UV-Vis spectra of crystalline **5.3a** (left) and **5.3b** (right) in DCM (1×10^{-5} M) and UV-Vis of **5.2a** (left) and **5.2b** (right) in DCM (1×10^{-5} M) overlaid to show the lack of clean isosbestic points.

Moreover, monitoring the reactions over extended periods of time also revealed the emergence of Ph_2NH (Figure 5.22) over several hours, which we ascribe to the introduction of adventitious water, further complicating our kinetic analyses. While we are unable to

obtain experimental $\Delta G^{\ddagger}$ values, our results nonetheless suggest that the stepwise ST + ET mechanism is highly unlikely (Figure 5.16), whereas both stepwise ET + ST or near barrierless concerted EST pathways are possible for the transformations of **5.2→5.3** (Scheme 5.5). The low experimental and computational ΔG°_{ET} values obtained would, however, render it difficult to distinguish between the two.
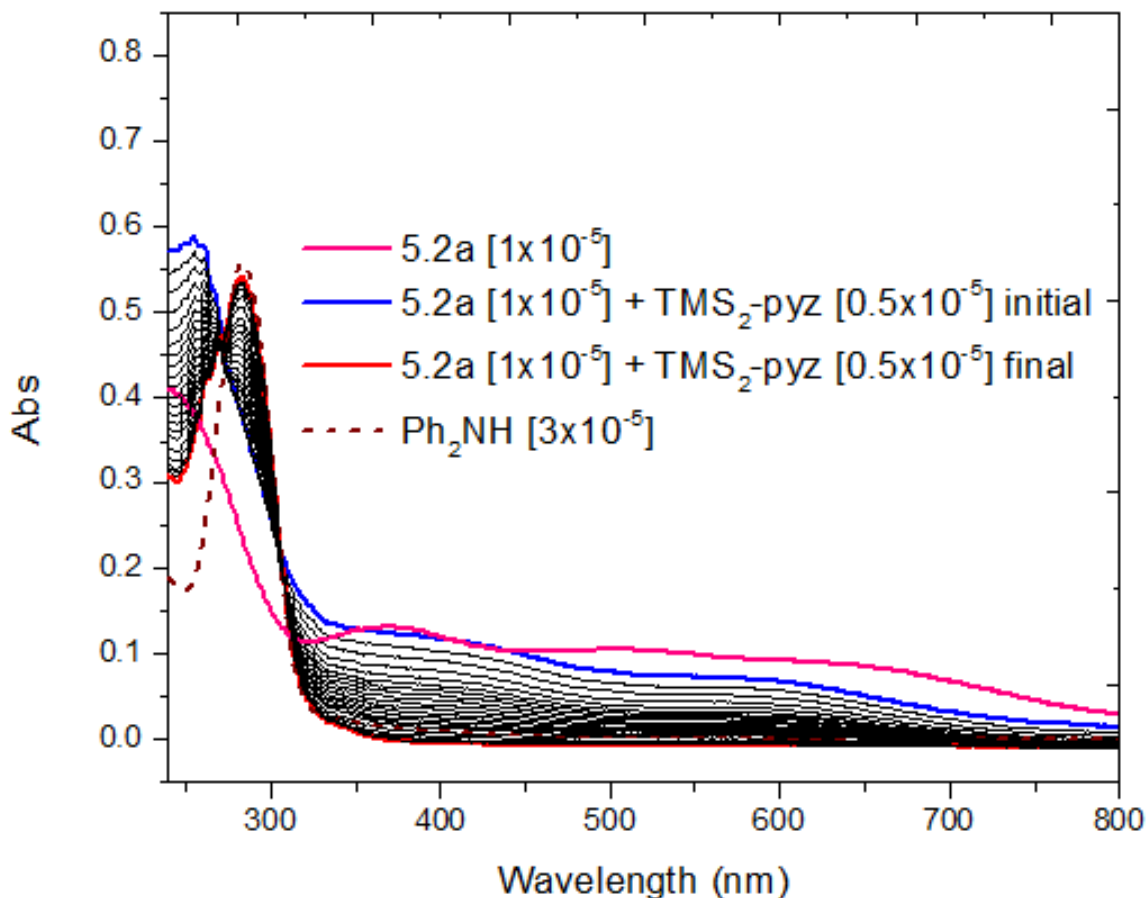
Figure 5.22: UV-Vis spectra of the reaction between **5.2a** (2×10^{-5} M) and TMS$_2$-pyz (1×10^{-5} M) in DCM taken in a J-young capped cuvette. The initial spectrum taken after addition of TMS2-pyz to **5.2a** (blue trace) after approximately 1 minute shows the rapid formation of **5.3a** (see Figure 5.21). However, over 4 hrs. the bands from 320-800 nm slowly decrease while the band at 281 nm increases to give the final spectrum (red trace), consistent with

formation of Ph_2NH (brown dotted trace). This is likely indicative of a slow decomposition pathway perhaps due to adventitious water. The starting material **5.2a** (pink trace) is also shown as a reference.

5.3 Conclusion

In summary, we have demonstrated a clear example of reactivity at a terminal $P^V=O$ bond mimicking the proposed ROA/PCET mechanism for VPO catalysis (Scheme 5.1) using a TMS• donor (TMS_2-pyz) as a "bulky hydrogen atom" surrogate. With the use of a square scheme and resulting experimentally and computationally derived thermochemical values, we have determined that a stepwise ST + ET mechanism is highly unlikely; however, stepwise ET + ST or concerted EST pathways are viable. Together, this study has provided the first experimental evidence supporting a ROA mechanism involving the proposed VPO support-initiated C–H bond functionalization (Scheme 5.1a), and may further benefit future studies in homogeneous or heterogeneous C–H activation chemistry.[55] Moreover, these results have highlighted new main group/transition metal based cooperative redox reactivity which may form the basis for new bond reactivity studies. This, as well as possible applications of TMS• donors as bulky hydrogen atom surrogates, are currently being investigated in our laboratory.

5.4 Experimental Section

5.4.1 General Considerations

All manipulations were performed under an atmosphere of dry, oxygen-free N2 or Ar by means of standard Schlenk or glovebox techniques (MBraun UNIlab Pro SP Eco equipped with a -38 °C freezer). Pentane, toluene, benzene, diethyl ether, tetrahydrofuran (THF), and dichloromethane (DCM) were dried using an MBraun solvent purification system. Benzene-d_6, bromobenzene-d_5, and tetrahydrofuran-d_8 were purchased from Aldrich and dried over CaH_2 for several days prior to distillation. All solvents were degassed by freeze-pump-thaw and stored on activated 4 Å molecular sieves prior to use. Ph_2NH, ^nBuLi (1.6 M in Hexanes), $VCl_3(THF)_3$, Me_3SiN_3, $^iPr_2NH$, Ph_2POCl, $(C_5Me_5)_2Co$, $(C_5H_5)_2Co$, Me_3SiCl, Me_3SiOTf, Et_3SiH, $[Ph_3C][B(C_6F_5)_4]$, and D_2 were purchased from Aldrich, Strem, or other commercial vendors and were used as received. $(C_6F_5)_2POCl$,[26] 1,4-bis(trimethylsilyl)pyrazine (TMS$_2$-pyz),[36] $[Ph_3P(OSiMe_3)][OTf]$,[46] $CpCrH(CO)_3$,[30] $[CpCr(CO)_3]_2$[32] and **5.1**[25] were prepared according to literature procedures. Elemental analyses (C, N, H) were performed at the University of California, Berkeley using a Perkin Elmer 2400 Series II combustion analyzer.

NMR spectra were obtained on a Varian Unity Inova 500 MHz or Agilent Technologies 400 MHz spectrometer, and referenced to residual solvent or externally (^{11}B: $BF_3 \cdot Et_2O$; ^{19}F: $CFCl_3$; ^{51}V: $VOCl_3$; ^{31}P: 85% H_3PO_4). Chemical shifts (δ) are recorded in ppm and the coupling constants are in Hz. X-band EPR spectra were collected on a Bruker EMX EPR Spectrometer equipped with an Oxford ESR 900 liquid helium cryostat. A modulation frequency of 100 kHz was used for all EPR spectra and the data was plotted using SpinCount. EPR simulations used the program QPOWA by Belford and co-workers, as modified by J. Telser.[56] UV-Vis spectroscopy was performed using a Shimadzu UV-2401PC spectrophotometer with quartz cuvettes equipped with air tight J-young adaptors.

Data was collected on a Bruker KAPPA APEX II diffractometer equipped with an APEX II CCD detector using a TRIUMPH monochromator with a Mo Kα X-ray source (α = 0.71073 Å). The crystals were mounted on a cryoloop with Paratone-N oil, and all data were collected at 100(2) K using an Oxford nitrogen gas cryostream system. A hemisphere of data was collected using ω scans with 0.5° frame widths. Data collection and cell parameter determination were conducted using the SMART program. Integration of the data frames and final cell parameter refinement were performed using SAINT software. Absorption correction of the data was carried out using SADABS. Structure determination was done using direct or Patterson methods and difference Fourier techniques. All hydrogen atom positions were idealized and rode on the atom of attachment. Structure solution, refinement, graphics, and creation of publication materials were performed using SHELXTL or OLEX^2.

Cyclic voltammetry was performed on a CH Instruments 630E electrochemical analysis potentiostat, equipped with a 3 mm diameter glassy carbon working electrode, a Ag wire pseudo-reference electrode, and a Pt counter electrode with [Bu$_4$N][PF$_6$] (0.1 M) supporting electrolyte solution in CH$_2$Cl$_2$. The glassy carbon working electrode was cleaned prior to each experiment by polishing with 1, 0.3, 0.05 mm alumina (CH Instruments) in descending order, followed by sonication in distilled water for two minutes. Background scans were conducted for each experiment in a solution containing only electrolyte, and was then subtracted from each experiment. All voltammograms were referenced to the Fc/Fc$^+$ redox couple.

DFT calculations were performed using Gaussian 09.2. Geometry optimization of all the molecules and intermediates were carried out using the wB97XD method with

Ahlrichs' def2-SVP basis set, and with the relativistic effect of iodine, which was accounted for by the Stuttgart-Dresden ECP, implemented in the Gaussian 09 software. The solvation in DCM was calculated using polarizable continuum model (PCM). Thermal energy corrections were extracted from the results of frequency analysis performed at the same level of theory. Frequency analysis of all the molecules and intermediates contained no imaginary frequency showing that these are energy minima.

5.4.2 Synthesis of Compounds

Synthesis of (Ph₂N)₃VNPO(C₆F₅)₂ (5.2a). In the glovebox, a solution of $(C_6F_5)_2POCl$ (208 mg, 0.5 mmol) in 3 mL of benzene was added dropwise to a solution of complex **5.1** (415 mg, 0.5 mmol) in 10 mL of benzene and briefly shaken. The resulting black solution stood at room temperature for 1 h. The LiCl precipitate was removed by filtration over celite using a fine porosity filter and the solvent was then removed *in vacuo*. The black residue was washed with cold pentane (2 x 5 mL) to afford a dark brown solid (400 mg, 0.42 mmol, 84% yield). Dark black crystals suitable for XRD studies were grown by slow vapor diffusion of pentane into a concentrated solution of **5.2a** in diethyl ether at room temperature.

¹H NMR (400 MHz, C_6D_6, 25 °C): δ = 6.84 (m, 24H; *o*-Ar*H* and *m*-Ar*H*), 6.69 (m, 6H; *p*-Ar*H*). **¹³C** (100 MHz, C_6D_6, 25 °C): δ = 154.1, 128.9, 126.0, 123.0 (N*Ph₂*). The signal-to-noise ratio was too low for properly identifying any C_6F_5 ¹³C resonance. **⁵¹V** (105 MHz, C_6D_6, 25 °C): δ = 117.3 (br). **³¹P** (162 MHz, C_6D_6, 25 °C): δ = -20.0 (br m). **¹⁹F** (376 MHz, C_6D_6, 25 °C): δ = -131.6 (br, 4F; *o*-C_6F_5), -148.2 (br, 2F; *p*-C_6F_5), -160.3 (br, 4F; *m*-C_6F_5).

Anal. Calc. for $C_{48}H_{30}F_{10}N_4OPV$: C, 60.64; H, 3.18; N, 5.89. Found: C, 60.64; H, 3.29; N, 5.91.

Synthesis of (Ph₂N)₃VNPOPh₂ (5.2b). In the glovebox, a solution of Ph_2POCl (82.8 mg, 0.35 mmol) in 3 mL of THF was added dropwise to a solution of complex **5.1** (290 mg, 0.35 mmol) in 10 mL of THF and briefly shaken. The resulting black solution stood at room temperature for 1 h before the solvent was removed *in vacuo*. The black residue was extracted into benzene (8 mL) and filtered over a pad of celite. The filtrate solvent was removed *in vacuo* and the residue was recrystallized from ether at -35 °C over 24 h to afford a dark brown solid (260 mg, 0.322 mmol, 92% yield). Dark brown crystals suitable for XRD studies were grown by cooling a concentrated solution of **5.2b** in ether to -35 °C and standing overnight.

¹H NMR (400 MHz, C_6D_6, 25 °C): δ = 7.55 (m, 4H; Ar*H* of Ph_2PO), 7.07-6.97 (m, 6H; Ar*H* of Ph_2PO), 6.94 (d, $^3J_{HH}$ = 8.0 Hz, 12H; *o*-Ar*H* of NPh_2), 6.89 (t, $^3J_{HH}$ = 8.0 Hz, 12H; *m*-Ar*H* of NPh_2), 6.77 (t, $^3J_{HH}$ = 7.2 Hz, 6H; *p*-Ar*H* of NPh_2). **¹³C** (100 MHz, C_6D_6, 25 °C): δ = 154.4 (*Ph₂*N), 135.2 (d, J_{PC} = 124.7 Hz; *Ph₂*P), 132.3 (s; *Ph₂*P), 131.7 (d, J_{PC} = 117.8 Hz; *Ph₂*P), 129.1 (*Ph₂*N), 125.3 (*Ph₂*N), 123.6 (*Ph₂*N). **⁵¹V** (105 MHz, C_6D_6, 25 °C): δ = -6.1 (br). **³¹P** (162 MHz, C_6D_6, 25 °C): δ = 19.9 (br m). **Anal. Calc**. for $C_{48}H_{40}N_4OPV$: C, 74.80; H, 5.23; N, 7.27. Found: C, 74.77; H, 5.14; N, 7.28.

Synthesis of (Ph₂N)₃VNP(OSiMe₃)(C₆F₅)₂ (5.3a).

Method 1. In the glovebox, a solution of **5.2a** (82 mg, 0.086 mmol) in cold toluene (3 mL, -35 °C) was added dropwise to a solution of TMS$_2$-pyz (9.8 mg, 0.043 mmol) in cold toluene (2 mL, -35 °C), and the resulting black solution was kept at -35 °C for 0.5 h. The volatiles were removed *in vacuo* to give a dark brown solid, which was washed with cold pentane (1 mL) to give a dark brown solid (80 mg, 91% yield). Dark red crystals suitable for XRD studies were grown by slow vapor diffusion of pentane into a concentrated solution of **5.3a** in toluene at -35 °C over several days.

Anal. Calc. for C$_{51}$H$_{39}$F$_{10}$OPSiV: C, 59.83; H, 3.84; N, 5.47. Found: C, 59.75; H, 3.66; N, 5.45.

Method 2. In the glovebox, a solution of **5.2a** (47.5 mg, 0.05 mmol) in fluorobenzene (3 mL) was added dropwise to a solution of Cp*$_2$Co (16.5 mg, 0.05 mmol) in fluorobenzene (1 mL). The resulting dark brown solution was stirred using a magnetic stirbar at ambient temperature for 0.5 h. A separate solution of trimethylsilyl trifluoromethanesulfonate (11.1 mg, 0.05 mmol) in fluorobenzene (1 mL) was added dropwise to the reaction solution. The reaction solution turned dark red and was allowed to stir at ambient temperature for another 0.5 h. The volatiles were removed *in vacuo* and the dark brown solid mixture was washed with cold pentane (2 x 2 mL) to afford a dark brown solid. The product was extracted into benzene (2 x 3 mL), filtered over a pad of celite, and the solvent was removed *in vacuo.* The resulting brown solid was washed with cold pentane (2 mL) to give a dark brown powder (44 mg, 0.043 mmol, 86% yield).

Anal. Calc. for C$_{51}$H$_{39}$F$_{10}$OPSiV: C, 59.83; H, 3.84; N, 5.47. Found: C, 59.60; H, 4.00; N, 5.44.

Synthesis of (Ph$_2$N)$_3$VNP(OSiMe$_3$)Ph$_2$ (5.3b).

Method 1. A solution of **5.2b** (81 mg, 0.1 mmol) in cold fluorobenzene (3 mL, -35 °C) was mixed with a solution of TMS$_2$-pyz (11.3 mg, 0.05 mmol) in cold fluorobenzene (1 mL, -35 °C), and the mixed solution was kept at -35 °C for 0.5 h. The volatiles were removed *in vacuo* to give a dark brown greasy solid mixture, which was washed with cold pentane (2 x 2 mL) to give a dark brown solid (45 mg, 0.053 mmol, 53% yield). Dark blue crystals suitable for XRD studies were grown from a concentrated solution of **5.3b** in pentane at -35 °C over several days. Satisfactory elemental analysis could not be obtained from this method due to the contamination of pyrazine.

Method 2. In the glovebox, a solution of **5.2b** (81 mg, 0.1 mmol) in dichloromethane (3 mL) was added dropwise to a solution of Cp*$_2$Co (33 mg, 0.1 mmol) in dichloromethane (1 mL). The resulting dark brown solution was allowed to stir using a magnetic stirbar at ambient temperature for 0.5 h. A separate solution of trimethylsilyl trifluoromethanesulfonate (22.2 mg, 0.1 mmol) in dichloromethane (1 mL) was added dropwise to the reaction solution. The resulting dark red solution was again allowed to stir at ambient temperature for another 0.5 h. The volatiles were removed *in vacuo* to give a dark brown residue, which was washed with cold pentane (2 x 2 mL) to afford a dark brown solid. The product was extracted into ether (2 x 3 mL), filtered over a pad of celite, and then the solvent was removed *in vacuo*. The resulting brown solid was washed with cold pentane (2 mL) to give a fluffy brown powder (48 mg, 0.057 mmol, 57% yield).

Anal. Calc. for C$_{51}$H$_{49}$N$_4$OPSiV: C, 72.58; H, 5.85; N, 6.64. Found: C, 71.47; H, 5.56; N, 6.60. Attempts to obtain satisfactory elemental analysis consistently resulted in reduced carbon percentages likely due to incomplete combustion.[57]

Synthesis of [(Ph₂N)₃VNPO(C₆F₅)₂][Cp*₂Co] (5.2a⁻). In the glovebox, a solution of Cp*₂Co (25.3 mg, 0.0768 mmol) in 2 mL of fluorobenzene was added dropwise to a solution of complex **5.2a** (73 mg, 0.0768 mmol) in 3 mL of fluorobenzene. The resulting dark red solution stood at room temperature for 4 h and the volume was reduced to about 0.5 mL *in vacuo*. Pentane (2 mL) was slowly added dropwise to the concentrated solution to afford an orange-red precipitate. The precipitate was filtered, washed with pentane (5 mL), and dried *in vacuo* to afford an orange-red solid (92 mg, 0.0719 mmol, 94% yield). Dark brown needles suitable for XRD studies were grown by slow diffusion of pentane into a concentrated solution of **5.2a⁻** in fluorobenzene at room temperature.

Anal. Calc. for $C_{68}H_{60}CoF_{10}N_4OPV$: C, 63.80; H, 4.72; N, 4.38. Found: C, 63.56; H, 4.99; N, 4.13.

Synthesis of [(Ph₂N)₃VNPO(C₆H₅)₂][Cp*₂Co] (5.2b⁻). In the glovebox, a solution of Cp*₂Co (24.7 mg, 0.075 mmol) in 2 mL of fluorobenzene was added dropwise to a solution of complex **5.2b** (60.6 mg, 0.075 mmol) in 3 mL of fluorobenzene. The resulting dark red solution stood at room temperature for 3 h and the volume was reduced to about 0.5 mL *in vacuo*. Pentane (2 mL) was slowly added dropwise to the concentrated reaction solution to afford an orange red precipitate. The precipitate was filtered, washed with pentane (5 mL), and dried *in vacuo* to afford an orange-red solid (92 mg, 0.0719 mmol, 94% yield). Dark brown crystals suitable for XRD studies were grown by slow diffusion of pentane into a concentrated solution of **5.2b⁻** in THF at -35 ᵒC. (77 mg, 0.070 mmol, 93% yield).

Anal. Calc. for $C_{68}H_{70}CoN_4OPV$: C, 74.24; H, 6.41; N, 5.09. Found: C, 73.87; H, 6.65; N, 4.94.

Synthesis of $[(Ph_2N)_3VNP(OSiEt_3)(C_6F_5)_2][B(C_6F_5)_4]$ (5.2a-Si⁺). In the glovebox, neat Et_3SiH (1.5 mL, 9.39 mmol) was mixed with $[Ph_3C][B(C_6F_5)_4]$ (46 mg, 0.05 mmol). The reaction mixture was allowed to stir for 12 h and a white precipitate crashed out of solution. The excess silane was decanted, and the white solid was washed with pentane (2 x 4 mL) and dried *in vacuo*. A separate solution of **5.2a** (47 mg, 0.05 mmol) in benzene (3 mL) was added dropwise to the white solid, and the resulting dark green solution was stirred under ambient temperature for 0.5 h. The volatiles were removed *in vacuo* and washed with pentane (2 mL x 2) to afford a green solid (84 mg, 0.048 mmol, 96% yield). Dark green needles suitable for XRD studies were grown by slow diffusion of pentane into a concentrated solution of **5.2a-Si⁺** in dichloromethane at room temperature.

¹H NMR (400 MHz, C_6D_5Br, 25 °C): δ = 7.14-6.92 (m, 30H; *Ph*₂NH), 0.80 (t, $^3J_{HH}$ = 7.2 Hz, 9H; $SiCH_2CH_3$), 0.58 (q, $^3J_{HH}$ = 7.2 Hz, 6H; $SiCH_2CH_3$). **⁵¹V** (105 MHz, C_6D_5Br, 25 °C): δ = 521.0 (d, J = 172.2 Hz). **³¹P** (162 MHz, C_6D_5Br, 25 °C): δ = -21 (br). **¹⁹F** (376 MHz, C_6D_5Br, 25 °C): δ = -129.5 (br, 4F; *o*-P(C_6F_5)₂), -131.8 (br, 8F; *o*-B(C_6F_5)₄), -138.9 (br, 2F; *p*-P(C_6F_5)₂), -155.3 (br, 4F; *m*-P(C_6F_5)₂), -162.5 (br, 4F; *p*-B(C_6F_5)₄), -166.3 (br, 8F; *m*-B(C_6F_5)₄). **¹³C** (100 MHz, C_6D_5Br, 25 °C): δ = 153.8, 129.1, 128.6, 121.4 (N*Ph*₂), 6.1, 5.4 (Si*Et*₃). The signal-to-noise ratio was too low for properly identifying any C_6F_5 ¹³C resonance. **Anal. Calc**. for $C_{78}H_{45}B$ $F_{30}N_4OPSiV$: C, 53.69; H, 2.60; N, 3.21. Found: C, 53.46; H, 2.71; N, 3.27.

Synthesis of [(Ph₂N)₃VNP(OSiMe₃)(C₆H₅)₂][OTf] (5.2b-Si⁺). In the glovebox, a solution of **5.2b** (142 mg, 0.176 mmol) in DCM (4 mL) was added dropwise to a solution of Me₃SiOTf (39 mg, 0.176 mmol) in DCM (1 mL). The resulting dark brown solution was allowed to stir at ambient temperature for 10 min. The volatiles were removed *in vacuo* and the brown residue was washed with pentane (5 mL x 2) to afford a dark brown solid (165 mg, 0.166 mmol, 94% yield). Dark brown needles suitable for XRD studies were grown by slow diffusion of pentane into a concentrated solution of **5.2b-Si⁺** in dichloromethane at room temperature.

¹H NMR (400 MHz, THF-d_8, 25 °C): δ = 7.71 (t, $^3J_{HH}$ = 7.8 Hz, 2H; *p*-H of POPh₂), 7.51 (td, $^3J_{HH}$ = 7.8 Hz, $^4J_{PH}$ = 3.6 Hz, 4H; *m*-H of POPh₂), 7.28 (dd, $^3J_{PH}$ = 14.4 Hz, $^3J_{HH}$ = 7.2 Hz, 4H; *o*-H of POPh₂), 7.17 (t, $^3J_{HH}$ = 7.8 Hz, 12H; *m*-H of NPh₂), 7.11 (t, $^3J_{HH}$ = 7.8 Hz, 6H; *p*-H of NPh₂), 6.70 (d, $^3J_{HH}$ = 7.8 Hz, 12H; *o*-H of NPh₂), 0.15 (s, 9H; Si*Me₃*). **¹³C** (100 MHz, THF-d_8, 25 °C): δ = 154.5 (*Ph₂*N), 135.1 (*Ph₂*P), 132.6 (d, J_{PC} = 12.7 Hz; *Ph₂*P), 130.2 (d, J_{PC} = 14.5 Hz; *Ph₂*P), 129.7 (*Ph₂*N), 127.5 (*Ph₂*N), 122.9 (*Ph₂*N), 0.8 (Si*Me₃*). **⁵¹V** (105 MHz, THF-d_8, 25 °C): δ = 229.8 (br). **³¹P** (162 MHz, THF-d_8, 25 °C): δ = 22 (br). **Anal. Calc**. for C₅₂H₄₉F₃N₄O₄PSSiV: C, 62.89; H, 4.97; N, 5.64. Found: C, 62.79; H, 5.01; N, 5.84

5.4.3 Crystallographic Data for Select Complexes

	5.2a	5.2b	5.3a
Empirical formula	$C_{48}H_{30}F_{10}N_4OPV$	$C_{56}H_{60}N_4O_3PV$	$C_{51}H_{39}F_{10}N_4OPSiV$
Formula weight	950.67	918.99	*1023.86*
Temperature (K)	100(2)	100(2)	*99(2)*
Crystal system	Monoclinic	Monoclinic	*Triclinic*
Space group	P 21/c	P 21/n	*P-1*
a (Å)	22.904(4)	15.7590(12)	*11.123(2)*
b (Å)	18.478(2)	13.8266(9)	*11.304(2)*
c (Å)	9.8154(17)	23.4425(17)	*20.103(4)*
α (deg)	90.00	90.00	*86.349(4)*
β (deg)	98.016(9)	94.270(4)	*83.120(4)*
γ (deg)	90.00	90.00	*64.869(4)*
Volume (Å³)	4113.4(11)	5093.8(6)	*2271.7(8)*
Z	4	4	*2*
Dcalc (g/cm³)	1.535	1.198	*1.497*
F(000)	1928	1944	*1046*
θ Range (deg)	1.421-24.130	1.507-24.730	*1.990-27.268*
no. of rflns collected	31258	19771	*14224*
no. of unique rflns	6463	8638	*9784*
no. of obsd rflns	5121	3620	*6933*
no. of params	490	572	*625*
Final R, R_w (I > 2σ(I))	0.1410, 0.2652	0.1028, 0.2507	*0.0460, 0.0894*
Goodness-of-fit on F^2	1.178	1.017	*1.008*
Δρ$_{max, min}$, (eÅ^{-3})	**0.496, -0.591**	**1.597, -0.670**	**0.433, -0.367**

	5.3b	5.2a⁻	5.3b⁻
Empirical formula	$C_{51}H_{49}N_4OPSiV$	$C_{71}H_{62}CoF_{10.50}N_4OPV$	$C_{68}H_{70}CoN_4OPV$
Formula weight	843.94	1327.58	*1100.12*
Temperature (K)	113(2)	100(2)	*100(2)*
Crystal system	Triclinic	Monoclinic	*Monoclinic*
Space group	P-1	C 2/c	*P 21/c*
a (Å)	10.070(8)	15.851(3)	*13.070(4)*
b (Å)	11.163(9)	17.848(4)	*26.267(9)*
c (Å)	20.610(18)	41.744(10)	*33.074(11)*
α (deg)	91.307(18)	90	*90.00*
β (deg)	101.044(18)	97.977(14)	*90.71(2)*
γ (deg)	92.562(17)	90	*90.00*
Volume (Å³)	2271(3)	11696(5)	*11354(6)*
Z	2	8	*8*
Dcalc (g/cm³)	1.234	1.508	*1.287*
F(000)	886.0	5468	*4632*
θ Range (deg)	1.007-25.608	0.985-24.502	*0.990-24.895*
no. of rflns collected	14945	21187	*61226*
no. of unique rflns	8574	9604	*19432*
no. of obsd rflns	4101	6798	*5402*
no. of params	566	762	*762*
Final R, R_w (I > 2σ(I))	0.0728, 0.2030	0.1751, 0.4086	*0.1751, 0.4086*
Goodness-of-fit on F^2		1.202	*1.202*
Δρ_{max, min}, (eÅ⁻³)		**1.347, -1.185**	***1.347, -1.185***

	5.2a-Si$^+$	5.2b-Si$^+$	
Empirical formula	$C_{79}H_{47}BCl_2F_{30}N_4$ OPSiV	$C_{54}H_{53}Cl_4F_3N_4O_4$ PSSiV	
Formula weight	1829.91	1162.86	
Temperature (K)	100(2)	100(2)	
Crystal system	Monoclinic	Monoclinic	
Space group	P 21/n	P 21/n	
a (Å)	13.735(6)	12.989(14)	
b (Å)	13.546(6)	13.604(11)	
c (Å)	40.419(16)	31.33(6)	
α (deg)	90	90.00	
β (deg)	92.518(4)	92.53(13)	
γ (deg)	90	90.00	
Volume (Å^3)	7513(5)	5531(12)	
Z	4	4	
Dcalc (g/cm^3)	1.618	1.396	
F(000)	3672	2400	
θ Range (deg)	1.009-23.183	1.301-24.421	
no. of rflns collected	25233	20502	
no. of unique rflns	10325	8793	
no. of obsd rflns	3401	2029	
no. of params	1078	406	
Final R, R$_w$ (I > 2σ(I))	0.0931, 0.1918	0.1316, 0.2138	
Goodness-of-fit on F^2	0.938	0.883	
Δρ$_{max, min}$, (eÅ^{-3})	**0.458, -0.682**	**0.476, -0.580**	

5.5 References

(1)   Hudson, L. K., Misra; C. , P., A. J.; Wefers, K.; Williams, F. S. In *Ullmann's Encyclopedia of Industrial Chemistry*, 2000; Vol. 2, pp 607-645.

(2)   Curtis, M. D., In *Transition Metal Sulfur Chemistry*, American Chemical Society: 1996; Vol. 653, pp 154-175.

(3)   McDaniel, M. P., Chapter 3 - A Review of the Phillips Supported Chromium Catalyst and Its Commercial Use for Ethylene Polymerization. In *Advances in Catalysis*, Gates, B. C.; Knözinger, H., Eds. Academic Press: 2010; Vol. 53, pp 123-606.

(4)   Centi, G.; Trifiro, F.; Ebner, J. R.; Franchetti, V. M. *Chem. Rev.* **1988,** *88*, 55-80.

(5)   Tauster, S. J.; Fung, S. C.; Garten, R. L. *J. Am. Chem. Soc.* **1978,** *100*, 170-175.

(6)   Conner, W. C.; Falconer, J. L. *Chem. Rev.* **1995,** *95*, 759-788.

(7)   Hübner, S.; de Vries, J. G.; Farina, V. *Adv. Synth. Catal.* **2016,** *358*, 3-25.

(8)   Tauster, S. J. *Acc. Chem. Res.* **1987,** *20*, 389-394.

(9)   Zhanglin, Y.; Forissier, M.; Sneeden, R. P.; Vedrine, J. C.; Volta, J. C. *J. Catal.* **1994,** *145*, 256-266.

(10)   Coulston, G. W.; Bare, S. R.; Kung, H.; Birkeland, K.; Bethke, G. K.; Harlow, R.; Herron, N.; Lee, P. L. *Science* **1997,** *275*, 191-193.

(11)   Herron, N.; Thorn, D. L.; Harlow, R. L.; Coulston, G. W. *J. Am. Chem. Soc.* **1997,** *119*, 7149-7150.

(12)   Chen, B.; Munson, E. J. *J. Am. Chem. Soc.* **2002,** *124*, 1638-1652.

(13)   Chen, B.; Munson, E. J. *J. Am. Chem. Soc.* **1999,** *121*, 11024-11025.

(14)   Cheng, M.-J.; Goddard, W. A. *J. Am. Chem. Soc.* **2013,** *135*, 4600-4603.

(15)   Cheng, M.-J.; Fu, R.; Goddard, I. I. I. W. A. *Chem. Commun.* **2014,** *50*, 1748-1750.

(16)   Cheng, M.-J.; Goddard, W. A.; Fu, R. *Top. Catal.* **2014,** *57*, 1171-1187.

(17)   Warren, J. J.; Tronic, T. A.; Mayer, J. M. *Chem. Rev.* **2010,** *110*, 6961-7001.

(18)   Weinberg, D. R.; Gagliardi, C. J.; Hull, J. F.; Murphy, C. F.; Kent, C. A.; Westlake, B. C.; Paul, A.; Ess, D. H.; McCafferty, D. G.; Meyer, T. J. *Chem. Rev.* **2012,** *112*, 4016-4093.

(19)   Mora, S. J.; Odella, E.; Moore, G. F.; Gust, D.; Moore, T. A.; Moore, A. L. *Acc. Chem. Res.* **2018,** *51*, 445-453.

(20)   Carroll, T. G.; Garwick, R.; Telser, J.; Wu, G.; Ménard, G. *Organometallics* **2018,** *37*, 848-854.

(21)   Carroll, T. G.; Garwick, R.; Wu, G.; Ménard, G. *Inorg. Chem.* **2018**, *16*, 2447-2558

(22)   Fleming, I. Tilden Lecture.. *Chem. Soc. Rev.* **1981,** *10*, 83-111.

(23)   Hwu, J. R.; Wetzel, J. M. *J. Org. Chem.* **1985,** *50*, 3946-3948.

(24)   Hwu, J. R.; Khoudhary, k. P.; Tsay, S.-C. *J. Organomet. Chem.* **1990,** *399*, C13-C17.

(25)   Song, J.-I.; Gambarotta, S. *Chem. Eur. J.* **1996,** *2*, 1258-1263.

(26)   Sharova, E. V.; Genkina, G. K.; Matveeva, E. V.; Goryunova, I. B.; Goryunov, E. I.; Artyushin, O. I.; Brel, V. K. *Russ. Chem. Bull.* **2014,** *63*, 2546-2550.

(27)   CCDC 1862640-1862647 contain the supplementary crystallographic data for this paper. These data are provided free of charge by The Cambridge Crystallographic Data Centre.

(28)   Porter, T. R.; Capitao, D.; Kaminsky, W.; Qian, Z.; Mayer, J. M. *Inorg. Chem.* **2016,** *55*, 5467-5475.

(29)   Pappas, I.; Chirik, P. J. *J. Am. Chem. Soc.* **2016,** *138*, 13379-13389.

(30)   Piper, T. S.; Wilkinson, G. *J. Inorg. Nucl. Chem.* **1956,** *3*, 104-124.

(31)   Kubas, G. J.; Kiss, G.; Hoff, C. D. *Organometallics* **1991,** *10*, 2870-2876.

(32)   Birdwhistell, R.; Hackett, P.; Manning, A. R. *J. Organomet. Chem.* **1978,** *157*, 239-241.

(33)   Choi, J.; Tang, L.; Norton, J. R. *J. Am. Chem. Soc.* **2007,** *129*, 234-240.

(34)   Sulzbach, R. A.; Iqbal, A. F. M. *Angew. Chem. Int. Ed.* **1971,** *10*, 127-127.

(35)   Kaim, W. *J. Am. Chem. Soc.* **1983,** *105*, 707-713.

(36)   Saito, T.; Nishiyama, H.; Tanahashi, H.; Kawakita, K.; Tsurugi, H.; Mashima, K. *J. Am. Chem. Soc.* **2014,** *136*, 5161-5170.

(37)   Saito, T.; Nishiyama, H.; Kawakita, K.; Nechayev, M.; Kriegel, B.; Tsurugi, H.; Arnold, J.; Mashima, K.. *Inorg. Chem.* **2015,** *54*, 6004-6009.

(38)   Yurino, T.; Ueda, Y.; Shimizu, Y.; Tanaka, S.; Nishiyama, H.; Tsurugi, H.; Sato, K.; Mashima, K. *Angew. Chem. Int. Ed.* **2015,** *54*, 14437-14441.

(39)   Allen, F. H.; Kennard, O.; Watson, D. G.; Brammer, L.; Orpen, A. G.; Taylor, R. *J. Chem. Soc., Perkin Trans. 2* **1987**, S1-S19.

(40)   Agarwal, P.; Piro, N. A.; Meyer, K.; Müller, P.; Cummins, C. C. *Angew. Chem. Int. Ed.* **2007,** *46*, 3111-3114.

(41)   Back, O.; Donnadieu, B.; von Hopffgarten, M.; Klein, S.; Tonner, R.; Frenking, G.; Bertrand, G. *Chem. Sci.* **2011,** *2*, 858-861.

(42)   Mayer, J. M.; Rhile, I. J. *Biochim. Biophys. Acta* **2004,** *1655*, 51-58.

(43)   Dissolving **2a** in neat [TMS][OTf] (a very large excess) resulted in a shifted [51]V

NMR resonance analogous to **2a-Si⁺** and indicative of a shifted equilibrium.

Removing the [TMS][OTf] *in vacuo* resulted in the regeneration of **2a**.

(44)   Lambert, J. B.; Zhang, S.; Ciro, S. M. *Organometallics* **1994,** *13*, 2430-2443.

(45)   Bassindale, A. R.; Stout, T. *Tetrahedron Lett.* **1985,** *26*, 3403-3406.

(46)   Robertson, A. P. M.; Chitnis, S. S.; Chhina, S.; Cortes S, H. J.; Patrick, B. O.;

Jenkins, H. A.; Burford, N. *Can. J. Chem.* **2016,** *94*, 424-429.

(47)   Chai, J.-D.; Head-Gordon, M. *J. Chem. Phys.* **2008,** *128*, 084106.

(48)   Chai, J.-D.; Head-Gordon, M. *Phys. Chem. Chem. Phys.* **2008,** *10*, 6615-6620.

(49)   Weigend, F.; Ahlrichs, R. *Phys. Chem. Chem. Phys.* **2005,** *7*, 3297-3305.

(50)   Schwerdtfeger, P.; Dolg, M.; Schwarz, W. H. E.; Bowmaker, G. A.; Boyd, P. D.

W. *J. Chem. Phys.* **1989,** *91*, 1762-1774.

(51)   Miertuš, S.; Scrocco, E.; Tomasi, J. *Chem. Phys.* **1981,** *55*, 117-129.

(52)   Cammi, R.; Tomasi, J. *J. Comput. Chem.* **1995,** *16*, 1449-1458.

(53)   Connelly, N. G.; Geiger, W. E. *Chem. Rev.* **1996,** *96*, 877-910.

(54)   Noviandri, I.; Brown, K. N.; Fleming, D. S.; Gulyas, P. T.; Lay, P. A.; Masters,

A. F.; Phillips, L. *J. Phys. Chem. B.* **1999,** *103*, 6713-6722.

(55)   Yang, J.-D.; Ji, P.; Xue, X.-S.; Cheng, J.-P. *J. Am. Chem. Soc.* **2018,** *140*, 8611-

8623.

(56)   Belford, R. L.; Belford, G. G. *J. Chem. Phys.* **1973,** *59*, 853-854.

(57)   Worrell, W. L.; Chipman, J. *J. Phys. Chem.* **1964,** *68*, 860-866.

Chapter 6

Targeting C–H bond activation using transient Oxidizing Vanadium(V) Phosphinate complexes.

6.1 Introduction

C–H bond functionalization remains a central theme in organometallic chemistry research.[1-4] In recent years, substantial progress has been made in the development of transition metal methodologies for C–H bond activation and functionalization involving hydrogen atom transfer (HAT) processes.[5-11] However, despite decades of research, current strategies of (mostly noble) metal-mediated C–H bond activation have largely failed to produce large-scale applications in industry. The reason for this stems from the difficulty in activating strong and localized C–C and C–H bonds, but also from a deficient understanding of HAT processes. While HAT processes have a long history in synthetic chemistry,[12-13] it has been shown recently that many transformations thought to occur through concerted HAT process may actually proceed through a proton-coupled electron transfer (PCET) mechanism, wherein the proton and electron transfer to different orbitals in the product.[14-16] To be more specific, recent studies have also shown that multisite PCET (MS-PCET) mechanisms – where the proton and electron travel to two distinct molecular acceptors – can feasibly activate aliphatic C–H bonds.[14, 17-18] For example, theoretical mechanistic studies on the surface of the heterogeneous vanadium phosphorus oxide (VPO) catalyst, have proposed a MS-PCET type mechanism for the initial C-H bond activation of *n*-butane to maleic anhydride.[19-22] While the oxidized surface V^V=O bonds of the VPO

catalyst were always assumed to be responsible for the C–H activating steps, recent computational studies suggest that C–H bond activation occurs at the typically redox-inactive P^V=O linkages of the support, which are activated through resonance communication to neighboring $V^{IV/V}$ redox couples through a "reduction coupled oxo-activation" (ROA) or MS-PCET mechanism (Figure 6.1a). Additionally, experimental work from Alexanian, Knowles, and co-workers demonstrated C–H alkylation catalyzed by a noncovalent complex formed between an iridium(III) photocatalyst and a monobasic phosphate base via a similar MS-PCET mechanism (Figure 6.1b).[23]

We have recently demonstrated an example of reactivity at a terminal P^V=O bond mimicking the proposed ROA/MS-PCET mechanism for VPO catalysis (Scheme 6.1c) using a L_3V=N-P(O)Ar$_2$ model complex (L = NPh$_2$, Ar = C$_6$F$_5$/Ph) and a Me$_3$Si• donor (1,4-bis(trimethylsilyl)-pyrazine) as a "bulky hydrogen atom" surrogate (Figure 6.1c).[24] These complexes were reactive towards very weak H-atom donors (HADs), such as Cp(CO)$_3$Cr–H (BDFE$_{MeCN}$ = 57.3 kcal/mol) (Cp = μ^5-C$_5$H$_5$),[25-27] but remained inactive towards stronger C–H bonds and HADs. The reason for this may be in part due to the relatively low reduction potential of the vanadium(V) center, which thermodynamically inhibits the electron transfer step.

In this chapter, we focus on tuning the family of L_3V=N-P(O)Ar$_2$ model complexes to increase the oxidizing power of the vanadium(V) center, and target C–H bond activation through a MS-PCET mechanism (Figure 6.1d). Judicious choice of the ancillary ligands (L) has been shown to dramatically impact the overall reduction potential of the metal center based on inductive and resonance effects.[28] We investigate the effects of exchanging the electron donating diphenylamine ligands (L = NPh$_2$) for more electron withdrawing

ligands (L = OC_6F_5, $OC_{12}F_9$, $OC(CF_3)_3$). As a result of this study we show how the choice of ligand within the first coordination sphere of the complex can impart quantitative C–H bond activation on a variety of common HADs with higher BDFEs than what we have previously reported.

a) *Computational ROA/MS-PCET mechanism for butane oxidation on VPO catalyst*

VPO
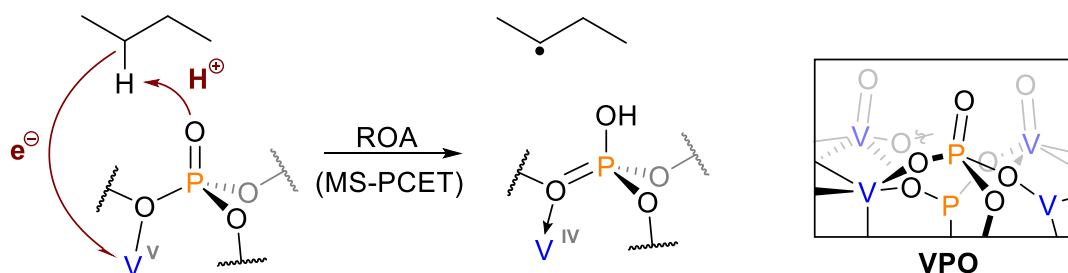
b) *Intermolecular C-H bond MS-PCET via hydrogen bound Ir*-Phosphate Complex* (2019)

Intermolecular C-H
MS-PCET

Ir*-Phosphate complex
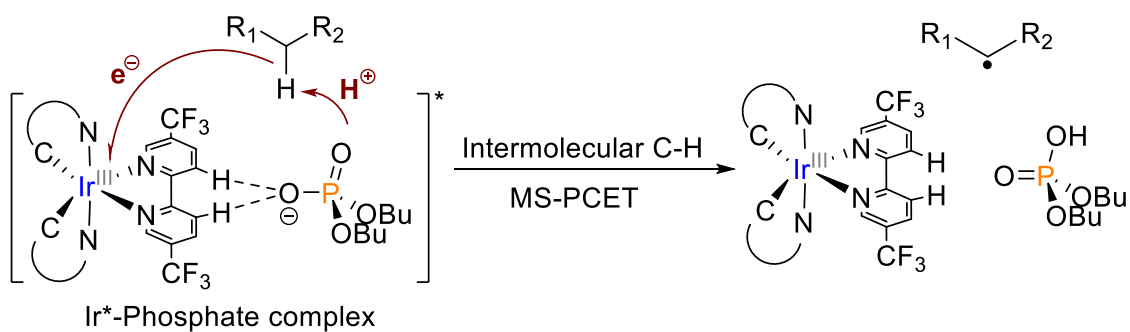
c) *Previous Work: MS-PCET using a "bulky hydrogen" surrogate (Me₃Si•)* (2018)

MS -"Bulky Hydrogen"
Transfer

Ar = C₆F₅, Ph
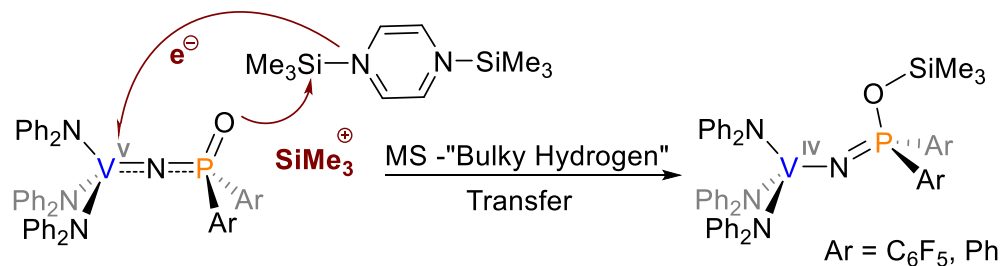
d) *This Work: Investigating C-H bond MS-PCET via ligand substitution*

C-H bond MS-PCET

Ar = C₆F₅, Ph

Proposed Reactive Intermediate
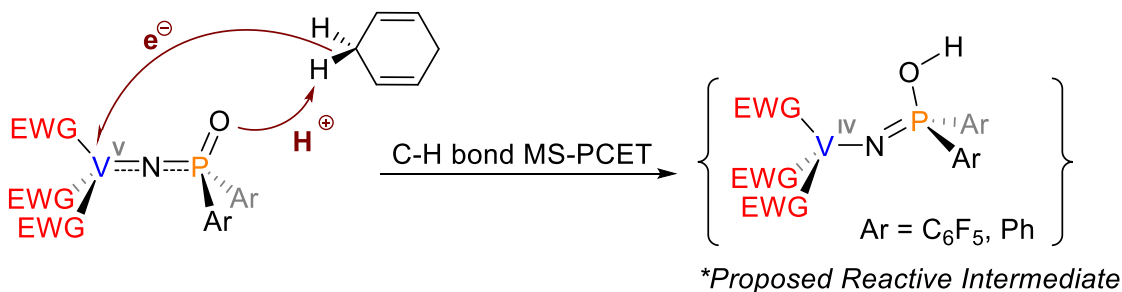
Figure 6.1: Mechanisms for multisite-PCET. (a) Computationally proposed "reduction coupled oxo-activation" (ROA)/Multisite-PCET (MS-PCET) mechanism for the initial C–H bond activation of butane on the heterogeneous Vanadium Phosphorus Oxide (VPO) industrial catalyst. (b) Proof of concept - mechanism for intermolecular C–H bond multisite-PCET via a noncovalent iridium photocatalyst and phosphate base complex. (c) Previous work using a $L_3V=N-P(O)Ar_2$ model complex (L = NPh_2, Ar = C_6F_5/Ph) and a $Me_3Si\bullet$ donor (1,4-bis(trimethylsilyl)-pyrazine) as a "bulky hydrogen atom" surrogate to model the proposed ROA/MS-PCET mechanism. (d) Current work in using electron withdrawing groups (EWG) as ligands to engender enhance C–H bond reactivity through the MS-PCET mechanism.

6.2 Results and Discussion

6.2.1 Synthesis, characterization, and reactivity of electron deficient Vanadium(V) phosphinate complexes

Based on our previous report, we indicated that cooperative ROA type reactivity may proceed through an electron transfer followed by a stepwise proton/silyl cation transfer.[24] In order to thermodynamically drive the initial electron-transfer step and concurrent reduction from vanadium(V) to vanadium(IV), we sought to make the vanadium center more oxidizing by incorporating increasing electron-withdrawing ligands. Initially we attempted to substitute the electron donating diphenylamide (Ph_2N^-) ligands for nonafluoro-*tert*-butoxide (($CF_3)_3CO^-$) by means of simple protonolysis of the complex **6.1** (Scheme 6.1).

Scheme 6.1: Proposed protonolysis pathway of complex **6.1** with acidic fluorinated alcohols
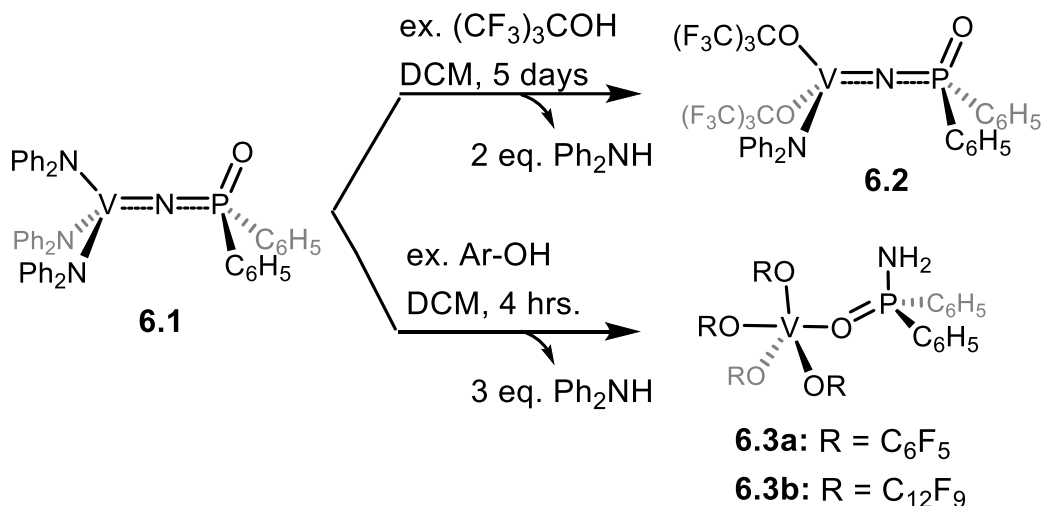
Addition of excess neat nonafluoro-*tert*-butanol ((CF_3)$_3$COH) to a dichloromethane (DCM) solution of complex **6.1** resulted in a bright red solution over the course of 24 hours. An *in situ* analysis of the reaction mixture by ^{51}V spectroscopy revealed a new diamagnetic vanadium signal at -225 ppm, which was significantly shifted relative to **6.1** (117 ppm) and consistent with an increasingly shielded vanadium center. In contrast, the ^{31}P NMR resonances followed the opposite trend with a broad signal (due to coupling to the quadrupolar ($I = 7/2$) ^{51}V) at 32 ppm; shifted upfield by ~50 ppm relative to the starting material. Diagnostic aryl signals indicative of the protonated diphenylamine (Ph$_2$NH) ligands were observed by ^{1}H NMR spectroscopy, but also indicated incomplete substitution with multiple sets of aryl signals. Upon work-up, large red single crystals suitable for XRD studies were grown from hexanes at -40 °C.
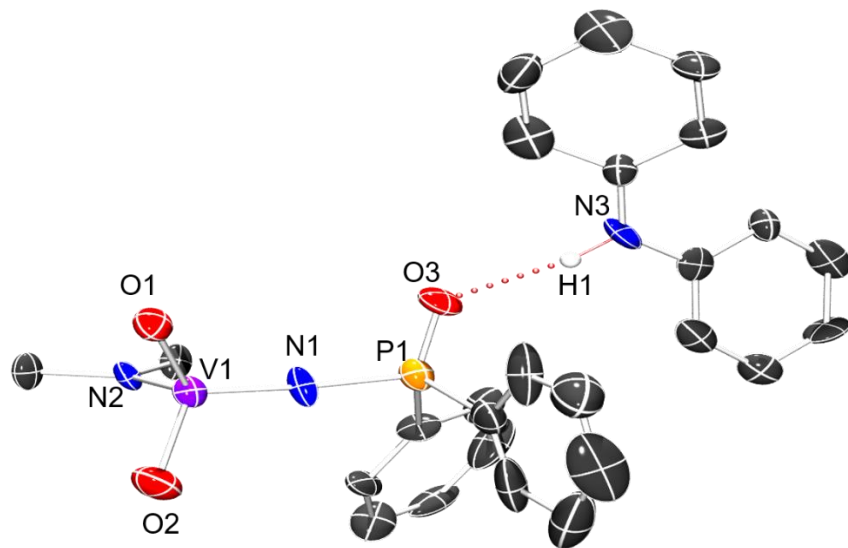
Figure 6.2: **S**olid-state molecular structure of **6.2**. Hydrogen atoms, phenyl rings, and nonafluoro-*tert*-butyl groups, and co-crystallized solvent are omitted for clarity. The dashed line indicates hydrogen bonding.

The solid-state molecular structure revealed the incomplete di-substitution of the Ph_2N^- ligands for the electron withdrawing $(CF_3)_3CO^-$ ligands to yield complex **6.2** (Figure 6.2). The complete tri-substitution of the Ph_2N^- ligands proved to be unsuccessful even after adding an excess of $(CF_3)_3COH$ and allowing the reaction to stir for five days. It is likely the $(CF_3)_3CO^-$ ligands are too bulky to accommodate an additional unit around the vanadium center and/or that upon successive protonolysis each electron donating Ph_2N^- ligand becomes increasing bound to the electron deficient V^V center. Interestingly, we also observed that one equivalent of the protonated Ph_2NH from the reaction mixture hydrogen bonded (2.05 Å) to the $P^V=O$ bond. Repeated recrystallizations, washings, and work-up proved unsuccessful in separating the hydrogen bound diphenylamine from complex **6.2**, as monitored through the ^1H NMR resonance signals for Ph_2NH. Bond lengths and angles

for **6.1** and **6.2** are compiled in Table 6.1. Notable are the slightly truncated V1–N1 bonds

in **6.2** (1.646(7) Å) relative to **6.1** (1.662(11) Å), as well as the slightly elongated N1–P1

bonds in **6.2** (1.697(7) Å) compared to **6.1** (1.661(11) Å). Combined with the near linear

V1–N1–P1 angles 175.604(5)° of **6.2**, this suggests that the delocalized π manifold, in

which there is electronic communication between the vanadium and phosphorus through

the nitrogen linker, is maintained following ligand substitution. This is also supported by

the broad vanadium coupling seen in the ^{31}P NMR spectrum.

Table 6.1: Selected Bond Distances (Å) and Angles (°) for **6.1** and **6.2**

Bond Metrics	6.1	6.2
V1–N1	1.662(11)	1.646(7)
N1–P1	1.661(11)	1.697(7)
P1–O1	1.484(8)	1.434(9)
V1–N1–P1	175.9(7)	175.60(4)
N1–P1–O1	115.8(5)	112.68(4)
O1–H1	-	2.036

We next aimed to test the reactivity of the P^v=O bond with common hydrogen atom

donors (HADs) such as 9,10-dihydroanthracene (C–H BDFE$_{DMSO}$ = 76.0 kcal/mol) and

1,4-cyclohexadiene (C–H BDFE$_{tol}$ = 72.6 kcal/mol).[29-30] However, monitoring the reaction

of **6.2** with excess HADs by NMR spectroscopy revealed little to no reactivity over the

course of two days. This lack of reactivity may be due to the strongly bound Ph$_2$NH unit

shielding the terminal P^v=O bond. Regardless, while the (CF$_3$)$_3$CO$^-$ ligands showed the

propensity to undergo di-substitution of the Ph$_2$N$^-$ ligands of **6.1**, the inability to completely

isolate complex **6.2** from the Ph$_2$NH adduct led us to investigate other electron withdrawing

ligands.

We next focused on the less sterically encumbered pentafluorophenol (C_6F_5OH) as an electron withdrawing ligand to engender complete substitution of the Ph_2N^- ligands of **6.1** (Scheme 6.1). Addition of excess C_6F_5OH to a DCM solution of complex **6.1** resulted in a dark blue solution over the course of 2 hours. An initial *in situ* ^{51}V NMR spectrum of the reaction mixture revealed a new diamagnetic vanadium signal at -295 ppm, which was significantly shifted relative to **6.1** (117 ppm) in a similar direction and magnitude to complex **6.2** (-225 ppm). The initial *in situ* ^1H NMR spectrum displayed diagnostic aryl signals indicative of the protonated Ph_2NH ligands. However, over the course of a day, the new diamagnetic vanadium signal went silent, indicating a reduction of the V^V center to a paramagnetic species. Upon work-up and repeated recrystallizations, complex **6.3a** was isolated as small blue X-ray quality crystals (Figure 6.3).
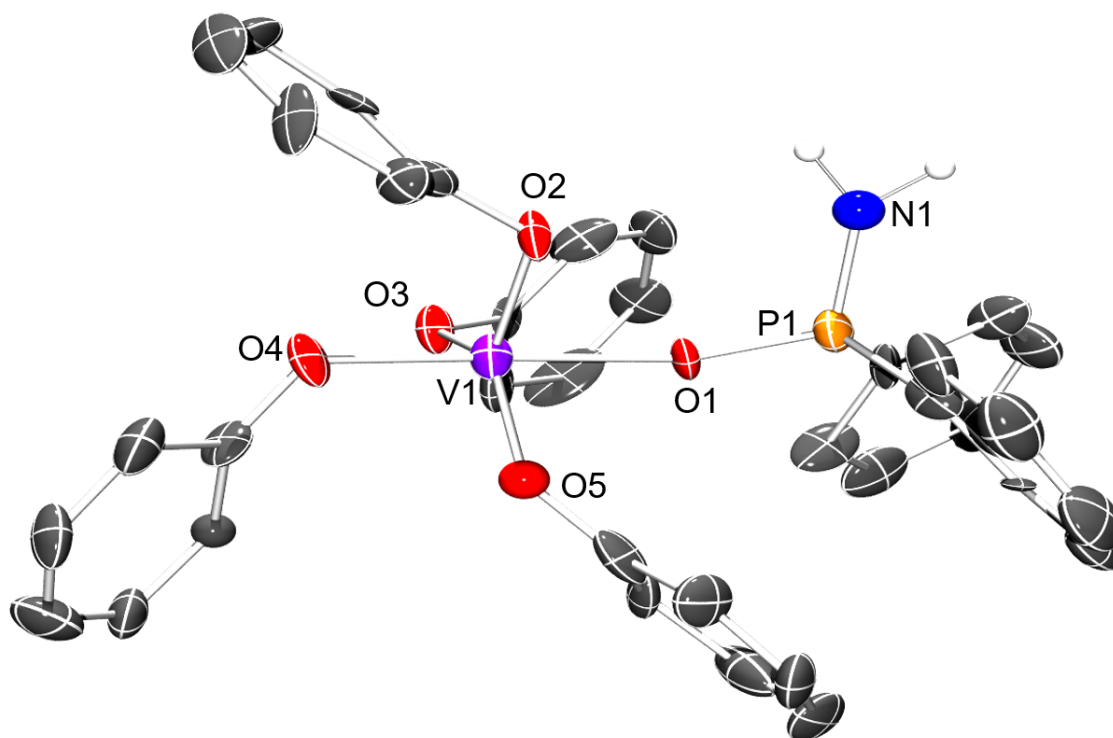
Figure 6.3: **S**olid-state molecular structure of **6.3a**. Phenyl hydrogen and fluorine atoms are omitted for clarity.

Based on the solid-state molecular structure in Figure 6.3 it is clear that the substitution of the electron donating Ph_2N^- ligands for the electron withdrawing $C_6F_5O^-$ ligands did not produce the expected tri-substituted product. First, complex **6.3a** adopts a trigonal bipyramidal geometry with the incorporation of four $C_6F_5O^-$ ligands around the vanadium center, indicating that the less bulky $C_6F_5O^-$ is indeed capable of complete substitution as opposed to the sterically encumbered $(CF_3)_3CO^-$. Second, based on the relative bond metrics, the long V1–O1 bond length (1.993(3) Å) in conjunction with the short O1–P1 bond length (1.494(3) Å) and bent V1–O1–P1 bond angle (156.975°) is consistent with a P=O double bond coordinating in an L-type[31] fashion to the vanadium center. Third, the relatively long P1–N1 bond length (1.642(3) Å) combined with hydrogen mapping indicates a formally single P^V–NH_2 bond. Combined together, the solid-state structure suggests that upon substitution, **6.1** undergoes some sort of HAT reaction that results in the phosphinate ligand flipping from an anionic V1–N1 coordination to neutral V1–O1 coordination with concurrent addition of a fourth $C_6F_5O^-$ ligand. Additionally, there is an apparent reduction from V^V to V^{IV} as evident from the paramagnetic heteronuclear NMR spectra and *in situ* EPR resonance which showcased the expected 8-line splitting patterns at 100 K due to hyperfine coupling of the d^1 electron to the ^{51}V center ($I = 7/2$, ~100% abundance) (Figure 6.4).
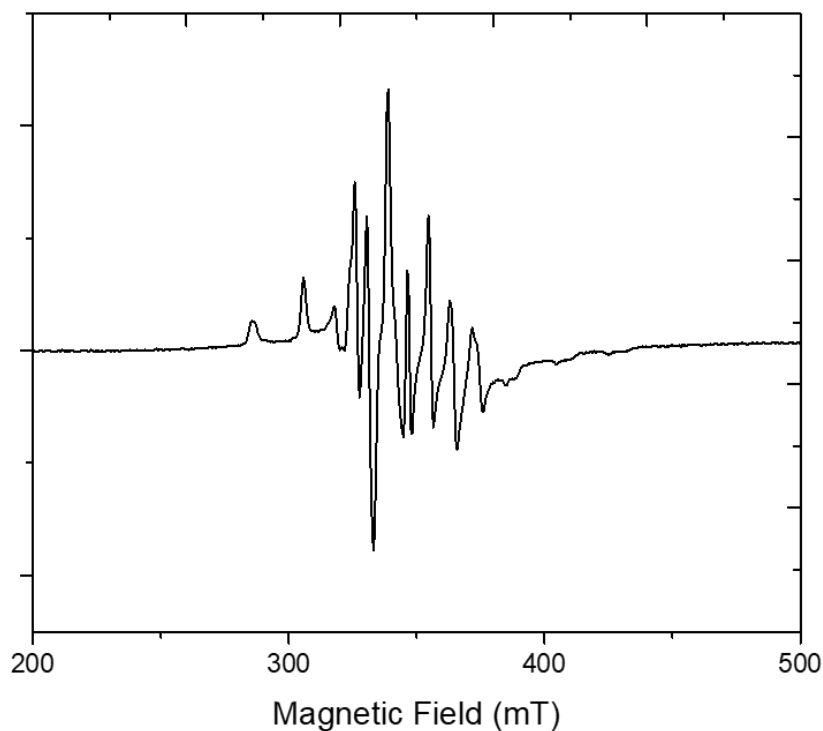
Figure 6.4: X-band EPR spectrum of reaction product between **6.1** and excess C_6F_5OH (DCM, 100 K, g = 1.968).

Similar reactivity was noted when nonafluorobiphenyl-2-ol ($C_{12}F_9OH$) was used in accordance with Scheme 6.1. Upon addition of excess $C_{12}F_9OH$ to a DCM solution of **6.1**, the dark black solution slowly turned a blue/green color over the course of 24 h. Upon work-up, analysis by ^{1}H NMR spectroscopy revealed the production of free Ph_2NH, and silent [51]V and ^{31}P NMR resonances indicated the formation of a paramagnetic product similar to **6.3a**. Repeated recrystallizations resulted in the isolation of **6.3b** as big turquoise crystals suitable for XRD (Figure 6.5).
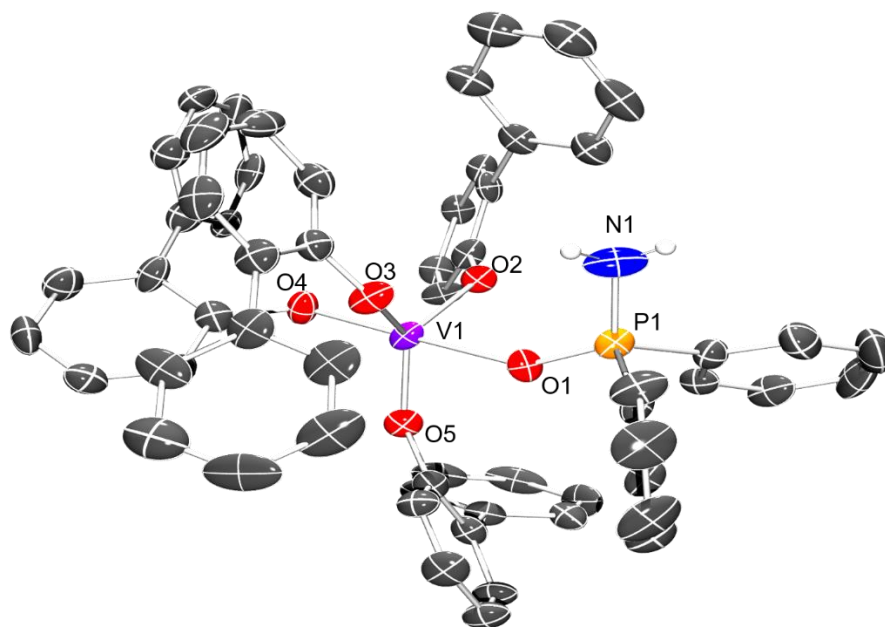
Figure 6.5: Solid-state molecular structure of **6.3b**. Fluorine atoms, and co-crystallized solvent are omitted for clarity.

The solid-state structure of **6.3b** revealed identical reactivity to **6.3a** in which the phosphinate ligand reacts to form a flipped phosphinic amide coordinated to the reduced V^{IV} center through the P^{V}=O bond. The relative bond lengths and angles of **6.3a/b** are fairly consistent as shown in Table 6.2.

Table 6.2: Selected Bond Distances (Å) and Angles (º) for **6.3a** and **6.3b**

Bond Metrics	6.3a	6.3b
V1–O1	1.994(2)	2.050(7)
O1–P1	1.494(2)	1.477(7)
P1–N1	1.640(2)	1.606(5)
V1–O1-P1	147.132(4)	147.184(5)
O1–P1–N1	115.8(4)	113.694(5)
V1–O4	1.868(2)	1.866(3)
V1–O3	1.834(2)	1.854(3)

Both **6.3a** and **6.3b** undergo HAT, however the source of hydrogen atoms is still unclear. It may be that upon tri-substitution diphenylamine can act as a H-atom source, or perhaps the excess fluorinated alcohol acts as the HAD. Without successful isolation of the byproducts of the reactions, we were unable to resolve the complete balanced equation. Nevertheless, we were intrigued by the propensity for this complex to engage in HAT, so we aimed to target C–H activation through *in situ* addition of 1,4-cyclohexadiene and 9,10-dihydroanthracene.

As shown in our previous work, complex **6.1** displayed no signs of reactivity with 1,4-cyclohexadiene, however, addition of excess C_6F_5OH to a deuterated DCM solution of **6.1** with excess 1,4-cyclohexadiene resulted in the quantitative conversion of half an equivalent of the respective C–H activation product benzene (Scheme 6.2).

Scheme 6.2: Proposed reaction pathway of diphenylamine substitution of **6.1** and subsequent C–H bond activation of 1,4-cyclohexadiene
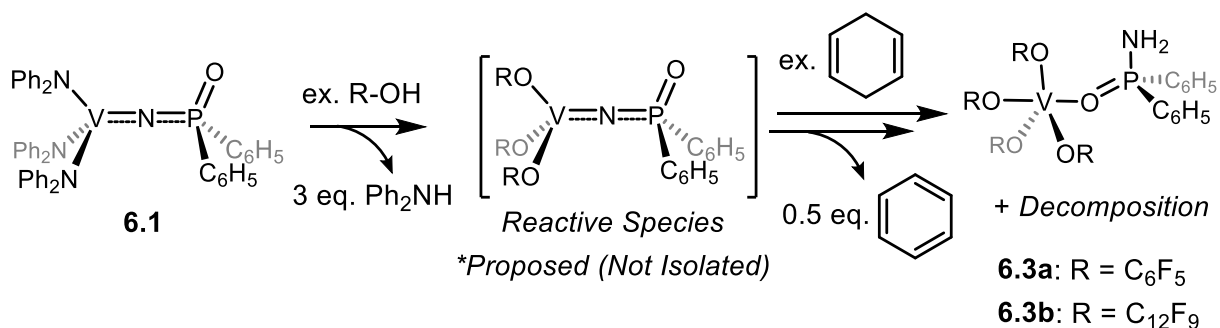
Over the course of several hours, the reaction mixture changed from black to dark blue and the reaction progress was monitored by ^{1}H NMR spectroscopy using

hexamethylbenzene as an internal standard. Figure 6.6 shows that even after twenty minutes there is significant production of the C–H activation product (benzene) from the reaction mixture (blue dot), integrating to approximately half of an equivalent of **6.1**. Additionally, there is immediate protonation and substitution of the Ph_2N^- ligands as evidenced by the aryl peaks (Figure 6.6, yellow dots) integrating to three equivalents compared to the hexamethylbenzene internal standard. The reaction was monitored by ^1H NMR spectroscopy for a total of twelve hours, however little change in the relative integrations was observed after approximately 20 minutes.
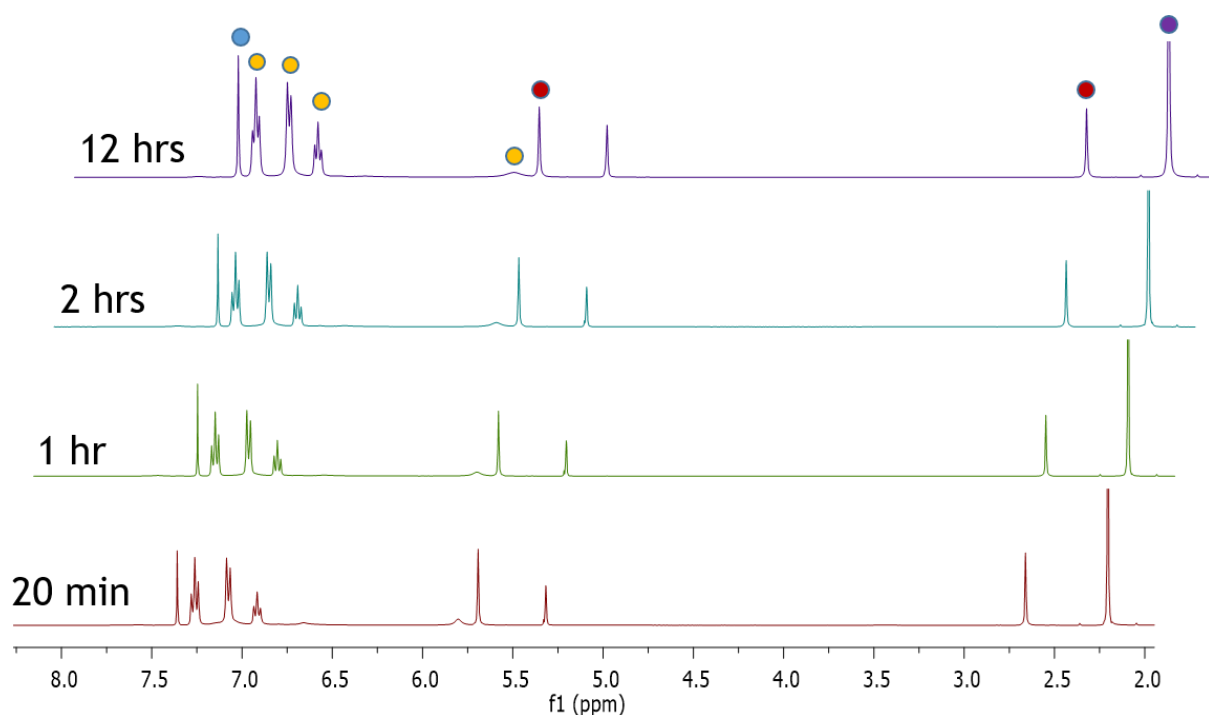
Figure 6.6: *in situ* ^1H NMR spectra taken at various timescales in d_2-DCM of the reaction mixture involving **6.1**, excess C_6F_5OH, and excess 1,4-cyclohexadiene. Blue dot = C_6H_6 (C–H activation product), yellow dot = Ph_2NH (ligand substitution product), red dot = 1,4-cyclohexadiene (excess HAD), purple dot = hexamethylbenzene (internal standard).

Similar reactivity was observed when C_6F_5OH was swapped for the bulkier $C_{12}F_9OH$ alcohol, albeit on a slower timescale. Upon work-up of the reaction mixture and repeated recrystallizations, blue x-ray quality crystals were isolated confirming the production of **6.3a**. While other paramagnetic decomposition products made it difficult to isolate **6.3a** on a large scale, it is clear that the incorporation of less bulky electron withdrawing ligands to our V–N–P=O framework leads to modified reactivity, including C–H bond activation, as compared to the $P_{h2}N^-$ substituted complex (6.1).

We next tested the reactivity of the *in situ* generated reactive species (Scheme 6.2) using other HADs. When 9,10-dihydroanthracene was added to the reaction mixture, half an equivalent of the C–H activation product (anthracene) was generated over the course of 24 hours similar to 1,4-cyclohexadiene. While the BDFE of 9,10-dihydroanthracene (76.0 kcal/mol) is similar to 1,4-cyclohexadiene (72.6 kcal/mol), the rate of reaction is much slower possibly due to the increased steric bulk or the increased BDFE. Hydrogen atom abstraction (HAA) reactions from toluene (BDFE = 87 kcal/mol) and cyclohexane (BDFE = 97 kcal) were unsuccessful, suggesting an upper limit to reactivity.[29] While we were able to engender new C–H bond activation, without isolation of the reactive species we were unable to determine the role of the P^V=O bond in the enhanced reactivity. Therefore, we aimed to target vanadium phosphine complexes so as to exclude the proposed reactive P^V=O motif.

6.2.2 Synthesis, characterization, and reactivity of vanadium phosphine derivatives

The initial vanadium phosphine target complexes (**6.4a**, **6.4b**) were synthesized by salt metathesis of the reported[25] vanadium nitride, $(Ph_2N)_3V(\mu\text{-}N)Li(THF)_3$, with chlorodiarylphoshines, $(C_6F_5)_2PCl$[26] or $(C_6H_5)_2PCl$[26] (Scheme 6.3).

Scheme 6.3: Synthesis of complexes **6.4a** and **6.4b**

6.4a: Ar = C_6F_5
6.4b: Ar = C_6H_5
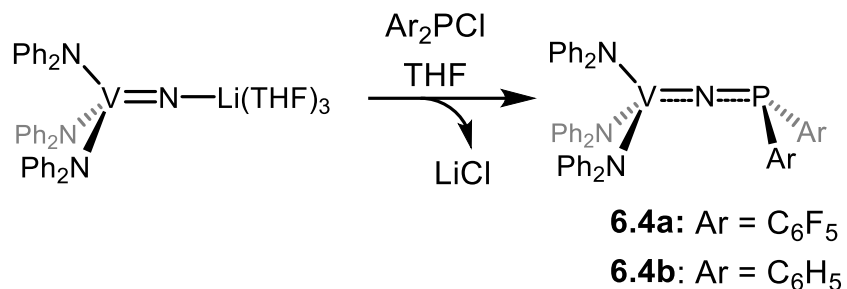
Both V^V complexes displayed significantly shifted, broad ^{51}V NMR resonances at 65 ppm (**6.4a**) and 25 ppm (**6.4b**) relative to the lithiated starting material (-217 ppm), consistent with an increasingly deshielded V center. The ^{31}P NMR spectra revealed broad signals at 63 and 142 ppm, respectively, both shifted downfield relative to the starting materials. The ^1H NMR spectrum displayed diagnostic aryl signals for the diphenyl amine ligands, and **6.4a** could also be characterized by ^{19}F NMR spectroscopy by three distinct *ortho*, *para*, and *meta* signals. Single crystals of **6.4a** suitable for X-ray diffraction (XRD) studies were grown from hexanes (Figure 6.7).
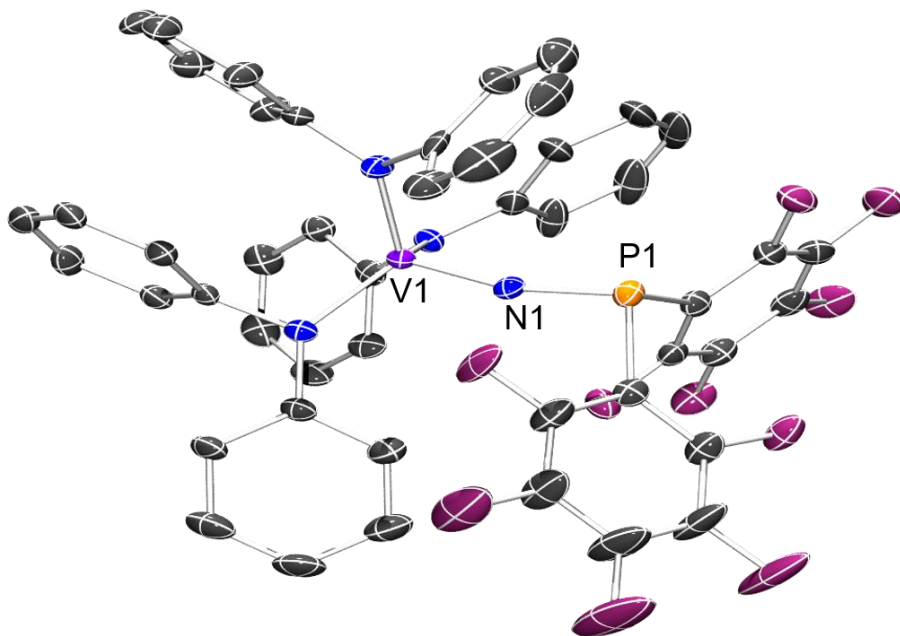
Figure 6.7: **S**olid-state molecular structure of **6.4a**. Hydrogen atoms and co-crystallized solvent are omitted for clarity.

After the successful synthesis and isolation of the vanadium phosphine complexes **6.4a/b,** we next targeted ancillary ligand substitution. Exposure of isolated **6.4a** to three equivalents of C_6F_5OH resulted in a gradual color change from black to brick red, representative of Ph_2N^- protonation and substitution for the electron withdrawing $C_6F_5O^-$ ligands to yield complex **6.5** (Scheme 6.4). Following purification, the ^{51}V NMR resonance significantly shifted upfield to -320 ppm, while the ^{31}P NMR resonances shifted upfield to 100 ppm relative to the starting material. Bright red single crystals of **6.5** were grown out of DCM and pentane at -40 °C (Figure 6.8).

Scheme 6.4: Synthesis of complex **6.5** and reduction of **6.4a**.
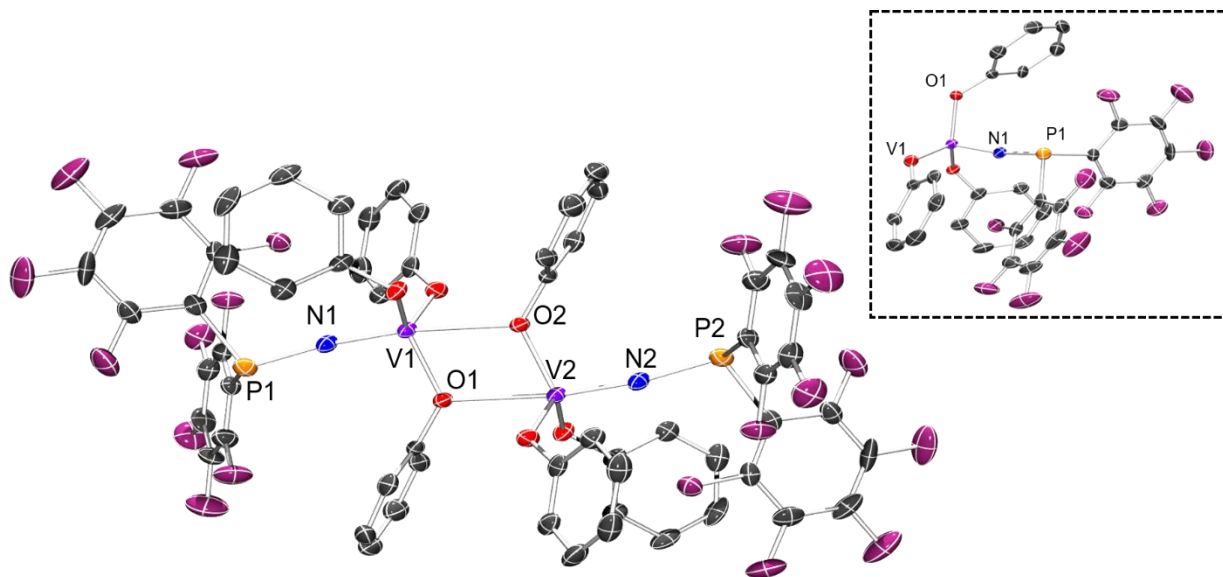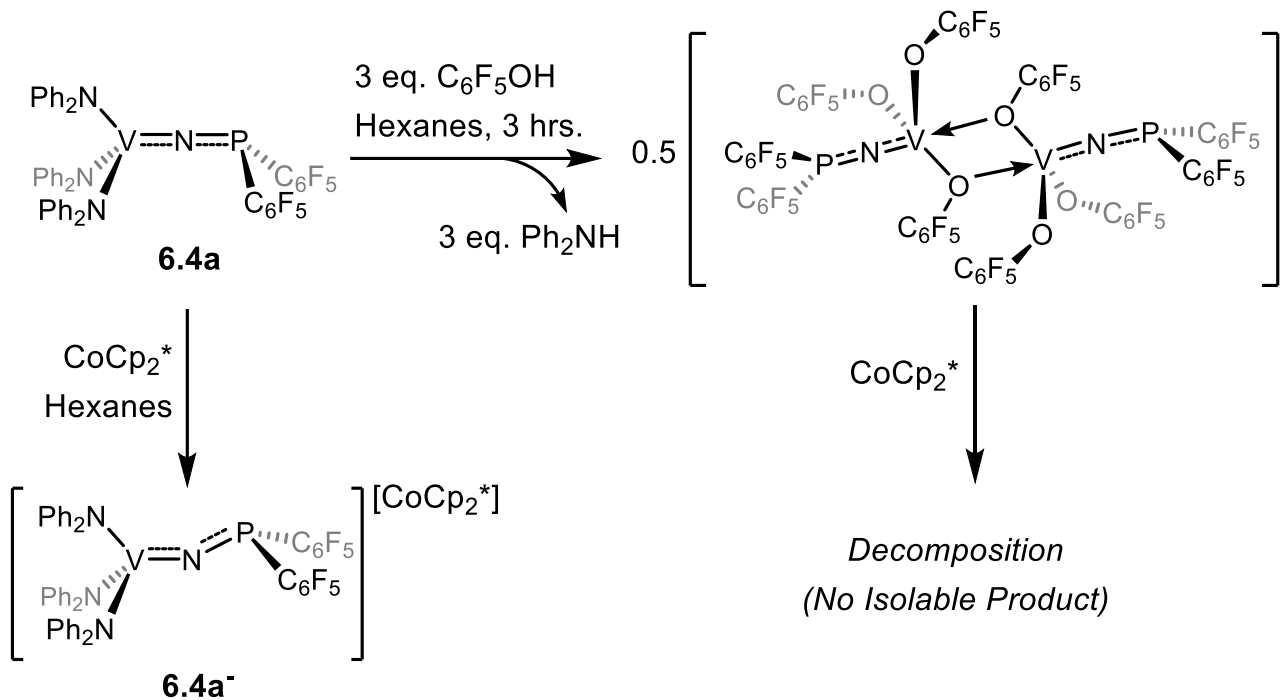
Figure 6.8: Solid-State dimeric structure of **6.5**. Inset: monomeric representation of complex **6.5**. Hydrogen atoms, fluorine atoms, and co-crystallized solvent are omitted for clarity.

The solid-state molecular structure reveals that **6.5** dimerizes through a bridging phenoxide ligand adopting a pseudo trigonal bipyramidal geometry around each vanadium atom. The dimeric nature of **6.5** is not surprising given the relatively low steric bulk of the $C_6F_5O^-$ ligands coupled with the high oxygen affinity of electron poor vanadium complexes. The bond metrics of **6.5** remain surprisingly similar to **6.4a** with only a slight contraction of the V1–N1 bond length (1.644(5) Å (**6.5**) vs. 1.669(5) Å (**6.4a**)?). Attempts to synthesize the $C_6F_5O^-$ congener of **6.4b** (Ar = C_6H_5) following Scheme 6.4 proved to be unsuccessful, and instead resulted in a mixture of unisolable paramagnetic products.

In order to investigate the perceived increase in oxidative potential, we probed the redox properties of **6.4a** and **6.5** by cyclic voltammetry (CV).[32] The CVs of **6.4a**, and **6.5** were taken at a 50 mV/s scan rate in DCM with $[Bu_4N][PF_6]$ supporting electrolyte and referenced to the ferrocene/ferrocenium (Fc/Fc$^+$) redox couple (Figure 6.9). The voltammogram for **6.4a** displays a single reversible reduction event at $E_{1/2}$ = -1.42 V vs. Fc/Fc$^+$ corresponding to the one-electron reduction of the V^V metal center. In contrast, the voltammogram for **6.5** shows a quasi-reversible reduction event centered at $E_{1/2}$ = -0.44 V with an apparent double hump, which we attribute to the sequential reduction of each V^V center in the solution-state dimer. The CVs clearly demonstrate that substituting the electron donating Ph_2N^- ligands for electron withdrawing $C_6F_5O^-$ substituents dramatically increases the V^V/V^{IV} reduction event – with an almost 1.00 V difference in potential between complexes **6.4a** and **6.5** – thus indicating a more electron deficient and oxidizing metal center.
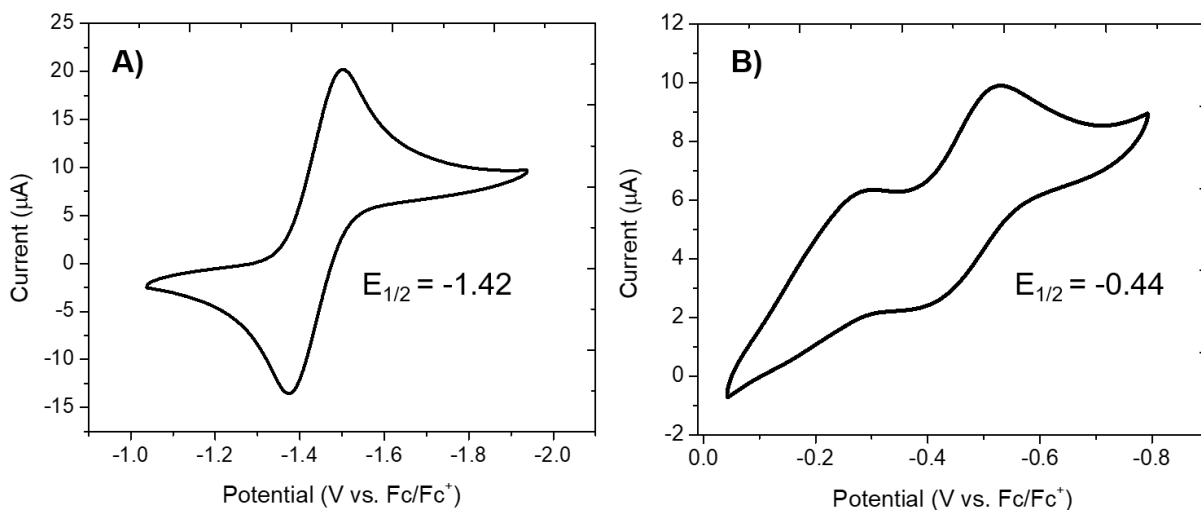
Figure 6.9: A) CV of **6.4a** in DCM (1.5 mM) with 0.1 M [Bu$_4$N][PF$_6$] electrolyte in DCM using a glassy carbon working electrode, platinum wire counter electrode, and Ag/Ag$^+$ wire pseudo reference electrode. Scan rate 50 mV/s, referenced to Fc/Fc$^+$. B) CV of **6.5** in DCM (1.0 mM) with 0.1 M [Bu$_4$N][PF$_6$] electrolyte in DCM using a glassy carbon working electrode, platinum wire counter electrode, and Ag/Ag$^+$ wire pseudo reference electrode. Scan rate 50 mV/s, referenced to Fc/Fc$^+$.

Chemical isolation of the reduced form of **6.4a** was possible using CoCp*$_2$ ($E_{1/2}$ = -1.94 V vs. Fc/Fc$^+$)[33]. Addition of one equivalent of CoCp*$_2$ to **6.4a** in hexanes resulted in the precipitation of **6.4a**$^-$ as a red/orange solid which was isolated in 87% yield (Scheme 6.4). Single crystals were grown by slow vapor diffusion at -40°C and they were structurally characterized using XRD (Figure 6.10). Bond metrics for **6.4a**$^-$ revealed a bent V1–N1–P1 (137.25(1)°) fragment similar to previously reported reduced vanadium phosphinate complexes[24] (145.90(13)°), as well as an elongated V1–N1 (1.729(8) Å) bond relative to **6.4a** (1.669(5) Å). Clearly, the reduction of the vanadium center has an impact

of the electron delocalization across the V1–N1–P1 bond as evidenced from the increase in pyramidalization across the bridging nitrogen atom. While the NMR signals were altogether silent, a characteristic 8-line hyperfine EPR signal was observed at room temperature and 100 K. Attempts to reduce and isolate complex **6.5** under similar conditions, as well as with other common reductants such as potassium graphite, proved ineffective – leading to a mixture of unidentifiable paramagnetic byproducts.
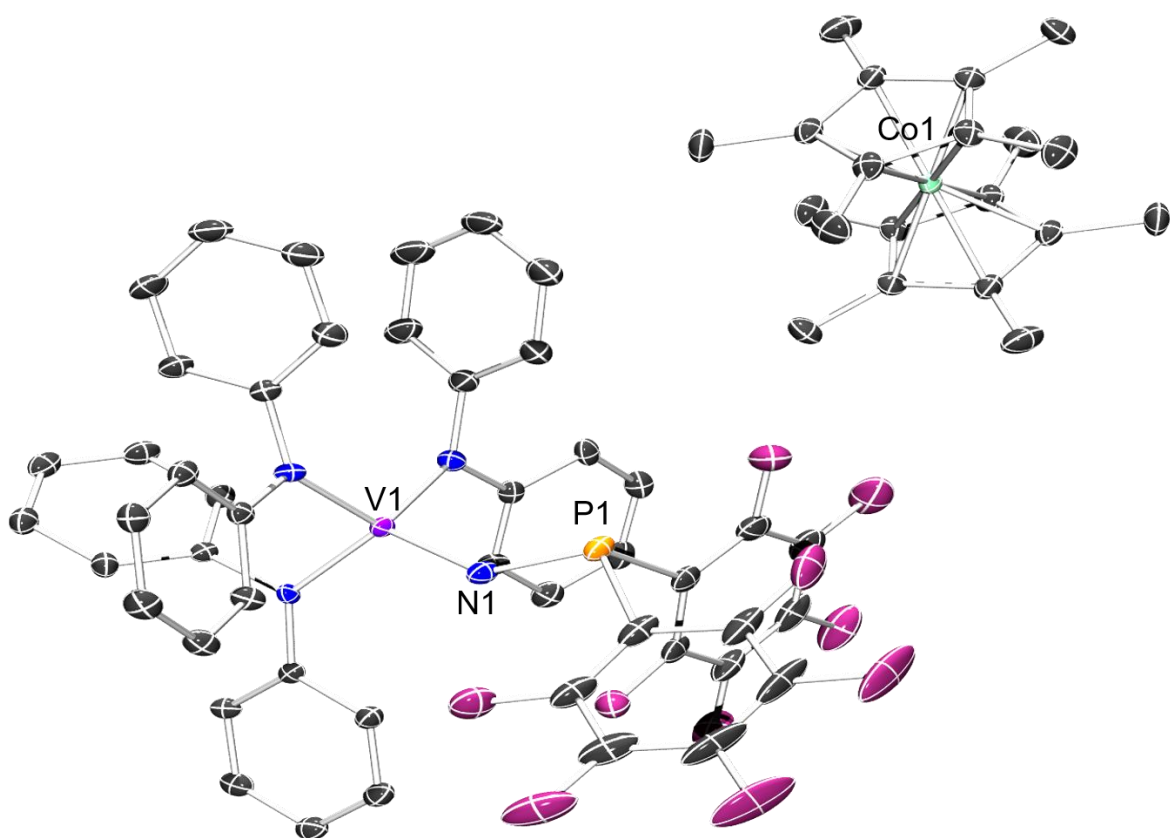
Figure 6.10: Solid-State molecular structure of **6.4a⁻**. I. Hydrogen atoms and co-crystallized solvent are omitted for clarity.

With complex **6.5** in hand, we wanted to test its reactivity with common HADs. In contrast to the *in situ* H-atom transfer reactions with **6.1** (Figure 6.6), exposure of **6.5** with excess 1,4-cyclohexadiene or 9,10-dihydroanthracene over the course of several days showed no reactivity or production of the respective H-atom transfer products by ^{1}H NMR spectroscopy. We hypothesized that the absence of the basic $P^V=O$ motif in **6.5** "turns off" the C–H bond reactivity in accordance with the proposed ROA mechanism. In order to test this hypothesis, we aimed to "turn on" the C–H bond reactivity of **6.5** through targeted oxidation of the phosphine ligand.

6.2.3 Oxygen-atom transfer reactions of pentafluorophenoxide substituted vanadium phosphine complexes.

Our investigation into the oxidation of the vanadium complexes led us to survey an array of O-atom transfer reagents. When addition of one equivalent of trimethylamine N-oxide was added to a DCM solution of **6.4a** or **6.4b**, quantitative conversion to the phosphine oxide was observed (**6.1a/b**) based on heteronuclear NMR spectroscopy. However, when trimethylamine N-oxide was added to a DCM solution of **6.5**, the corresponding $P^V=O$ oxidation was not observed (Scheme 6.5). Upon work-up of the reaction mixture, dark purple single crystals suitable for X-ray diffraction studies were grown by vapor diffusion of pentane into a concentrated DCM solution of **6.6.** The solid-state structure of **6.6** (Figure 6.11) revealed the formation of a bridging vanadium(V)-oxo motif with expulsion of the phosphine ligand. Similar to the starting material, **6.6** underwent dimerization through the phenoxide ligands – adopting a pseudo square pyramidal geometry around each vanadium center. The bond metrics of **6.6** are fairly

unremarkable; however, the trimethylamine byproduct of the O-atom transfer reaction was co-crystallized and closely associated with the vanadium oxo. Complex **6.6** was further characterized by heteronuclear NMR spectroscopy. The ^{51}V NMR spectrum displays a sharp singlet shifted to -375 ppm – characteristic of a deshielded vanadium center decorated with electron withdrawing ligands. The ^{19}F NMR spectrum exhibits equivalent and diagnostic *ortho*, *para*, and *meta* resonances. Lastly, the fate of the ejected phosphine ligand remains unknown, and could not be isolated.

Scheme 6.5: Survey of O-atom transfer reactions with **6.5** and subsequent reactivity.
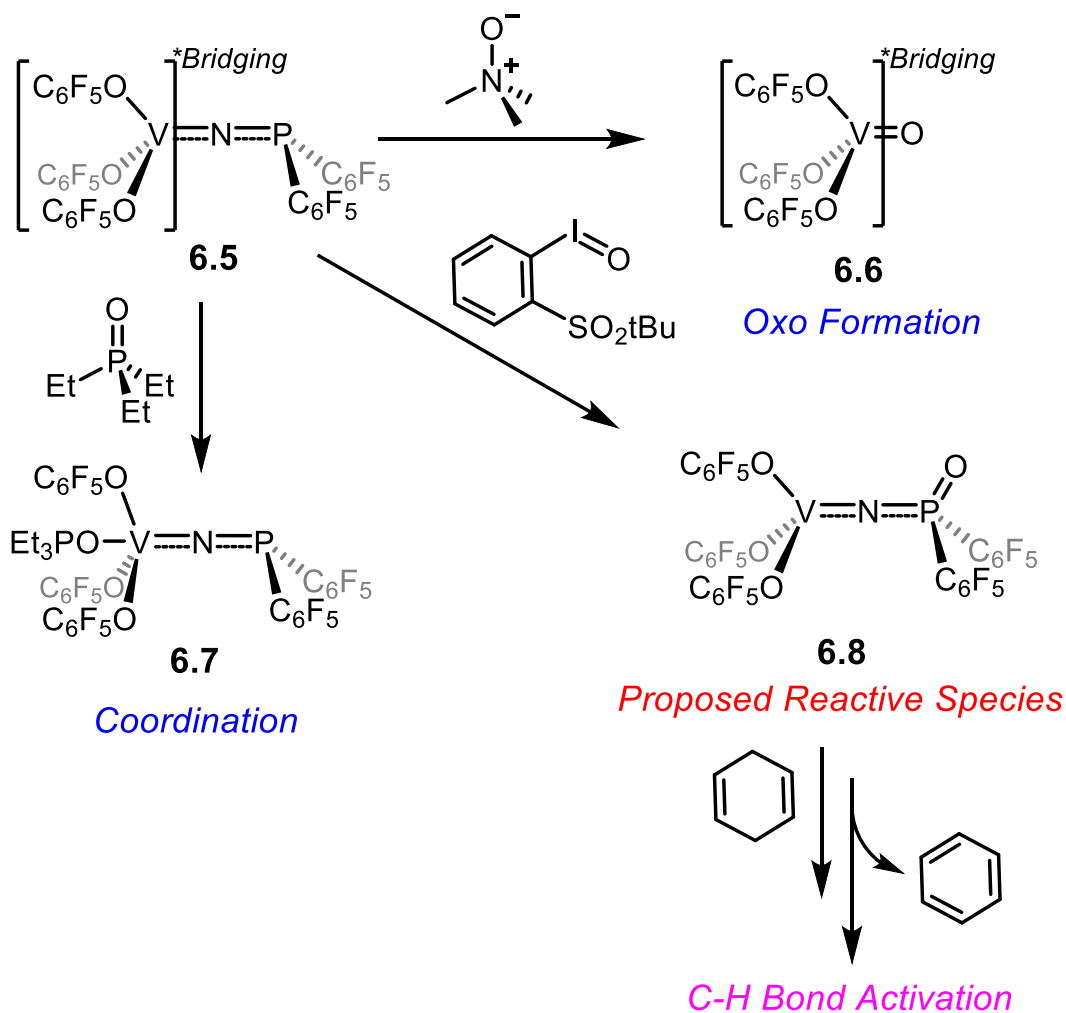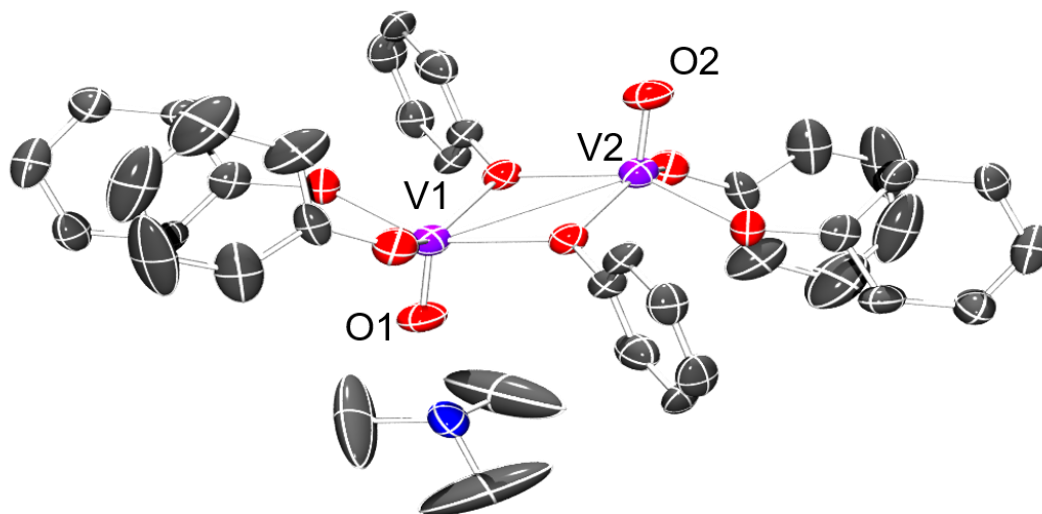
Figure 6.11: Solid-State molecular structure of **6.6**. Hydrogen atoms, fluorine atoms, and co-crystallized solvent omitted for clarity.

While the reaction with trimethylamine N-oxide did not lead to the desired P^V=O product, we were nonetheless intrigued by the isolation of **6.6**. Specifically, we were interested if **6.6** could undergo C-H bond activation through the V^V=O motif. Exposure of a solution **6.6** in d-DCM to excess 1,4-cyclohexadiene or 9,10-dihydroanthracene showed no signs of reactivity by ^{1}H NMR spectroscopy, indicating the C–H activation pathway through the V^V=O motif is not operable, and further supporting the proposed ROA pathway.

We next attempted to oxidize **6.5** using triethylphospine oxide. Addition of one equivalent of triethylphosphine oxide to a solution of **6.5** in DCM resulted in direct coordination to the vanadium(V) center and isolation of complex **6.7** (Scheme 6.5). The ^{51}V NMR spectrum exhibited a broad singlet at -106 ppm - shifted upfield by over 200

ppm relative to the starting material (-320 ppm). From the crude reaction, bright red x-ray quality crystals were grown over the course of a day. The solid-state molecular structure clearly shows that triethylphosphine coordination breaks apart dimerized **6.5** into a coordinately saturated monomer with pseudo trigonal bipyramidal geometry. While addition of triethylphosphine once again did not lead to the desired P^V=O product, it did indicate that **6.5** is susceptible to coordination by L-type ligands.[31] We also observed similar shifts in the ^{51}V NMR when **6.5** was exposed to coordinating solvents such as acetonitrile, diethyl ether, tetrahydrofuran (THF), and trimethylphosphine. Lastly, exposure of a solution of **6.7** in d-DCM to excess 1,4-cyclohexadiene or 9,10-dihydroanthracene showed no signs of reactivity.

In our survey of O-atom transfer reagents we noted promising reactivity with iodosylbenzene (PhIO). However, due to the insolubility of PhIO, which results from the polymeric structure derived from the intermolecular I–O bond[34-35], the reaction produced inconsistent mechanistic data regarding oxygen atom transfer from PhIO, as well as a mixture of oxidation products. To gain insight into the reaction products, the soluble 1-(*tert*-butylsulfonyl)-2-iodosylbenzene derivative (ArIO) was synthesized by introducing an intramolecular I–O bond to avoid the formation of polymeric structure (Scheme 6.5). Slow addition of one equivalent of ArIO to a bright orange slurry of **6.5** in hexanes led to the gradual formation of a dark yellow-green homogeneous solution over 12 h. Analysis by ^1H NMR spectroscopy clearly indicated the clean production of the O-atom transfer byproduct 1-(*tert*-butylsulfonyl)-2-iodobenzene (ArI). The ^{51}V NMR spectrum exhibited an upfield shifted (≈ 85 ppm) broad singlet at -405 ppm – which is consistent with the observed shifts between the isolated Ph_2N^- substituted vanadium phosphinate (**6.1a** - ^{51}V NMR = 117 ppm)

and vanadium phosphine (**6.4a** – ^{51}V NMR = 65 ppm) derivatives. The ^{31}P NMR spectrum also displayed a broad singlet at 15 ppm, which is similarly shifted upfield relative to the starting material (100 ppm), and is once again consistent with the ^{31}P NMR resonance shifts associated with **6.4a** and **6.1a** (63 ppm and -20 ppm respectively). Taken together, the heteronuclear NMR spectroscopy data suggests phosphine oxidation and formation of **6.8** (Scheme 6.5), which could not be isolated away from the ArI sideproduct, and is susceptible to decomposition at room temperature over the course of a day. The decomposition products remain unknown, and x-ray quality crystals could not be generated to confirm the solid state structure.

Despite lacking XRD characterization, we managed to study the reactivity of **6.8** with 1,4-cyclohexadiene using heteronuclear NMR spectroscopy. Over the course of several hours the reaction mixture changed from yellow-green to dark blue. Figure 6.12 shows the gradual production of the C–H activation product (benzene) from the reaction mixture (blue dot) integrating to about half an equivalent of **6.8**. The reaction was monitored for a total of 12 h, and the ^{19}F, ^{31}P, and ^{51}V diamagnetic resonance signals of **6.8** quickly went silent indicating the formation of a paramagnetic product similar to the *in situ* substitution reactions with **6.1** (*vide supra*). The O-atom transfer byproduct, ArI (Figure 6.12, yellow dots) shows no change over the course of 12 h. Additionally, all independent controls, such as ArIO with 1,4-cyclohexadiene in the absence of **6.8**, indicated no HAT reactivity.
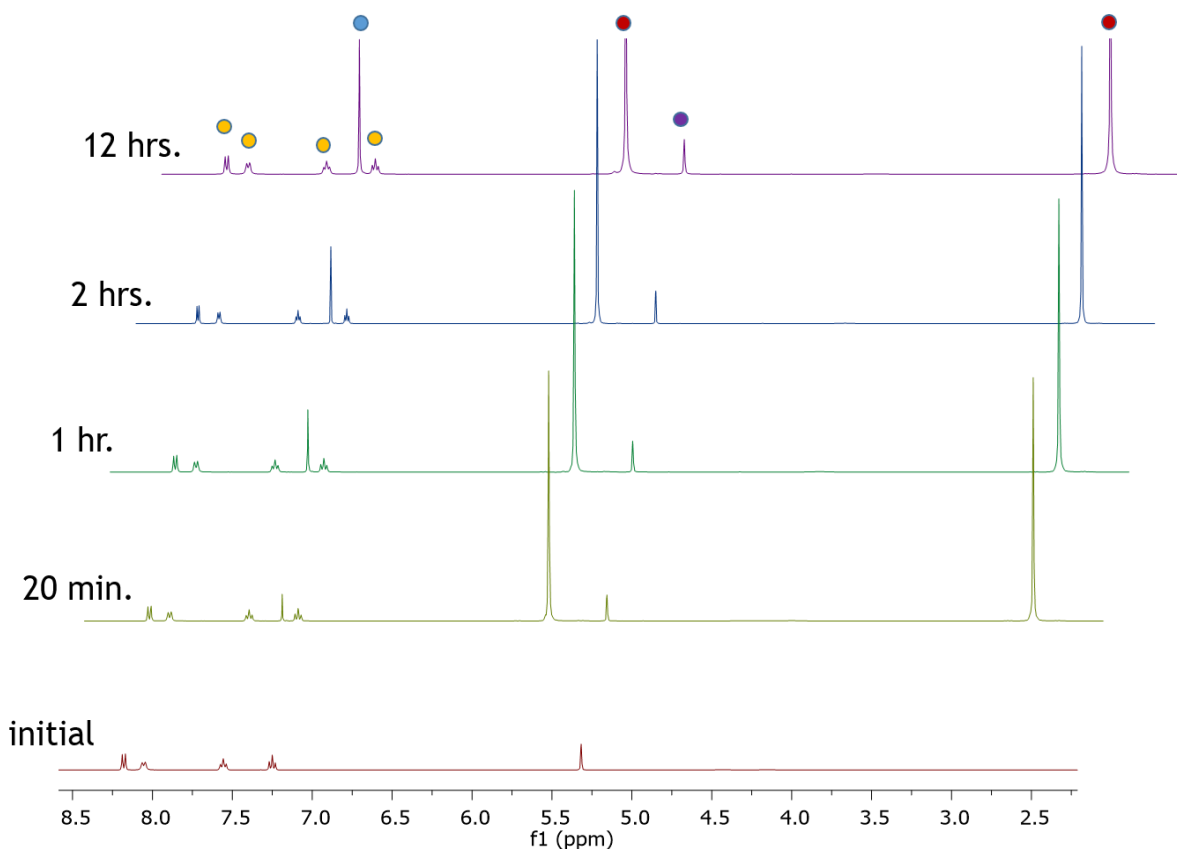
Figure 6.12: *in situ* ^{1}H NMR spectra taken at various timescales in d-DCM of the reaction mixture involving **6.8** and excess 1,4-cyclohexadiene. Blue dot = C$_6$H$_6$ (C–H activation product), yellow dot = 1-(*tert*-butylsulfonyl)-2-iodobenzene (O-atom transfer byproduct), red dot = 1,4-cyclohexadiene (excess HAD), purple dot = d-DCM.

6.3 Conclusion

In summary, we have investigated C–H bond reactivity involving electron deficient vanadium centers and P^V=O bonds - mimicking the proposed ROA/PCET mechanism for VPO catalysis. We have determined that the *in situ* substitution of the electron donating Ph$_2$N$^-$ ligands of **6.1** for electron withdrawing ligands increases the overall reduction

potential and enables new C–H bond reactivity with common HADs such as 1,4-cyclohexadiene and 9,10-dihydroanthracene. We have also shown that we can "turn-off" the C–H bond reactivity by removing the proposed reactive P^V=O motif and isolating vanadium phosphine derivatives (**6.5**). Furthermore, we have concluded that we can subsequently "turn-on" the C–H bond reactivity of **6.5** with judicious choice of O-atom transfer reagent. While addition of trimethylamine N-oxide and triethylphosphine oxide resulted in vanadium-oxo formation and direct coordination respectively, ArIO could be used to generate a reactive complex capable of activating the C–H bonds of 1,4-cyclohexadiene. Together, this study has provided experimental evidence supporting a ROA mechanism involving the proposed VPO support-initiated C–H bond functionalization (Scheme 5.1a), and may further benefit future studies in homogeneous or heterogeneous C–H activation chemistry.[36] Moreover, these results have highlighted new main group/transition metal based cooperative redox reactivity which may form the basis for new bond reactivity studies. In the future we aim to build and study more robust electron withdrawing ligand frameworks, such as tripodal tren derivatives, that can be more easily isolated and characterized.

6.4 Experimental Section

6.4.1 General Considerations

All manipulations were performed under an atmosphere of dry, oxygen-free N_2 or Ar by means of standard Schlenk or glovebox techniques (MBraun UNIlab Pro SP Eco equipped with a -38 °C freezer). Pentane, toluene, benzene, diethyl ether, tetrahydrofuran

(THF), and dichloromethane (DCM) were dried using an MBraun solvent purification system. Benzene-d_6, bromobenzene-d_5, and tetrahydrofuran-d_8 were purchased from Aldrich and dried over CaH_2 for several days prior to distillation. All solvents were degassed by freeze-pump-thaw and stored on activated 4 Å molecular sieves prior to use. Ph_2NH, ^nBuLi (1.6 M in Hexanes), $VCl_3(THF)_3$, Me_3SiN_3, $^iPr_2NH$, Ph_2POCl, Ph_2PCl, $(C_5Me_5)_2Co$, C_6F_5OH, $(CF_3)_3COH$, $(CH_3)_3NO$, Et_3PO, 1,4-cyclohexadiene, and 9,10-dihydroanthracene, were purchased from Aldrich, Strem, or other commercial vendors and were used as received. $(C_6F_5)_2POCl$,[37] $(C_6F_5)_2PCl$,[37] $(Ph_2N)_3VNLi(THF)_3$,[38] $C_{12}F_9OH$, were prepared according to literature procedures. Elemental analyses (C, N, H) were performed at the University of California, Berkeley using a Perkin Elmer 2400 Series II combustion analyzer.

NMR spectra were obtained on a Varian Unity Inova 500 MHz or Agilent Technologies 400 MHz spectrometer, and referenced to residual solvent or externally (^{19}F: $CFCl_3$; ^{51}V: $VOCl_3$; ^{31}P: 85% H_3PO_4). Chemical shifts (δ) are recorded in ppm and the coupling constants are in Hz. X-band EPR spectra were collected on a Bruker EMX EPR Spectrometer equipped with an Oxford ESR 900 liquid helium cryostat. A modulation frequency of 100 kHz was used for all EPR spectra and the data was plotted using SpinCount. UV-Vis spectroscopy was performed using a Shimadzu UV-2401PC spectrophotometer with quartz cuvettes equipped with air tight J-young adaptors.

Data was collected on a Bruker KAPPA APEX II diffractometer equipped with an APEX II CCD detector using a TRIUMPH monochromator with a Mo Kα X-ray source (α = 0.71073 Å). The crystals were mounted on a cryoloop with Paratone-N oil, and all data were collected at 100(2) K using an Oxford nitrogen gas cryostream system. A hemisphere

of data was collected using ω scans with 0.5° frame widths. Data collection and cell parameter determination were conducted using the SMART program. Integration of the data frames and final cell parameter refinement were performed using SAINT software. Absorption correction of the data was carried 2out using SADABS. Structure determination was done using direct or Patterson methods and difference Fourier techniques. All hydrogen atom positions were idealized and rode on the atom of attachment. Structure solution, refinement, graphics, and creation of publication materials were performed using SHELXTL or OLEX^2.

Cyclic voltammetry was performed on a CH Instruments 630E electrochemical analysis potentiostat, equipped with a 3 mm diameter glassy carbon working electrode, a Ag wire pseudo-reference electrode, and a Pt counter electrode with $[Bu_4N][PF_6]$ (0.1 M) supporting electrolyte solution in CH_2Cl_2. The glassy carbon working electrode was cleaned prior to each experiment by polishing with 1, 0.3, 0.05 mm alumina (CH Instruments) in descending order, followed by sonication in distilled water for two minutes. Background scans were conducted for each experiment in a solution containing only electrolyte, and was then subtracted from each experiment. All voltammograms were referenced to the Fc/Fc^+ redox couple.

6.4.2 Synthesis of Compounds

Synthesis of $(Ph_2N)_3VNPO(Ph)_2$ (6.1a). In the glovebox, a solution of $(C_6H_5)_2POCl$ (208 mg, 0.5 mmol) in 3 mL of benzene was added dropwise to a solution of complex $(Ph_2N)_3VNLi(THF)_3$ (415 mg, 0.5 mmol) in 10 mL of benzene and briefly shaken. The

resulting black solution stood at room temperature for 1 h. The LiCl precipitate was removed by filtration over celite using a fine porosity filter and the solvent was then removed *in vacuo*. The black residue was washed with cold pentane (2 x 5 mL) to afford a dark brown solid (400 mg, 0.42 mmol, 84% yield). Dark black crystals suitable for XRD studies were grown by slow vapor diffusion of pentane into a concentrated solution of **6.1a** in diethyl ether at room temperature.

¹H NMR (400 MHz, C_6D_6, 25 °C): δ = 7.55 (m, 4H; Ar*H* of Ph_2PO), 7.07-6.97 (m, 6H; Ar*H* of Ph_2PO), 6.94 (d, $^3J_{HH}$ = 8.0 Hz, 12H; *o*-Ar*H* of NPh_2), 6.89 (t, $^3J_{HH}$ = 8.0 Hz, 12H; *m*-Ar*H* of NPh_2), 6.77 (t, $^3J_{HH}$ = 7.2 Hz, 6H; *p*-Ar*H* of NPh_2). **¹³C** (100 MHz, C_6D_6, 25 °C): δ = 154.4 (*Ph*$_2$N), 135.2 (d, J_{PC} = 124.7 Hz; *Ph*$_2$P), 132.3 (s; *Ph*$_2$P), 131.7 (d, J_{PC} = 117.8 Hz; *Ph*$_2$P), 129.1 (*Ph*$_2$N), 125.3 (*Ph*$_2$N), 123.6 (*Ph*$_2$N). **⁵¹V** (105 MHz, C_6D_6, 25 °C): δ = -6.1 (br). **³¹P** (162 MHz, C_6D_6, 25 °C): δ = 19.9 (br m). **Anal. Calc.** for $C_{48}H_{40}N_4OPV$: C, 74.80; H, 5.23; N, 7.27. Found: C, 74.77; H, 5.14; N, 7.28.

Synthesis of $(Ph_2N)_3VNPO(C_6F_5)_2$ (6.1b). In the glovebox, a solution of Ph_2POCl (82.8 mg, 0.35 mmol) in 3 mL of THF was added dropwise to a solution of complex $(Ph_2N)_3VNLi(THF)_3$ (290 mg, 0.35 mmol) in 10 mL of THF and briefly shaken. The resulting black solution stood at room temperature for 1 h before the solvent was removed *in vacuo*. The black residue was extracted into benzene (8 mL) and filtered over a pad of celite. The filtrate solvent was removed *in vacuo* and the residue was recrystallized from ether at -35 °C over 24 h to afford a dark brown solid (260 mg, 0.322 mmol, 92% yield). Dark brown crystals suitable for XRD studies were grown by cooling a concentrated solution of **5.2b** in ether to -35 °C and standing overnight.

¹H NMR (400 MHz, C₆D₆, 25 °C): δ = 6.84 (m, 24H; *o*-Ar*H* and *m*-Ar*H*), 6.69 (m, 6H; *p*-Ar*H*). **¹³C** (100 MHz, C₆D₆, 25 °C): δ = 154.1, 128.9, 126.0, 123.0 (N*Ph₂*). The signal-to-noise ratio was too low for properly identifying any C₆F₅ ¹³C resonance. **⁵¹V** (105 MHz, C₆D₆, 25 °C): δ = 117.3 (br). **³¹P** (162 MHz, C₆D₆, 25 °C): δ = -20.0 (br m). **¹⁹F** (376 MHz, C₆D₆, 25 °C): δ = -131.6 (br, 4F; *o*-C₆F₅), -148.2 (br, 2F; *p*-C₆F₅), -160.3 (br, 4F; *m*-C₆F₅). **Anal. Calc**. for C₄₈H₃₀F₁₀N₄OPV: C, 60.64; H, 3.18; N, 5.89. Found: C, 60.64; H, 3.29; N, 5.91

Synthesis of (Ph₂N)(C₆F₅O)₂VNPO(Ph)₂ (6.2): In the glovebox, a bright red solution of **6.1a** (40.0 mg, 0.052 mmol) was prepared in 10 mL of DCM. A ten-fold excess of Nonafluoro-*tert*-butanol (122 mg, 0.520 mmol) was added neat dropwise. The resulting deep red solution was allowed to stir for 16 hrs. at room temperature and then dried *in vacuo*. The residue was brought up in hexanes (10 mL) and filtered through a pipette column of celite. The red hexanes solution was concentrated under vacuum to about 5 mL and then stored at -40°C for three days to afford dark red crystals suitable for XRD studies (15.0 mg, 0.014 mmol, 27% yield). The product is co-crystallized with hydrogen bound Ph₂NH.

¹H NMR (400 MHz, CD₂Cl₂, 25 °C): δ = 7.53 (m, 6H; *o*-Ar*H* and *m*-Ar*H*), 7.38 (m, 4H; *p*-Ar*H*), 7.29 (broad s, 4H, *m*-N(C₆H₅)₂) H-bound), 7.25 (t, 4H, *m*-N(C₆H₅)₂), 7.17 (broad s, 2H, *p*-N(C₆H₅)₂) H-bound), 7.05 (d, 4H, *o*-N(C₆H₅)₂), 7.02 (broad s, 4H, *o*-N(C₆H₅)₂) H-bound), 6.89 (t, 2H, *p*-N(C₆H₅)₂). **⁵¹V** (105 MHz, C CD₂Cl₂, 25 °C): δ = -245.7 (broad m). **³¹P** (162 MHz, C₆D₆, 25 °C): δ = 29.8 - 34.6 (br m). **¹⁹F** (376 MHz, CD₂Cl₂, 25 °C): δ = -74.9 (s, 18F; -C*F₃*).

Synthesis of (C₆F₅O)₄VOP(Ph)₂NH₂ (6.3a): In the glovebox, a solution of pentafluorophenol (36.0 mg, 0.200 mmol) in 5 mL of DCM was added dropwise to a dark black solution of **6.1** (40.0 mg, 0.047 mmol) in DCM (5 mL). The resulting solution was allowed to stir at room temperature for 4 hrs to yield a dark blue solution. The solvent was removed *in vacuo* and the residue was washed with pentane (10 mL) and hexanes (10 mL). The black residue was brought up in a minimal amount of DCM (2 mL) and layered with pentane (5 mL), and stored at -40°C. Repeated recrystallizations over the course of 2-weeks led to blue x-ray quality crystals suitable for XRD studies (6.00 mg, 0.006 mmol). The remaining byproducts of the reaction could not be isolated.

Synthesis of (C₁₂F₉O)₄VOP(Ph)₂NH₂ (6.3b): In the glovebox, a solution of nonafluorobiphenyl-2-ol (56.0 mg, 0.168 mmol) in 3 mL of DCM was added dropwise to a dark black solution of **6.1** (40.0 mg, 0.047 mmol) in DCM (5 mL). After 3 hours the solution turned a dark red. The reaction was allowed to stir for 24 hours until the solution turned a dark green/blue color. The solvent was removed *in vacuo* and the residue was washed with pentane (20 mL). The residue was brought up in a minimal amount of DCM (3 mL) and layered with pentane (5 mL), and stored at -40°C. Repeated recrystallizations over the course of 2-weeks led to blue x-ray quality crystals suitable for XRD studies (10.0 mg, 0.006 mmol). The remaining byproducts of the reaction could not be isolated.

Synthesis of (Ph₂N)₃VNPO(C₆F₅)₂ (6.4a). In the glovebox, a solution of (C₆F₅)₂PCl (421 mg, 1.05 mmol) in 5 mL of benzene was added dropwise to a stirring solution of complex (Ph₂N)₃VNLi(THF)₃ (830 mg, 1.05 mmol) in 30 mL of benzene. The resulting solution instantly turned black and was allowed to stand at room temperature for 1 h. The LiCl

precipitate was removed by filtration over celite using a fine porosity filter and the solvent was then removed *in vacuo*. The black residue was washed with cold pentane (3 x 10 mL) to yield **6.4a** as a black solid (740 mg, 0.79 mmol, 75.3% yield).

¹H NMR (400 MHz, CD$_2$Cl$_2$, 25 °C): δ = 7.06 (m, 12H; *m*-N*Ph₂*), 6.95 (t, 6H; *p*-N*Ph₂*), 6.71 (d, 12H; *o*-N*Ph₂*). **¹³C** (100 MHz, CD$_2$Cl$_2$, 25 °C): δ = 153.1, 128.5, 124.5, 122.6 (N*Ph₂*). The signal-to-noise ratio was too low for properly identifying any C$_6$F$_5$ ¹³C resonance. **⁵¹V** (105 MHz, CD$_2$Cl$_2$, 25 °C): δ = 61.8 (br). **³¹P** (162 MHz, CD$_2$Cl$_2$, 25 °C): δ = 64.5 (br s). **¹⁹F** (376 MHz, CD$_2$Cl$_2$, 25 °C): δ = -130.2 (t, 4F; *o*-C$_6$F$_5$), -150.7 (t, 2F; *p*-C$_6$F$_5$), -161.3 (m, 4F; *m*-C$_6$F$_5$). **Anal. Calc**. for C$_{48}$H$_{30}$F$_{10}$N$_4$PV: C, 61.68; H, 3.24; N, 5.99. Found: C, 60.54; H, 3.19; N, 5.91.

Synthesis of (Ph₂N)₃VNPO(Ph)₂ (6.4b). In the glovebox, a solution of (C$_6$H$_5$)$_2$PCl (53.0 mg, 0.241 mmol) in 3 mL of benzene was added dropwise to a stirring solution of complex (Ph₂N)₃VNLi(THF)₃ (200 mg, 0.241 mmol) in 10 mL of benzene. The resulting dark red solution stood at room temperature for 1 h. The LiCl precipitate was removed by filtration over celite using a fine porosity filter and the solvent was then removed *in vacuo*. The red residue was triturated with cold pentane (3 x 5 mL) to afford a dark red fluffy solid (110 mg, 0.146 mmol, 61% yield).

¹H NMR (400 MHz, CD$_2$Cl$_2$, 25 °C): δ = 7.28 (t, 2H; *p*-Ar*H*), 7.16 (t, 4H; *m*-Ar*H*), 6.98 (m, 12H; *m*-N*Ph₂*), 6.95 (m, 4H; *o*-Ar*H*), 6.94 (m, 6H; *p*-N*Ph₂*), 6.70 (d, 12H; *o*-N*Ph₂*). **⁵¹V** (105 MHz, CD$_2$Cl$_2$, 25 °C): δ = 25.0 (br). **³¹P** (162 MHz, CD$_2$Cl$_2$, 25 °C): δ = 142.0 (br s). **Anal. Calc**. for C$_{48}$H$_{40}$N$_4$PV: C, 76.38; H, 5.34; N, 7.42. Found: C, 76.12; H, 5.29; N, 7.81.

Synthesis of [(Ph$_2$N)$_3$VNPO(C$_6$F$_5$)$_2$][CoCp$_2$*] (6.4a$^-$). In the glovebox, a slurry of Cp$^*_2$Co (17 mg, 0.052 mmol) in 5 mL of hexanes was added dropwise to a stirring solution of complex **6.4a** (49.0 mg, 0.052 mmol) in 10 mL of Hexanes. After complete addition there was precipitation of a brown-orange solid. The mixture was stirred at room temperature for 30 minutes, then allowed to sit for 1 hr. prior to filtering through a fine porosity frit. The precipitate was washed with pentane (5 mL) and hexanes (10 mL) and dried *in vacuo* to afford an orange-red solid (40 mg, 0.032 mmol, 61% yield). Dark orange crystals suitable for XRD studies were grown by slow diffusion of pentane into a concentrated solution of **6.4a$^-$** in DCM at -40 °C.

Synthesis of [(C$_6$F$_5$O)$_3$VNP(C$_6$F$_5$)$_2$]$_2$ (6.5): In the glovebox, a solution of pentafluorophenol (213 mg, 1.156 mmol) in 5 mL of hexanes was added dropwise to a stirring solution of **6.4a** (360 mg, 0.385 mmol) in hexanes (30 mL). The resulting solution was allowed to stir at room temperature for 4 hrs. and a bright orange precipitate crashed out of solution. The mixture was filtered over a fine porosity frit and the precipitate was washed with pentane (10 mL), hexanes (30 mL), and chilled DCM (10 mL). The precipitate was collected and dried *in vacuo* to yield **6.5** as a bright red powder (330 mg, 0.340 mmol, 87.5% yield) Bright red crystals suitable for XRD studies were grown by slow vapor diffusion of pentane into a concentrated solution of **6.5** in DCM at -40°C.

^{51}V (105 MHz, CD$_2$Cl$_2$, 25 °C): δ = -315.9 (br). **^{31}P** (162 MHz, CD$_2$Cl$_2$, 25 °C): δ = 99.5 (br s). **^{19}F** (376 MHz, CD$_2$Cl$_2$, 25 °C): δ = -131.1 (m, 4F; *o*-C$_6$F$_5$), -144.4 (t, 2F; *p*-C$_6$F$_5$), -

158.3 (d, 6F; *o*-OC$_6$*F$_5$*), -158.7 (m, 4F; *o*-C$_6$*F$_5$*), -163.2 (m, 3F; *p*-OC$_6$*F$_5$*), -164.27 (m, 6F; *m*-OC$_6$*F$_5$*).

Synthesis of [(C$_6$F$_5$O)$_3$VO]$_2$ (6.6): In the glovebox, to a frozen slurry of **6.5** (30 mg, 0.030 mmol) in 5 mL of DCM, a solution of trimethylamine N-oxide (2.0 mg, 0.030 mmol) in DCM (2 mL) was added slowly dropwise. The mixture was allowed to slowly warm to room temperature, at which it completely solubilized and turned a deep purple color. The solution was allowed to stir for 30 minutes and then was dried *in vacuo* to yield a purple/black residue. The residue was washed with pentane (10 mL) and hexanes (10 mL). The residue was recrystallized by vapor diffusion of pentane over a concentrated solution of **6.6** in DCM at -40°C over the course of several days to yield dark purple crystals suitable for XRD studies (10 mg, 0.016 mmol, 51% yield).

^{51}V (105 MHz, CD$_2$Cl$_2$, 25 °C): δ = -369.4 (br). ^{19}F (376 MHz, CD$_2$Cl$_2$, 25 °C): δ = -159.3.1 (br, 6H; *o*-OC$_6$*F$_5$*), -166.8 (br, 6F; *m*-OC$_6$*F$_5$*), -169.0 (br, 3H; *p*-OC$_6$*F$_5$*).

Synthesis of (C$_6$F$_5$O)$_3$(Et$_3$PO)VNP(C$_6$F$_5$)$_2$ (6.7): In the glovebox, **6.5** (32 mg, 0.032 mmol) was partially dissolved in 5 mL of DCM. To the stirring slurry of **6.5** a solution of triethylphosphine oxide (4.0 mg, 0.032 mmol)in 2 mL of DCM was added dropwise. Upon addition the slurry instantly solubilized and turned a dark red color. The resulting solution was allowed to stir at room temperature for 4 hrs. and then the solvent was removed *in vacuo*. The red residue was washed with pentane (2 x 5 mL) and dried *in vacuo* to yield a gooey red solid (30 mg, 0.026 mmol, 84.3% yield) Bright red crystals suitable for XRD

studies were grown by slow vapor diffusion of pentane into a concentrated solution of **6.6** in DCM at -40ºC.

¹H NMR (400 MHz, CD_2Cl_2, 25 ºC): δ = 1.86 (m, 6H; -C*H₂*CH₃), 1.32 (m, 9H; -CH₂C*H₃*), 6.71 (d, 12H; *o*-N*Ph₂*). **⁵¹V** (105 MHz, CD_2Cl_2, 25 ºC): δ = 109.7 (br). **³¹P** (162 MHz, CD_2Cl_2, 25 ºC): δ = 76.43 (V=N=*P*, br s), 68.12 (Et₃*P*O, s) **¹⁹F** (376 MHz, CD_2Cl_2, 25 ºC): δ = -131.9 (m, 4F; *o*-C₆*F₅*), -148.2 (t, 2F; *p*-C₆*F₅*), -161.4 (d, 6F; *o*-OC₆*F₅*), -161.8 (m, 4F; *o*-C₆*F₅*), -168.2 (m, 3F; *p*-OC₆*F₅*), -170.3 (m, 6F; *m*-OC₆*F₅*).

6.5 References

(1)   Labinger, J. A.; Bercaw, J. E. *Nature*, **2002**, *417*, 507514

(2)   Bergman, R.; *Nature*, **2007**, *446*, 391-393

(3)   Dick, A. R.; Sanford, M. S. *Tetrahedron*, **2006**, *62*, 2439

(4)   Hartwig, J. F. *J. Am. Chem. Soc.*, **2016**, *138*, 2

(5)   Liu, W.; Yang, W.; Zhu, J.; Guo, Y.; Wang, N.; Ke, J.; Yu, P.; He, C.; *ACS Catal.*, **2020**, 7207-7215

(6)   Dong, Y.; Clarke, R. M.; Porter, G. J.; Betley, T. A. *J. Am. Chem. Soc.,* **2020**

(7)   Li, C.; Lang, K.; Lu, H.; Hu, Y.; Cui, X.; Wojtas, L.; Zhang, X. P. *Angew. Chem., Int. Ed*. **2018**, *57*, 16837.

(8)   Lu, H.; Hu, Y.; Jiang, H.; Wojtas, L.; Zhang, X. P. *Org. Lett.* **2012**, *14,* 5158.

(9)   Lu, H.; Jiang, H.; Hu, Y.; Wojtas, L.; Zhang, X. P. *Chem. Sci*. **2011**, *2*, 2361.

(10)   Lu, H.; Lang, K.; Jiang, H.; Wojtas, L.; Zhang, X. P. *Chem. Sci.* **2016**, *7*, 6934.

(11)   Lu, H.; Li, C.; Jiang, H.; Lizardi, C. L.; Zhang, X. P. *Angew. Chem., Int. Ed*. **2014**, *53,* 7028.

(12)   Chen, M. S.; White, M. C. *Science* **2007**, *318*, 783– 787

(13)   Hynes, J. T.; Klinman, J. P.; Limbach, H. H.; Schowen, R. L. *Hydrogen-Transfer Reactions*; Wiley-VCH: **2007**.

(14)   Darcy, J. W.; Koronkiewicz, B.; Parada, G. A.; Mayer, J. M. *Acc. Chem. Res.* **2018**, *51*, 2391– 2399.

(15)   Yosca, T. H.; Rittle, J.; Krest, C. M.; Onderko, E. L.; Silakov, A.; Calixto, J. C.; Behan, R. K.; Green, M. T. *Science* **2013**, *342*, 825– 829.

(16)   Choi, G. J.; Zhu, Q.; Miller, D. C.; Gu, C. J.; Knowles, R. R. *Nature,* **2016**, *539*, 268-271.

(17)   Darcy, J. W.; Kolmar, S. S.; Mayer, J. M. *J. Am. Chem. Soc.,* **2019**, *141*, 10777-10787.

(18)   Markle, T. F.; Darcy, J. W.; Mayer, J. M. *Sci. Adv.* **2018**, *4*, 5776.

(19)   Cheng, M.-J.; Goddard, W. A. *J. Am. Chem. Soc.* **2013,** *135*, 4600-4603.

(20)   Cheng, M.-J.; Fu, R.; Goddard, I. I. I. W. A. *Chem. Commun.* **2014,** *50*, 1748-1750.

(21)   Cheng, M.-J.; Goddard, W. A.; Fu, R. *Top. Catal.* **2014,** *57*, 1171-1187.

(22)   O'Leary, W. C.; Goddard, W. A.; Cheng, M.-J. *J. Phys. Chem. C.,* **2017**, *121*, 24069- 24076

(23)   Morton, C. A.; Zhu, Q.; Ripberger, H.; Troian-Gautier, L.; Toa, Z. S. D.; Knowles, R. R.; Alexanian, E. J. *J. Am. Chem. Soc.* **2019**, *141*, 13253-13260

(24)   Chu, J.; Carroll, T. G.; Wu, G.; Telser, R.; Dobrovestky, R.; Ménard, G. *J. Am. Chem. Soc.*, **2018**, *140*, 15375.

(25)   Pappas, I.; Chirik, P. J. *J. Am. Chem. Soc.* **2016,** *138*, 13379-13389.

(26)   Piper, T. S.; Wilkinson, G. *J. Inorg. Nucl. Chem.* **1956,** *3*, 104-124.

(27)   Kubas, G. J.; Kiss, G.; Hoff, C. D. *Organometallics* **1991,** *10*, 2870-2876.

(28)   Vlček, A. A. *Coord. Chem. Rev.* **1982**, *43*, 39-62

(29)   Warren, J. J.; Tronic, T. A.; Mayer, J. M. *Chem. Rev.* **2010,** *110*, 6961-7001.

(30)   Porter, T. R.; Capitao, D.; Kaminsky, W.; Qian, Z.; Mayer, J. M. *Inorg. Chem.* **2016,** *55*, 5467-5475.

(31)   Green, M. L. H. *J, Organomet. Chem.,* **1995**, *500*, 127-148

(32)   Fleming, I. Tilden Lecture.. *Chem. Soc. Rev.* **1981,** *10*, 83-111.

(33)   Connelly, N. G.; Geiger, W. E. *Chem. Rev.* **1996,** *96*, 877-910.

(34)   Nee M. W.; Bruice T. C. *J. Am. Chem. Soc.* **1982**, *104*, 6123–6125.

(35)   Zhdankin V. V.; Stang P. J. *Chem. Rev.* **2008**, *108*, 5299–5358.

(36)   Yang, J.-D.; Ji, P.; Xue, X.-S.; Cheng, J.-P. *J. Am. Chem. Soc.* **2018,** *140*, 8611-8623.

(37)   Sharova, E. V.; Genkina, G. K.; Matveeva, E. V.; Goryunova, I. B.; Goryunov, E. I.; Artyushin, O. I.; Brel, V. K. *Russ. Chem. Bull.* **2014,** *63*, 2546-2550.

(38)   Song, J.-I.; Gambarotta, S. *Chem. Eur. J.* **1996,** *2*, 1258-1263.